The University of Nottingham

Faculty of Engineering

CENTRIFUGE MODELLING OF THE GROUND REACTION CURVE IN FIBRE-REINFORCED SOIL

CRAIG MARK COX
BEng (Hons)

Thesis submitted to the University of Nottingham for the degree of Doctor of Philosophy

December 2014

ABSTRACT

The phenomenon known as the 'arching effect' occurs when a portion of granular mass yields relative to an adjacent stationary region. The movement is resisted by shearing stresses which act to reduce the pressure on the yielding support and increase the pressure on the adjacent stationary supporting zones. Arching is widely observed in both natural and man-made structures such as piled embankments, tunnelling, and above mine works and sinkholes.

In this research the arching effect is recreated in the increased gravity environment of a geotechnical centrifuge where the pressure distribution across both the yielding and supporting soil masses is measured and the resulting soil displacements observed. A motor driven 'trapdoor' apparatus was built inside a plane strain container to model the yielding support. Both the trapdoor and an adjacent support were instrumented to measure the force (and derived pressure) distribution. Soil and trapdoor displacements are determined by analysis of digital images taken in-flight through a Perspex wall of the container.

One method of increasing soil shear strength and its resistance to deformation is the reinforcement of soil with randomly distributed discrete fibres. The degree of improvement has been shown to be directly related to the fibre content in the soil, the fibre aspect ratio, orientation and mechanical properties.

In this research the effect of fibre reinforcement on the arching process and resulting deformation is examined by variation of fibre parameters such as fibre aspect ratio and volumetric content of fibre. The influence of fibre and model scale effects were investigated by conducting a modelling of models exercise whereby trapdoor scale and effective stress were varied whilst maintaining a constant cover depth to structure width ratio, and compaction effort.

The results were compared directly with those obtained for unreinforced soil trapdoor tests in order to determine the extent of improvement offered by fibre-reinforcement.

Intentionally blank page

ACKNOWLEDGEMENTS

During the course of the PhD I have received a great deal of help for which I would like to thank many people. Firstly, my supervisor Dr Alec Marshall without whose guidance, patience and time this whole process would have been a far more arduous and daunting task. Thanks to Dr Edward Ellis for gaining the initial support and backing for these studies and for his help during the early stages.

In the laboratory I have had considerable assistance from technical staff throughout. I would like to thank Jim Meakin, for his mechanical know-how and general good humour. Thanks to Mike Langford, for his assistance in model design. Thanks to Steve Lawton for his help with the tiresome task of preparing the fibres. I would like to thank Wenbo Yang, Itai Elkayam and Andrea Franza for their assistance, suggestions and time.

I would like to thank my father Steve Cox for his support, general advice and for getting me interested in engineering and the sciences in the first place.

Lastly and mostly thanks to Sarah Huggett for her enduring patience, love and support throughout.

Intentionally blank page

CONTENTS

Intentionally blank page

TABLE OF FIGURES

LIST OF TABLES

Intentionally blank page

NOTATION

Dimension and area

a = Width of pile cap (m).

A_{tu}. = Area of the tunnel face, (m^2)

B = Width of trapdoor (m)

d_f = Diameter of fibre (mm).

d_{xp} = Horizontal patch size (mm).

d_{zp} = Vertical patch size (mm).

d_{50} = Average particle size of the soil (mm).

F_L = Length of fibre (mm)

h_e = Embankment height (m)

H = Soil height measured from the trapdoor (m)

H_C = Critical height measured from the trapdoor (m)

p_{LS} = Lead-screw pitch (m)

S_{max} = Maximum settlement (mm)

S_{maxf} = Maximum settlement of fibre reinforced soil (mm)

S_{maxi} = Maximum settlement improvement (mm)

S_{maxu} = Maximum settlement of unreinforced soil (mm)

$S_{v(x)}$ = Vertical displacement of the soil at the distance, x, (m).

$S_v{}^*$ = Scaled vertical displacement of the soil, (m)

$S_{x(x)}$ = Horizontal displacement of the soil at the distance, x, (m).

$S_x{}^*$ = Scaled horizontal displacement of the soil, (m)

S_{xa} = Approximated horizontal displacement derived from the curve fitting process (m).

S_{xc} = Horizontal displacement derived from the curve fitting process (m).

s = Centre-to centre spacing of pile caps (m).

t = Thickness of shear band (m)

V_{sl} = Soil volume loss (m^2)

V_{slf} = Volume loss for fibre-reinforced soil (m^2)

V_{slu} = Volume loss for unreinforced soil (m^2)

V_{sli} = Improvement in soil volume loss (m^2)

w_f = Width of fibre (mm).

x = Distance from trapdoor centreline (m)

x_t = Distance to the tunnel centreline (m)

x_s, = horizontal displacement from direct shear test (m)

z = Depth in soil (m)

z_0 = Tunnel depth (m)

δ = Trapdoor displacement (m).

δ_{ed} = Differential settlement (m).

δ_{em} = Embankment settlement (m).

δ_s = Subsoil settlement (m).

Stress

σ_0 = Stress due to the infilling material beneath an arch (kN/m^2).

σ_h = Horizontal stress (kN/m^2).

σ_i = Stress at the interface between arch and in-fill material (kN/m^2)

$\sigma_n = \sigma_v$ = Normal (vertical) stress (kN/m^2).

σ_s = vertical stress acting on the subsoil (kN/m^2).

σ_{td} = vertical stress acting on the trapdoor (kN/m^2).

σ_r = Radial stress immediately beneath an arch (kN/m^2).

Material properties

c = cohesion intercept of the soil (kN/m^2).

e = Void ratio (dimensionless)

G_s = Specific gravity for silica soil.

I_D = Relative density of the soil.

K = Coefficient of lateral earth pressure for use in calculation of Equation 2.26

K_a = Active earth pressure coefficient.

K_P = Passive earth pressure coefficient.

M_E = Stress parameter used in calculation of macroscopic friction angle, $\bar{\phi}$ (-)

θ = Angle used for calculation of coefficient of lateral earth pressure (°).

v = Poisson’s ratio (-).

θ = Complementary friction angle (°)

θ_0= Inclinational angle of fibre (°)

θ_i= Angle of shear inclination (°)

ψ = Angle of soil dilatancy (°)

φ'= Angle of external shear plane (°)

ϕ = Friction angle of the soil (°)

$\bar{\phi}$ = Macroscopic internal friction angle of the soil (°)

ϕ_b = Friction angle of the soil at trapdoor width, *B*, (°).

ϕ_{fs} = Equivalent friction angle of fibre-reinforced soil (°).

ϕ_{pk} = Peak friction angle of the soil (°).

ϕ_r = Residual friction angle of the soil (°).

ϕ_W = Peak interface angle of friction between fibre and soil (°).

ρ_w = Density of fresh water (1000 kg/m^3)

ρ_s = Density of soil sample (kg/m^3)

γ_s = Unit weight of soil (kN/m^3).

Others

C = Value used for calculation of critical height, H_C

dx_p = Horizontal increment for calculation of strains (mm)

dz_p = Vertical increment for calculation of strains (mm)

E = Excitation voltage (V)

e_0 = Output voltage (V)

F_{TB} = Total force across all strain gauged beams, from F_{B1} to F_{B9} (N)

F_{Tg} = Theoretical total force acting on the beams at the design g-level, $F_{g1} = F_{gn}$ (N)

F_{TD} = Force acting on the trapdoor (N)

G = Strain gauge factor (-).

g = Acceleration due to Earth’s gravity (g = 9.81 m/s^2).

k_i = Constant related to the strength of the overburden material in above tunnel.

M_A = Modulus of initial arching (-)

$M_A{}'$ = Equivalent modulus of initial arching (-)

M_{Am} = Modulus of initial arching at model scale (-)

M_B = Secant Modulus of arching (-)

n = Number of fibres.

n_1, n_2 = Gear box ratios.

N = Scale factor of centrifuge model to prototype

N_{TD} = Motor speed (RPM)

p = Loading on trapdoor (N)

p^* = Normalised loading on trapdoor (-)

p_0 = Geostatic load on trapdoor (N)

$p_1 - p_9$ = Coefficients used for estimation of horizontal displacement.

p_m = Minimum loading on trapdoor (N)

p_s = Load on support structure (N).

p_{s0} = Geostatic load on support structure (N).

r_{fi} = Improvement ratio of fibre-reinforced to unreinforced soil (-).

R_{1-4}= Gauge resistances (Ω).

S = Soil strength (kN/m^2).

SF_v = Factor used for scaling vertical settlements (-)

SF_x = Factor used for scaling horizontal settlements (-)

T_{TD} = Torque requirement of the trapdoor mechanism (Nm).

t_f = Fibre-induced distributed tension (kPa).

V_{TD} = Volume of soil above the trapdoor (m^3)

v_{TD} = Velocity of trapdoor (mm/s)

ε_v = Volumetric strain (%)

ε_{xx} = Horizontal strain (%)

ε_{xz} = Shear strain (%)

ε_{zz} = Vertical strain (%)

γ = Engineering shear strain (%)

γ_a = Averaged engineering shear strain (%)

γ_e = Estimated engineering shear strain (%)

τ = Shear strength of the unreinforced soil (kPa).

τ_b = Shear strength of the unreinforced soil with trapdoor width, *B*, (kPa)

τ_{eq} = Equivalent shear strength of fibre-reinforced specimen (kPa).

τ_{fp} = Peak strength of the fibre-reinforced soil (kPa).

τ_{fr} = Residual strength of the fibre-reinforced soil (kPa).

τ_{pk} = Peak strength of the unreinforced soil (kPa).

τ_r = Residual strength of the unreinforced soil (kPa).

η = Fibre aspect ratio (-)

χ = Volumetric content of fibre (%)

χ_w = Fibre content by mass (%)

CHAPTER 1 INTRODUCTION

1.1 Soil arching

It is important for civil engineers to assess the effect that ground movements and consequent changes in local stress conditions may have on the stability of nearby structures.

In geotechnics, this generally applies to the problems of tunnelling, piled embankments and mine works. In granular soils, these activities can result in the formation of well-defined zones of displacing (yielding) and stationary (stable) soil.

This phenomenon, commonly known as arching, results in a significant decrease in pressure beneath the yielding portion of soil compared to the geostatic pressure. The pressure is redistributed such that the majority of the force is transferred from the yielding area to the rigid surrounding areas.

1.2 Fibre reinforced soils

One ground improvement technique finding increasing popularity with geotechnical engineers is soil reinforcement by inclusion of randomly mixed discrete fibres. Several studies (Maher and Gray 1990; Zornberg 2002; Michalowski and Cermak 2003) have been undertaken to determine the extent of improvement in shear strength offered by fibre reinforced soils (FRS) and to provide an analytical framework for studying FRS.

1.3 Centrifuge modelling

Numerical analysis has reached a level of sophistication and convenience in geotechnical engineering such that it can be used effectively for routine design. However, when design conditions are extreme or unfamiliar, rather than routine, or when response up to and including failure is required, their use is limited. In these cases, physical modelling of the whole system becomes the essential first step in understanding the event, and collecting data. Only then can the development of suitable methods of engineering analysis be undertaken.

Centrifuge testing concerns the study of geotechnical events using small-scale models subjected to acceleration fields of magnitude many times Earth's gravity. Scaled model experiments must be based on similarity laws derived from fundamental equations governing the phenomena to be investigated. Of critical importance is the stress/strain behaviour of granular soils, which is non-linear, and a function of stress level and stress history. In order to simulate the equivalent full scale 'prototype' accurately at small scale, the in-situ stresses must be reproduced correctly in the model.

In order to replicate the gravity induced stresses of a prototype in a *1/Nth* scale model, it is necessary to test the model in a gravitational field *N* times larger than that of the prototype. Thus, the dimensions and many of the physical processes can be scaled correctly if an *Nth* scale model is accelerated by *N* times the acceleration due to gravity.

1.4 Aims and objectives

The aim of the research presented was to investigate the effects of fibre reinforcement on buried structure loading, soil displacements, and failure mechanism.

The following objectives are to be met to satisfy this aim:

- Accurately model a ground loss structures subjected to sub-surface displacements in small scale centrifuge tests.
- Determine general loading characteristics, both on the buried structure and the adjacent support area.
- Form fibre-soil composites and investigate the general effect of randomly distributed fibre inclusion on the general behaviour of the soil subjected to a loss of support; focussing on redistribution of loading and displacements at the surface and throughout the soil depth.
- Compare the general failure mechanisms of unreinforced and fibre-reinforced soil in terms of volumetric and shear strains developed within the soil mass.
- Explore the effect of variation of key fibre properties.

- Investigate scaling effects of varying fibre to structure and soil grain size to structure ratios on loading and displacement characteristics.

1.7 Methodology

In order to meet the aims and objectives of this research a trapdoor apparatus was developed to simulate typical ground-loss situations in geotechnical centrifuge tests, whereby a loss of support in the overlying soil layer is induced by vertical displacement of the trapdoor. The loading on the trapdoor and the adjacent support structure is measured to define the load transfer mechanism. Soil displacements are determined using photogrammetry and compared to trapdoor displacements to investigate the induced changes in soil volume, and how displacements and strains are propagated to the surface.

Fibre-soil composites were prepared where the variables defining the strength behaviour of the composite were changed to determine the effect on the soil response in loading, displacement and strain terms.

The obtained results are then compared with results published in the literature.

1.8 Layout of the report

This thesis consists of six chapters. Chapter 1 has given a brief insight into the research topic. Chapter 2 contains the literature review and summarises some of the work carried out by researchers in the areas of soil arching and fibre-soil reinforcement. Chapter 3 details the experimental method. Chapter 4 presents the results. Trapdoor loading, displacements and strains for the unreinforced soil trapdoor tests are presented before moving on to detail fibre inclusion effects.

The results and their general implications are discussed in detail in Chapter 5 where comparisons are made between results and theoretical predictions. Conclusions and suggestions for further work are offered in Chapter 6.

Intentionally blank page

CHAPTER 2 LITERATURE REVIEW

2.1 Concept and application of soil arching

Soil arching has been described as “one of the most universal phenomena encountered in soil both in the field and in the laboratory” (Terzaghi, 1943).

Soil arching is mostly studied and encountered in piled embankments but is also recognised in underground structures, for example, tunnels and conduits. It also plays a role in geological structures like sinkholes. The arching action can be observed in underground openings and provides a reduction in the overburden pressure.

Substantial research has been carried out over the decades to gain an understanding of the mechanisms involved in arching, including; theoretical and analytical methods, numerical analyses, and experimental investigations. Although sporadic, much progress has undoubtedly been made. However, the phenomenon remains quite poorly understood and there is not yet a universal model that can be agreed upon by the international geotechnical community.

In soils arching occurs when there is an inclusion within a ground mass, or a yielding portion relative to adjacent supported areas (as shown in Figure 2.1). A loss of support occurs in the yielding area or inclusion causing deformation and a local redistribution of stress. This results in a decrease in loading over this area, as well as an increase over adjoining stiffer areas. The experimental setup used to recreate and study the phenomenon is sometimes called a ‘trapdoor’.

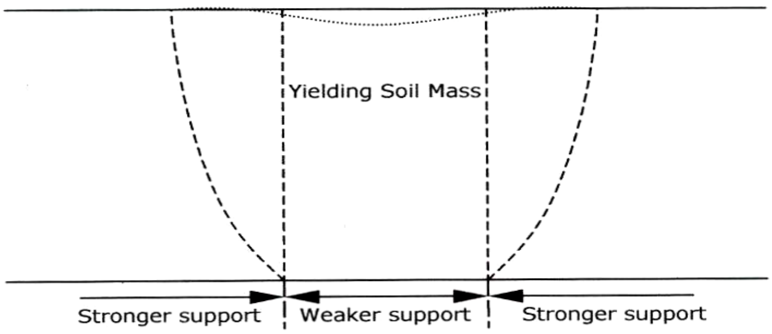

Figure 2.1: The ‘trapdoor effect’

As shown in Figure 2.1, if one part of a support system underlying a mass of soil displaces relative to a stationary section of support then some differential movement occurs within the soil (Terzaghi, 1943). This movement will set up shear planes within the soil above the displacing (weaker) and stationary (stronger) supports, indicated by the dotted lines in Figure 2.1. The shearing resistance acting on shear planes tends to keep the moving mass in its original position; it reduces the pressures on the displacing weaker supported area of soil and increases the pressures on the stationary stronger supports. This transfer of pressure from a yielding mass of soil onto adjoining stationary parts is commonly called the arching effect, and the soil is said to arch over the yielding part of the support" (Terzaghi, 1943).

The shape and mechanism of the formed arch is seldom agreed upon by researchers. Engesser (1882) postulates a parabola over the inclusion with the sides inclined, relative to the horizontal, at an angle equal to the friction angle of the granular medium. Terzaghi's (1943) theory, however, assumes that the shearing resistance of the soil during arching is mobilised along vertical planes through the sides of the inclusion.

2.2 Terzaghi's contributions

Terzaghi was the first to test and quantify the soil arching process experimentally. In his 'Theoretical Soil Mechanics' (1943) he argued that slightly lowering a narrow strip of trapdoor beneath a layer of soil will cause the soil overlying the trapdoor to yield. Terzaghi observed that the yielding material tends to settle, and this movement is opposed by shearing resistance along the boundaries between the moving and stationary mass of sand. As a consequence, the total pressure on the trapdoor is reduced whilst pressure on the adjoining supports is significantly increased.

Terzaghi postulated that as the trapdoor was lowered, the soil particles near to the top of the trapdoor move down with the trapdoor leaving behind void spaces. The void spaces left by these particles are then filled by the remaining particles that begin to settle. While the particles reposition themselves, due to their angularity, they begin to interlock with one another and a shear failure occurs on a sliding surface between the yielding mass of sand and the adjoining stationary sand mass. A significant proportion of the pressure previously exerted on the trapdoor is transferred onto the adjoining stationary platforms.

Since Terzaghi performed his simple yet effective trapdoor experiment, many other researchers and engineers have done similar but more complex experiments examining the arching concept even further. Hewlett and Randolph (1988), for example, investigated the arching concept in a three-dimensional case above piles with individual pile caps and showed that arching occurs in a three-dimensional dome with straight sides along the base, see Section 2.3. Iglesia et al (1999) investigated the effect using a trapdoor apparatus in a geotechnical centrifuge and postulated the loading profile on the trapdoor (detailed in Section 2.3) as well as postulating the shape of the vertical shear planes.

2.2.1 Terzaghi's arching theories

φ'

Terzaghi's theory of arching makes the assumption that the lateral load transfer occurs through the shear stresses along vertical soil planes emanating from the edge of the trapdoor. An expression for the change in vertical stress, $d\sigma_v$, due to change in height, dH, in a 2-dimensional case (infinitely long trapdoor) is given by Equation 2.1.

$$d\sigma_v = \left(\gamma_s - 4\frac{S}{B}\right)dH \qquad (2.1)$$

Where:

B = Width of trapdoor (m)

σ_v = Vertical stress in the soil above the trapdoor, at depth, $z = H - dH$, (kN/m^2)

H = Soil height measured from the trapdoor (m)

S = Soil strength (kN/m^2)

γ_s = Unit weight of soil (kN/m^3).

The soil shear strength along a vertical plane is given by:

$$S = \sigma_h \tan\phi + c \qquad (2.2)$$

Where:

c = cohesion intercept of the soil (kN/m^2)

σ_h = Horizontal stress at depth z, (kN/m^2)

ϕ = Friction angle of the soil (°)

The horizontal stress is related to the vertical stress by Equation 2.3.

$$\sigma_h = K\sigma_v \qquad (2.3)$$

Where:

K = Coefficient of lateral earth pressure

Mckelvey (1994) also performed similar research, and confirmed Terzaghi’s findings. Equation 2.4 is the stress acting on the soft ground trapdoor for a cohensionless soil without any surcharge (Mckelvery 1994):

$$\sigma_v = \frac{B\gamma_s}{2K\tan\phi}\left(1 - e^{-2K\tan\phi H/B}\right) \quad (2.4)$$

The value of K used in Equation 2.4 is the source of some disagreement between those who have studied the phenomenon as the stress state of the soil in the arching zone is still not fully understood. The most commonly used is the active lateral earth pressure coefficient, K_a , proposed by Terzaghi in Equation 2.5.

$$K = K_a = \frac{1 - \sin\phi}{1 + \sin\phi} \quad (2.5)$$

Handy (1985) proposed the modification given by Equation 2.6.

$$K = 1.06(\cos^2\theta + K_a\sin^2\theta) \quad (2.6)$$

Where:

$$\theta = 45° + {}^{\phi}/_{2} \quad (2.7)$$

Iglesia et al (1990) proposed the formulation given by Equation 2.8.

$$K = \frac{1 - \sin^2\phi}{1 + \sin^2\phi} \quad (2.8)$$

Jaky’s coefficient of earth pressure at rest may also be used from Equation. 2.9.

$$K = 1 - \sin\phi \quad (2.9)$$

Figure 2.2 shows the vertical stress acting on the trapdoor at the base of the embankment calculated using Equation 2.4 with the coefficients of lateral earth pressure of unity and those given by Equations 2.5 to 2.9 and an embankment height, H, of 5 m.

With a trapdoor width of 3 m, the value of the vertical stress acting on the trapdoor increases from 30 kN/m^2 (with $K = 1$) to 60 kN/m^2 using the active earth pressure coefficient from Equation 2.5. The sensitivity of Equation 2.4 is clearly illustrated by the disparity between different estimates of vertical stress based on different formulations of K.

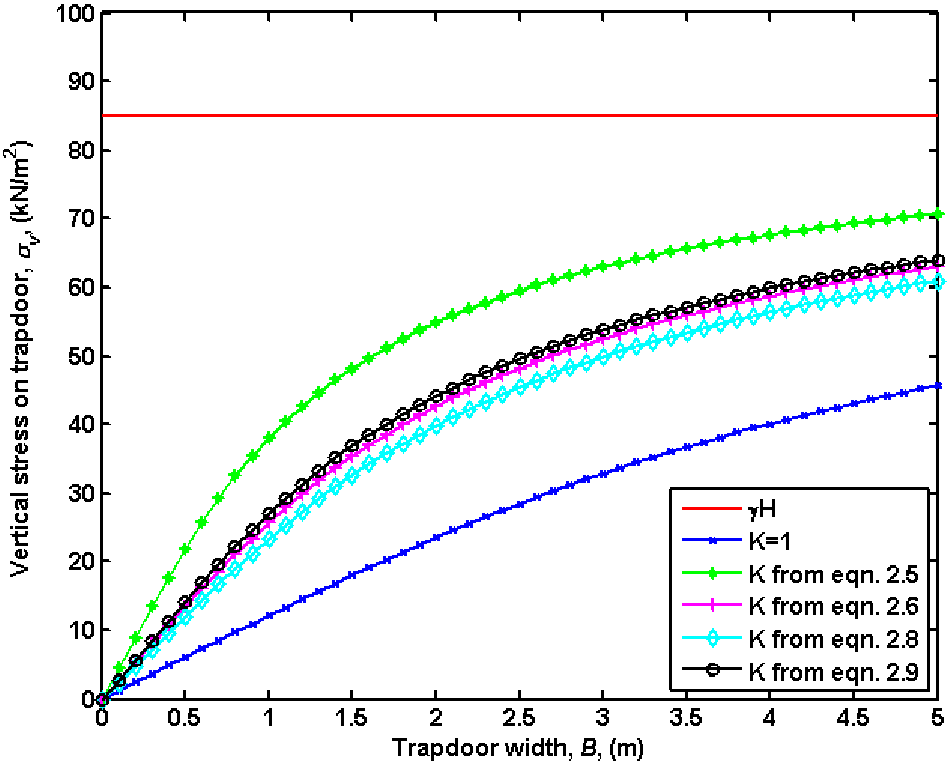

Figure 2.2 Vertical stress vs trapdoor width, varying K

2.3 Semi-circular arching

Hewlett and Randolph also investigated the arching theory. In the general case of a piled embankment, a section through which is shown in Figure 2.3. From experimental evidence, Hewlett and Randolph (1988) postulated that a piled embankment is supported by three distinct actions. Firstly, the piles reinforce and stiffen the underlying subsoil. Secondly, the piles give direct support to the embankment by means of arching action between adjacent pile caps. Thirdly, where a geogrid is used, and laid over the pile caps, its tension will provide support and prevent lateral spreading of the embankment.

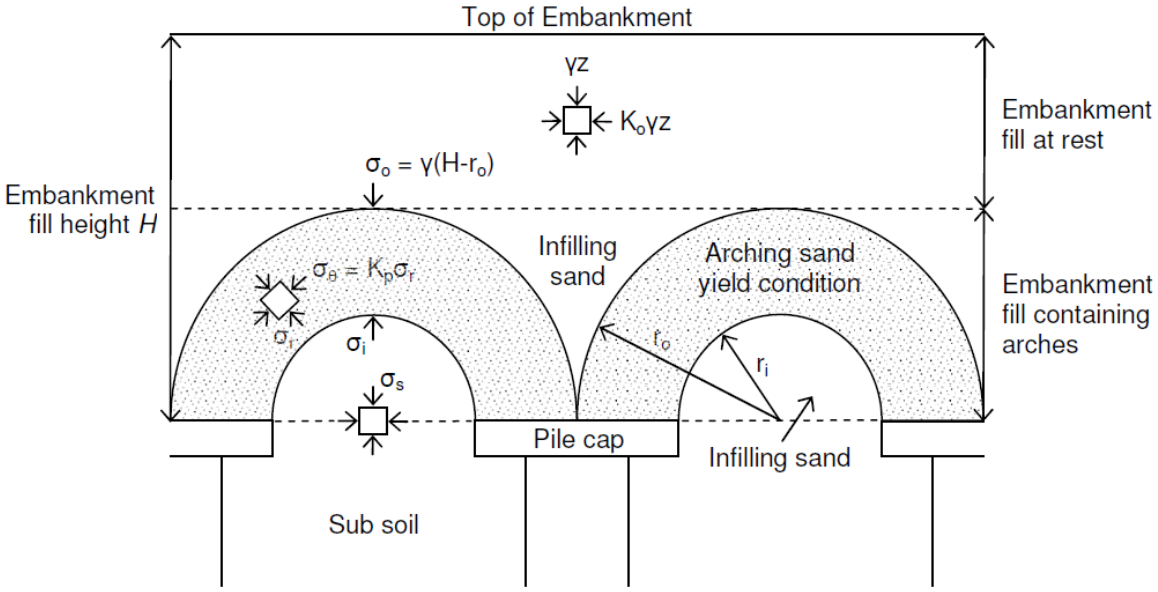

Figure 2.3 Section through piled embankment (Hewlett and Randolph, 1988)

The method considers actual arches in the soil, as shown in Figure 2.4 rather than vertical boundaries as considered by Terzaghi. These arches transmit the majority of the embankment load onto the pile caps, with the subsoil carrying the load from only the infill material below the arches. The arches are assumed to be semi-circular (in 2D) and of uniform thickness, with no overlap of arches (Hewlett and Randolph, 1988). The method also assumes uniform pressure acting on the subsoil. In each arch, the tangential (horizontal) direction is the direction of major principal stress and the radial (vertical) direction is the direction of minor principal stress, related by the passive earth pressure coefficient, K_P.

Hewlett and Randolph (1988) state that static equilibrium calls for the arches to be semi-circular, of uniform thickness and span adjacent pile caps with no overlap of the arches (as shown in Figure 2.3). It assumes the soil arching as a series of domes, with uniform stress state around each arch, supported by the pile caps.

Hewlett and Randolph (1988) proved that for the 2D case the critical point in the arch is either at the crown or the pile cap thus checking other points is unnecessary. The analysis considers equilibrium of an element at the ‘crown’ of the soil arch (see Figure 2.3). The vertical stress acting on the subsoil, σ_s, can be determined by consideration of the vertical equilibrium of this element, and applying the boundary condition that the stress acting on the arching layer at the crown is equal to the weight of material above acting on the outer radius of the arch.

$$\sigma_s = \sigma_i + \frac{\gamma_s(s-a)}{2} \qquad (2.10)$$

Where:

σ_i is the stress at the interface between arch and in-fill material (kN/m^2)

Considering the pile cap of Figure 2.3, the tangential (horizontal) stress is the major principal stress, and the radial (vertical) stress is now the minor principal stress (the reverse of the situation at the crown). The value of subsoil stress, σ_s, is obtained by considering the limit condition where the ratio of the major to minor stress is equal to $\mathrm{K_P}$. However, yielding of the subsoil occurs in an active condition where the radial (vertical) stress is the major principal stress. Calculation of σ_i involves consideration of the pile cap geometry, specifically the ratio of pile cap width to pile spacing, $^a/_s$. In a piled embankment this factor determines the width of the arch, which, in this method, is limited to $^a/_2$ due to the arching action taking place between the same pile cap and adjacent pile (see Figure 2.3). The width of the arch is unlimited by adjacent arching action when considering other types of ground inclusion such as those simulated using a trapdoor.

2.4 Other arching mechanisms

Whilst there is general agreement that the frictional properties of the soil are the root cause of arching, the postulated shape and mode of soil deformation is the subject of debate. Terzhagi (1943) and McKelvey (1994) assume a rectangular prism of soil above the void. The ‘Guido method’ first introduced by Guido et al (1987) and later investigated by Russell & Pierpoint (1997) postulates that the arch is a triangular shape with a 45º ‘load spread’ angle. This method was developed considering multiple layers of geogrid reinforcement in the soil, so may not be applicable to the unreinforced arching case. Carlsson (1987) and Han & Gabr (2002) assume a trapezoidal shape with an internal apex angle of

30°. Naughton (2007) uses a critical height approach where the height is a function of the friction angle. As already considered in Section 2.3, Hewlett and Randolph (1988) assume semi-circular arches forming in a piled embankment situation where only the critical point of the arch need be considered.

The British Standard BS8006 calculates average stress on the pile cap itself rather than that applied to the subsoil. BS8006 uses a modified form of Marston's equation for positive projecting subsurface conduits to calculate the ratio of vertical stress acting on top of the pile caps to the average vertical stress at the base of the embankment. The BS8006 method was initially developed by Jones et al. (1995) for designing geosynthetic reinforced piled embankments.

Whereas other researchers have chosen one shape to represent the 'arch', centrifuge tests performed by Iglesia et al (1999) on underground structures suggest that the arch goes through a series of stages, as shown in Figure 2.4. This sequence of arching led to the creation of Iglesia's Ground Reaction Curve (GRC) shown in Figure 2.5, for a 2D situation.

This is plotted as stress on an underground structure (normalised by the nominal overburden stress) as this varies with displacement of the structure roof (normalised by width of the structure, *B*).

2.4.1 Introduction to the Ground Reaction Curve

The arching theories considered thus far approximate the shape of the formed arch with a single shape. Iglesia et al (1999) showed that the arch goes through a series of stages by combining experimental data from centrifuge trapdoor tests with existing arching theories. Central to the approach is the 'ground reaction curve' (GRC), which is essentially the variation in stress acting on an underground structure (or subsoil) as the structure deforms, giving rise to arching conditions. Iglesia's 1999 work suggests the arch goes through a series of transformations between circular, triangular and prismatic stages (similar to Terzaghi's sliding block) before coming to rest or collapsing.

As illustrated in Figure 2.4, as the trapdoor is gradually lowered, representing deformation of the structure or subsoil, an arch evolves from an initially semi-circular shape (1) to a triangular one (2), before ultimately collapsing with the appearance of a prismatic sliding mass bounded by two vertical shear planes emanating from the side of the trapdoor (3), (Iglesia et al., 1999).

Compared to analysis of a piled embankment the trapdoor structure is analogous to the soft yielding subsoil being reinforced by the piles. The trapdoor mechanism can also be applied to other ground-loss scenarios caused by mining extractions, tunnel or conduit volume loss or, at large displacements, sinkhole phenomena.

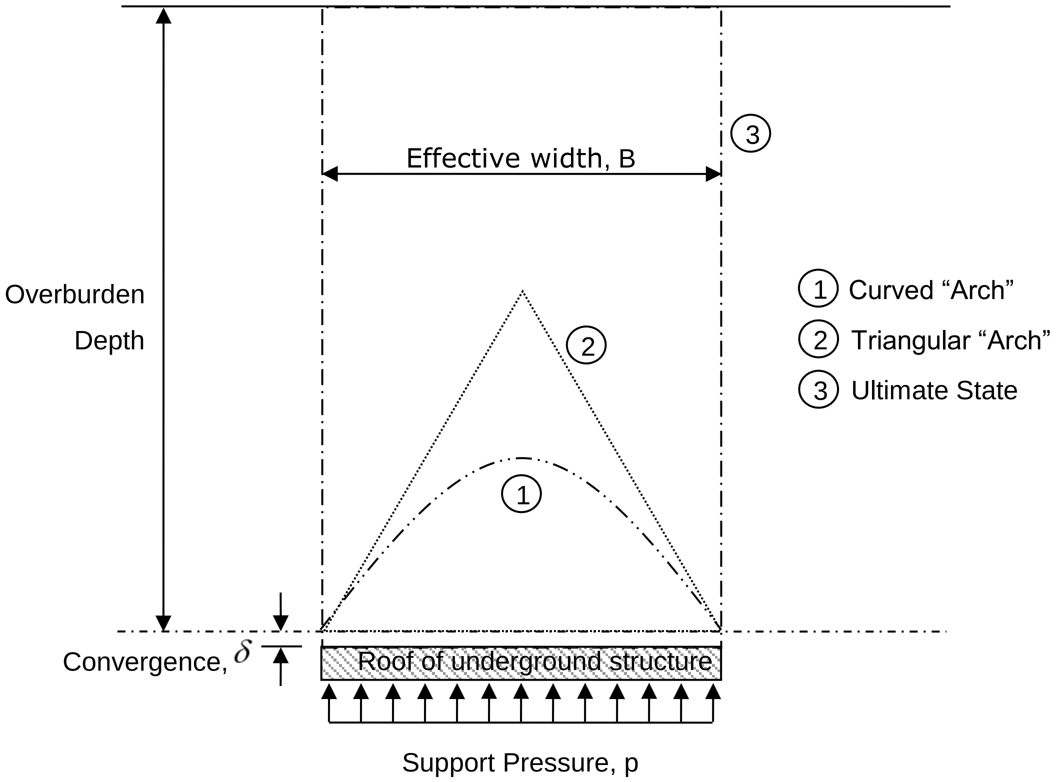

Figure 2.4 Arching evolution (Iglesia et al., 1999)

The GRC is the characteristic curve of stress to displacement. A dimensionless stress (p^*), normalised by the nominal overburden stress, $\gamma_s H$, is plotted against displacement (δ^*) normalised by trapdoor width,:*B*

$$p^* = \frac{p}{\gamma_s H} \qquad (2.11)$$

$$\delta^* = \frac{\delta}{B} \qquad (2.12)$$

Where:

p is the vertical stress on the roof of the structure (kN/m^2)

δ is the settlement of the structure (m)

The GRC is shown Figure 2.5 illustrating loading during the evolution of the arch and is divided into four parts (described in detail below) – the initial arching phase, the maximum arching (minimum loading) condition, the loading recovery stage, and the ultimate state.

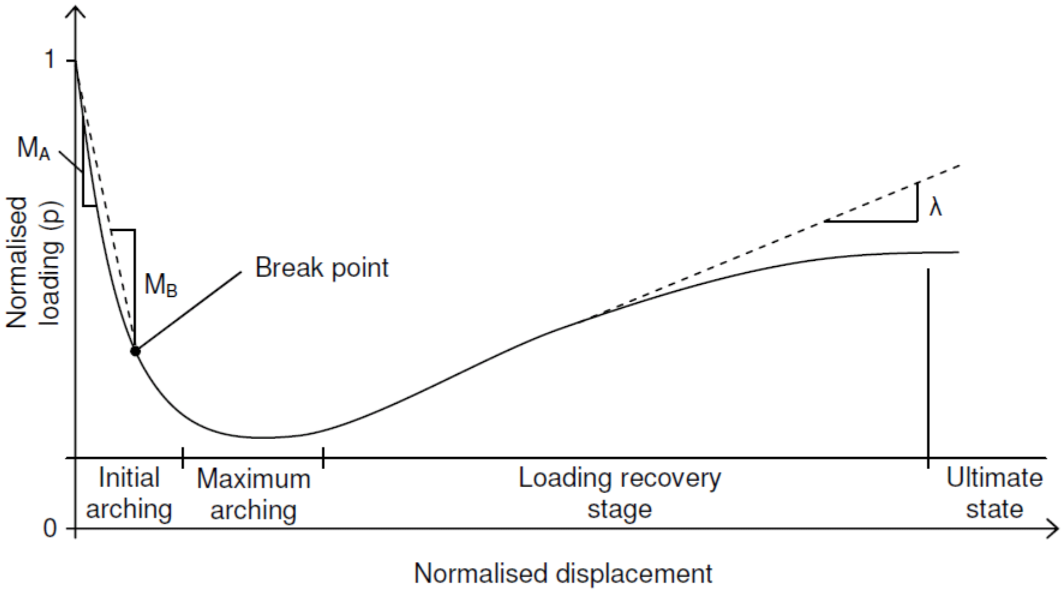

Figure 2.5 Generalised ground reaction curve (GRC) (Iglesia et al,1999)

1 Initial arching

The GRC starts with the geostatic condition where the loading is equal to the overburden stress ($p_0 = \gamma_s H$). The initial response to subsoil or trapdoor structure displacement is extremely stiff, as the stress acting on it is significantly reduced with small relative displacement. Iglesia postulates that a semi-circular arch begins to form over the trapdoor at this phase. The modulus of initial arching, M_A, is defined as the initial rate of stress decrease. Iglesia proposes a value for the modulus of around 125 (for the normalised plot) based on centrifuge trapdoor experiments with granular media. This effectively means for a displacement of only ~0.1% of the trapdoor width, the stress acting on the trapdoor is reduced by 1/8th.

2 Break point and maximum arching

Iglesia et al (1999) observed that the break-point of the curve appears to occur at displacements of around 1% trapdoor width. The breakpoint can be estimated using a straight-line fit from the geostatic intercept at a slope of ~63 (the ‘secant’ modulus, M_B, from Figure 2.5) to a normalised trapdoor displacement of 1%.

As can be seen in Figure 2.5, as the underground opening converges towards a state of maximum arching (minimum loading), the GRC changes from this approximately linear phase to a curve (since p^* can only approach zero and certainly cannot be negative).

Iglesia et al. (1999) propose a method of determining the approximate shape of this part of the curve in their original paper. Equation 2.13 gives an expression for the minimum loading, p_m normalised by the geostatic load:

$$\frac{p_m}{p_0} = \frac{B}{H}\left(\frac{K}{2\cot\phi + \frac{B}{H}K} + \frac{\cot\phi}{6}\right) \quad (2.13)$$

Maximum arching occurs when the vertical loading on the underground structure reaches a minimum, as shown in the figure. Iglesia et al. (1999) describe this as corresponding to a condition in which a physical arch forms a parabolic shape immediately above the underground structure. This state is proposed to occur when the relative displacement between the yielding underground structure and the surrounding soil is about 2 to 6 % of the effective width of the structure.

3 Loading recovery stage

This stage is the transition from the maximum arching (minimum loading) condition to the ultimate state in Figure 2.5. Iglesia et al. (1999) illustrate this transition might be linear in idealisation and characterised by the load recovery index (λ). This aspect of behaviour is potentially of considerable significance, since it represents a breakdown in arching response, where arching becomes increasingly less effective as displacement increases. Iglesia proposes that the load recovery increases with trapdoor width to average grain size ratio,

${}^{B}/_{d_{50}}$.Equation 2.14 gives an estimate for the load recovery index, λ, empirically derived from centrifuge tests in Iglesia et al (1999).

$$\lambda = \left[2.5 + 5.7 \log \frac{B}{10 d_{50}}\right] e^{-0.65(H/B)} \qquad (2.14)$$

4 Ultimate state

As the surrounding soil continually 'converges' toward the underground structure, the arch will eventually collapse. A prismatic sliding mass will emerge, which is bounded by a pair of vertical shear planes (Figure 2.5).

Iglesia et al. use Equation 2.4 (Terzaghi's method for 2D situation) to determine the ultimate stress on the structure.

Further detail regarding the centrifuge tests conducted and theoretical derivations for the stresses at various key stages of the GRC can be found in Iglesia et al (1999 and 2014).

2.4.2 Other trapdoor experiments

Evans (1983) conducted a number of different trapdoor experiments at 1*g* using different trapdoor geometries and *H/B* ratios. The proposed mechanism of active arching and failure is presented in Figure 2.6, (a) represents the direction of major principal stress, σ_1, acting throughout the soil layer. Evans and others have proposed a triangular region forms above the trapdoor with displacement where significant dilation occurs. The direction σ_1 is generally assumed to be horizontal in the region above the trapdoor. Areas of soil adjacent to the trapdoor receive stress transferred from the zone of soil above the trapdoor, whilst the horizontal stresses in the soil above the supporting area increased, allowing some lateral expansion and undergoing vertical contraction. Figure 2.6 (b) illustrates the direction of major principal stress throughout the plastically deforming field. Soil above the trapdoor is in the active state whilst above the support it is passive. When the angle of dilatancy, ψ, is close to the angle of friction; $\psi{\sim}\phi$, a mechanism like that illustrated in Figure 2.6 (c) is taking place where the components of shear and normal forces , T and N in the illustration respectively, acting on the edges of the differential element are equal and opposite in magnitude, contributing no net vertical force (Evans, 1983). The force acting on the trapdoor will then only result from the weight of the material within the free-body defined by the triangular area with an apex angle equal to 2ψ. A solution for the force acting on the trapdoor in the transitional phase, where the dilatancy angle is in the range; $0 < \psi < \phi$, is not readily apparent since the stresses on the side boundaries of the elements are related by the long form expression for shear strength, given in Equation 2.15.

$$\tau = \sigma_n \frac{\cos\psi \sin\phi}{1 - \sin\psi \sin\phi} \quad (2.15)$$

$$\tau = \sigma_n \sin\phi \quad (2.16)$$

It is not known what value of normal stress σ_n to use in this region, since the true value of ϕ lies between peak, ϕ_{pk} and residual estimates, ϕ_r. Evans (1983) reasonably suggests that the value of force acting on the trapdoor lie within the limits set by the conditions where $\psi = \phi_{pk}$ and $\psi = 0$.

The force acting on the trapdoor when $\psi = 0$, as shown in Figure 2.6 (d), can be approximated by considering the reduced expression for shear strength given in Equation 2.16. Where σ_n can be approximated using the expression for vertical stress, σ_v provided by Terzaghi in Equation 2.4. This is the ultimate stage where shear has occurred along vertical planes (as postulated by Terzaghi (1943), Jaky (1944) in Section 2.1.1 and Iglesia (1999) in Section 2.3.1).

A number of researchers have used both physical and numerical models of active trapdoor systems to investigate the arching phenomenon. Koutsabeloulis and Griffiths (1989) developed a numerical model of the trapdoor. Stone and Muir Wood (1992) used a physical model of a trapdoor to investigate particle size and dilatancy effects in centrifuge tests. Santichaianaint (2002) conducted physical modelling tests with circular trapdoor geometries. These researchers reported responses for systems under deep and shallow conditions, as characterised by soil cover ratios, H/B. Costa et al (2009) investigated failure mechanisms in sand over a deep active trapdoor in both 1*g* and 45*g* centrifuge models

Figure 2.7 shows a schematic of the shape of a typical failure surface reported in studies involving shallow conditions. A single failure surface is reported to initiate from the corners of the trapdoor propagating towards the centre, from point *O* to *A* in Figure 2.7. The inclination of the failure surface to the vertical in the vicinity of the trapdoor edge is represented by the angle, θ_{i-OA}, which equals the soil dilatancy angle, ψ, at point *O.* The path followed by the surface *OA* is defined by the soil density and its confinement, which are variables that govern the soil dilatancy (Costa et al, 2008). As the trapdoor displaces further; a new failure surface is developed at inclination θ_{i-OB} from the trapdoor edge, propagating towards point *B.* The angle of dilatancy reduces further as the trapdoor is displaced until it reaches zero and the failure surface extends vertically from the trapdoor edge; from point *O* to point *C*. Since the stress level at point *A* in the soil is lower than at the trapdoor edge, the dilatancy angle at *A* is consequently larger. This is represented in Figure 2.7 by the increase in angle θ_{i-A} over θ_{i-OA}. The failure surface exhibits a curved shape which has been attributed to the effect of overburden stress with depth on dilatancy.

For relatively large trapdoor movements, the soil can be assumed to have reached the ultimate state and achieved critical state conditions, consistent with the development of a vertical failure surface. Reported results under shallow conditions, where: $H/B \leq 1.5$, show that the angle θ_i is approximately constant with displacement. Shearing in this case was reported to suddenly stop in the failure surface and to immediately continue in the subsequent one (Stone and Muir Wood, 1992). Costa et al (2009) report that under deep conditions, $H/B > 1.5$, the angle θ_i gradually decreases with increasing trapdoor displacements. This mechanism in essence is very similar to that reported by Iglesia et al (1999) where the arch shape for a given trapdoor displacement is determined by the shear surface initiating at the trapdoor corners (see Figure 2.4 for comparison with Figure 2.7).

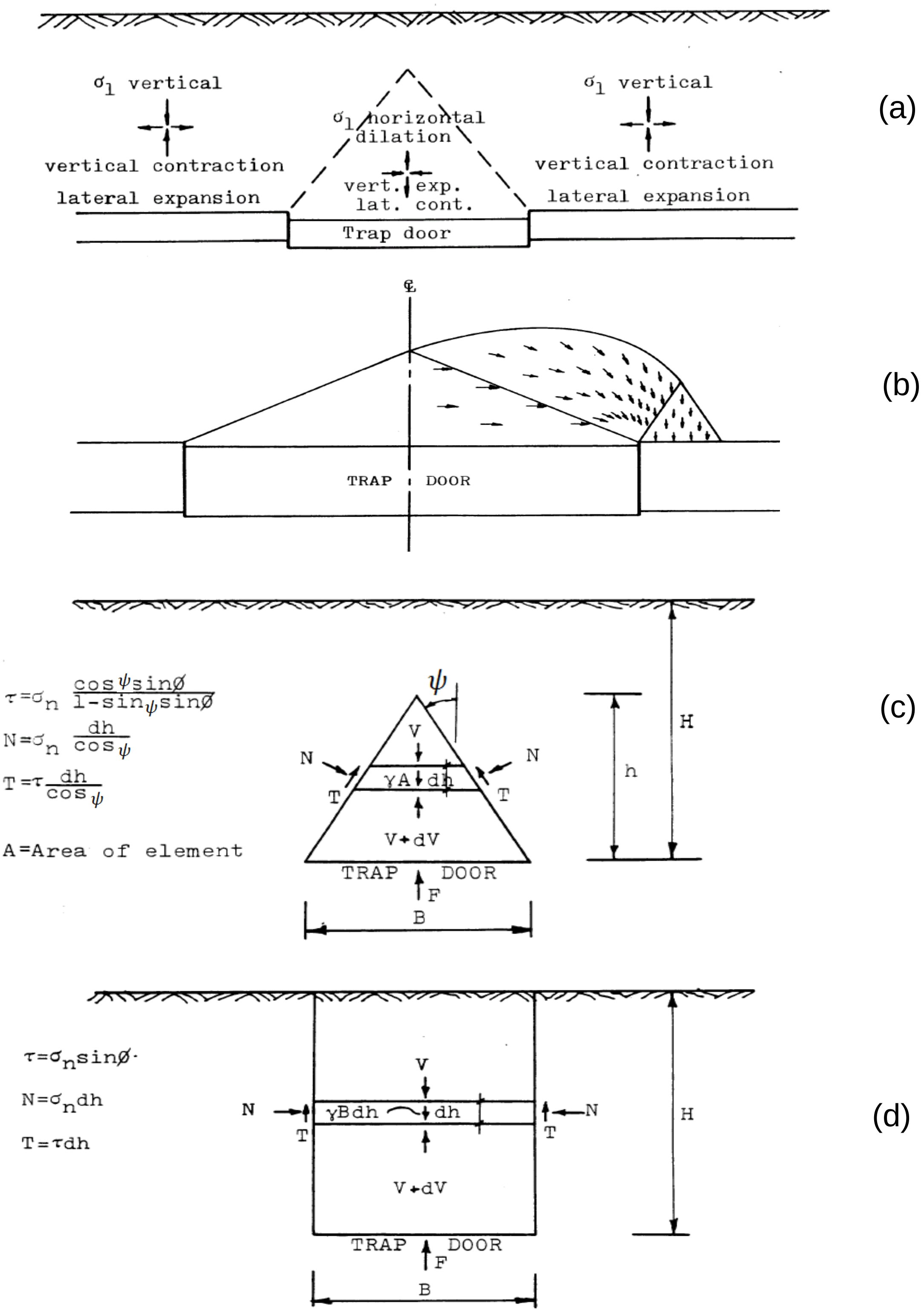

Figure 2.6 General soil behaviour above an active trapdoor Evans (1983); (a) principal stresses and volumetric strain behaviour, (b) principal stress direction, (c) free-body diagram for $\psi>0$, (d) free-body diagram for $\psi=0$.

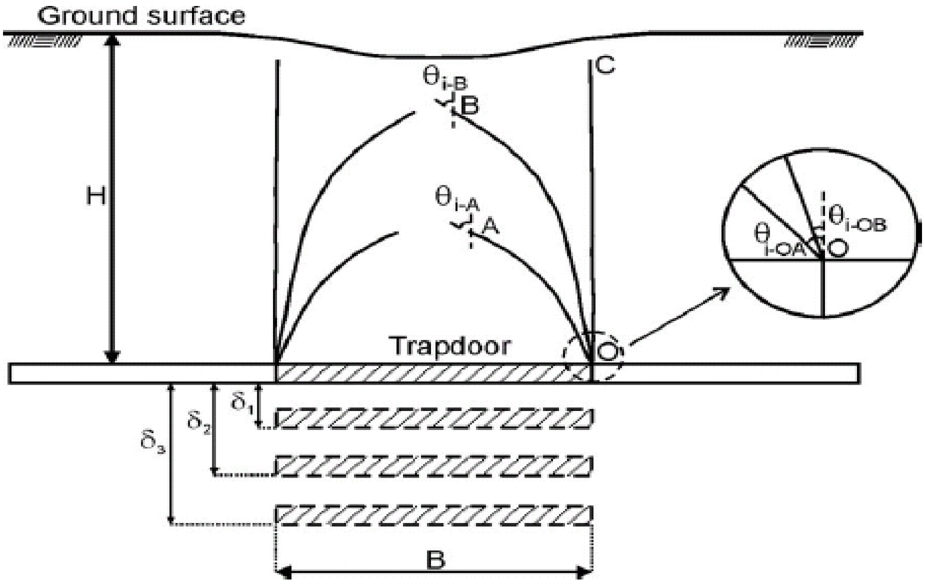

Figure 2.7 Propagation of trapdoor failure surfaces under shallow conditions (Costa et al, 2009)

2.4.3 Rectangular pyramidal and trapezoidal arching

The empirically derived Guido design method (Guido (1987) and Russell & Pierpoint, 1997) considers an improvement in the angle of friction achieved by reinforcing the granular soil with layers of geogrid material. Multiple layers of geogrid material serve to improve the bearing capacity of the geogrid-soil composite. The method postulates a load spreading effect where the ‘load spread’ angle in the reinforced soil beneath the footing was proposed to be 45º (see Figure 2.8).

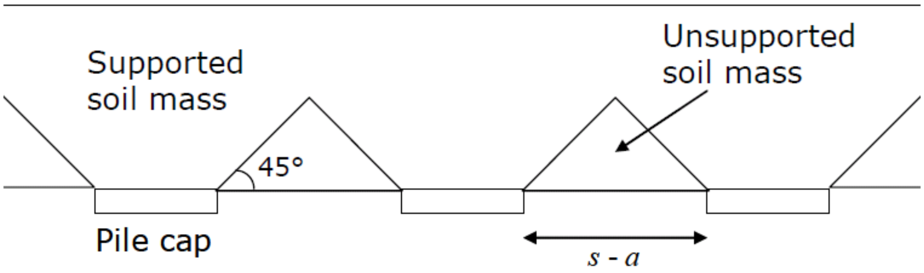

Figure 2.8 Guido design method; pyramidal load spreading (Guido (1987) and Russell & Pierpoint, 1997)

An expression for the vertical stress acting on the subsoil, σ_s, can be determined by considering the unsupported soil mass. For the 2D plane strain situation the value is equal to the triangular volume multiplied by the soil unit weight then divided by the area across which the soil prism acts.

$$\sigma_s = \frac{\gamma_s(s-a)}{4} \quad (2.17)$$

Where:

s is the spacing between piles (m)

a is the pile cap width (m).

The quantity $(s-a)$ from Equation 2.17 is the effective width of the inclusion between adjacent pile caps and is directly analogous to the trapdoor width B from Tergahzi's arching theories.

Equation 2.17 yields a very low magnitude subsoil stress, σ_s, when compared to the stress from the full 'prism' of soil, $\gamma_s H$, (15% with a 5 m soil layer). This is due to the strengthening action of the geogrid. Equation 2.17 shows that the soil layer height has no effect on the pressure acting on subsoil. No direct attempt is made to include friction angle, ϕ, in this expression as the postulated load spread angle effectively assumes a 45º angle of friction for the soil-geogrid composite. The load spread angle is assumed to be justified for compacted granular fill reinforced with multiple layers of geogrid.

Carlsson (1987) and Han & Gabr (2002) postulated that the triangle is truncated to form a trapezoidal shape. In plane strain a trapezoidal wedge with an internal apex angle equal to 30º is assumed to form under the arching soil as shown in Figure 2.9. The method employs a critical height approach, a value beyond which the soil pressure is transferred to the support structure. In plane strain it follows that the critical height, H_C, is equal to 1.87*B.*

Which, for a soil layer of height ~5 m, corresponds to a reduction in vertical stress, σ_v of ~63% from the geostatic overburden stress, p_0.

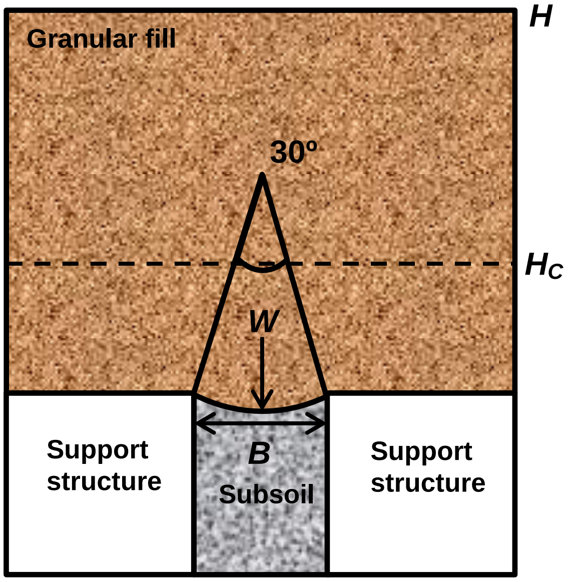

Figure 2.9 Soil wedge assumed by Carlsson (1987) and Han & Gabr (2002)

Naughton (2007) also proposed a method for calculating the magnitude of arching, based on the critical height for arching in the soil layer. The critical height was calculated assuming that the extent of yielding in the soil layer fill was delimited by a log spiral emanating from the edge of the supports (see Figure 2.10).

The Naughton (2007) method determines the critical height as:

$$H_C = CB \quad (2.18)$$

Where:

$$C = 0.5e^{\frac{\pi}{2}\tan\phi} \quad (2.19)$$

The vertical stress on the subsoil then becomes:

$$\sigma_s = \gamma_s H_C = \gamma_s CB \quad (2.20)$$

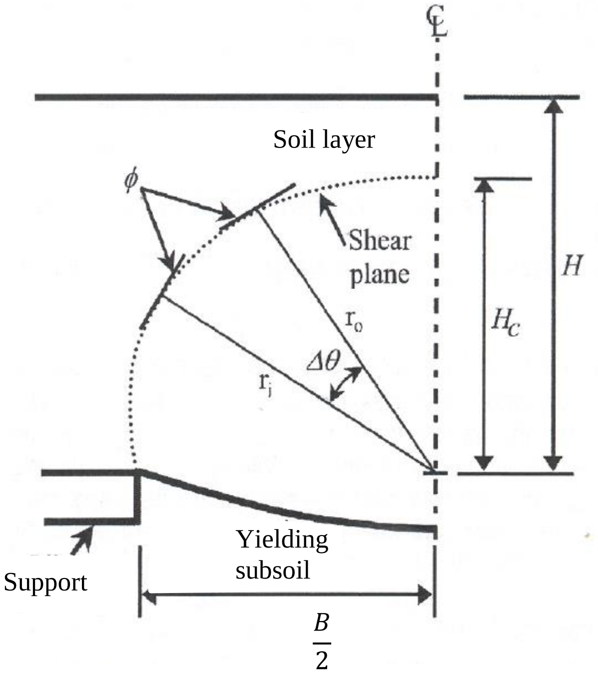

Figure 2.10 Geometry of yield zone assumed by Naughton (2007)

Soil friction angle is used directly in this method. Naughton calculated the variation in critical height due to a range of friction angle of 30 to 45°. Parameter C variation with friction angle is shown in Figure 2.11. The critical height increases proportionally with friction angle from 1.24*B* to 2.4*B*. The implication being that the stress acting on the subsoil also increases with friction angle (see Equation 2.19) which is unexpected behaviour.

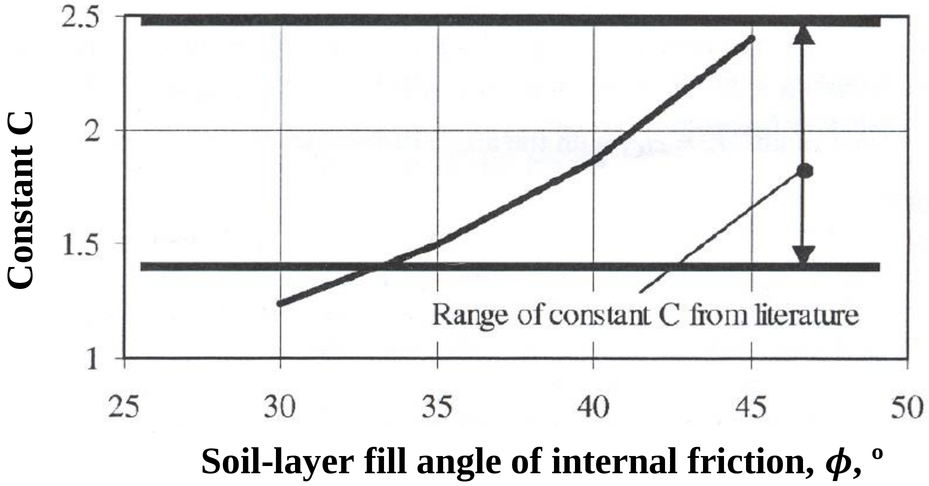

Figure 2.11 Variation of C with friction angle, ϕ (Naughton, 2007).

2.5 Differential settlement

Differential settlement at the surface and throughout the soil is dependent on trapdoor displacement and the height of the soil-layer above the trapdoor. Negligible surface displacements were observed in Iglesia et al (1999) tests, which is consistent with the formation and maintenance of a soil arch at the displacements tested.

McKelvey (1994) shows that differential settlement of the soil prism above the trapdoor decreases as the vertical distance between the soil elements under consideration and the trapdoor increases (see Figure 2.12)

McKelvey proposes that there will be a point where the differential settlement between the soil element and the adjacent soil is zero.

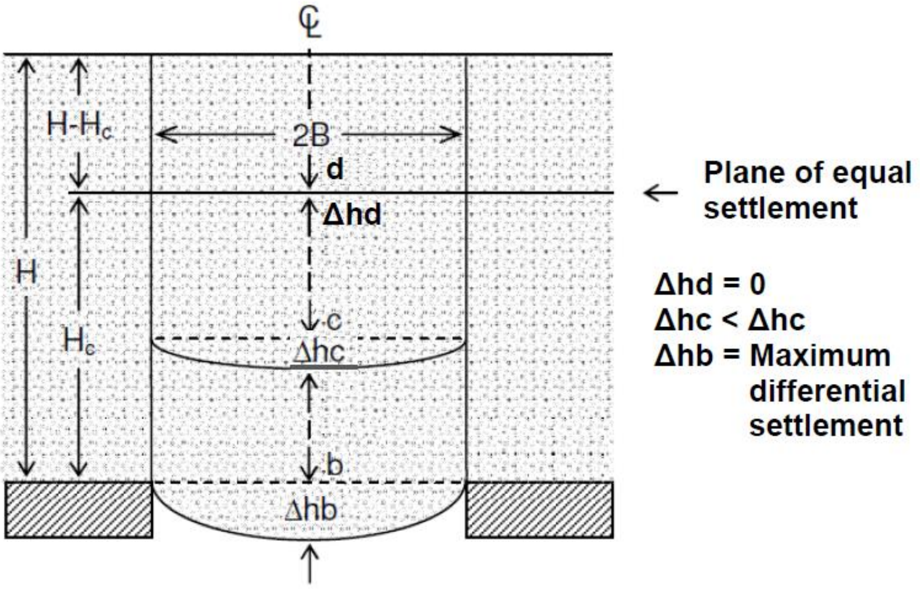

Figure 2.12 Plane of equal settlement (McKelvey, 1994)

2.5.1 Piled embankments

A series of centrifuge tests have recently been performed by Ellis and Aslam (2009a and b) to investigate arching in both unreinforced and geosynthetic reinforced piled embankments and the resultant differential settlement. Aslam (2008) investigated the effect of pile spacing, embankment height (effectively varying the *H/B* ratio) in a 3D model. Figure 2.13 shows the relationship between differential settlement, δ_{ed} determined photogrammetrically, and embankment height, h_e. normalised by the inclusion width between pile caps: $(s-a)$.

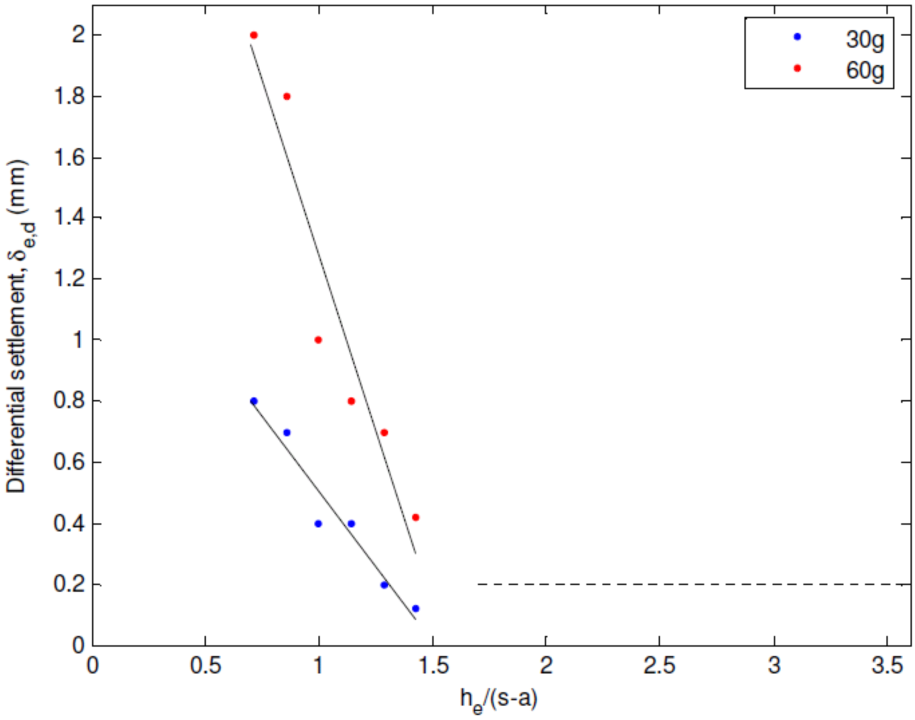

Figure 2.13 Relationship between differential settlement and embankment height in piled embankment tests, (Aslam, 2008)

The data in Figure 2.13 was obtained at two different prototype scales (30*g* and 60*g*). This in effect means that the stress on the model subsoil is increased by a factor of two causing an unequal amount of subsoil deformation, δ_s, between the two data sets. The dotted line represents the level below which settlement could not be reliably determined.

As $h_e/(s-\mathrm{a})$ increases to 2.0 the stress on the subsoil does not increase significantly (and thus there is significant evidence of arching), and differential settlement at the embankment surface tends to zero (Aslam, 2008). These findings are consistent with McKelvey's 'plane of equal settlement' supposition.

Yan (2009) created a numerical model to study arching in piled embankments and specifically recreate the ground reaction curve in simulation.

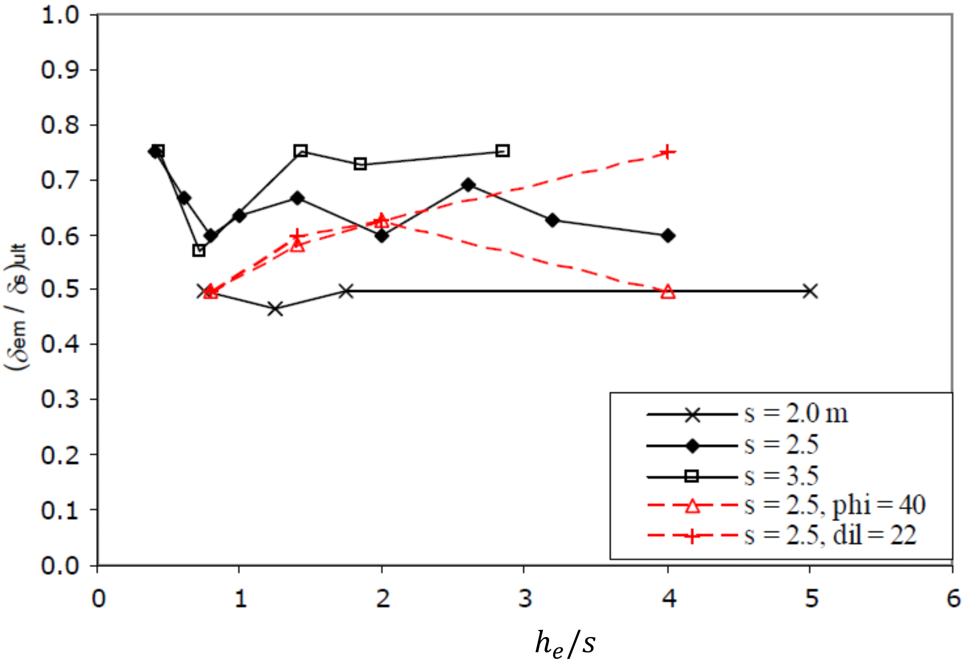

Figure 2.14 Ratio of maximum ultimate embankment settlement, δ_{em}, to subsoil settlement, δ_s, h_e/s. vs normalised embankment height. (Yan, 2009)

In the numerical case the subsoil settlement is implicitly known. The variation of maximum embankment settlement, δ_{em} (normalised by subsoil settlement, δ_s) with h_e/s is plotted in Figure 2.14. For each pile spacing investigated the figure shows that the ratio of δ_{em}/δ_s at the ultimate state, remains approximately constant for ratios of h_e/s >1.5. Yan (2009) investigated a wider range of h_e/s than Aslam (2008) but returned a similar result. This result is consistent with McKelvey's plane of equal settlement theory and observations by Iglesia et al (1999) that no additional vertical settlement is present when the embankment height, h_e is increased beyond a critical level.

2.5.2 Mining subsidence analysis

Subsidence Engineer's Handbook provides a set of empirically derived curves for predicting subsidence, or surface settlement, above mine extractions. The subsidence data was gathered from observations above UK mining works. The data was gathered over a wide range of overburden materials, at depths far greater than considered herein, however the geometrical similarity between the trapdoor test and mining excavations give rise to settlements with comparable magnitude and shape characteristics. Figure 2.15 shows the ratio of maximum settlement S_{max}, (normalised by trapdoor displacement, δ) to trapdoor width (normalised by soil layer height, *B/H*, obtained from compiled data given in SEH (1965,1977). In mining subsidence terminology the extracted panel width to depth ratio, *w/h*, is equivalent to *B/H* in trapdoor geometry (see Figure 2.4). The extracted seam height, M is equivalent to trapdoor displacement, δ. The curve shows a characteristic increase in relative settlement with trapdoor width for a given soil height. The curve shows agreement with other observed settlement behaviour in that at high *H/B* ratios, the settlement tends towards zero (Mckelvey (1994), Aslam, (2008) and Yan (2009)).

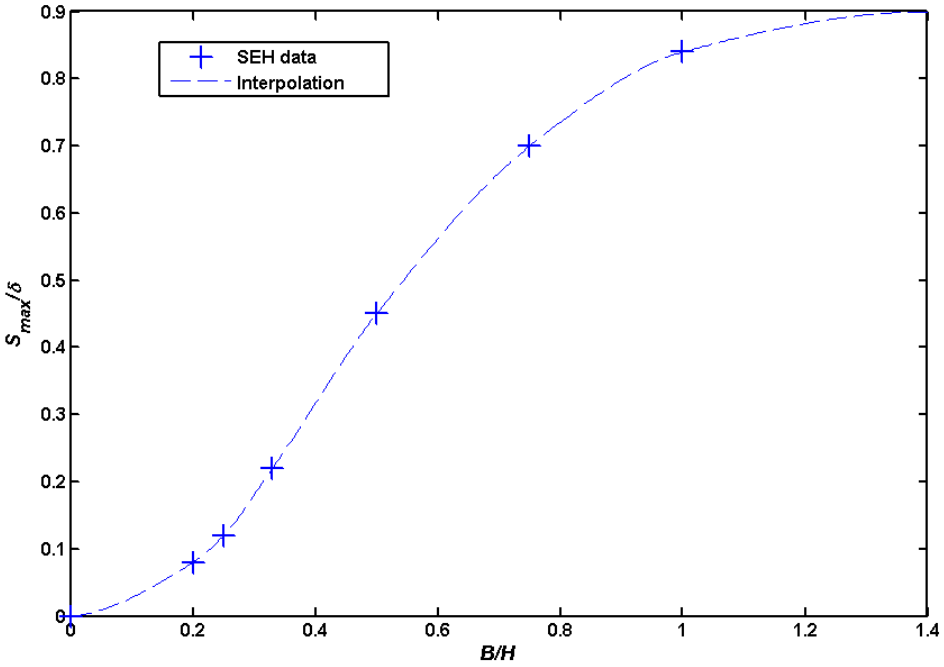

Figure 2.15 Normalised maximum settlement, S_{max}, to trapdoor width (normalised by soil layer height, *B/H*, ratio SEH (1965,1977).

Once the maximum settlement estimate, S_{max} has been deduced the SEH method can be used to approximate the shape of the settlement trough using a series of prediction curves to determine the height of the trough at a specified distance from the centre of the trapdoor, d. Figure 2.16 shows the SEH design graph for prediction of settlement profiles (SEH, 1975). A horizontal line can be drawn from the corresponding w/h ratio the inception points with the lines of equal subsidence are read off to give the distance from the centre of the panel (Whittaker and Reddish, 1989). This approach assumes that the trough shape has a constant profile with trapdoor displacement, δ.

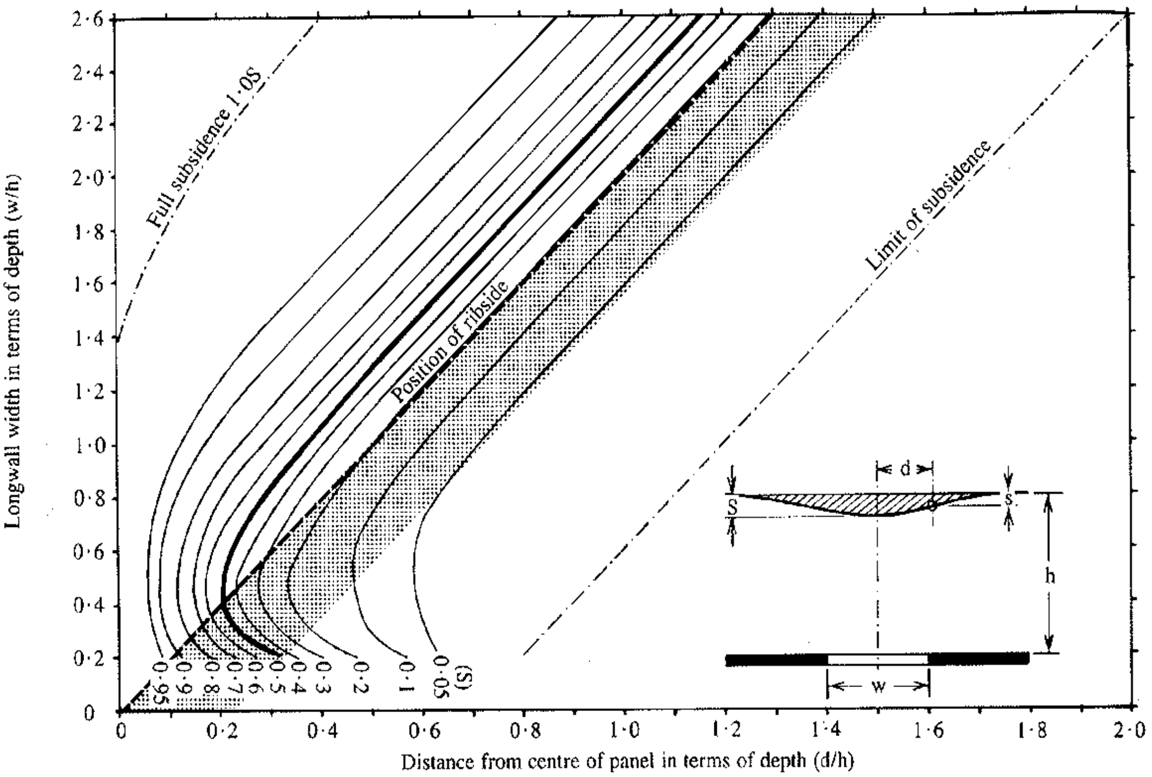

Figure 2.16 Prediction of subsidence profiles above UK mining works (SEH, 1975)

2.5.3 Settlement above tunnels

Much interest has been paid to studying displacements above tunnels resulting from tunnel volume loss as the tunnel deforms under the overburden pressure. A general estimate of maximum settlement is given in Equation 2.21.

$$S_{max} = \frac{A_{tu}V_i}{2\pi i} \quad (2.21)$$

$$i = k_i z \quad (2.22)$$

Where:

A_{tu}. is the area of the tunnel face, (m^2)

V_i. is percentage volume loss occurring at the tunnel (%).

k_i. is a constant related to the strength of the overburden material.

i is the inflection point of the curve at depth, z

The graphic of Figure 2.17 shows a visualisation of the formation of settlement curves above tunnels (Marshall et al, 2012). Of key importance in tunnel displacement analysis is the determination of the inflection point (i) of the curve and it's variation with depth, *z*.

In general, a 'chimney-like' displacement mechanism is observed above tunnels, where the mechanism propagates from the tunnel crown towards the surface as the volume loss increases.

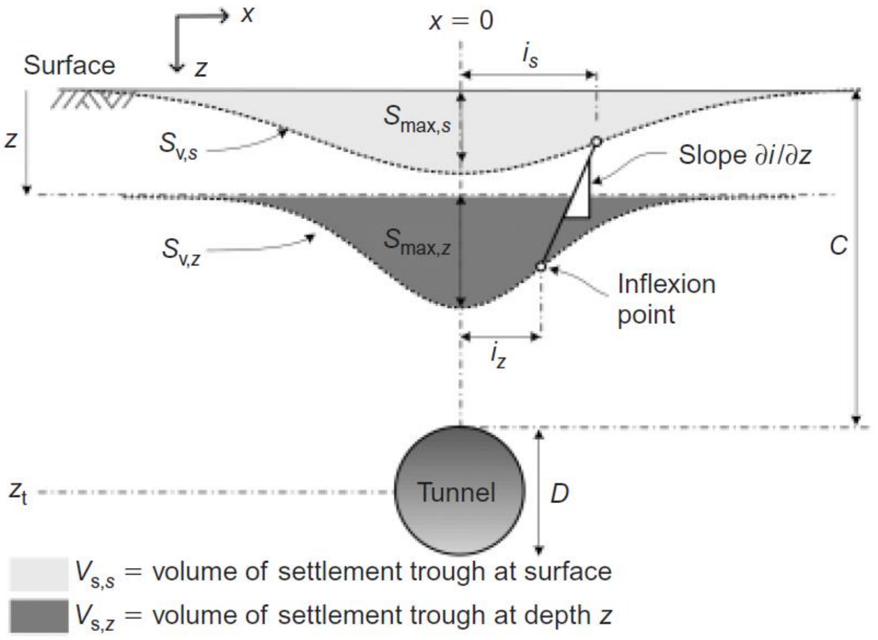

Figure 2.17 Volume loss and maximum settlement above tunnels (Marshall et al, 2012)

The general shape of settlement trough, with horizontal distance from the tunnel centreline, *x*, can be approximated using a Gaussian curve of the form given in Equation 2.23 (after Peck, 1969).

$$S_{v(x)} = S_{max} e^{-(\frac{x^2}{2i^2})} \quad (2.23)$$

Where:

$S_{v(x)}$ is the vertical settlement of the soil at distance, *x* (m).

Curves with higher degrees of freedom than Equation 2.23, such as modified Gaussian (Vorster et al, 2005) and yield density (Celestino et al, 2000) can provide a better fit to the settlement data. The modified Gaussian curve suggested by Vorster et al is given in Equations 2.24 and 2.25. The parameter α is introduced to increase the degree of freedom of the curve fit.

$$S_{v(x)} = \frac{n_v S_{max}}{(n_v - 1) + e^{\alpha(x^2/i^2)}} \quad (2.24)$$

Where:

$$n_v = e^{\alpha}\frac{2\alpha - 1}{2\alpha + 1} + 1 \quad (2.25)$$

Figure 2.18 shows various Gaussian type curves which have the same inflection point. The modified Gaussian method curve provides an estimate of settlement trough shape which is flexible enough to model settlements above a range of buried structure geometries.

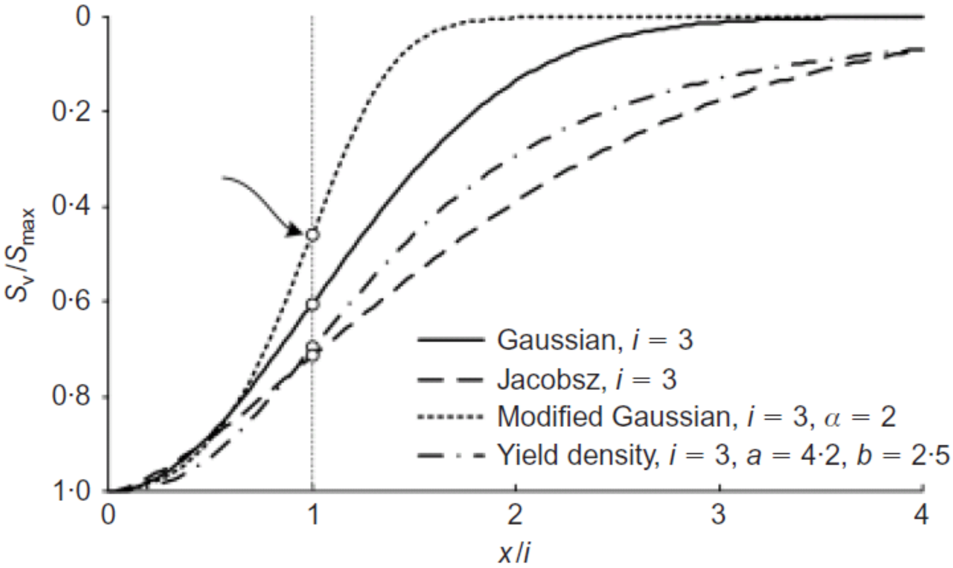

Figure 2.18 Various curves to model tunnel induced settlement

An estimate of horizontal displacement derived from tunnelling experiments, and based on vertical displacements, can be obtained from Attewell et al (1986).

$$S_{x(x)} = -\frac{(x - x_t)}{z_0} S_{v(x)} \quad (2.26)$$

Where:

z_0 is the tunnel depth (m)

x_t is the distance to the tunnel centreline (m)

This estimation assumes the soil displaces towards the tunnel centreline proportionally with vertical displacement. This may not be the case for prismatic trapdoor-like inclusions.

2.6 Fibre Reinforced Soils (FRS)

Soil reinforcement is a widely used technique where natural or synthesised additives are used to improve the mechanical properties of soils. The use of fibrous material randomly mixed with soil in order to improve the strength and durability of construction materials dates back millennia. One of the most well-known historical applications is the adobe mud brick (see Figure 2.19 (d)) where natural fibres such as straw or bamboo were mixed with clay and sun-dried to form a fibre-soil composite material with considerably increased strength characteristics when compared to the unreinforced clay brick. Reinforcement is primarily used to improve the soil mass stability, increase bearing capacity and reduce settlements and lateral spreading. Applications where fibre reinforcement can be beneficial include: slopes and embankments (Figure 2.19 (e) and (f)), retaining walls, abutments, foundations and underground structures.

Figure 2.19 (a) to (c) show some commonly used fibre types. Fibre materials ranging from polyester, polypropylene, steel, glass, and biodegradable fibres have been proven to be particularly effective for soil reinforcement (Santoni and Webster, 2001).

Some recent initiatives also use waste materials such as tyre shred, waste fishing nets, and waster plastics as reinforcing fibres (Zornberg et al. 2004; Kim et al. 2008).

Fibre can also be used for reinforcing poor soil quality waste materials, such as fly ash, so that it can be utilised in construction.

Soil reinforcement using randomly mixed fibres is now a geotechnical engineering solution for many soil improvement field applications. Much soil testing has been undertaken to determine the mechanical properties of fibre reinforced soil such as direct and triaxial shear, CBR tests.

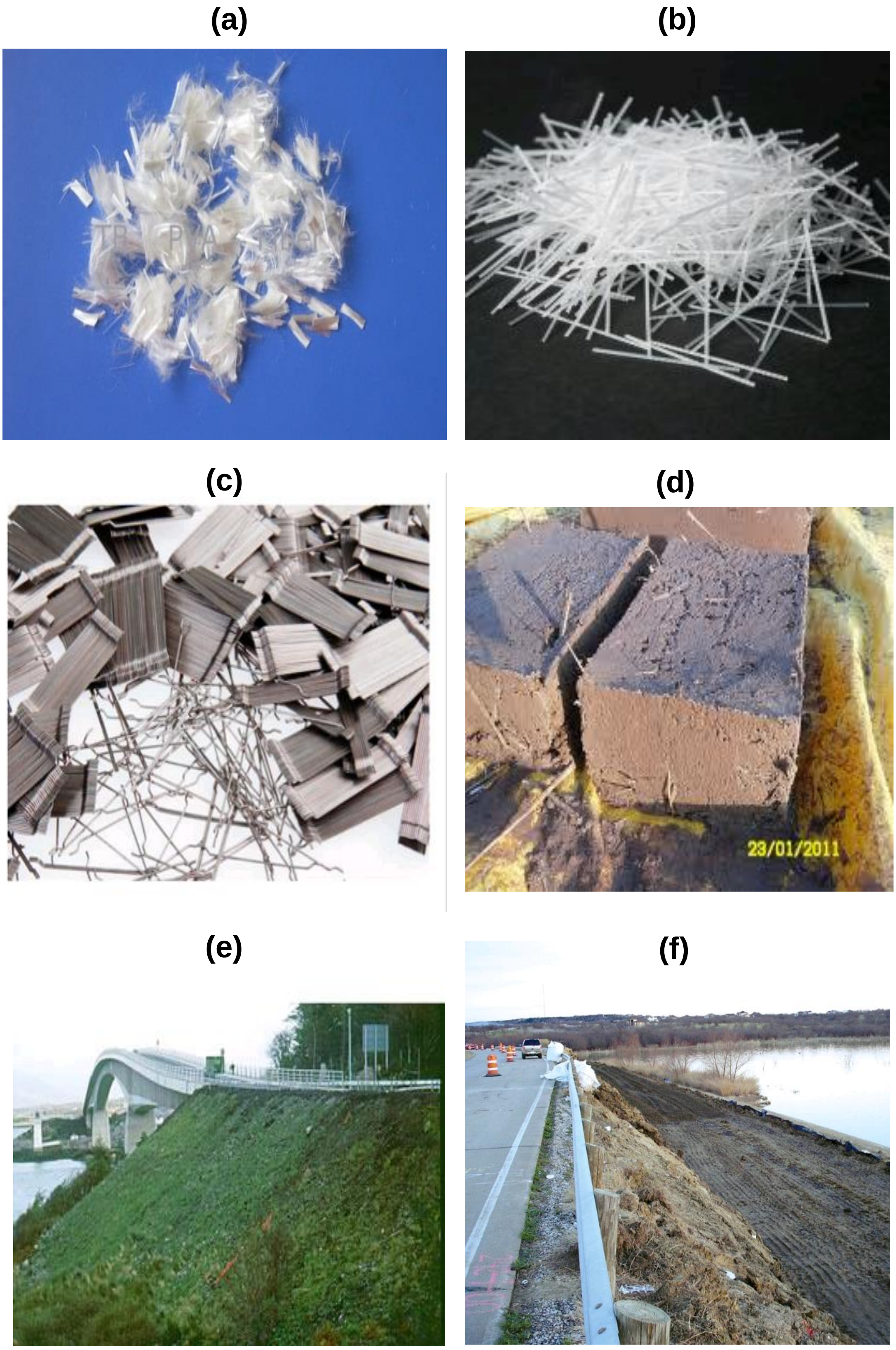

Figure 2.19 Different fibre types; (a) and (b) polypropylene (c) steel. Fibre reinforcement applications: (d) adobe style brick, (e) sloped bridge embankment, (f) roadside embankment.

Figure 2.20 illustrates fibre-soil interaction where the fibre is subjected to tensile forces due to the relative movement of particles in contact with the fibre (Viswanadham et al, 2009). Fibre reinforced soil behaves as a composite material in which fibres of relatively high tensile strength are embedded within the soil matrix. The tensile resistance of the fibres is mobilised when the composite is subjected to shear stresses, consequently, the tensile resistance of the fibre imparts greater strength to the soil.

Many researchers have performed a variety of soil tests on fibre soil composites to determine the extent of improvement in strength with varying fibre and soil properties. Predictive models have been developed to estimate the composite behaviour based on the properties of soil and fibre.

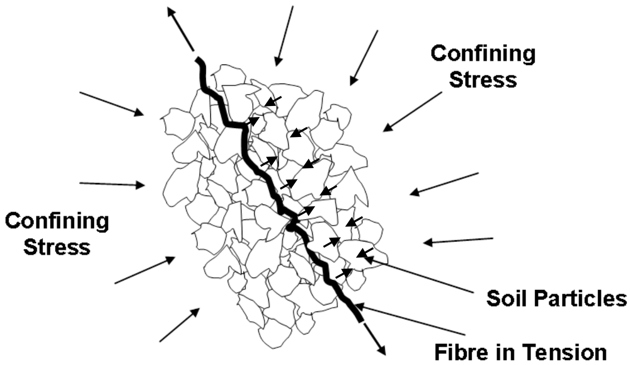

Figure 2.20 Fibre-soil interaction; fibre in tension.

Key fibre characteristics affecting the interaction and effectiveness of the fibre-soil composite are the relative fibre length, F_L to width, w_f, or diameter, d_f 'aspect' ratio, η. The volumetric content of fibre in the soil, χ. As well as the skin friction of the fibre and the fibre yield strength. The fibre orientation relative to the shear plane also plays a key role as this determines whether the fibre is actively able to mobilise its tensile shear strength and contribute to the overall strength of the composite. The reinforcing fibres can be either be placed randomly to maintain isotropic strength or in a desired orientation to provide optimal reinforcement for a particular application. In general, the fibre's high tensile strength and extendibility tends to help effectively reduce the compressibility and brittleness of the host soil.

2.6.1 FRS theory and testing

Zornberg establishes a discrete framework for prediction of the equivalent shear strength of FRS and discusses the appropriateness of using the peak or residual shear strength of the unreinforced soil for predicting the equivalent shear strength of the FRS (Zornberg, 2002). Figure 2.21 (a) shows a representation of the equivalent shear strength of FRS and an unreinforced host soil; (b) shows an assumed stress strain characteristic for the FRS and the unreinforced soil. The fibre-soil composite exhibits a considerable increase in strength and post-peak residual strength when compared to the unreinforced soil. Fibre-soil composites generally have similar residual and peak strengths. Zornberg advises that the residual strength should be used for predicting the fibre-soil composite strength. Equation 2.27 shows the equivalent shear strength, τ_{eq} of a FRS specimen at a normal stress, σ_n.

For a cohesionless soil:

$$\tau_{eq} = \tau + c_\alpha t_f = \sigma_n \tan\phi + c_\alpha t_f \quad (2.27)$$

Where:

τ_{eq} is the equivalent shear strength of fibre-reinforced specimen, (kPa)

t_f is the fibre-induced distributed tension (kPa).

τ is the shear strength of the unreinforced soil (kPa).

c_α is an empirical coefficient that accounts for the orientation of the fibres.

In order to characterise the limit conditions Zornberg derived an expression for the fibre tension at pull-out, t_p defined as the tensile force per unit area induced in a soil mass by randomly distributed fibres, and ϕ the friction angle of the unreinforced soil (Equation 2.28).

$$t_p = \chi \eta c_{i\phi} \tan\phi \qquad (2.28)$$

Where:

χ is the volumetric fibre content in the soil.

η is the fibre aspect ratio, F_L/w_f for tape type fibres or F_L/d_f for cylindrical.

$c_{i\phi}$ is the coefficient of interaction between fibre and soil which is used in soil-reinforcement interaction studies to relate the interface shear strength to the shear strength of the soil. Zornberg assumes a value of ~0.8 based on pull-out test results.

The critical normal stress (Equation 2.29), σ_{nc}, is the normal stress at which failure occurs simultaneously by pull-out and tensile breakage of the fibres. At average normal stresses greater than this value, $\sigma_{na} > \sigma_{nc}$ the behaviour of the composite is governed by the residual strength of the unreinforced soil, ϕ_r, as the fibres no longer contribute to the composite strength.

$$\sigma_{nc} = \frac{\sigma_{fu}}{\eta c_{i\phi} \tan \phi_{pk}} \quad (2.29)$$

Where σ_{fu} is the ultimate tensile strength of the fibre determined from tensile breakage tests (see Section 3.3.2).

The equivalent strength of the fibre soil composite, ϕ_{fs}, can be determined from Equation 2.30.

$$\frac{\tan \phi_{fs}}{\tan \phi_{pk}} = 1 + c_\alpha \eta \chi c_{i\phi} \quad (2.30)$$

Zornberg (2002) recommended using a factor, c_α of 1.0 for randomly distributed fibres to describe their orientation relative to the shear plane. For c_α less than 1.0 corresponds to the case in which the orientation of the shear plane is close to the preferential orientation of the fibres.

A preferential fibre orientation (typically, horizontal) may still exist for randomly mixed fibres as a result of the effect of self-weight.

The concept of root-reinforcement of soil was used by Gray and Ohashi (1983) and Gray and Al-Refeai (1986) to describe the deformation and failure mechanism of fibre-reinforced soil and to find the increase in shear strength for oriented fibres crossing a shear plane. Figure 2.22 illustrates the model proposed by Gray and Ohashi (1983) in essence the model considers a long, elastic fibre extending an equal length on either side of the shear plane. The fibre orientation is considered initially perpendicular to the shear plane, or at an arbitrary angle to it (see Figure 2.22). The shearing of soil causes the fibre to distort, thereby mobilising tensile resistance in the fibre. The tensile force in the fibre is resolved into forces normal and tangential to the shear plane. The normal component results in an increase in confining stress on the failure plane and the tangential component directly resists shear.

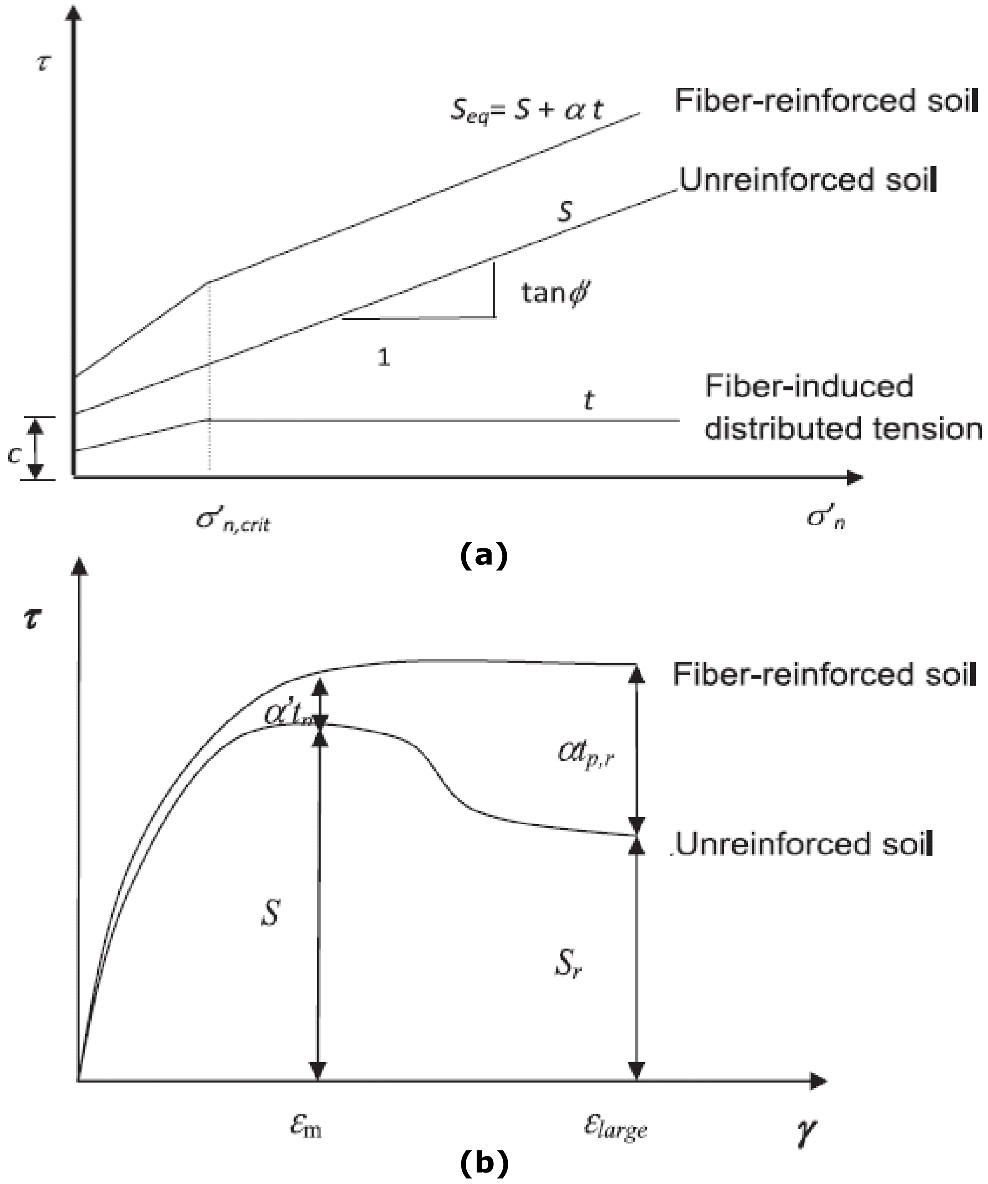

Figure 2.21 General fibre-soil composite behaviour; (a) Equivalent shear strength, (b) Stress-strain curves. (Zornberg, 2002)

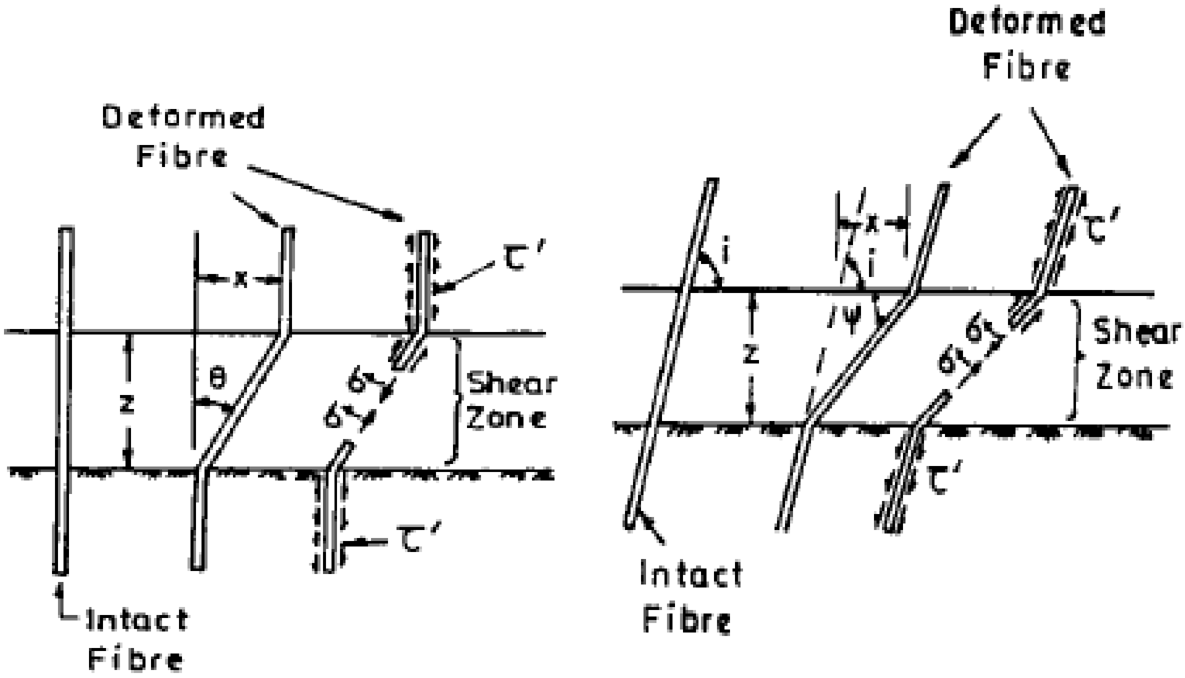

Figure 2.22 Model of oriented FRS (Gray and Ohashi, 1983)

Other researchers (Sadek et al. (2010)) conducted direct shear tests on FRS and reported that a value of c_{α} of 0.4 provided good predictions for the shear strength results in which the shear plane coincided with the preferential orientation of the fibres. Figure 2.23 shows the determined extent of strength improvement versus fibre content reported by Sadek et al (2010). Sadek tested two different fibre types with coarse and fine grained sands. These results typify the observed magnitudes of improvement in strength reported by many investigators (Gray and Ohashi 1983; Gray and Al-Refeai 1986; Maher and Gray, 1990)

The real shear behaviour of the FRS depends typically on the loading direction largely as a result of anisotropic fibre orientation.

Michalowski and Cermák (2002) employed a fibre distribution function to characterise the fibre orientation anisotropy and, hence, the anisotropic strength of the composite soil. A model for prediction of the failure stress in triaxial compression was developed.

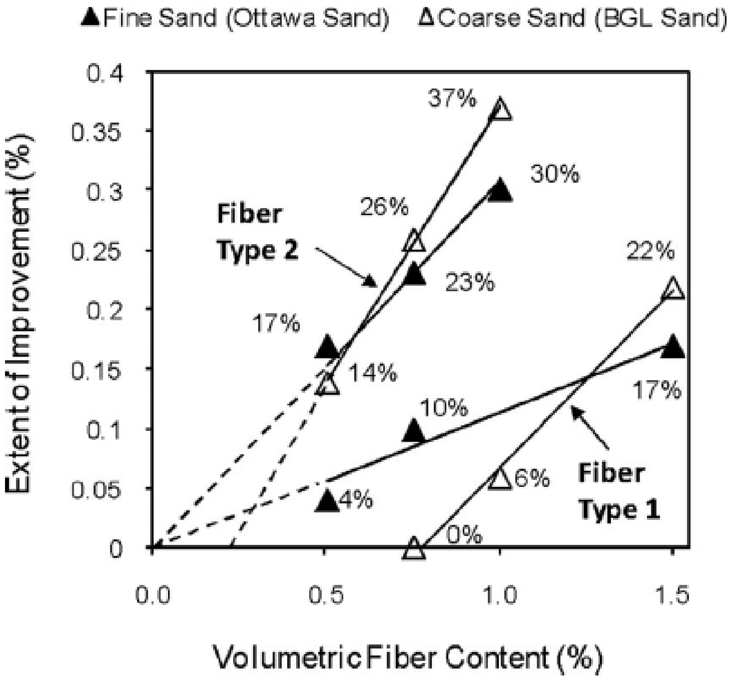

Figure 2.23 Extent of improvement in shear strength of fibre-reinforced fine and coarse sand (Sadek, 2010)

The failure envelope has two segments: a linear part associated with fibre pull out, and a nonlinear one related to yielding or breakage of the fibre material. The yielding of fibres occurs well beyond the stress range encountered in practical situations.

The concept of a macroscopic internal friction angle was introduced to describe the failure criterion of a fibre-reinforced soil. The method is a direct way to include fibre reinforcement in stability analyses of earth structures. Equations 2.31 to 2.33 can be used to calculate the macroscopic internal friction angle, $\bar{\phi}$. Figure 2.24 shows the variation of $\bar{\phi}$ with $\chi\eta$.

$$\bar{\phi} = 2\tan^{-1}\sqrt{\frac{\chi\eta M_e \tan\phi_W + 6K_P}{6 - \chi\eta M_e \tan\phi_W}} - \frac{\pi}{2} \quad (2.31)$$

$$M_e = K_P \sin\theta_0 \quad (2.32)$$

$$\theta_0 = \tan^{-1}\sqrt{\frac{K_P}{2}} \quad (2.33)$$

Where:

ϕ_W is the peak interface angle of friction between fibre and soil

K_P is the passive pressure coefficient, the inverse of active earth pressure K_a discussed in Section 2.2.1 (Equation 2.5).

θ_0 is the inclination angle, where the strain rate of the fibre approaches zero. Stress parameter M_e is determined from the expressions for work dissipation rate derived from triaxial compression tests detailed in Michalowski and Cermák (2002). It represents a tensile strength coefficient calculated at the inclination θ_0. Fibres at orientations above θ_0 act in compression, where those below this angle are in tension. The friction at the fibre-soil interface, ϕ_W, was found to be in the range 15 - 18º for the fine and coarse sand and polymer fibre types tested (Michalowski and Cermák, 2002).

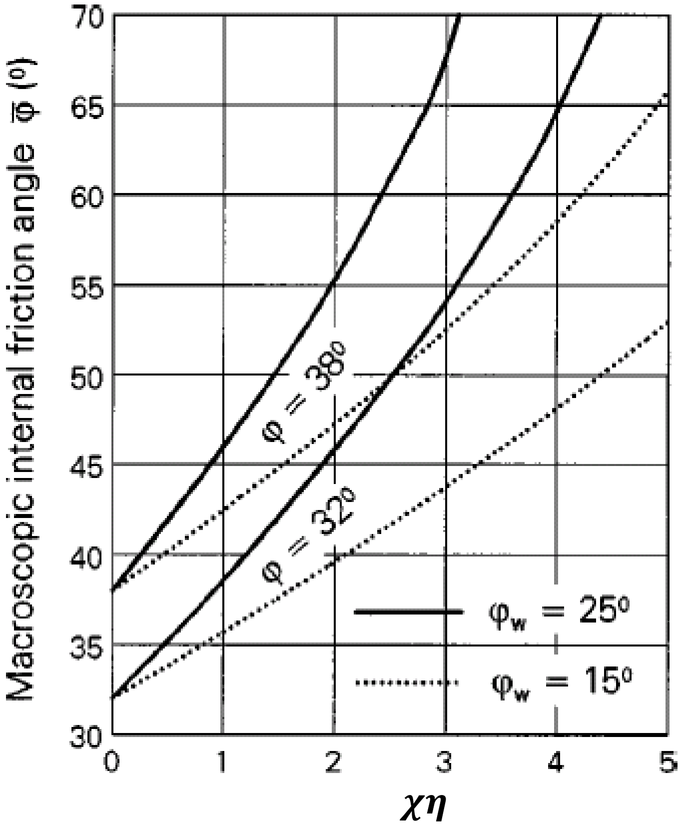

Figure 2.24 Macroscopic internal friction angle, $\bar{\phi}$, increase with the product of volumetric fibre content, χ and aspect ratio, η (Michalowski and Cermák, 2002).

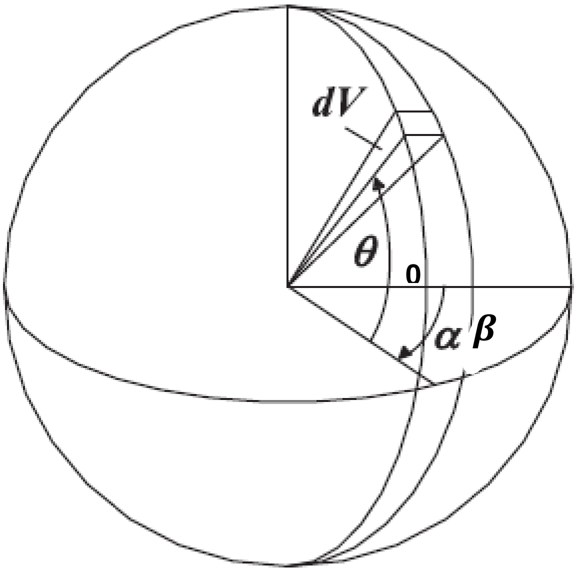

Figure 2.25 Spherical coordinate system used for determining distribution of fibre orientation (Michalowski and Cermák, 2002).

Michalowski and Cermák (2002) determined a range of fibre aspect ratio, η, to soil particle size effects. The reinforcing effect is dependent on the fibre aspect ratio. The larger the aspect ratio, the more effective the fibres were found to be. However, if the fibre length is varied but aspect ratio and volumetric content, χ, are kept constant then longer fibres contribute more to the composite strength than do shorter fibres.

Michalowski and Cermák (2002) conclude that the reinforcement is more effective when the fibre length is large in comparison with soil grain size. The length of fibre needs to be at least one order of magnitude larger than the average size of the grains, otherwise the fabric of the composite does not allow for an effective soil-fibre interaction.

Diambra and Muir Wood et al (2009) conducted experiments to investigate the effect of crimped polypropylene fibres on the mechanical behaviour of sand. A simple modelling approach for fibre reinforced sand, based on the rule of mixtures, is presented which models the FRS as a single material or continuum.

The technique for the determination of the fibre orientation distribution is described by Diambra et al. (2007). The fibre orientation function is defined in a spherical coordinate system shown in Figure 2.25 initially proposed by Michalowski and Cermák (2002).

The angles; θ_0, introduced in Equation 2.33, and β define the orientation of the fibre in a cylindrical specimen. This spherical integration space is then used to define the distribution of fibre orientation (where all fibres are moved to the origin of the sphere). The method can be used to eliminate fibres acting in compression and therefore not contributing to the overall strength of the composite.

Diambra et al. (2009) devised a method for determining the fibre distribution experimentally by physically counting the number of fibres intersecting horizontal and vertical planes cut through cylindrical samples.

The model based simulations of the composite exhibit key characteristics of the response observed in experimental tests and any distribution of fibre orientations can be accounted for. The determined fibre orientation distribution shows that generally densification techniques tend to generate preferential horizontal orientation of fibres.

The reinforcement effect is strongly dependent on the relative orientation between the loading direction and the preferred fibre orientation indicating a preferential orientation to place the fibres in an optimal way during construction.

Fibre reinforcement is commonly used in the stabilisation of soil slopes (Gregory and Chill, 1998). The example of a homogeneous slope with a potential slip surface is shown in Figure 2.26. The figure shows the stress-state that the individual soil elements A-D are subjected to at locations along the slip surface.

The stress-state for a soil element along the failure surface at various depths can be described by the angle between the major principal stress direction (σ_1 and σ_3) and the vertical, ξ. In the analysis of Gao et al (2013), optimal fibre reinforcement is achieved when the major principal stress direction is perpendicular to the preferred fibre orientation plane, β at each critical location of the slip.

The slope illustrates a general conceptual model to describe the interaction of oriented fibres at locations along a complex slip surface.

FRSs have been used in many physical modelling experiments; slopes Kaniraj and Havanagi (2001), carried out centrifuge modelling of polypropylene fibre reinforced fly ash slopes.

Viswanadham et al, (2009) conducted centrifuge modelling of fibre reinforced soil in waste liners where both active and passive arching was induced in the tests to model waste decomposition and the heave response of expansive soils respectively.

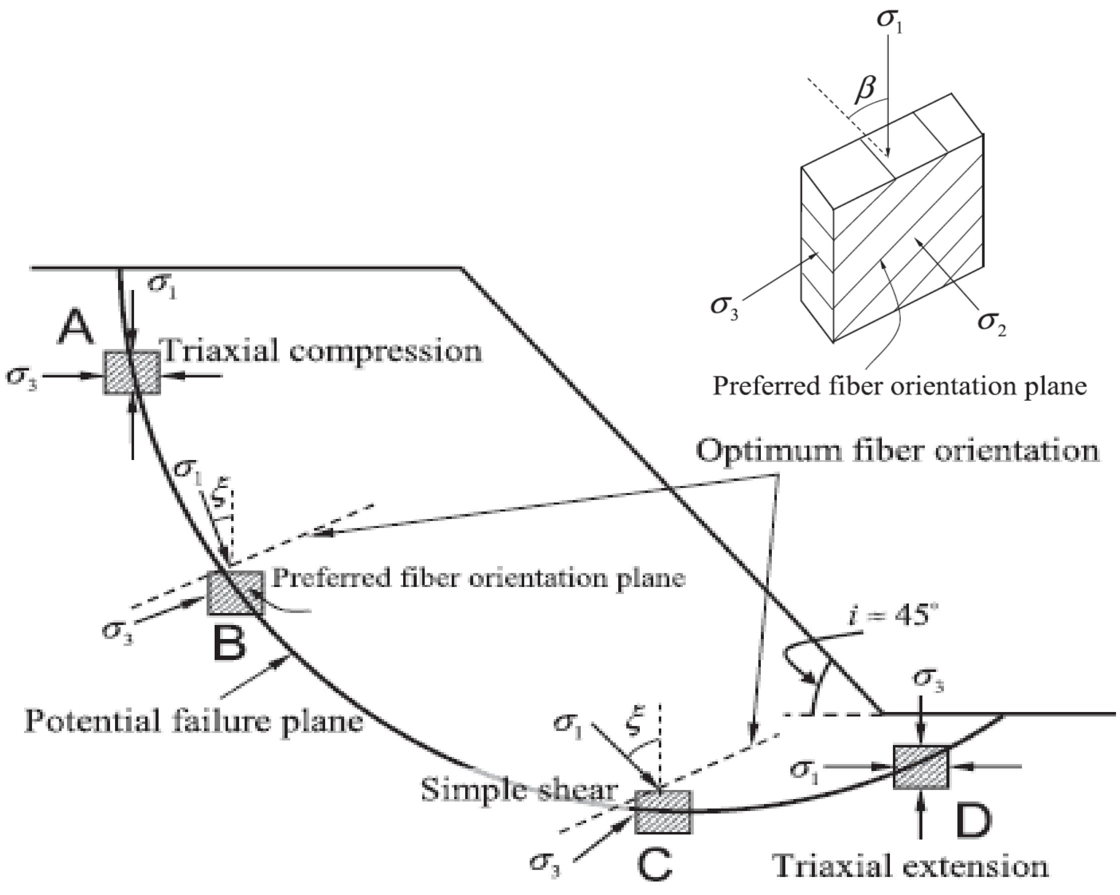

Figure 2.26 Fibre orientation plane and relative loading direction in slope failure (Gao and Zhou 2013)

2.7 Summary

A number of theories have been discussed which attempt to quantify the active arching response in soil based on specific geometrical arrangements found to be of interest to researchers. These theories often give significantly different results based on the assumptions made regarding the geometry of the formed arch. For example Terzaghi assumed a prismatic shaped arch, while Randolph and Hewlett describe semi-circular dome shaped arches. Iglesia et al stipulate that the shape of the formed arch changes with displacement of the underground structure and give a method for constructing a ground reaction curve based on geometrical and soil properties.

Surface settlement features observed above ‘yielding’ structures where arching is taking place such as piled embankments, mines and tunnels have been defined.

Fibre reinforced soil has been introduced as a means of soil-layer strengthening. Theories and experimental evidence for determining the extent of soil improvement based on the properties of the fibre soil composite have been presented. Key fibre properties such as fibre type, content, length, aspect ratio and strength have been found to have an effect on the performance of the composite.

Analytical methods to determine the distribution of fibre orientation within a sample and therefore quantify the effectiveness of the composite are introduced.

Hence there exists a significant amount of relevant literature from studies of arching phenomena, differential settlement and fibre reinforcement with which to compare the experimental results of this research with.

CHAPTER 3 EXPERIMENTAL METHOD

3.1 Introduction

In order to accurately model the general field conditions experienced during ground-loss scenarios a trapdoor apparatus was designed for incorporation into a plane-strain container to be used in a series of centrifuge tests. The apparatus can be used to model a variety of generalised geotechnical situations which give rise to a redistribution of soil pressure between a buried structure and surrounding supporting areas. The experimental setup can be used to investigate the soil-structure behaviour within the above soil layer and to determine settlements at the soil surface.

3.1.1 Aim

The aim of the centrifuge test series is to provide data on the effect of fibre inclusion in the soil layer. The setup allows variation of fibre-soil composite characteristics whilst keeping other key aspects, such as prototype model geometries, constant. In this way the performance of the fibre-soil composite can be assessed and compared with that of the unreinforced soil and with other theoretical predictions.

3.1.2 Centrifuge Modelling

Centrifuges have been put to great use in geotechnical engineering to conduct model tests of most conceivable geotechnical design problems that can be both static and dynamic in nature. Centrifuge modelling allows insight into the mechanical behaviour of geotechnical systems through the application of scaling laws to achieve similitude between a reduced scale model and a full scale prototype structure. Applications include determining the strength, stiffness and capacity of foundations for bridges and buildings, settlement of embankments, stability of slopes, earth retaining structures, tunnel stability and geo-textile reinforced earth structures. In recent decades the centrifuge has also been applied to environmental problems such as predicting levee failure.

The general principle of centrifuge modelling is that a particular full-scale prototype stress regime can be achieved by subjecting a reduced-scale model to an inertial acceleration field many times the magnitude of Earth’s gravity, g.

In order to replicate the prototype stresses in a 1/*N*th scale model of the prototype it is necessary to artificially increase the gravity in the model by a factor of *N*. A more complete discussion can be found in Taylor (1995).

Table 3.1 summarises the most common scaling relationships between model-scale values and the equivalent full scale prototype.

Table 3.1 Scaling relationships in centrifuge modelling

Quantity	**Units**	**Scaling Factor *model/prototype***
Acceleration	m/s^2	*1/N*
Density	kg/m^3	*1*
Unit weight	N/m^3	*1/N*
Linear dimension	m	*N*
Area	m^2	N^2
Volume	m^3	N^3
Stress	N/m^2	*1*
Strain	dimensionless	*1*
Force	N	N^2
Force/unit width	N/m	*N*

It is common to use the same size of soil particles in a centrifuge model as that in the prototype construction. According to scaling law, the typical particle size should be *N* times smaller in the model than in the prototype. For example, provided that average particle size of sand of 0.1 mm is used in prototype tests, sand particle size of 0.001 mm should be subjected to an acceleration of 100*g* according to scaling law. Not only is this unrealistic in a centrifuge model but it is also not meaningful in centrifuge tests because of a critical change in the engineering behaviour of soil. Particle size effects are generally assumed to be insignificant, provided that the ratio of model dimension to mean particle size, d_{50}, is sufficiently large. Ovensen (1979) carried out centrifuge tests and developed guidelines that suggested the ratio between the major model dimension and the average grain size diameter should be greater than 15. Work conducted by Foray et al. (1998) showed that shear band thickness is related to average grain size. Generally prototype soil is used in centrifuge model tests to replicate full scale behaviour. In the same way that the correct behaviour of the soil is achieved using the same soil; inclusions in the soil, such as fibres, should be prototype scale (Viswanadam, 2009). Assuming the tensile and bond stresses in the fibre in both model and prototype follow the same constitutive law; the tensile fibre stains are identical in both model and prototype. This research investigates the relationship between the ratio of fibre length to structure, F_L/B, as there is a major disparity between prototype and model scales in this regard, since the ratio is much larger for reduced scale centrifuge models where the fibre is a significant proportion of the structure size.

Inertial gravitational fields produced in the centrifuge are non-uniform and result in stress errors for a model of a given dimension. The stress error can be assessed by considering the ratio of model height to effective centrifuge radius as well as maximum under- and over-stress in the stress profile of a prototype and a model (occurring as an increase of a corresponding depth). The inertial gravitational acceleration is proportional to the radius which leads to a variation with depth in the model; thus a centrifuge with a large rotational radius can duplicate more precisely real in-situ stress conditions.

Zeng and Lim (2002) presented a numerical simulation of the effects of the variation in radial centrifugal acceleration on the stress distribution in a centrifuge model. They showed that as the centrifuge radius and the size of model container increases, the difference in horizontal and vertical stress distribution can be reduced. Experimental results attained from the centrifuge will be similar to results of prototype events. Events of major interest in centrifuge modelling normally occur around the model structure placed at the middle of the container where it is least affected by non-uniform stress. Additionally, the stress field generated by non-uniform centrifugal acceleration also leads to the effects of Coriolis acceleration which is developed when there is free movement of the particles within the model placed on the plane of rotation in-flight. Coriolis effects can be considered negligible if the Coriolis acceleration is less than 10% of the inertial acceleration of the model.

As, due to available space, centrifuge models are mounted within the finite boundaries of a model container it is widely recognised that the boundaries of a model container lead to some inaccuracies in simulation of field situations. The effects are mainly caused by side-wall friction, adhesion and lateral displacement. However as mentioned above, the common practice is to place important aspects of a model in the centre of the container to avoid non-uniform accelerations, this will also minimise boundary effect considerations if the ratio of model width to height is significantly large.

3.2 Test Equipment

3.2.1 NCG Geotechnical Centrifuge

Detailed discussion of the Nottingham Centre for Geomechanics (NCG) geotechnical centrifuge facility can be found in Ellis et al. (2006). The NCG centrifuge is a typical medium-size beam centrifuge with one swinging platform with a 2.0 m platform radius. The stated capacity of the centrifuge is 50*g*-Ton (capable of accelerating a payload of 500 kg to an acceleration of 100*g*). The centrifuge was designed and manufactured by Thomas Broadbent & Sons (Huddersfield, UK).

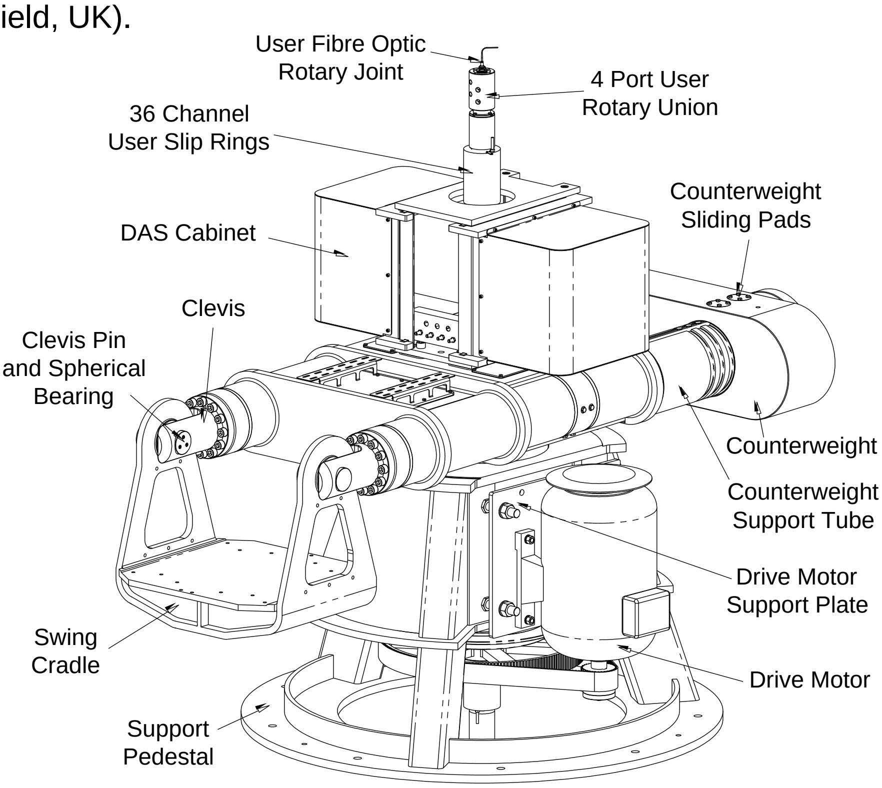

Figure 3.1 Main Centrifuge Components

The major components of the machine are shown in Figure 3.1, a schematic diagram of the major components of the machine is shown in Figure 3.3.

The machine consists of a main body with rotating arms, swing platform for a model container, an electric motor for the control of rotational speed and fibre optic rotary joint and slip rings for transmission of data and electrical signals from transducers. The inertial acceleration of a model is achieved through direct control of rotational speed through a 75 kW 3-phase motor, driven by a variable frequency inverter.

Figure 3.2: Centrifuge as viewed through aperture in chamber roof

Coarse balancing of the payload is achieved by movement of a fixed-mass counterweight (see Figure 3.1) prior to centrifuge flight. The machine can be finely balanced, to within +/- 50 kgm, ‘In-flight’ by movement of oil in the tubular rotor arms from one side of the main axis to the other. Out-of-balance forces are determined by a strain sensor sensitive to deflection of the support pedestal at the location of one of the legs.

Fig. 3.3 shows a schematic of the control system. Normal operation and protection functions are provided by an industrial PLC (Programmable Logic Controller). Normal operating functions include start/stop sequencing, speed control, and automatic in-flight balancing. During the start sequence the system predicts whether the in-flight balancing capacity may be exceeded and gives the opportunity for the centrifuge to be stopped for the counterweight position to be adjusted.

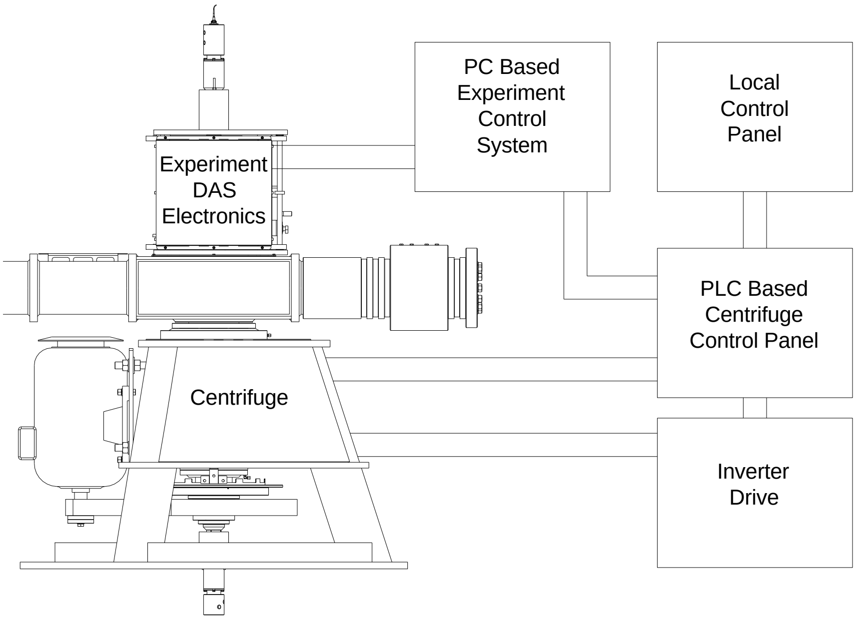

Figure 3.3 Centrifuge control system

If the in-flight balancing system cannot compensate sufficiently for imbalance between the payload and counterweight, increases in speed are prevented. The operator runs the machine via a ‘local control panel’, which can be used to start, stop and change speed. A secondary system consisting of hardwired circuitry will initiate shut down in the event that the PLC should fail or critical safety conditions, such as over-speed or excessive out-of-balance, are detected.

The data acquisition system has a capacity of 128 channels for transducer interfacing. The majority of the system is located in an environment where the gravitational acceleration is significantly lower; close to the axis of rotation. Each channel is amplified and filtered by the electronics junction boxes close to the model payload such that the amount of signal noise on each channel is kept to a minimum. All channels are then multiplexed and fed to the electronics rack located in the DAS cabinet (see Figures 3.1 and 3.3) where they are digitised and transferred to a fibre optic link to the control room PC network (via a fibre optic rotary joint). Also located in the DAS cabinet is the experiment control electronics, consisting of 4 analogue outputs, 64 analogue inputs and 48 configurable digital I/O. These are to be used primarily for control of test equipment such as motors, actuators and valves located on the model. Half of the analogue input channels are configured for interfacing to small signal transducers such as load cells, strain gauges, pressure transducers and thermocouples. The remaining 32 channels are for use with general transducers with larger output signals such as linear variable differential transducers (LVDTs) and are more flexible in their configuration.

Additional to the fibre optic link, there is a rack-mounted PC which can be used to interface to cameras and other bespoke PC based sensors and acquisition equipment. There are 36 slip-ring signal channels for experimental use or supplying power.

Data acquisition and experiment control is carried out by two PCs located in the control room. One of the PCs is dedicated to data acquisition and control using experiment specific LabVIEW software to perform both tasks (see Section 3.2.2.5). The other PC is used to remotely login to the rack based PC to control cameras and other equipment.

3.2.2 Test Apparatus

The basic experimental design principle is to achieve 2D arching conditions within the overlying soil by means of simulating ground movement and measure features of behaviour which are of interest. This can be achieved with a ‘trapdoor’ apparatus, a similar mechanism to that of Terzaghi’s as shown in Figure 2.2. The trapdoor apparatus detailed herein was designed by the author to allow a variation of trapdoor widths to be tested in order to study the effect of variation of trapdoor width to soil and fibre dimensions.

3.2.2.1 Plane Strain Containers

The plane strain model boxes of the type shown in Figure 3.4 were used in the tests. The sides and base of the containers are machined from a single aluminium block in order to withstand the high stresses inherent to centrifuge testing. The boxes have a 50 mm thick detachable aluminium back wall and a 100 mm thick detachable Perspex front to afford a view of the model during test. For small and medium trapdoor widths, a container with internal dimensions 700 mm x 200 mm x 500 mm (LxWxD) was used. In order to allow a view of the complete model, a container with a depth of 750 mm was used in the large trapdoor tests since the height of the model soil layer is increased with trapdoor size significantly increasing the overall height of the model.

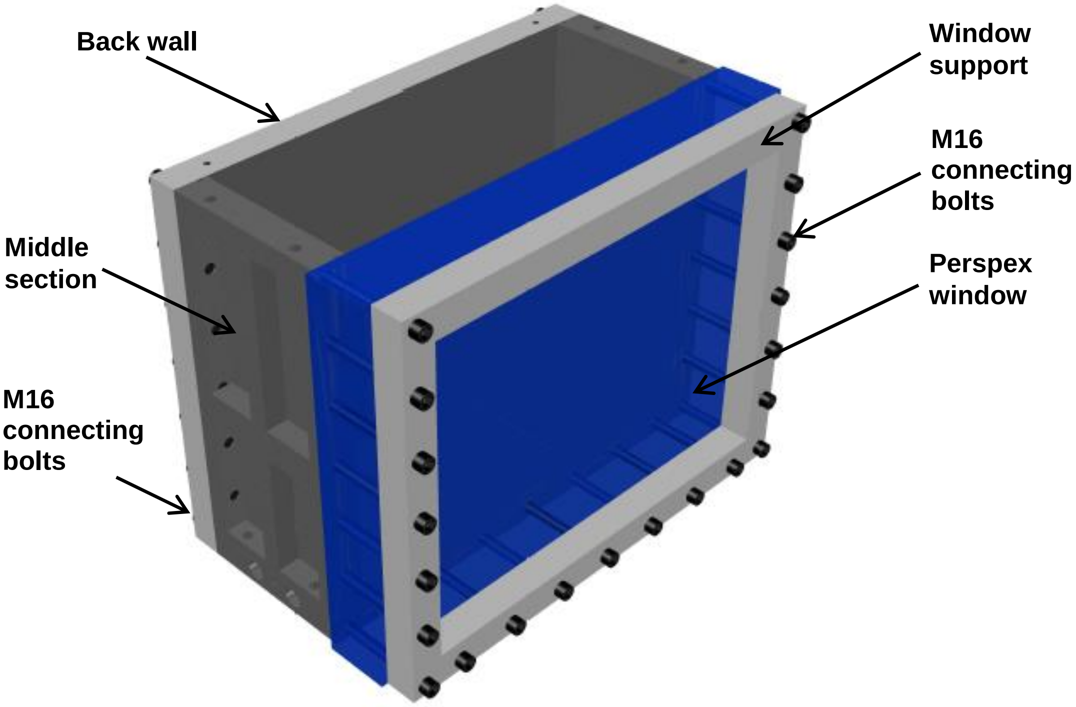

Figure 3.4 Plane strain container

3.2.2.2 Trapdoor and Support Structure

A trapdoor is a device commonly used to model ground movement and experimentally investigate the arching phenomenon (Terzaghi, 1943). The general mechanism and apparatus used for this research is illustrated in Figure 3.5. The apparatus was designed to fit into the plane strain containers detailed in Section 3.2.2.1.

A vertical translation table was designed for use as a trapdoor to induce active arching within the soil. Two timber blocks, formed from MDF, were used to provide the rigid supporting structure adjoining the trapdoor. Aluminium top plates were mounted on the supporting structure in order to house instrumentation. The lateral position of the top plates can be adjusted in order to incorporate different trapdoor widths. For large trapdoor tests, a portion of the supporting structure was removed allowing for the same basic setup to be used for all tests with minimal reconfiguration effort.

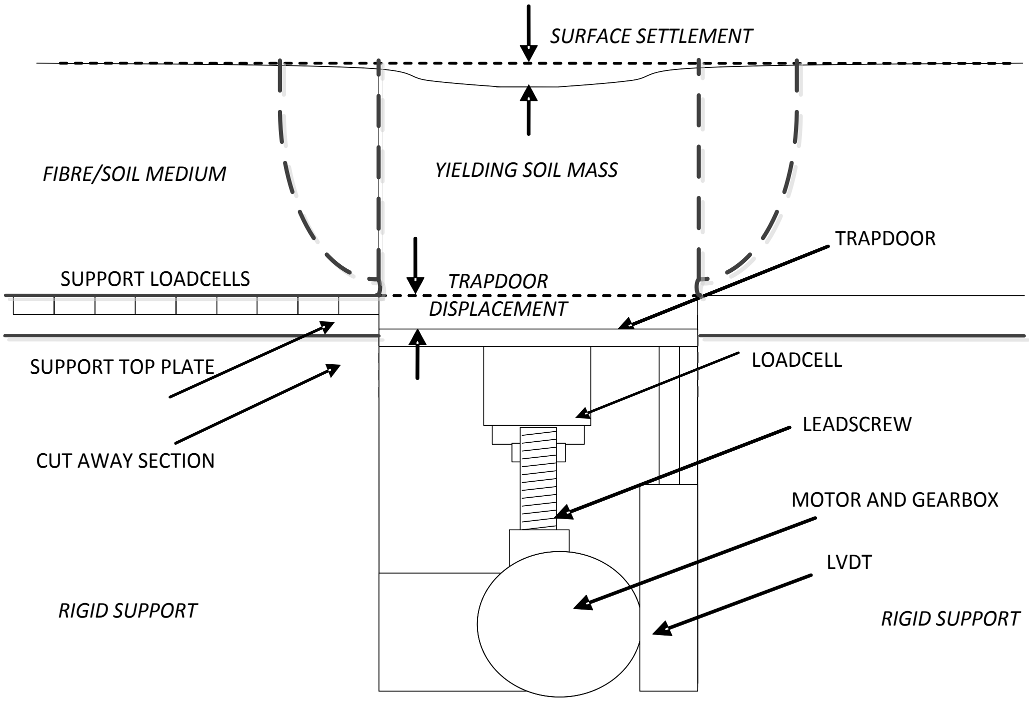

Figure 3.5: Overview of trapdoor experiment

Figure 3.6 shows an isometric view of the trapdoor mechanism drawn to scale. The trapdoor translation is achieved by means of a DC motor with reduced gearing used to rotate a leadscrew that translates the rotation into axial movement through a threaded nut. The nut is bolted to an s-type load-cell, directly connecting the nut to the trapdoor above. The loadcell is used to measure the axial load from the overlying soil. The apparatus is set such that the leadscrew centre of rotation occurs at the centre of the trapdoor where axial load is measured. Tracks with linear bearings are mounted in the corners of the trapdoor space in order to resist lateral rotation of the trapdoor. The trapdoor is connected through the linear bearings using connecting blocks as illustrated. The design ensures that the axial load is all transmitted through the load cell located at the trapdoor centre. The trapdoor was designed to fit into a 60 mm wide gap between the timber supports. The trapdoor width can be adjusted by attachment of smaller or larger plates to the mechanism. In the case of the small trapdoor, the support top plates are moved closer to the centre of the model, in the large trapdoor case, a section was cut out of the timber supports to the depth of the allowable trapdoor movement as shown in Figure 3.5. Low-friction PTFE sheet of 3 mm thickness was attached to the edges of the supporting top plates and the trapdoor in order to reduce friction and prevent leakage of sand at the interface.

A Linear Variable Differential Transducer (LVDT) is used to measure the trapdoor displacement.

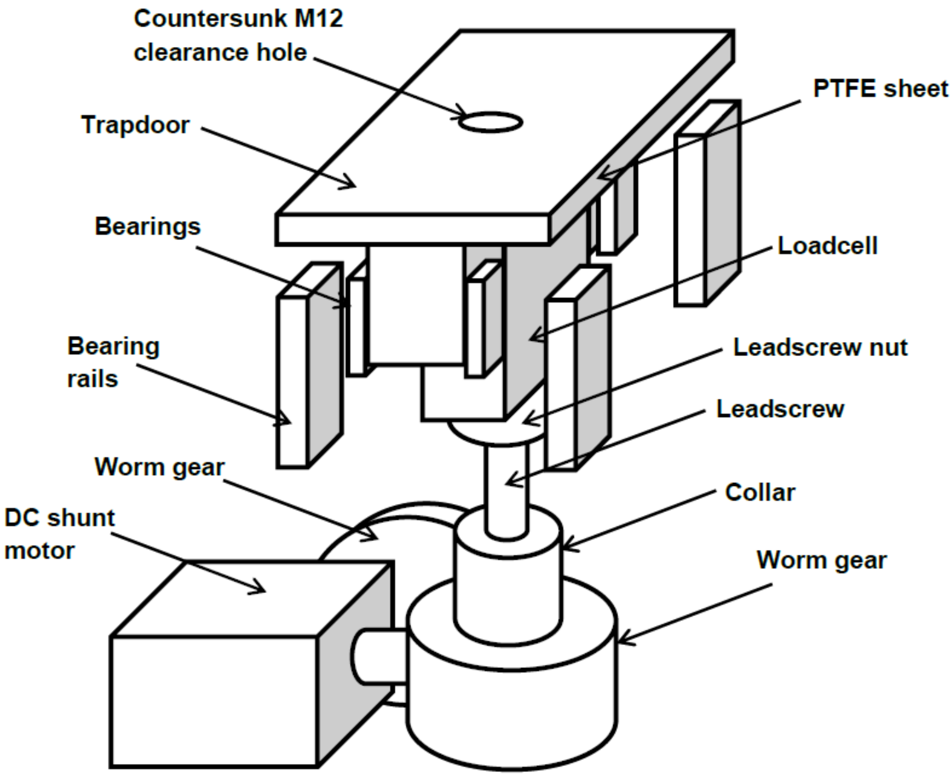

Figure 3.6: Trapdoor design detail.

A maximum trapdoor width of 100 mm and soil layer height of 200 mm were selected in order to calculate the maximum load applied to the trapdoor. Larger soil layers would mean the crown would not be visible in the images. The width of the soil layer is 200 mm as dictated by the dimensions of the plane strain container. The maximum acceleration that would be of interest in terms of the range of stress is 50*g* for a 100 mm width trapdoor. The testing parameters are discussed further in Section 3.5. The maximum load applied to the trapdoor is given in Equation 3.1.

$$F_{TD} = \gamma_s V_{TD} N \quad (3.1)$$

Where the unit weight of soil, γ, is ~17 kN/m^3 at 1g (see maximum density Section 3.3.1). Maximum volume of soil above the trapdoor is calculated as 0.004 m^3. In designing the trapdoor it was essential that the motor/leadscew was capable of supplying sufficient torque to support the overburden load and operate in a controlled manner under such load. Equation 3.2 below gives the required torque, T_{TD}, for a particular maximum load and lead screw pitch.

$$T_{TD} = \frac{F_{TD} p_{LS}}{2\pi} \qquad (3.2)$$

Where:

F_{TD} is the maximum force applied to the trapdoor from the soil (N) from Equation 3.1.

p_{LS} is the leadscrew pitch (m)

A 2 mm pitch leadscrew was chosen as this ensures relatively slow trapdoor speed. Calculated from Equation 3.1, a maximum load of ~3.4 kN will be applied to the trapdoor at 50g. The torque, T_{TD}, acting on the motor which it must counter, is ~1.1 Nm from Equation 3.2.

A 12-volt DC shunt motor with gearing reduction, via two worm drives, was chosen to provide the drive for the trapdoor motion. A shunt motor is controlled by supplying both a field voltage and an armature voltage. The field is proportional to the torque generated by the motor and the armature voltage controls speed. Although torque and speed control are not fully independent, the arrangement allows good control of the motor through existing equipment on the centrifuge. The geared motor torque was tested by hanging weights at a known distance from the shaft and driving the motor. The maximum torque the motor was capable of producing was found to be ~4 Nm. Equation 3.3 gives the calculation for trapdoor velocity, v_{TD}, where N_{TD} is the motor speed in rpm and n_1 and n_2 are the gear ratios of the first and second worm drives respectively. The stated speed of the motor, N_{TD}, is 1500 rpm and gear ratio is 72 per stage.

$$v_{TD} = \frac{N_{TD} p_{LS}}{n_1 n_2} \qquad (3.3)$$

The maximum speed of the trapdoor, v_{TD}, is calculated to be ~0.6 mm/min. This low speed provides ample opportunity for digital image capture during the trapdoor decent.

Figure 3.7 shows an image of the test setup from the location of the digital camera used in the initial series tests. The trapdoor assembly is attached to the left hand side timber support which has been cut away to accommodate the main body of the motor. The motor is controlled using a motor control board in response to demands issued from a PC in the control room.

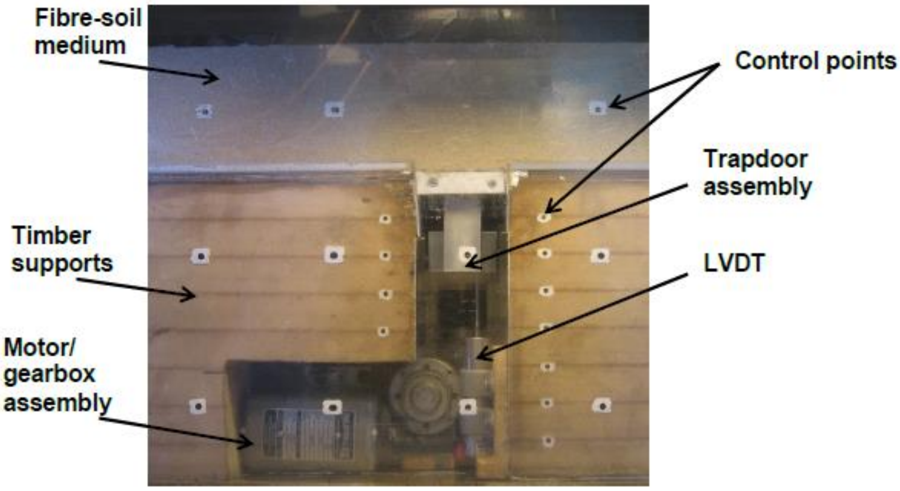

Figure 3.7 Test setup

Figure 3.8 shows the instrumented support plate which is attached to the left hand support block. The plate has a 50 mm breadth 6 mm deep channel cut through the centre in order to incorporate nine 15 mm wide, 50 mm breadth instrumented beams which are used to measure the loading distribution across the support structure. The lateral spacing of the plates can be adjusted using spacer plates. This allows for adjustment of the location of support measurements for different trapdoor widths to ensure similitude of measurement location for different model scales. A 2 mm thick PTFE plate was used to reduce friction at the trapdoor interface. A 1 mm thick steel plate was sandwiched between the top plate edge and the PTFE to add stiffness to the channel cut out.

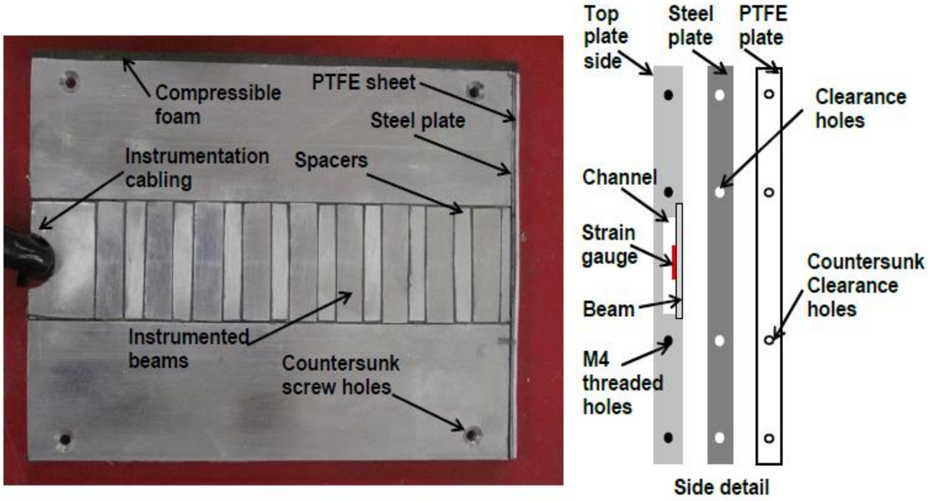

Figure 3.8 Instrumented support top plate

3.2.2.3 Instrumentation

Load on the trapdoor was measured by a commercially available S-type axial load-cell mounted along the trapdoor central axis as shown in Figure 3.9.

Figure 3.9 Trapdoor loadcell

The loadcell was calibrated on the centrifuge by using dead weight to simulate the expected loads of the overlying soil. This ‘in-situ’ calibration was performed in order to minimise any frictional and trapdoor misalignment effects on the load measurement which occur as a result of the constraints of the trapdoor apparatus and container. The speed of the centrifuge was increased, in steps, such that a maximum design load of 4 kN was applied to the trapdoor. The apparatus was then unloaded in the same steps. Some hysteresis was observed on the measurement during unloading. In order to account for hysteresis effects on the load measurement the trapdoor was loaded to the expected maximum soil load then unloaded (as is the case during active soil arching). The variation in loading is achieved by varying centrifuge speed, and hence applied trapdoor load from the dead weight, due to acceleration. The calibrated load-cell sensitivities for each trapdoor width are given in Table 3.2.

As described in the previous paragraph, loading distribution across the model support was measured using small instrumented aluminium beams (of dimensions 15 mm x 50 mm x 3 mm) mounted into a 50 mm wide channel cut into the support top-plate.

The beam mounted strain gauges are all full-bridge arrangement. Figure 3.10 (a) shows the Wheatstone bridge circuit for connection of 4 active strain gauges into a full-bridge loadcell. Figure 3.10 (b) shows the full-bridge strain gauges which were mounted on the underside of each beam. The gauges are designed such that the four individual strain gauges elements are connected to form the full-bridge circuit on the gauge foil such that no external wiring is required to form the bridge.

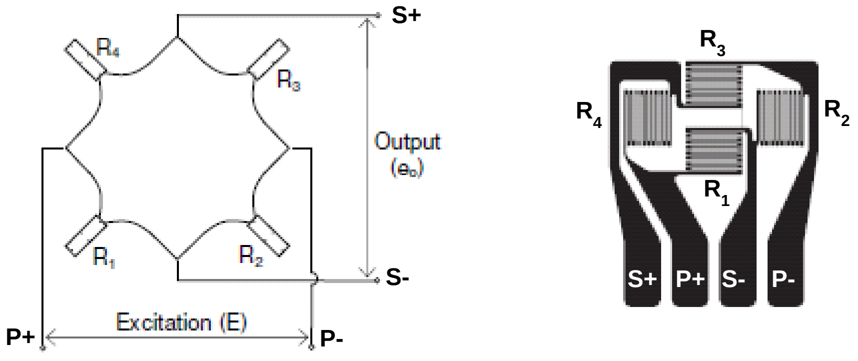

(a) **(b)**

Figure 3.10 Full-bridge loadcell arrangement: (a) Wheatstone bridge, (b) Gauge layout on foil

For the circuit shown in Figure 3.10, assuming strain gauge resistances (Ω) are R_1, R_2, R_3 and R_4 and the bridge excitation voltage (V) is E (the voltage differential between P+ and P- terminals), then output voltage (V), e_0, (the voltage differential between S+ and S- terminals) is obtained, by application of potential divider theory, from Equation 3.4.

$$e_0 = \frac{R_1R_3 - R_2R_4}{(R_1+R_2)(R_3+R_4)}E \quad (3.4)$$

Where:

e_0= Output voltage (V)

E = Excitation voltage (V)

R_{1-4}= Gauge resistances (Ω)

When the beam is deflected, the strain gauges R_2 and R_4 are subjected to tensile strain whilst R_1 and R_3 are in compression due to Poisson's ratio, v. When the gauges are compressed the nominal resistance, R, is increased ($R_{1,3} = R + v\Delta R$) while tension reduces the resistance ($R_{2,4} = R - \Delta R$).

Substituting the changes due to applied strain into Equation 3.4 the output voltage, e_0, becomes:

$$e_0 = \frac{(R + v\Delta R)^2 - (R - \Delta R)^2}{(2R + v\Delta R - \Delta R)^2}E = \frac{(1+v)}{2}\frac{\Delta R}{R}E = \frac{(1+v)}{2}G\varepsilon E \quad (3.5)$$

Where the relative change in resistance, $^{\Delta R}/_{R}$, resulting from the applied strain, ε, is known as the gauge factor, $G\varepsilon$, which typically has a value of ~2 for most gauge types.

The beams were calibrated in the centrifuge using small weights in the same way as the axial load cell; by application of load through centrifugal acceleration. The weights were built into a frame to ensure the beams were point loaded in their centre. As during testing the beams are loaded uniformly it was decided to calibrate the beams using a 'pin-screen' of the type shown in Figure 3.11. This device allows a flexible uniform load to be applied to the beam and is capable of maintaining the applied load under beam deflection. The calibrated sensitivities are given in Table 3.2 for each beam.

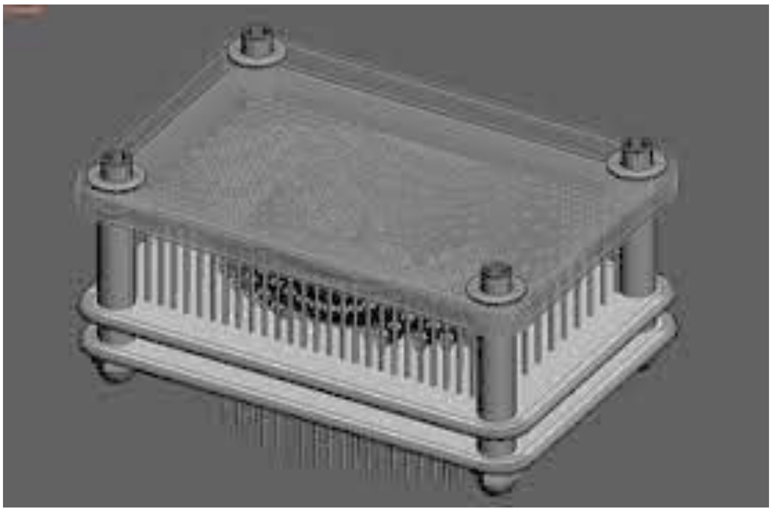

Figure 3.11 Pin-screen for calibration of instrumented beams

Table 3.2 Loadcell sensitivities

Loadcell	Sensitivity, *V/N*	
	Loading	Unloading
Trapdoor, small	$3.47x10^4$	$3.72x10^4$
Trapdoor, medium[1]	$8.70x10^4$	$9.30x10^4$
Trapdoor, medium[2]	$7.31x10^4$	$7.81x10^4$
Trapdoor, large	$8.33x10^4$	$9.72x10^4$
Beam 1	$-3.74x10^4$	$-3.75x10^4$
Beam 2	$-3.61x10^4$	$-3.64x10^4$
Beam 3	$3.55x10^4$	$3.58x10^4$
Beam 4	$1.19x10^4$	$1.20x10^4$
Beam 5	$1.83x10^4$	$1.85x10^4$
Beam 6	$1.24x10^4$	$1.25x10^4$
Beam 7	$-3.91x10^4$	$-3.93x10^4$
Beam 8	$3.35x10^4$	$3.37x10^4$
Beam 9	$2.31x10^4$	$2.33x10^4$

[1] Calibration from 1/2013
[2] Calibration from 6/2013

During the course of the testing it was found that there were slight differences between expected trapdoor loading due to soil displacement (arching) and that derived from the calibrations. Small-scale arching effects due to beam displacement were also found to be a considerable source of error affecting the loading estimate across the support structure. This is discussed in further detail in Section 4.2.1.

Frictional forces are developed along the edges of the descending trapdoor which are transferred to the loadcell. Significant effort was invested to determine the friction as a function of trapdoor displacement and load. Calibration tests were ran in the centrifuge in which the trapdoor was lowered whilst loaded with deadweight to simulate the soil load. The observed variation in load with displacement was attributed to trapdoor side friction. This process was performed before each test to minimise errors due to trapdoor misalignments during model preparation. The expected variation in load due to arching was simulated by reducing the centrifuge speed during the trapdoor's descent. Although the calibration significantly reduced the variability of the results, some frictional effects were observed which could not be compensated for due to the differences in loading assumed for the calibration and the actual arching induced loading during the tests. These effects were estimated to result in an error of around ±5% of the trapdoor loading during the tests.

A slight tilting of the trapdoor along the model breadth axis was observed to take place during trapdoor movement, resulting in a slight tilting of the order of ~2-5º along the trapdoor length. Any discrepancies between the vertical trapdoor position at the front of the model and at the back (relative to the supports) will cause variation in stress across the plate due to the soil arching effect. This variation in stress results in a bending moment applied to the trapdoor, which is in turn applied to the loadcell. Any bending moment applied to the loadcell causes significant differential strain across it, resulting in variation in axial load measurement and hence error.

The discrepancies could not be directly accounted for in a calibration (due to the unknown effects of variation of soil arching with trapdoor tilt) but were determined to be a relatively small source of systematic error present to the roughly the same degree across all tests.

In preliminary tests with unreinforced soil, using the preparation method outlined in Section 3.4, it was found that the variability of measurement in the face of the frictional and tilt-induced arching effects was found to be roughly ~5-8% of the measured trapdoor load.

The residual errors after calibrating for frictional effects were somewhat discounted on the basis that loading results were found to be relatively consistent for all tests (see Sections 4.2 and 5.2).

An LVDT with a linear range of ±25 mm was used to measure the displacement of the trapdoor during the test. The LVDT was found to have a calibration factor of 0.0172 V/V/mm. The LVDT was calibrated with a 10V excitation source.

3.2.2.4 Photogrammetry

A key requirement of the research is to provide an accurate measurement of soil movement during the trapdoor displacement. Digital images were captured remotely via a PC mounted on the centrifuge using a *Canon Powershot G10* camera mounted on a purpose built camera frame which is fixed to the swinging portion of the centrifuge, see Figure 3.12.

Images were processed using an image analysis software GeoPIV developed by White et al (2002). The software, which uses Particle Image Velocimetry (PIV) techniques, gives an accurate measurement of the displacement field in an image. Generally an area of soil (or material of a similar texture) is divided into a mesh of discrete ‘patches’, as shown in Figure 3.13. The texture (variation in pixel intensity or brightness) of the patches is tracked through a sequence of images by searching for a correlation peak between the patches in the current image, at location (x_{1m}, y_{1m}) in Figure 3.13, and those in the subsequent image, location (x_{2m}, y_{2m}). In principle, further processing of the correlation peak allows the displacement between images to be tracked to sub pixel accuracies. The GeoPIV technique can also be used to check the position of the trapdoor throughout the images. The sand, Leighton Buzzard Fraction C (described in more detail in Section 3.3.1) was found to have a large enough grain size and enough variation in texture to allow the patches to be accurately tracked from one image to the next.

The accuracy of the PIV process is dependent on a number of factors. Accuracy can be somewhat reduced when the patch size is too small to contain sufficient variation in texture and the uniqueness of the patch is lost resulting in erroneous displacement data or 'wild' vectors. This can also occur when the patch is obscured by poor camera focus and/or scratches on the Perspex surface. The post-processing software is run from within the Matlab programming environment and the displacement vectors generated for each patch are loaded into Matlab for further analysis and removal of erroneous 'wild' vectors. Other bespoke Matlab programs are then used to convert from image space (pixels) to 'real' object space coordinates (mm). This process involves the calculation of camera position and attitude by iteratively solving a set of collinearity equations relating image space coordinates to object space coordinates. This process uses a least squares fitting approach to determine a set of camera parameters which minimise the error between measured control point locations and those predicted by the photogrammetric model. The overall accuracy of the soil displacements using this technique was found to be generally better than 0.2 mm – provided sufficient care is taken to remove wild vectors from the data.

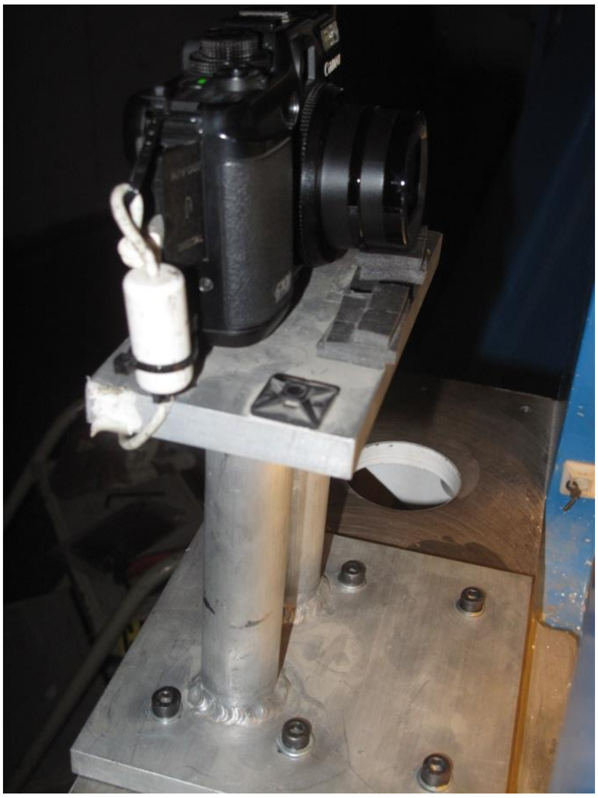

Figure 3.12 Camera mounting frame

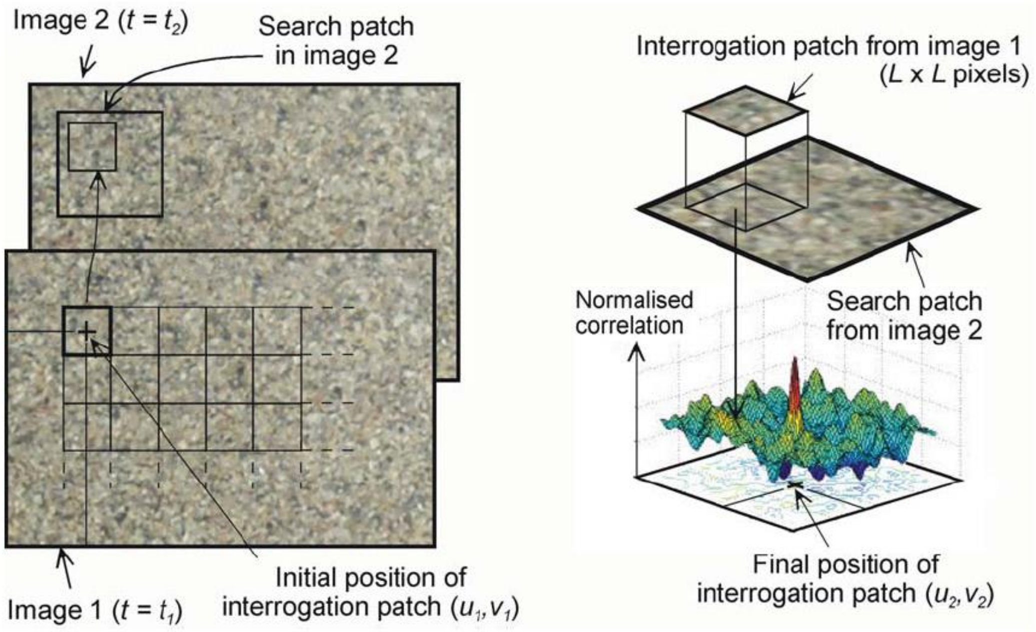

Figure 3.13: Principles behind PIV analysis (White et al 2004)

3.2.2.5 Data acquisition and control system

All loading and displacement data was acquired, stored and plotted using LabVIEW software. LabVIEW is a graphical programming language developed by National Instruments which is widely used throughout industrial and academic institutions to interface to sensors, actuators and a variety of other experimental equipment. Figure 3.14 shows the front panel view of the trapdoor control system developed within LabVIEW. The program was used to develop a closed-loop control system to control the displacement of the trapdoor during centrifuge spin-up when differences in stiffness between the trapdoor and the supports caused unwanted settlement of the trapdoor apparatus. The control system used feedback from the LVDT in order to regulate trapdoor movement to within tolerable levels. Once the centrifuge test design speed was reached; a voltage demand was issued to a servo motor amplifier which outputs a proportional pulse width modulated (PWM) signal to the servo motor of sufficient current in order to drive the motor. The demanded voltage is proportional to trapdoor descent speed.

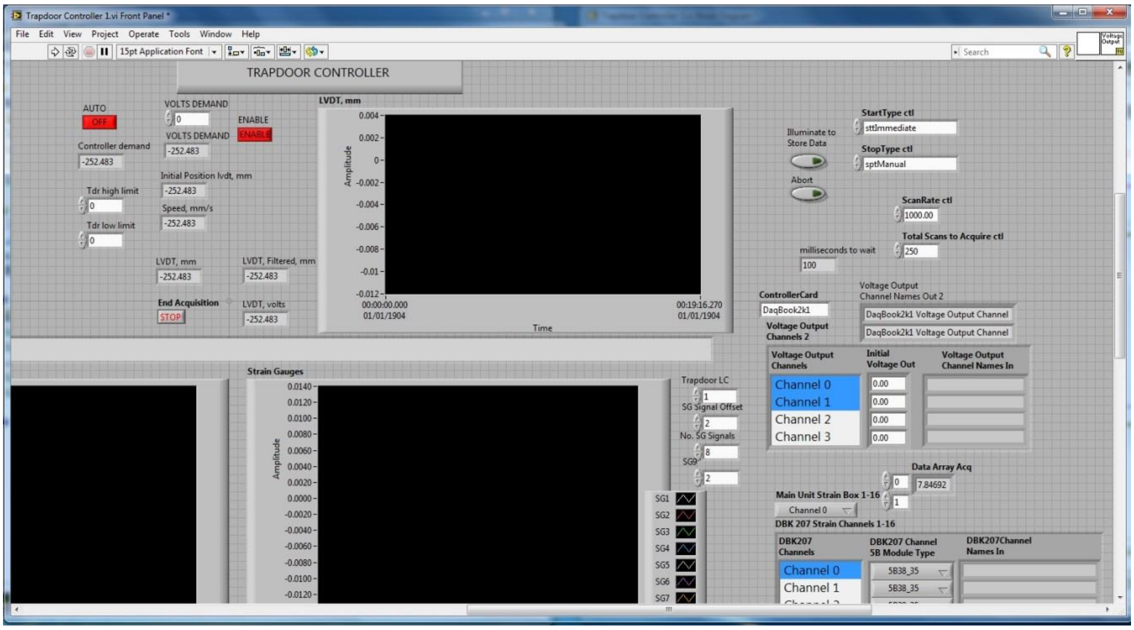

AUTO: OFF
VOLTS DEMAND: 0
VOLTS DEMAND: -252.483
Controller demand: -252.483
Initial Position lvdt, mm: -252.483
Tdr high limit: 0
Speed, mm/s: -252.483
Tdr low limit: 0
LVDT, mm: -252.483
LVDT, Filtered, mm: -252.483
End Acquisition: STOP
LVDT, volts: -252.483
StartType ctl: sttImmediate
StopType ctl: sptManual
ScanRate ctl: 1000.00
Total Scans to Acquire ctl: 250
milliseconds to wait: 100
ControllerCard: DaqBook2k1
Voltage Output Channels 2
Voltage Output Channel Names Out 2: DaqBook2k1 Voltage Output Channel; DaqBook2k1 Voltage Output Channel
Trapdoor LC: 1
SG Signal Offset: 2
No. SG Signals: 8
SG9: 2
Data Array Acq: 0, 1; 7.84692
Main Unit Strain Box 1-16: Channel 0
DBK 207 Strain Channels 1-16

Voltage Output Channels	Initial Voltage Out	Voltage Output Channel Names In
Channel 0	0.00	
Channel 1	0.00	
Channel 2	0.00	
Channel 3	0.00	

DBK207 Channels	DBK207 Channel 5B Module Type	DBK207Channel Names In
Channel 0	5B38_35	
Channel 1	5B38_35	

Figure 3.14 Trapdoor controller software

3.3 Test materials

3.3.1 Soil

Leighton Buzzard Fraction C was used for the soil layer, with an average particle size, d_{50}, of 0.5 mm.

Fraction C was chosen because its mechanical properties are well understood; a number of centrifuge and other laboratory experiments conducted in Nottingham have used the material (Aslam (2008), Liu (2010)). The grain size and natural texture of the material ensures that sufficient detail can be observed in test images to allow the PIV process to accurately track soil displacements.

For an average particle size of 0.5 mm there are will be sufficient particles in between the supports, e.g. for a minimum trapdoor width of 30 mm the ratio of trapdoor width (which is the major model dimension) to particle size is 60 which is four times the minimum of 15 recommended by Ovensen (1979), discussed in Section 3.1.2. This minimum ratio should therefore be sufficient for the arching process to take place without the influence of grain size scaling effects.

The soil properties for Leighton Buzzard fraction C sand are given in Table 3.3. The peak and residual friction angles of the soil, ϕ_{pk} and ϕ_r, respectively, were determined by shear box tests conducted by Aslam (2008).

Table 3.3 Leighton Buzzard fraction C properties

Parameter	Symbol	Value	Units
Peak friction angle	ϕ_{pk}	35	º
Residual friction angle	ϕ_{r}	25	º
Max. void ratio	$\mathrm{e}_{\mathrm{max}}$	0.81	dimensionless
Min. void ratio	$\mathrm{e}_{\mathrm{min}}$	0.55	dimensionless
Max. density	ρ_{max}	1709	kg/m3
Min. density	ρ_{min}	1464	kg/m3

Maximum and minimum densities were calculated using Equation 3.6. The corresponding relative densities are calculated using Equation 3.7.

$$e = G_s \frac{\rho_w}{\rho_s} - 1 \quad (3.6)$$

$$I_D = \frac{e_{max} - e}{e_{max} - e_{min}} \quad (3.7)$$

Where:

e is the calculated void ratio

G_s is the specific gravity for silica soil (2.65)

ρ_w is the density of fresh water (1000 kg/m^3)

ρ_s is the density of soil sample (kg/m^3)

I_D is the calculated relative density.

3.3.2 Fibre reinforcement

The fibre used in all tests was of polypropylene type with a diameter of 0.5 mm. The fibres were supplied by Pinnacle Brush ltd with an initial length of 100 mm. The fibres were cut to the required lengths by hand, giving rise to a variation in length across the sample for each fibre length. The fibres have a density of ~910 kg/m^3.

The fibres were subjected to tensile tests in order to determine the Young's modulus of the material. The obtained stress-strain responses are shown in Figure 3.16.

The modulus of the fibre, E_F, was estimated from the initial elastic portion of the responses shown in Figure 3.16 to be ~1.5 GPa. The tensile strength of the fibre was found to be ~40 MPa. These values are in good agreement with the typical ranges of tensile modulus and ultimate tensile strengths (~1-2 GPa and ~20-80 MPa, respectively) as reported in the literature for polypropylene fibre (Maier & Calafut, 1998).

It was decided to test a range of fibre lengths, ranging from short to relatively long, in order to determine the effect of variation of fibre to structure ratio on the displacement and loading response. Fibre lengths, F_L, of 8 mm (short), 12 mm (medium), 16 mm (medium-long) and 20 mm (long) were chosen. Figure 3.15 shows an image of a sample from each fibre length group.

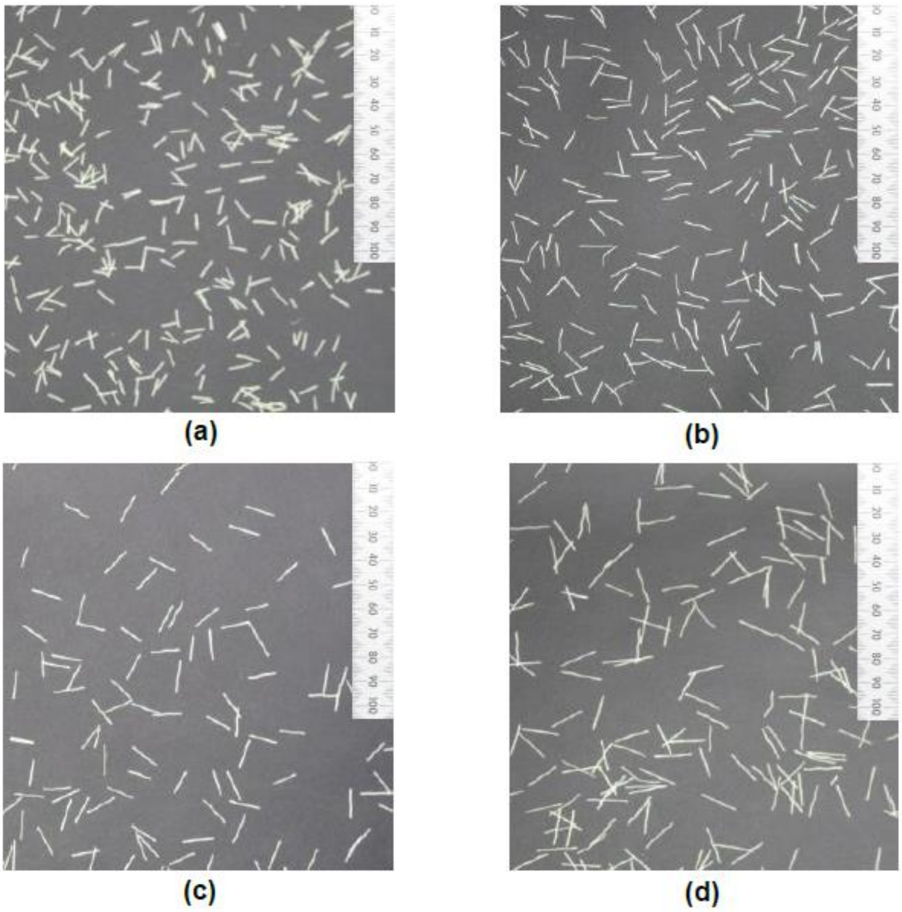

Figure 3.15 Fibre size comparison: (a) short fibres, (b) medium fibres, (c) medium-long fibres, (d) long fibres.

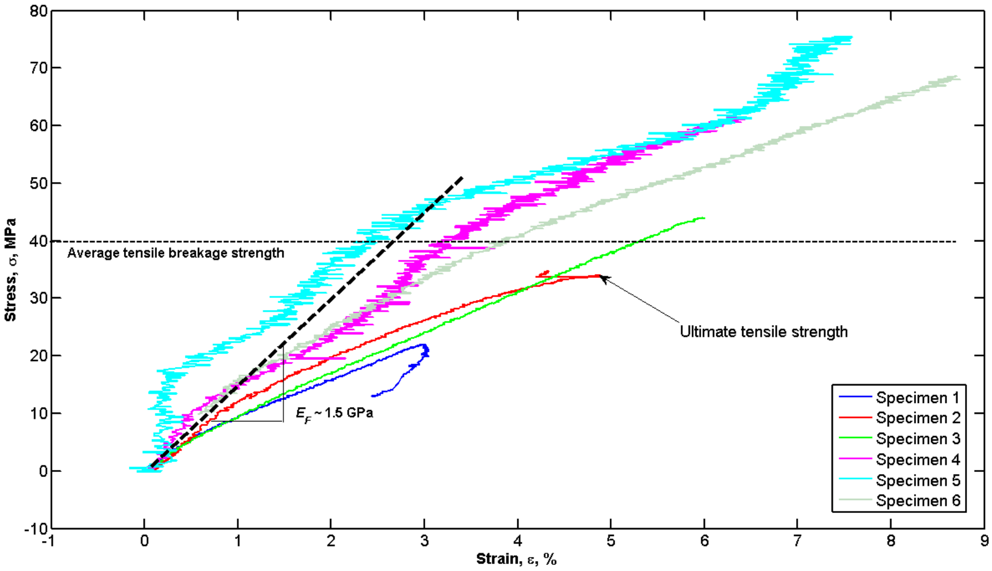

Figure 3.16 Fibre tensile strength testing results

Figure 3.17 shows the fibre size distribution of each test group determined by taking a number of images of a sample of the fibres and determining their individual lengths using basic photogrammetry techniques. The mean length of the short, medium, medium-long and long fibre groups was found to be 7.5, 12.5 15.5 and 20.2 mm respectively. The figure also shows the standard deviation (σ) based on the collected data.

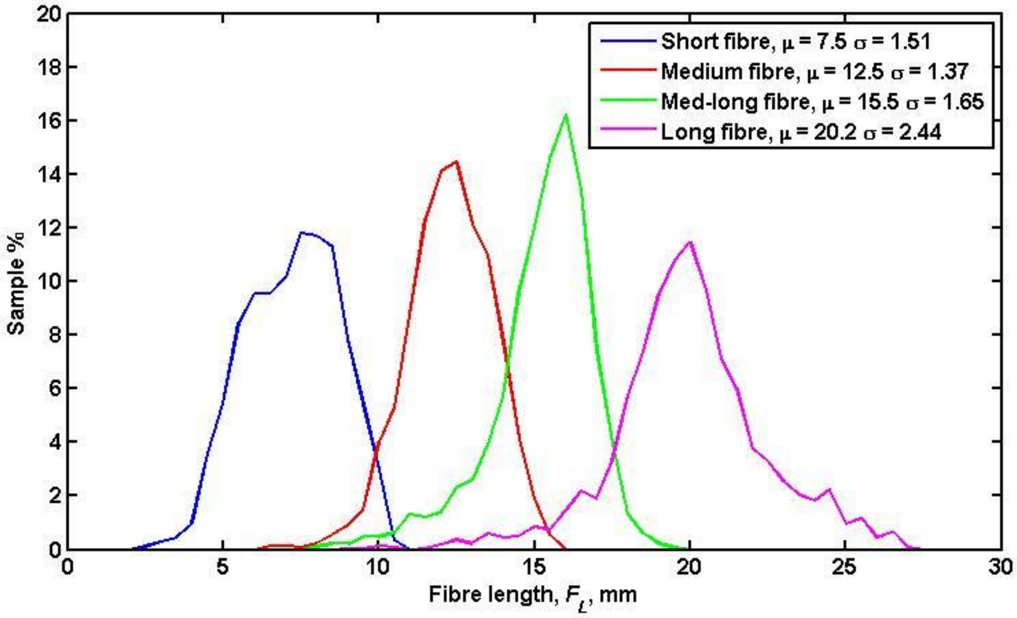

Figure 3.17 Fibre size distribution

3.4 Model preparation

It was decided to use high relative density fibre-soil composites in the tests in order to ensure the composites have high effective shear strength and therefore more resistance to gross deformations.

Early preliminary trapdoor tests using unreinforced soil showed that the repeatability of both the displacements and the loading response was improved when using dense soil samples.

Generally air pluviation is considered the best method to achieve repeatable design densities for centrifuge scale models. However, this method presents insurmountable difficulties when preparing fibre-soil composites, where the intention is to randomly distribute fibres throughout the soil. The fibres tend to collect in the pluviation hopper preventing them from dispersing evenly throughout the soil sample.

The sand was mixed thoroughly by hand with the fibres in a number of stages to make up the total height of the fibre-soil composite. Each sand layer (~30 mm) was then poured carefully by hand onto the assembled trapdoor apparatus before being levelled and compacted using a timber board to ensure uniformity of compaction across the sand layer. A vibrating hammer was then used to compact the sand across each layer. Some tests were conducted to determine the relationship between compaction effort and achieved relative density. It was found that relative densities in excess of 90% could be achieved by compacting each layer for over 4 minutes. The vibrating hammer was applied to a number of locations across the width of the sample to ensure uniformity.

Model construction is summarised as follows:

1. The trapdoor apparatus and timber support structure are assembled in the plane strain model container.
2. Insulation tape and foam is placed to prevent sand leaks at the interfaces between the support structure and container.
3. Model is loaded onto centrifuge platform. Trapdoor motor and instrumentation is connected to data acquisition and control equipment.
4. Silicone grease liberally applied to trapdoor sides to supports, trapdoor front to Perspex window and trapdoor rear to container back-plate interfaces.
5. Trapdoor is loaded with equivalent weight of soil and centrifuge is spun-up to design speed in order to pre-stress the trapdoor mechanism and ensure trapdoor settlement is kept to a minimum during initial loading when test is carried out.
6. Soil mass for a 30 mm layer, estimated at ~90% relative density is mixed thoroughly with fibre mass (calculated as a percentage of dry soil mass).
7. Fibre-soil composite is carefully poured onto assembled trapdoor and support and levelled.

8. Timber board applied to soil layer and vibrating hammer applied to equidistant locations across the board for a total of 4 minutes.
9. Repeat steps 6 to 8 until desired soil layer height is achieved.

3.5 Test program

Table 3.4 shows the test program for the research. It was designed to investigate a considerable range of fibre lengths, fibre content (by % of soil mass) and fibre to structure ratios. It was decided to use fibre content by mass, χ_w, as this is easier to achieve across the full test series than fixed volumetric fibre content, χ, due to the inherent variation in composite densities across all tests. For a composite with a relative density of ~90% the volumetric fibre content is roughly ~2 χ_w. Volumetric fibre content is used to predict the increase in strength due to fibre inclusion in Section 5.4. Three trapdoor widths of 30 mm, 60 mm and 105 mm were tested.

Table 3.4 Test schedule

Test ID	Trapdoor width, B	Fibre content, χ_w	Fibre length, F_L	Soil Height, H	*g*-level, *N*
CMC01	60 mm	0%	-	100 mm	50
CMC02	60 mm	0.25%	12 mm	100 mm	50
CMC03	60 mm	0.5%	12 mm	100 mm	50
CMC04	60 mm	1%	12 mm	100 mm	50
CMC05	60 mm	0.5%	8 mm	100 mm	50
CMC06	60 mm	0.5%	16 mm	100 mm	50
CMC07	60 mm	0.5%	20 mm	100 mm	50
CMC08	30 mm	0%	-	50 mm	100
CMC09	30 mm	0.25%	12 mm	50 mm	100
CMC10	30 mm	0.5%	12 mm	50 mm	100
CMC11	30 mm	1%	12 mm	50 mm	100
CMC12	30 mm	0.5%	8 mm	50 mm	100
CMC13	30 mm	0.5%	16 mm	50 mm	100
CMC14	30 mm	0.5%	20 mm	50 mm	100

Test ID	Trapdoor width, B	Fibre content, χ_w	Fibre length, F_L	Soil Height, H	*g*-level, *N*
CMC15	105 mm	0%	-	175 mm	30
CMC16	105 mm	0.25%	12 mm	175 mm	30
CMC17	105 mm	0.5%	12 mm	175 mm	30
CMC18	105 mm	1%	12 mm	175 mm	30
CMC19	105 mm	0.5%	8 mm	175 mm	30
CMC20	105 mm	0.5%	16 mm	175 mm	30
CMC21	105 mm	0.5%	20 mm	175 mm	30

The intention was to carry out a modelling of models exercise where g-level, soil layer height, *H*, and trapdoor width, *B* were varied to achieve the same prototype stresses throughout the soil and the same height to trapdoor width ratio, *H/B* = 1.66. This is considered a relatively shallow cover to depth ratio where the effects of soil arching are reduced in terms of load reduction on the trapdoor and increased displacement propagation to the surface. This ratio was chosen such that trapdoor displacements result in significant surface settlement in order to properly assess the influence of the fibre composite on improving the overall displacement behaviour. The fibre length to structure ratio, F_L/*B*, was varied from 0.076 to 0.66.

3.6 Summary

A trapdoor apparatus was constructed using a geared DC motor to provide vertical movement of the trapdoor. The trapdoor was designed to withstand the loads applied from the soil during tests. The trapdoor apparatus was instrumented with an axial loadcell to measure load. Two high density timber blocks were used to model the supporting structure. A support top-plate was constructed from aluminium to house a number of instrumented beams to measure loads across the structure. The trapdoor and the support structure loadcells were calibrated using the centrifuge where dead weight and centrifugal acceleration were used to apply similar loads to that expected from the soil during the tests.

The support top plate position was adjusted to incorporate different trapdoor widths. Trapdoor movement was measured using an LVDT where the instrument's spindle was physically attached to the trapdoor plate.

Three different trapdoor plates were made in order to investigate fibre size to trapdoor width scaling effects.

Soil displacements were determined from images taken through the Perspex window during the test. GeoPIV software was used to track the movement of soil 'patches' in image pixel space. The displacements were converted into object space dimensions using simple photogrammetric transformations written in Matlab.

The fibre-soil composites used in the models were prepared by compaction using a vibrating hammer. The same compaction effort was used for all tests

The motion control of the trapdoor and logging of sensor data was done within the LabVIEW environment.

Intentionally blank page

CHAPTER 4 TEST RESULTS

4.1 Introduction

This section presents the load, displacement and strain results of the tests defined in the test schedule (detailed in Table 3.4). This section serves to report general observations, for a more detailed discussion of the results the reader is referred to Chapter 5.

Firstly, the trapdoor loading results for the unreinforced soil cases for the three trapdoor scales (B = 30, 60 and 105 mm) are presented. Trapdoor loading is compared with loading on the support structure. The effects of fibre inclusion (in terms of both fibre length, F_L and fibre content by soil mass, χ) on trapdoor and support loading is then presented and summarised.

This chapter presents key data that can be used for examination of specific points of interest. The full set of loading results from unreinforced and fibre reinforced soil tests with small, medium and large trapdoor widths are presented in Appendix 1.

Vertical and horizontal displacement curves for the unreinforced cases are presented to compare the effects of trapdoor model scaling in tests with the same prototype scales (as a modelling of models exercise). The focus of the chapter is then directed to a single trapdoor scaling of B = 60 mm in order to describe the general mechanism observed across all trapdoor scales.

Volumetric and shear strains are defined, calculated and presented for both unreinforced soil and selected fibre inclusion tests of interest. Variation of key displacement parameters with fibre inclusion is then presented and summarised.

The benefit of fibre inclusion, in terms of maximum displacements and settlement trough area, is presented and summarised.

4.2 Ground Reaction Curves

4.2.1 Unreinforced soil

Figure 4.1 shows trapdoor loading, p, normalised by geostatic load, p_0 against normalised displacement, δ/B, (the definition of the GRC from Section 2.4.1) for the unreinforced soil case for small, medium and large trapdoor width (test IDs CMC01, CMC08 and CMC15 from Table 3.4, respectively).

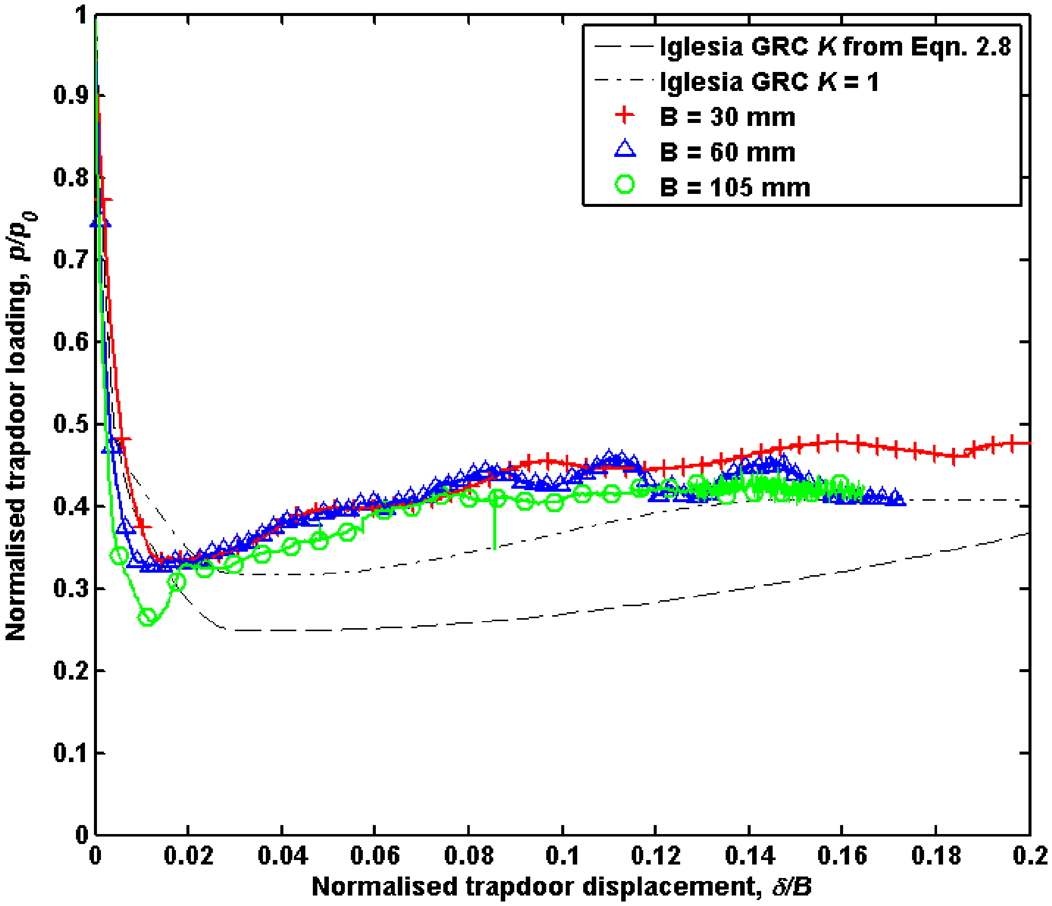

Figure 4.1 GRC for unreinforced soil.

The dashed lines represent the theoretical GRC obtained using the method of Iglesia et al., (1999) using different values for the active earth pressure coefficient, K_a (see Section 2.2) since there is some uncertainty on the value and formulation of K_a for use in calculation of arching induced stresses.

The theoretical curves shown have different minimum and ultimate loads but identical initial gradients and similar load recovery indices. All loading responses are very similar; all show good general agreement with the theoretical GRCs. The most significant difference between the test results is that the value of the initial gradient, M_A, appears to increase with trapdoor width. The predicted theoretical GRC curves are based on the geometry; *H/B* ratio, and other soil properties; peak friction angle, ϕ, and average grain size, d_{50}. See Equation 2.4 in Section 2.2.1 and Equations 2.11 to 2.14 in Section 2.4.1 for a full formulation of the GRC.

The predictions have a lower minimum loading and a marginally lower load recovery rate than all the measured GRCs. The GRC parameters for all tests conducted are given in Table 4.1.

Figure 4.2 shows the loading on the support structure at the ultimate state at the end of each test. The vertical axis shows the increase in support loading, p_s, normalised by the theoretical geostatic loading at the design g-level, p_{s0}. Note that p_s represents the increase in support load, hence, $p_s = p_{sn} - p_{s0}$, where p_{sn} is the support load at an arbitrary stage of testing.

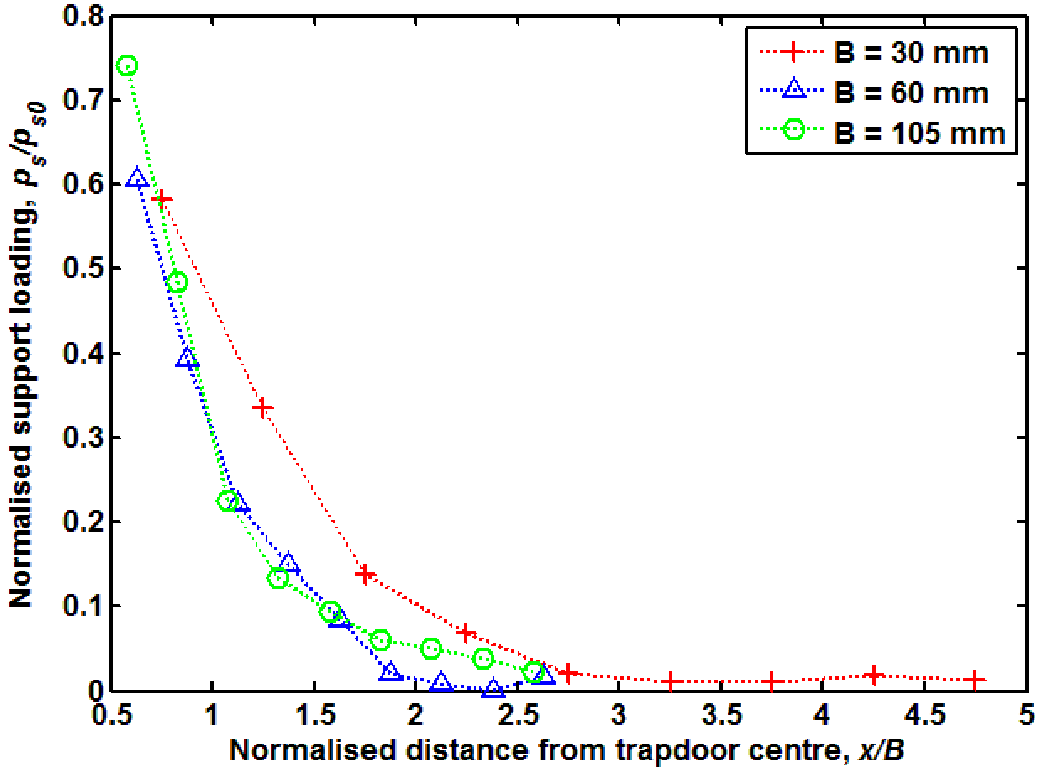

Figure 4.2 Ultimate support loading distribution for unreinforced soil

The horizontal axis is the normalised distance from the trapdoor centre, *x/B*. The traces show an approximate exponential decay with increasing lateral distance from the trapdoor. All traces show negligible increase at distances greater than 2.5*B*. The load distribution for the small trapdoor (denoted by ···+··· in Figure 4.2) appears to have a lower rate of decay with distance. This indicates the presence of some experimental error between the three trapdoor prototypes; since increase in the support loading due to the arching effect should be equivalent for each trapdoor scale.

The instrumented beams are a minimum width of ~15 mm, which represents 1.5 m at prototype scale in the small trapdoor tests (with 100*g* centrifuge acceleration), thus, 1.5 m is the resolution of the spacing between measurements at prototype scale.

The same width beams were used in the medium and large trapdoor tests (at 50*g* and 30*g,* respectively). At 50*g* the beams have a prototype width of 0.75 m, whilst at 30*g*, 10 mm spacer beams are placed in-between the instrumented beams such that the distance between beam centres is ~25 mm, giving a prototype spacing between lateral measurements of 0.75 m.

The measurements for the small trapdoor are effectively averaged across twice the width than those in the medium and large trapdoor cases. The differences observed between the small large trapdoors scales is thought to be caused partly by the increased variation in stress across the width of the beams at 100*g*, giving rise to lateral beam bending moments and partly due to some deformation caused by the increased self-weight of the beams at 100*g*.

Figure 4.3 compares the total increase in loading on the support structure, $\Sigma p_s/p_{s0}$, with the measured reduction in stress acting on the trapdoor, p/p_0, for the three trapdoor widths. The change in support loading was used to calculate the equivalent reduction in load acting on the trapdoor using the following basic approximation: $1 - 2\Sigma p_s/p_{s0}$. The increase in load on the support should theoretically be equal the decrease in load on the trapdoor, that is values of 1-$2\Sigma p_s/p_{s0}$ should equal p/p_0 throughout.

The difference between the normalised trapdoor and support load data is thought to be caused by small scale or micro-arching effects present across the breadth of the beams. As the load acting on an individual support beam is increased with increasing self-weight of the soil, then the beam is significantly deformed, causing a reduction in load acting on the beam as the soil arches onto the rigid portions of the beam which are built into the aluminium support (see Figure 3.8) and are unable to deflect. As the load on the support structure is increased, due to arching taking place across the trapdoor, the micro-arches across the beams will begin to collapse and more of the load from the overlying soil will be transferred onto the beams. This gives rise to a somewhat non-linear loading response across the support structure where the beams are prevented from deflecting further by the arching process taking place across them.

As δ/B increases, the values of $1 - 2\Sigma p_s/p_{s0}$ and p/p_0 approach one-another, indicating that the reduction of load on the trapdoor is taken by the increase in load on the supports. The ‘sensed’ loading on the beams increases (particularly those close to the trapdoor’s edge) as the micro-arching effects across these beams begin to diminish (as the arches across the beams collapse with increased load). More of the load is transferred to the beams causing further deflection, which is sensed directly by the instrumented beams as an increase in load. In effect, beams closer to the trapdoor, which are subjected to high vertical loads, become more sensitive to increasing loads. This micro-arching process makes it very difficult to accurately determine the loading across the support structure as a result of arching across the trapdoor.

Experimental factors such as errors introduced by averaging of a small number of ‘point’ load measurements across the affected support structure area, and by possible unequal loading acting on either side of the support structure may affect the support measurements. Trapdoor loading measurements are also subjected to errors due to frictional effects discussed in Section 3.2.2.3.

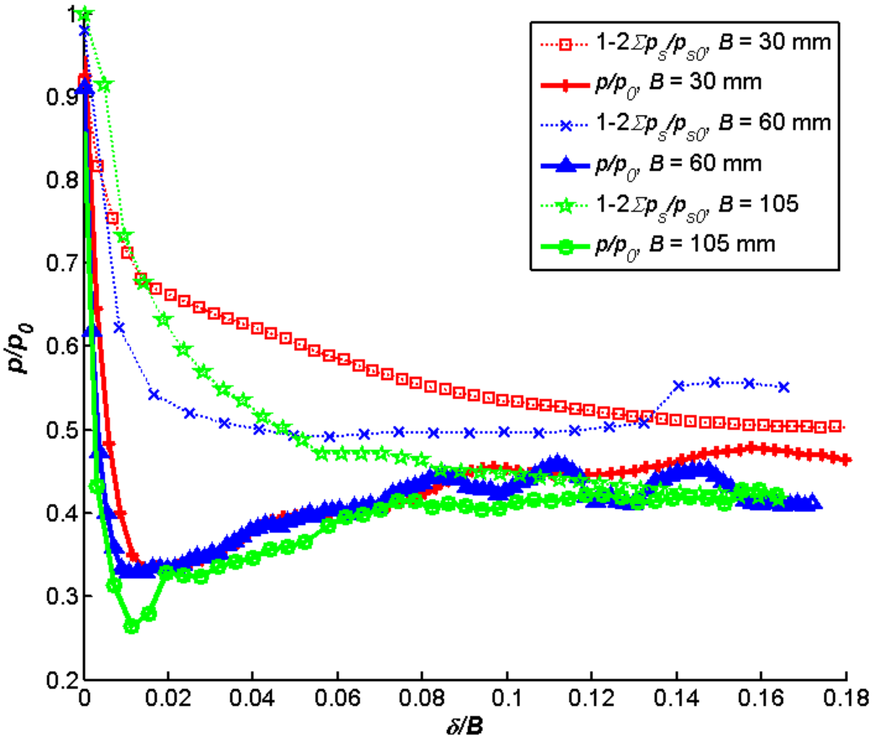

Figure 4.3 Comparison of trapdoor stress, p/p_0, with total stress increase on support structure, $\Sigma p_s/p_{s0}$.

4.2.2 Fibre-reinforced soil: fibre length variation

Figure 4.4 (a) to (d) shows the ground reaction curves for all trapdoor scales for fibre lengths, F_L, of 8, 12, 16 and 20 mm. The fibre content by mass, χ_w, was kept constant at ~0.5% for each case. The plots show relatively little variation in the general shape of the GRC between fibre length tests, or with variation of trapdoor width. The curves all show remarkably similar characteristics in terms of shape and minimum loading. The only significant difference between trapdoor scales appears to be that the initial gradient is lower for small trapdoor tests.

To compare the effect of fibre length variation across all trapdoor scales the average loading of all trapdoor scales for each fibre length was calculated. This also serves to aid clarity by reducing the number of traces and plots considered in the study of the general overall behaviour. The averaged response for each fibre length is shown in Figure 4.5 (where $\bar{p}$ denotes an average value), along with the unreinforced case. The load responses show very little variation with fibre length and no discernible trend can be observed. Also plotted is the calculated mean of all GRCs, μ, ±5%, which effectively forms an error band for the plots and gives an indication of how little variation is present between the results.

Figure 4.6 shows the normalised distribution of load across the trapdoor supports, p_s/p_{s0}, for variation of fibre length, F_L., against normalised distance, x/B.

The figure shows the general result that fibre length variation has no significant effect on the loading distribution despite some observable scatter in the data. This is to be expected since an insubstantial effect on trapdoor loading was observed; it follows that the support structure loading should also be invariant with fibre length.

The relationship between support structure load, $1-2\Sigma\, p_s/p_{s0}$, and trapdoor loading, p/p_0 with displacement, as shown in Figure 4.3 for unreinforced soil, was observed to be invariant with fibre length. The differences in loading magnitudes between trapdoor scales were found to be greater than the differences between all tests with the same trapdoor width; implying that the trapdoor scaling effects are more significant.

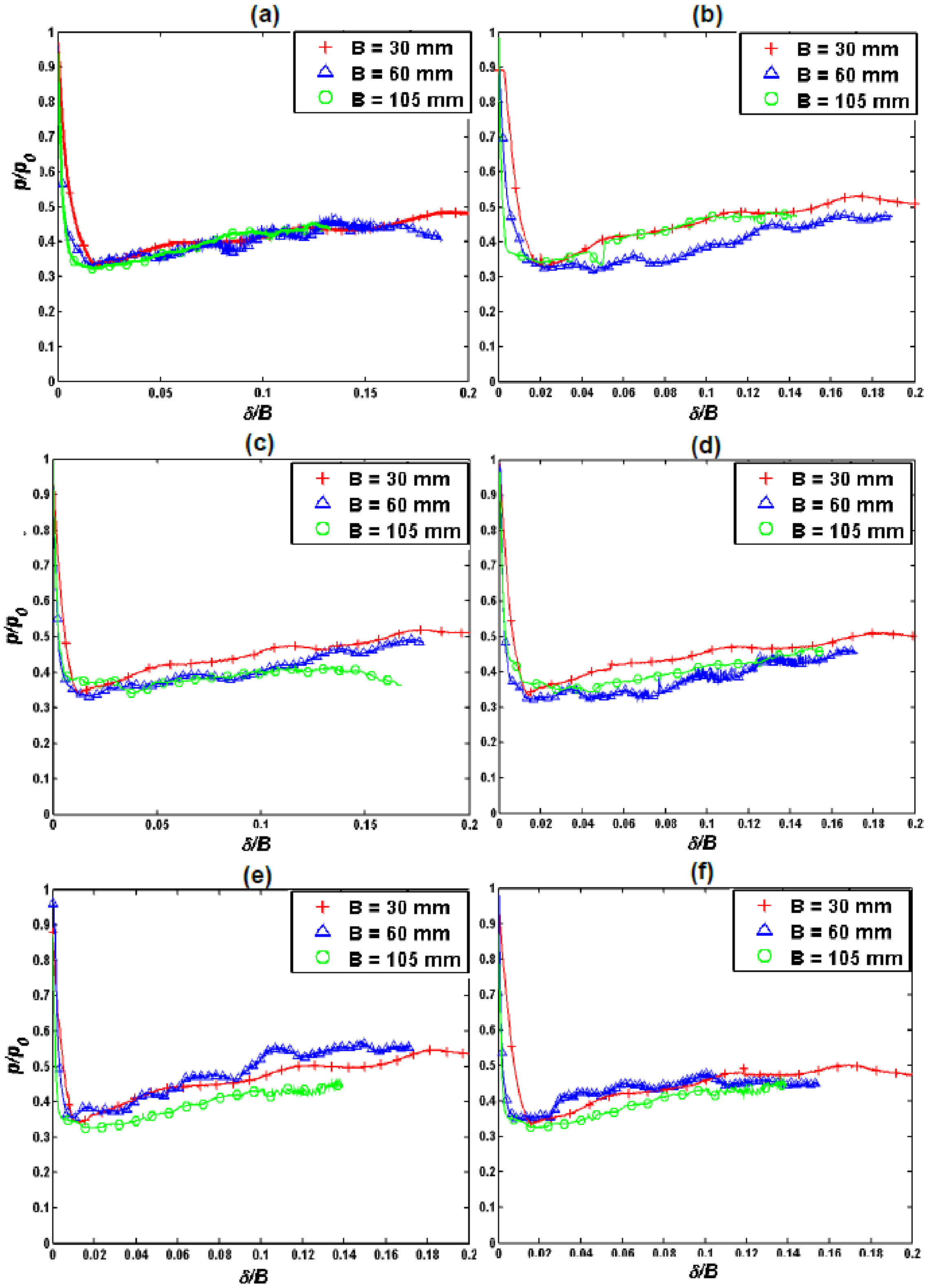

Figure 4.4 GRCs: (a) F_L = 8 mm, χ_w = 0.5%, (b) F_L = 12 mm, χ_w = 0.5%, (c) F_L = 16 mm, χ_w = 0.5%, (d) F_L = 16 mm, χ_w = 0.5%, (e) F_L = 12 mm, χ_w = 0.25%, (f) F_L = 12 mm, χ_w = 1%

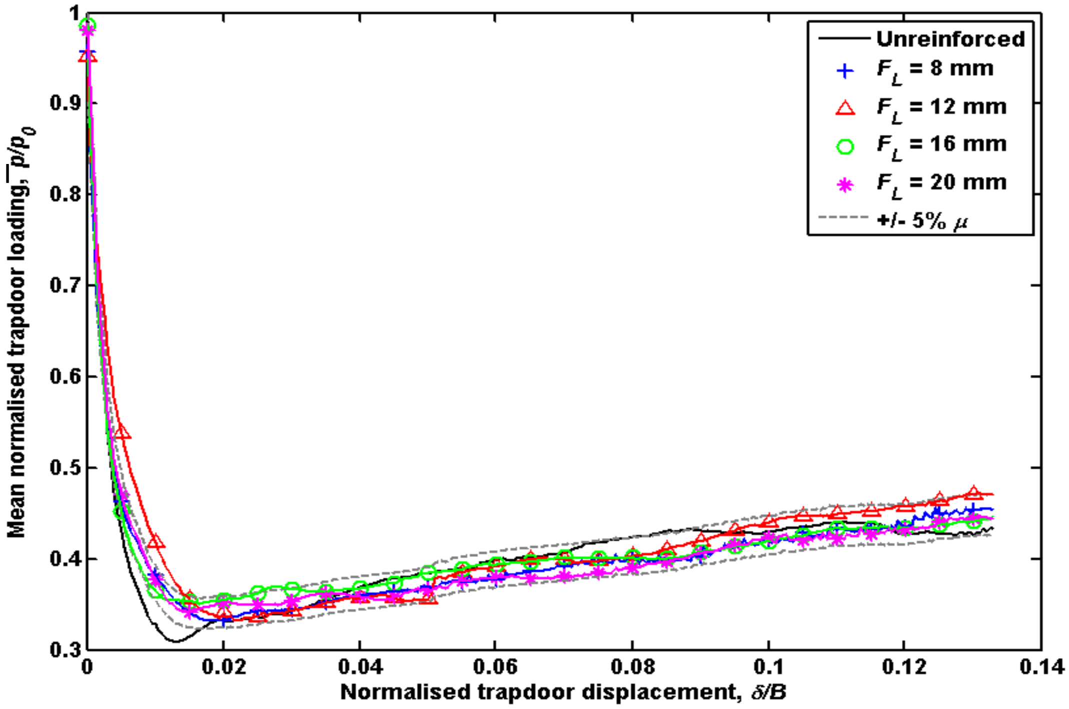

Figure 4.5 Averaged GRC variation with fibre length, F_L. $\chi_w = 0.5\%$

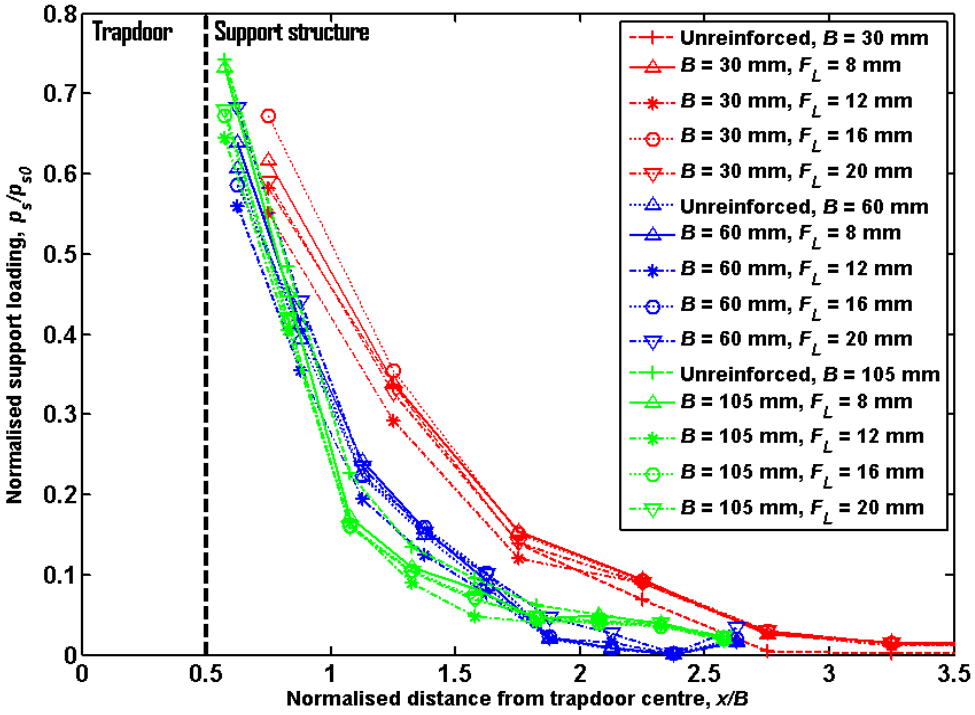

Figure 4.6 Ultimate support loading distribution variation with fibre length, χ_w = 0.5%

4.2.3 Fibre-reinforced soil: fibre content variation

Figure 4.4 (b), (e) and (f) show the GRC responses with fibre content by mass, χ_w, of 0.5%, 0.25% and 1% respectively. Fibres of length, F_L = 12 mm were used in all content variation tests in order to assess the effect of fibre concentration using the same fibre aspect ratio, η, as defined as F_L/d_f where the diameter of the fibre d_f was 0.5 mm.

The averaged response for each fibre concentration is shown in Figure 4.7. As is the case with the fibre length variation results of Section 4.2.2, the GRC results for varying fibre content are very similar, all lying between the ±7.5% of the mean, μ. The result shows some small variation in load reduction with fibre content. As fibre content is increased the curves show an apparent reduction in load. When fibre contents are compared, however, the unreinforced case shows the lowest overall load. This trend is unexpected, as the effect of fibre content on the soil behaviour should reduce with fibre content.

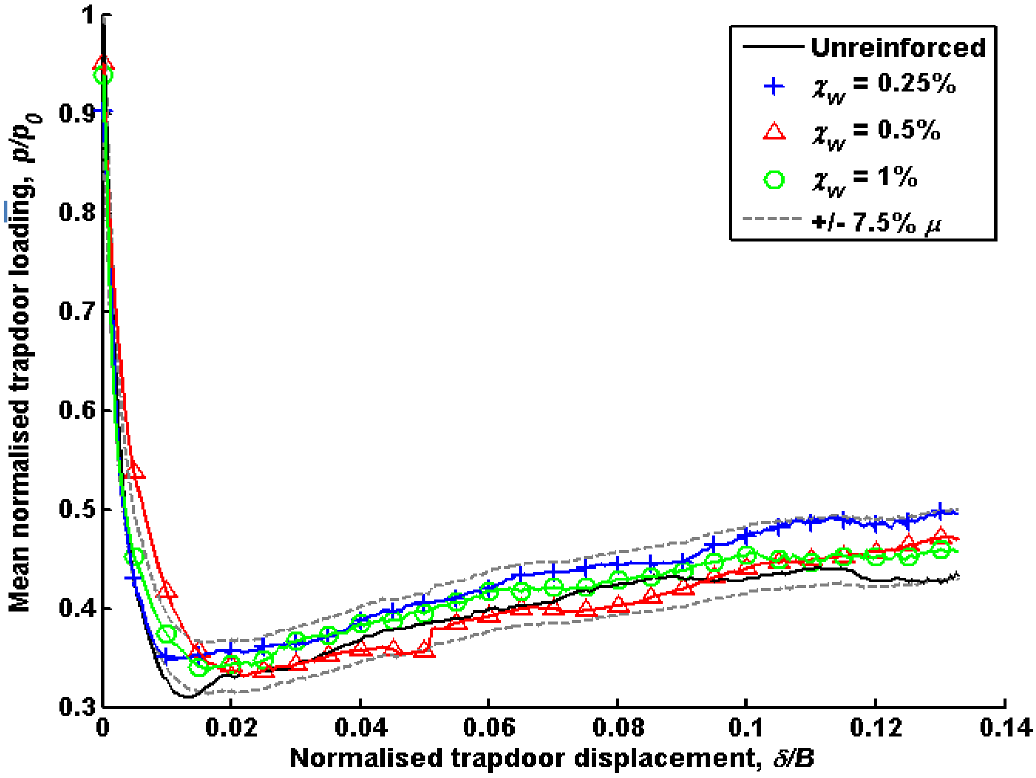

Figure 4.7 Averaged GRC variation with fibre content, χ_w. F_L = 12 mm.

Figure 4.8 shows the normalised distribution of load, p_s/p_{s0}, across the support structure width, x/B, for the variation in fibre content by mass, χ_w, with a constant fibre length, F_L, of 12 mm.

As is the case with the support loading variation with fibre length (Figure 4.6), the responses with fibre inclusion all appear to be very similar to the unreinforced case.

The general support loading distribution can be accurately approximated using an exponential curve of the form given in Equation 4.1.

$$\frac{p_s}{p_{s0}} = M_s e^{-R_s x} \quad (4.1)$$

Where:

M_s is the fitted value of support loading at x = 0.

R_s is the fitted rate of exponential decay across the support.

Fitted values for both these parameters are given in Table 4.1.

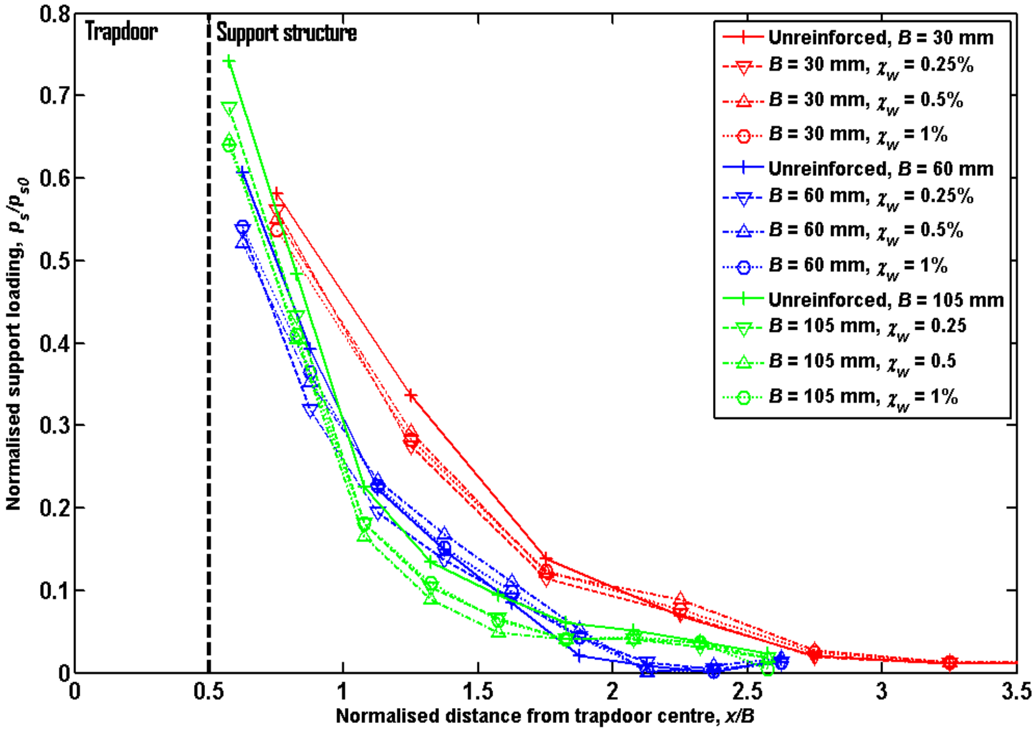

Figure 4.8 Ultimate support loading distribution variation with volumetric fibre content, χ_w. F_L= 12 mm.

4.2.4 GRC results summary

Table 4.1 gives the parameters to define the GRC response as proposed by Iglesia et al. (1999) and detailed in Section 2.4.1. The parameters for the exponential support loading approximation given in Equation 4.1 are also listed. The variation of all loading parameters is plotted in Figure 4.9 against the product of fibre aspect ratio, η, and volumetric fibre content, χ. The volumetric fibre content is roughly approximated by the relationship $\chi = 2\chi_w$

Michalowski and Cermak (2002) define the macroscopic friction angle, $\bar{\phi}$, (see Section 2.6.1) to determine the improvement in fibre soil composite shear strength, as a function of $\eta\chi$ (see Figure 2.26). From here on this quantity shall be referred to as the fibre factor.

As discussed in Section 2.6.1 the increase in strength with fibre content is broadly proportional to the product of fibre aspect ratio and fibre content, the 'fibre factor', $\eta\chi$ is expressed as a percentage, since η.is dimensionless.

As mentioned, the main difference between responses appears to be the initial gradient, M_A. This varies significantly between trapdoor sizes but not with fibre length or volumetric content. This effect is discussed in more detail in Section 5.2

The load recovery index, λ, appears to slightly reduce with increasing fibre length but remains invariant with fibre content. The GRC minimum and ultimate loading and the secant modulus, M_B defined in Iglesia et al. (1999) as the gradient between the geostatic intercept and the breakpoint (where the breakpoint is the normalised loading when normalised displacement is ~0.01, see Section 2.4.1) all appear relatively invariant with fibre length and content despite some observable scatter in the data.

Figure 4.9 shows small variation of the parameters to determine support loading (in terms of exponential decay described in Equation 4.1) with fibre length or content. This is to be expected from the similarity of the responses shown in Figures 4.5 and 4.7. There are some differences between support and trapdoor loading response due to the small-scale arching effects occurring across the support structure discussed in Section 4.2.1.

In general it can be concluded that fibre inclusion has no significant effect on the loading response. Figure 4.4 shows some variation in loading response with displacement for all tests carried out, particularly in the medium trapdoor GRC response. This deviation from the smooth curves predicted by Iglesia et al. (1999) is caused by frictional forces and bending moments acting on the trapdoor during its descent (due to unequal arching stresses along the trapdoor width and breadth, as a result of trapdoor tilt with displacement as discussed in Section 3.2.2.3.).

It is thought that these influences amount to variations in the GRC which are of similar magnitudes and influence on the measurement of trapdoor loading as those owing to fibre inclusion effects. It is estimated that the GRC cannot be determined to accuracies greater than ±5-7.5 % of the mean μ trapdoor response, as plotted in Figures 4.5 and 4.7.

Table 4.1 Ground reaction curve parameters.

Test ID	Trapdoor width, B, mm	Fibre length, F_L, mm	Fibre content, χ_w, %	Initial gradient, M_A	Secant gradient, M_B	Min. loading	Load recovery index, λ	Ultimate loading	Support max., M_S	Support decay rate, R_S
CMC01	60	–	0	169	67	0.33	1.58	0.43	2.18	2.02
CMC02	60	12	0.25	157	64	0.36	1.41	0.51	1.82	1.96
CMC03	60	12	0.5	115	56	0.32	1.16	0.47	2.08	2.08
CMC04	60	12	1	271	67	0.35	1.43	0.45	1.72	2.04
CMC05	60	8	0.5	215	59	0.33	1.42	0.44	2.26	1.99
CMC06	60	16	0.5	221	68	0.33	1.05	0.49	1.96	1.89
CMC07	60	20	0.5	189	62	0.36	0.91	0.40	2.42	2.01
CMC08	30	–	0	103	62	0.33	1.44	0.44	1.63	1.35
CMC09	30	12	0.25	77	56	0.34	1.17	0.55	1.65	1.35
CMC10	30	12	0.5	62	50	0.33	1.45	0.51	1.52	1.35

Test ID	Trapdoor width, B, mm	Fibre length, F_L, mm	Fibre content, χ_w, %	Initial gradient, M_A	Secant gradient, M_B	Min. loading	Load recovery index, λ	Ultimate loading	Support max., M_S	Support decay rate, R_S
CMC11	30	12	1	67	57	0.33	1.45	0.48	1.52	1.37
CMC12	30	8	0.5	90	54	0.34	1.55	0.45	1.67	1.32
CMC13	30	16	0.5	65	62	0.34	1.06	0.51	1.92	1.39
CMC14	30	20	0.5	85	60	0.33	0.91	0.51	1.60	1.32
CMC15	105	_	0	204	74	0.28	1.56	0.42	2.52	2.11
CMC16	105	12	0.25	293	53	0.32	1.07	0.44	2.66	2.33
CMC17	105	12	0.5	222	60	0.34	1.28	0.47	2.61	2.40
CMC18	105	12	1	291	66	0.32	1.38	0.45	2.35	2.24
CMC19	105	8	0.5	215	62	0.32	1.42	0.45	2.91	2.38
CMC20	105	16	0.5	232	63	0.36	0.9	0.41	1.92	1.39
CMC21	105	20	0.5	237	60	0.37	0.93	0.45	1.61	1.32

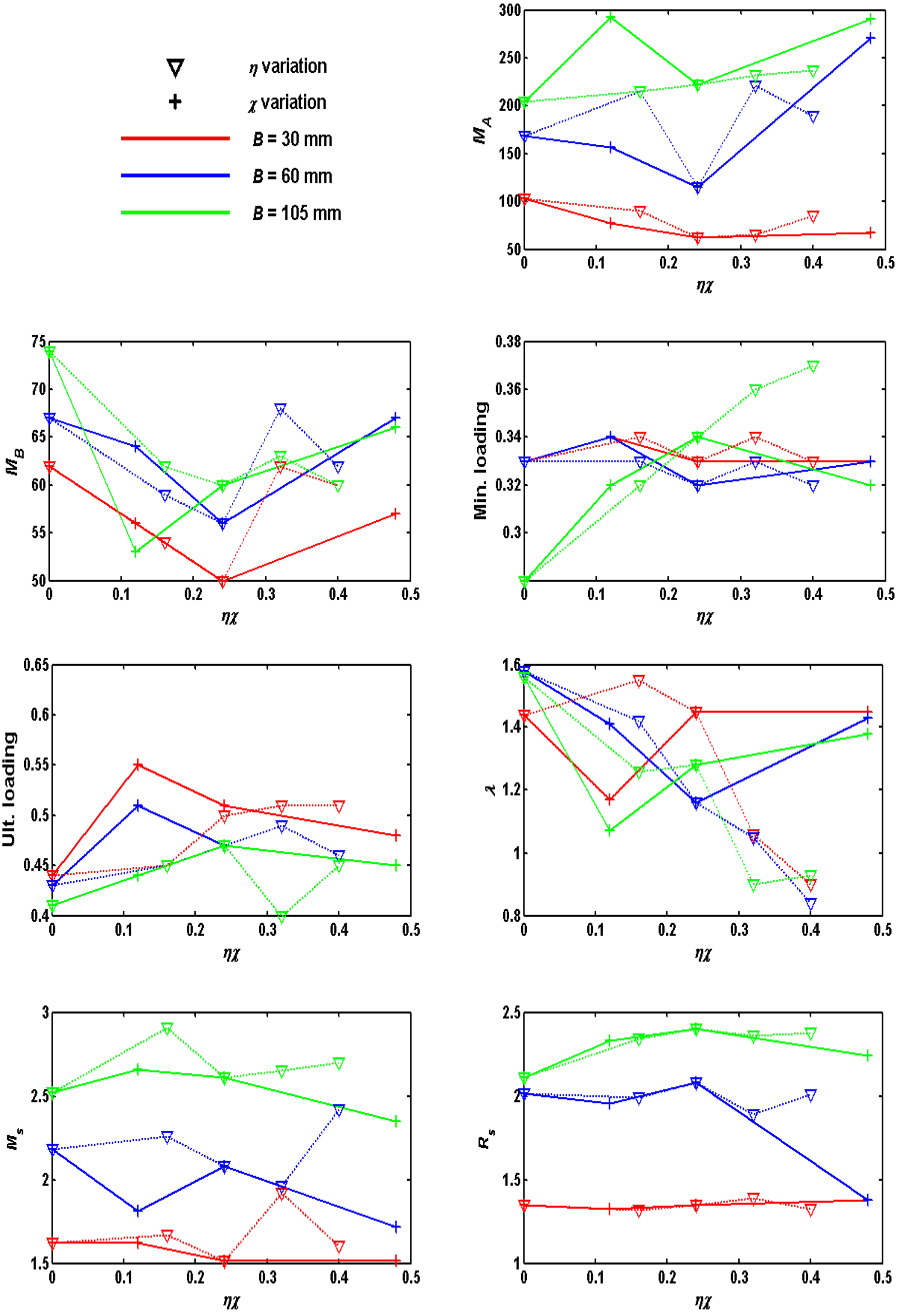

Figure 4.9 Trapdoor GRC and support loading parameters with variation of fibre factor, $\eta\chi$.

4.3 Displacement and strain results

4.3.1 Unreinforced soil

Figure 4.10 shows the development of the vertical displacement curves for the unreinforced soil test cases with small, medium and large trapdoor widths. The horizontal axis is normalised distance from the trapdoor centre, x/B, the vertical axis is trapdoor movement, δ/B. The curves show the magnitude of vertical settlement normalised by trapdoor width, S_V/B, at different stages of the test, indicated by markers. The settlement data was obtained from the PIV analysis, as described in Section 3.2.2.4.

The curves are the displacements at depths, z, throughout the soil; at the surface, $z = 0$, and at depths of $z = 0.25H$ and $z = 0.5H$

The plots show some significant differences between the different geometries; particularly at low depths where the maximum settlement for the small trapdoor is substantially smaller across the range of displacement.

The medium and large trapdoor cases show similar settlement magnitudes trends throughout the soil layer depth. The curves indicate that vertical displacements are asymmetric about the trapdoor centreline for the large trapdoor test, particularly at the surface.

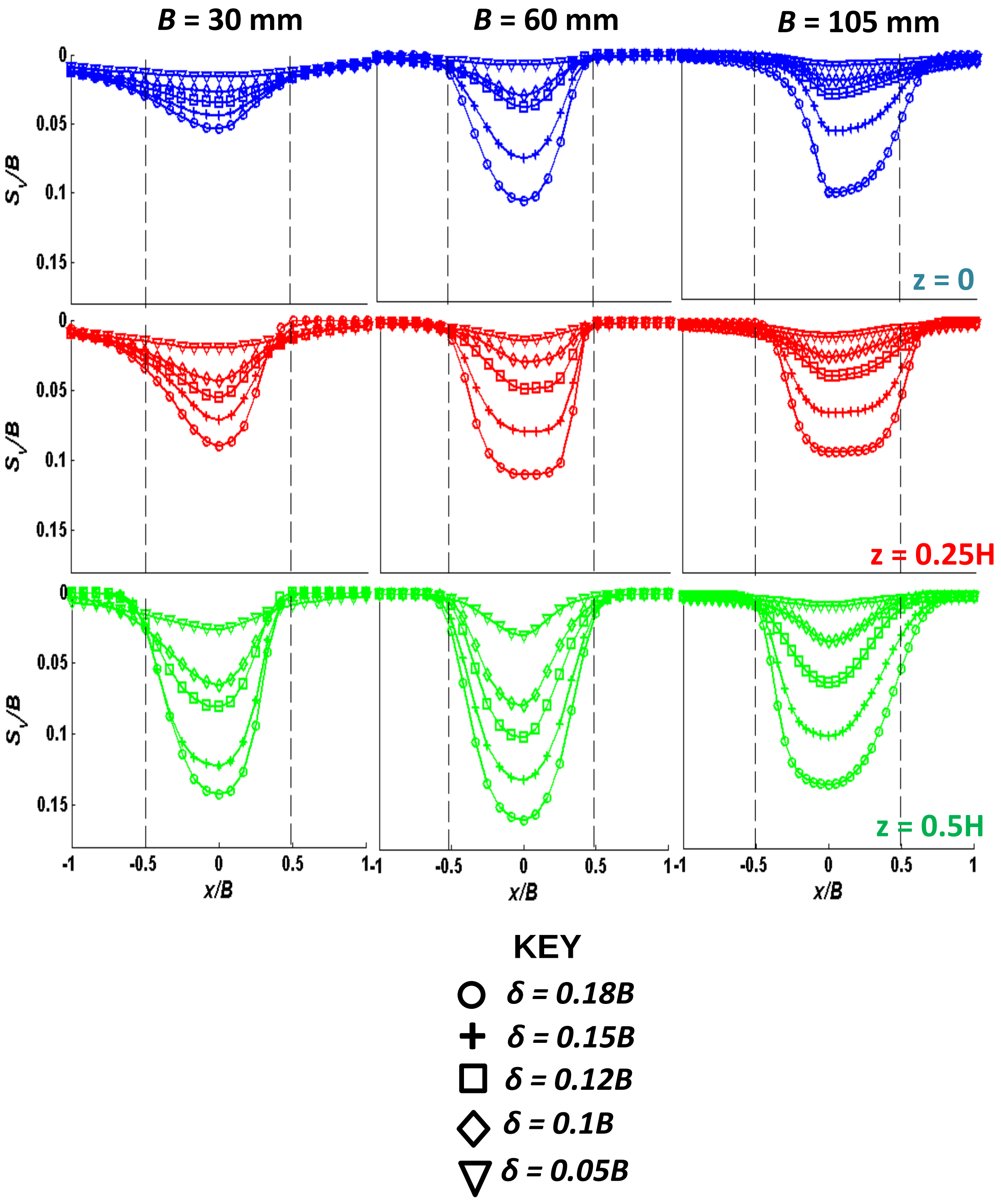

Figure 4.10 Normalised vertical displacement, S_v/B, curve development with trapdoor displacement, $\boldsymbol{\delta}$, for unreinforced soil at depths; $z = 0$, z = $0.25H$ and $z = 0.5H$.

In order to effectively filter out scatter in the measurement; curves were fitted to the experimental vertical settlement experimental data using the modified Gaussian model of Equation 2.24 detailed in Section 2.5.3. The vertical settlement approximation was found to provide an adequate fit to the PIV displacement data. The approximation is discussed further and compared in Sections 4.3.2 and 4.3.3.

The horizontal displacements were fitted to experimental data using a least squares curve fitting approach where a cost function was used to optimise a parameter set defining the shape of the curve. The horizontal displacement close to the centre of the trapdoor was found to be an adequate fit to a sinusoid described by Equation 4.2.

$$0 < x < 0.25B \qquad S_x = p_1 \sin(p_2\, x + p_3) \qquad (4.2)$$

Where:

p_1 is a fitted parameter describing sine wave amplitude

p_2 is a fitted parameter describing sine wave wavelength

p_3 is a fitted parameter describing sine wave phase shift

The displacements further from the trapdoor were found to be approximated by an exponential of the form given by Equation 4.3.

$$x > 0.25B \qquad S_x = p_4 e^{p_5 x} \qquad (4.3)$$

Where:

p_4 is a fitted parameter describing the amplitude of the exponential term

p_5 is a fitted parameter describing the decay of the exponential term

The curve obtained for one half of the trapdoor using Equations 4.2 and 4.3 was then used to approximate the displacement on the opposite side of the trapdoor using Equation 4.4.

$$x < 0 \qquad S_x = -p_6 S_x \qquad (4.4)$$

Where: S_x is the value of horizontal settlement calculated using Equations 4.2 and 4.3. The parameter p_6 describes the weighting of the curve, compared to the curve obtained for the right hand side of the trapdoor, and allows for some flexibility in the data fitting process where the magnitudes of displacement are asymmetrical about the trapdoor centre.

In tunnelling, the horizontal displacements can be estimated directly from the vertical displacements and the tunnel depth. Attewell et al, (1986) derived an expression for horizontal displacement based on the assumption that the soil is moving towards the tunnel centreline as the tunnel volume is reduced. Attewell's equation, specific to tunnelling induced displacement is presented in Equation 2.26 of Section 2.5.3.

Equation 4.5 presents an estimate of horizontal displacement, S_{xa}, based on the vertical displacement, S_v and the height of the soil.

$$S_{xa} = {}^{-xS_v}\!/_{Hp_7} \qquad (4.5)$$

Where p_7 is a parameter used to scale the horizontal displacement with depth. The horizontal displacements are not expected or observed to be of the same magnitude as those predicted by the estimate in Equation 4.5 due to the geometrical differences between volume loss in radial tunnel contractions and that induced by prismatic trapdoor movements. The parameter adequately models the observed decay in the influence of vertical displacement with depth. Equation 4.6 gives the final estimate of horizontal displacement from the curve fitting process, S_{xc}, which is a weighted function of the estimates obtained from Equations 4.2 to 4.4 and the estimate based on tunnelling from Equation 4.5.

$$S_{xc} = S_x p_8 + (1 - p_8) S_{xa} \qquad (4.6)$$

Where the parameter, p_8, is used to weight the estimates and is limited between zero and unity. The parameter provides a means of incorporating observed disparities between estimates based on simple sine and exponential approximations and those from vertical displacements into the curve fitting process.

The estimate was found to be a good overall fit to measured data throughout despite very small magnitudes of displacement and consequent scatter in the measurement. Figure 4.11 shows fitted curves (indicated by solid lines) compared to the measured horizontal displacement data (indicated by markers) for unreinforced soil and all trapdoor scales at the soil surface obtained at displacements of .

The smoothness of both vertical and horizontal estimates is essential in order to obtain clear strain estimates using the method described in this section below.

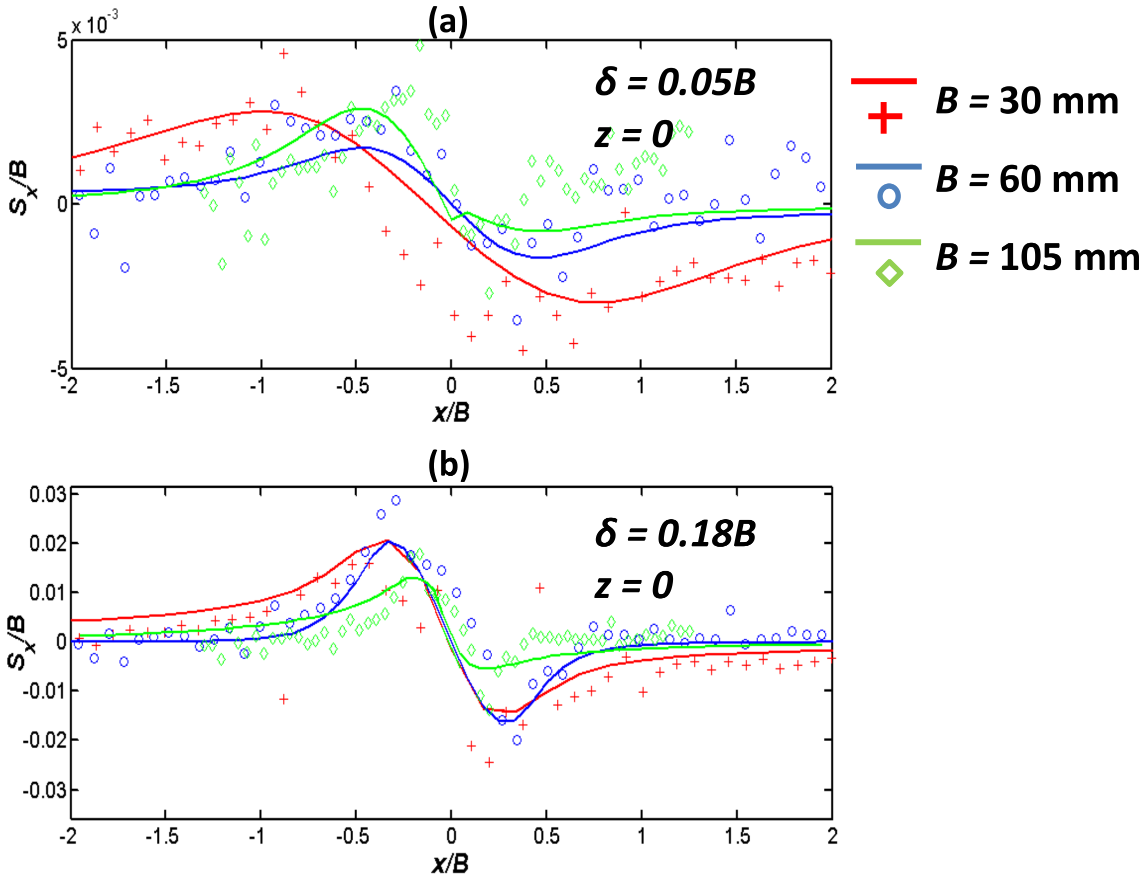

Figure 4.11 Comparison of normalised measured surface horizontal displacement data, S_x/B, with normalised fitted data, S_{xc}/B for unreinforced soil. (a) δ = 0.05B; (b) δ = 0.18B;

In order to clearly present the magnitude of settlement throughout the depth, the physical displacements, S_x and S_v are normalised by the trapdoor displacement, δ, and scaled such that displacements throughout the depth can be readily compared. Scaled and normalised vertical horizontal settlements are calculated using Equations 4.7 and 4.8.

$$S_v{}^* = \frac{-S_v SF_v}{\delta B} + \frac{z}{B} \quad (4.7)$$

$$S_x{}^* = \frac{S_x SF_x}{\delta B} + \frac{z}{B} \quad (4.8)$$

Scale factors of $SF_v = 10$ and $SF_x = 100$ are used throughout the study in plots of settlements to appropriately scale the settlements such that the displacements and height at which they occur are clearly shown at .

Axial vertical and horizontal strain estimates were calculated using Equation 4.9 and 4.10 respectively.

$$\varepsilon_{zz} = \frac{dS_v}{dz_p} \quad (4.9)$$

$$\varepsilon_{xx} = \frac{dS_x}{dx_p} \quad (4.10)$$

Where dz_p and dx_p are the distances between measurement points in the vertical and horizontal planes (defined by the patch size of the PIV mesh used). For all tests reported herein; $dx_p = dz_p$ The displacement field was interpolated to give displacements at 5 mm intervals. The volumetric strain, ε_v, is the sum of vertical and horizontal strains (assuming the strain parallel to the trapdoor, $\varepsilon_{yy} = 0$):

$$\varepsilon_v = \varepsilon_{xx} + \varepsilon_{zz} \quad (4.11)$$

In this study positive volumetric strain represents tensile strains (soil expansion) whereas negative volumetric strains represent contraction.

Engineering shear strain, γ, was calculated using Equation 4.12.

$$\gamma = \sqrt{(\varepsilon_{xx} - \varepsilon_{zz})^2 + 4\varepsilon_{xz}{}^2} \quad (4.12)$$

Where engineering shear strain, γ, is the diameter of the Mohr circle of strain. Calculated shear strain, ε_{xz}, is given in Equation 4.13.

$$\varepsilon_{xz} = -\frac{1}{2}\left(\frac{dS_x}{dz_p}+\frac{dS_v}{dx_p}\right) \qquad (4.13)$$

Figure 4.12 illustrates the Mohr circle relationships and definitions of axial, shear and principal strains and defines the trapdoor axes along which calculations of strain apply.

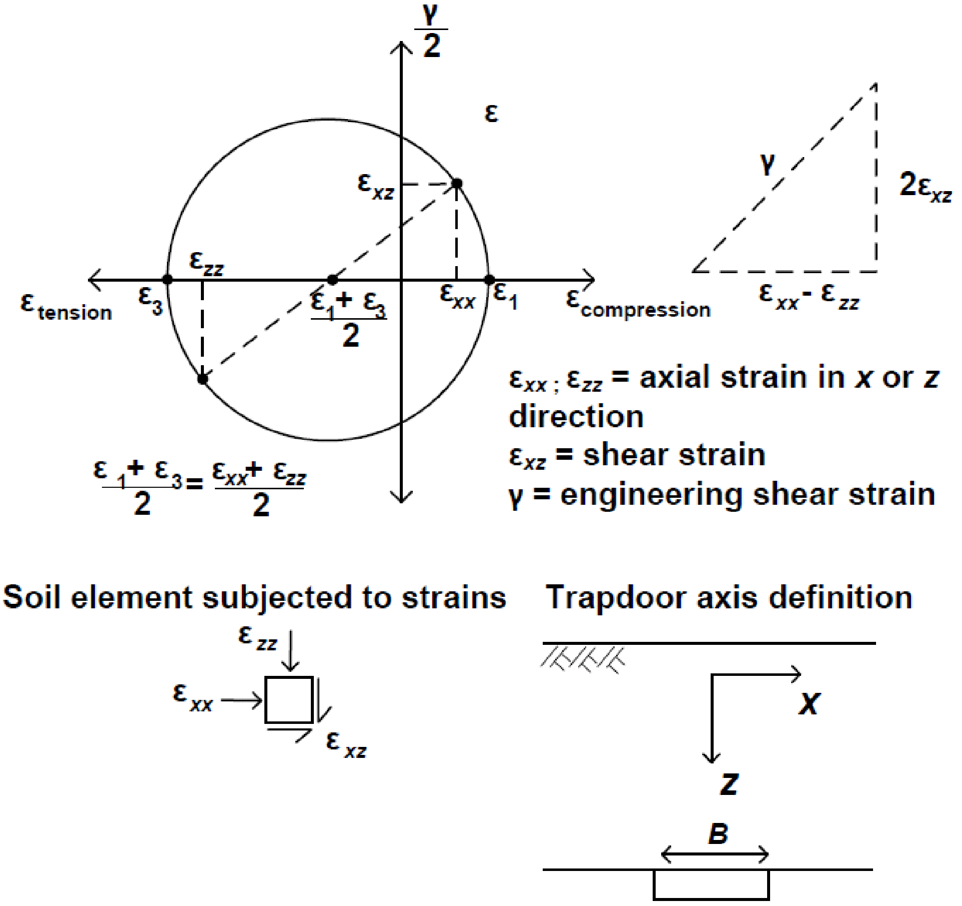

Figure 4.12 Mohr circle of strain

Figures 4.13, 4.14 and 4.15 show scaled vertical and horizontal displacement, S_v^* and S_x^* plotted against normalised distance from the trapdoor centre, *x/B*, for small (*B* = 30 mm), medium (*B* = 60 mm) and large (*B* = 105 mm) width trapdoor tests with unreinforced soil, respectively.

Normalised displacements where the ratio S_v/δ approaches unity indicate that the vertical displacement within the soil is equivalent to the trapdoor displacement. The figure gives a good indication of the relative settlement occurring throughout the soil at various critical stages of the test; the initial phase, where, $\delta = 0.02B$, the maximum arching phase, where, $\delta = 0.05B$, and the ultimate stage, where, $\delta = 0.18B$. The largest settlements, where, $S_v/\delta = 1$, occur at the trapdoor/soil interface depth, and are indicated on Figures 4.13 to 4.15 (a) for scale comparisons. The different coloured traces show the displacements at different stages throughout the test; the solid red traces show the displacements during the initial phase of trapdoor displacement ($\delta = 0.02B$), the dashed black traces show displacements close to the point of maximum arching, when the loading is at a minimum, ($\delta = 0.05B$). The dotted black traces show displacements at the ultimate stage of the test where trapdoor displacements are large ($\delta = 0.18B$).

Figures 4.13 to 4.15 (a) clearly show significant reduction in displacement occurring at shallow depth compared to the trapdoor displacement, δ. The shallow depth displacements are significantly smaller, relative to δ, at relatively small displacements ($\delta = 0.02B$ and $\delta = 0.05B$). The shape of the settlement troughs also vary with both depth and trapdoor displacement. The width of the settlement trough substantially reduces with depth. Small displacements generally give rise to narrower settlement troughs throughout.

Figures 4.16 to 4.18 show contours of vertical settlement, S_v/B, for small, medium and large trapdoors, respectively, at trapdoor displacements of (a) 2, (b) 5 and (c) 18% of the trapdoor width, *B*.

The vertical settlement results show that the soil area immediately above the trapdoor is displacing, or translating, at similar magnitudes to the trapdoor displacement, δ. The general pattern of displacement is shown to change with δ as discussed above. The small trapdoor displacements are notably different from those of the medium and large trapdoors, particularly at large displacements (δ = 0.18*B*).

The responses highlight the differences in displacement with trapdoor scaling, particularly with the small trapdoor, as already shown in Figures 4.9 to 4.15. Trapdoor scaling effects are discussed in further detail in Chapter 5. In light of the observed scaling differences for the small trapdoor, the medium and large trapdoor results will be discussed from hereon in to highlight the general displacement and strain mechanisms taking place as the results obtained at these trapdoor widths are broadly similar.

The relative vertical displacements occur over a greater width during the initial stage than observed at later stages. The initial and maximum arching stages (panes (a) and (b) in Figures 4.17 and 4.18) show a large degree of similarity, in both magnitude and shape, due to the fact that the difference in δ is only 3% of the trapdoor width, *B*, between the respective plots. The ultimate stage of the medium and large trapdoor tests as shown in black dashed lines of Figures 4.14 and 4.15 (a) and the contours of Figures 4.17 and 4.18 (c) clearly show the relative magnitude of displacement is significantly increased at the surface for large trapdoor displacements.

The horizontal displacements (Figures 4.13 to 4.15 (b)) are substantially larger at the surface than at depth, and increase in proportion to trapdoor displacement for all trapdoor scales. The displacements show a general tendency for the soil to migrate towards the trapdoor centre with trapdoor displacement, δ.

Figures 4.19 to 4.21 show the calculated volumetric strains, ε_v, for small, medium and large trapdoors, respectively, at trapdoor displacements of (a) 2, (b) 5 and (c) 18% of the trapdoor width, *B*. For the medium and large trapdoor tests at displacements of 2% and 5% of *B* the data in the figures indicate that an arch is developing in the area of soil above the trapdoor where significant volumetric strain is occurring (positive volumetric strain represents tensile strains (soil dilation) and negative values are compressive strains). For the small trapdoor the arch appears less defined in these stages.

Figures 4.22 to 4.24 show the and shear strains, γ, for small, medium and large trapdoors, respectively, at the same relative displacements as in Figures 4.13 to 4.18 (2, 5 and 18% of *B*). The figures indicate significant shear deformations are occurring throughout, in similar general areas affected by dilation, defining the failure surface within the soil.

All displacements and strains presented for unreinforced soil tests show an arch developing in the area of soil above the trapdoor where significant deformation of the soil is occurring. Based on the collected data, the general mechanism of displacement and deformation occurring within the unreinforced soil can be summarised as follows for the medium and large trapdoor cases:

1) At small trapdoor displacements, for δ < ~0.05*B*, shear strains and volumetric expansion of the soil occurs above the displacing trapdoor within an arch shaped zone. The region of high deformation outlines the failure surface within the soil; initiating from the trapdoor edges, at an angle to the vertical, θ_i, to form an arched region over the trapdoor as shown in the volumetric strains (Figures 4.20 and 4.21 (a)) and shear strains (Figures 4.23 and 4.24 (a)). The crown of the arch is observed to form within the soil above the trapdoor centreline. Soil surface displacements are small and occur over a wide area.

2) As the trapdoor displaces further, an increased area of soil appears to deform. The magnitude of volumetric expansion and shear strain increases. The failure surface, initiating from the trapdoor edges, appears to migrate vertically. The inclination to the vertical of the failure surface initiating from the trapdoor edges, appears to be marginally increased. Displacements at the surface are increased in an approximately linear fashion with trapdoor displacement.

3) At higher relative displacements, typically for δ > ~0.1*B,* shear planes are observed to extend from the crown area of the arch vertically towards the soil surface (see Figures 4.23 and 4.24 (c)). These shear planes describe an inverted triangular region of soil where the apex of the triangle is located at the crown of the arch and the other triangle vertices are to be found at the soil surface at the edges of the trapdoor in the horizontal axis. This suggests an arch failure has taken place in the crown region. Post failure, the triangular region of soil displaces at the same rate as the trapdoor and can be considered to behave as a translating rigid body of soil.

The strain responses for all trapdoor widths show a broadly similar characteristic dilative region forming in the soil with increasing trapdoor displacement in agreement with the general mechanism described above. The results for the *B* = 30 mm trapdoor test indicate that the overall region of volumetric expansion is comparatively larger in relation to trapdoor width. The calculated strains for the 30 mm trapdoor generally show a higher degree of scatter than those with larger trapdoor dimension. This is due in general to the smaller scale and limitations in the resolution of the PIV displacement measurements at this scale. It is worth noting that, at B = 30 mm scale, the absolute displacement of the trapdoor at the initial stages of the test is very small (~0.6 mm), comparable to the average particle size of the soil, d_{50}. Generally the displacements within the soil are significantly smaller than the trapdoor displacements. The limitations of the measurement technique become apparent at small scales and the resulting error could necessarily be responsible for the apparent differences between displacements and strains observed for the small trapdoor compared to larger scales. The absolute strains, as calculated from displacement, are consequently small and as such, are subjected to considerable scatter.

The shear strain plots for all trapdoor widths are generally similar in terms of the general shape of the failure surface, where lines of high strain initiate from the trapdoor edges propagating towards a point above the trapdoor centre at an angle to the vertical, θ_i, which can be seen to slightly reduce as the trapdoor displaces; a phenomenon observed by Costa et al (2009) and others. The change in θ_i with trapdoor displacement is slight and difficult to determine, particularly with the small trapdoor case due to a relatively large degree of scatter in the strain measurement. The observed variation of θ_i across the conducted tests is discussed further in Chapter 5.

All shear strain plots show that a similar mechanism is taking place. The region of high shear above the trapdoor centre appears to propagate towards the surface as the trapdoor displaces. For small to medium displacements of typically $\delta < 0.1B$ no shearing is observed at the surface. Thereafter, for medium and large trapdoor tests, a general surface failure begins to emerge along roughly vertical planes with the trapdoor edges. This general mechanism is discussed in more detail in Section 5.3.

For the small trapdoor tests no evidence of vertical shear bands reaching the surface was observed, indicating the same surface failure conditions were not apparent at small trapdoor scales.

There is some evidence to suggest that the thickness of the shear band, t, appears to increase with reducing trapdoor width.

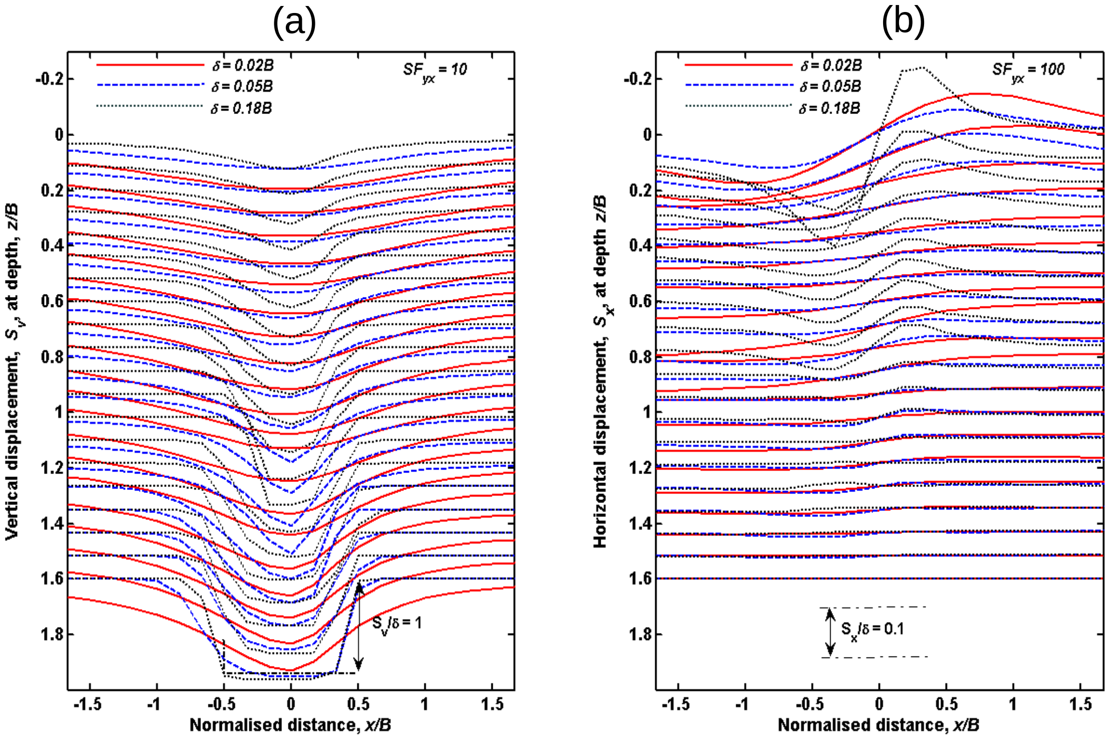

Figure 4.13 Scaled vertical and horizontal displacements, $S_v{}^*$ and $S_x{}^*$ for unreinforced soil, B = 30 mm; (a) Vertical; (b) Horizontal

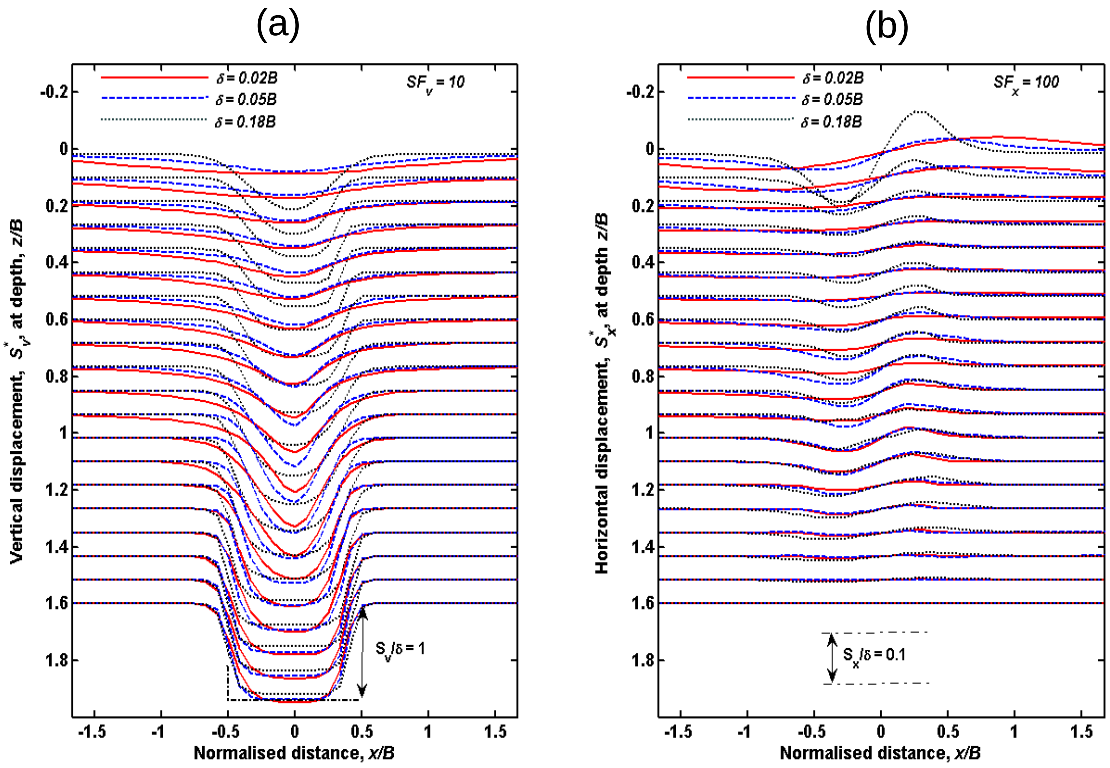

Figure 4.14 Scaled vertical and horizontal displacements, $S_v{}^*$ and $S_x{}^*$ for unreinforced soil, *B* = 60 mm; (a) Vertical; (b) Horizontal

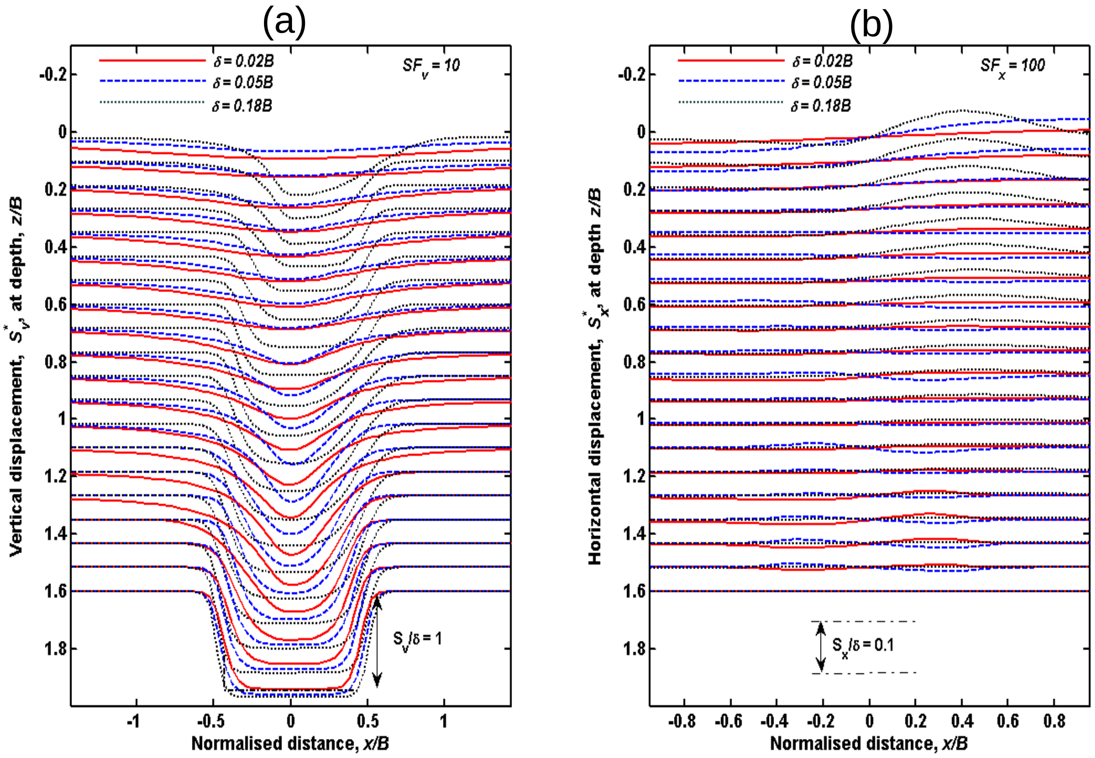

Figure 4.15 Scaled vertical and horizontal displacements, $S_v{}^*$ and $S_x{}^*$ for unreinforced soil, *B* = 105 mm;. (a) Vertical; (b) Horizontal

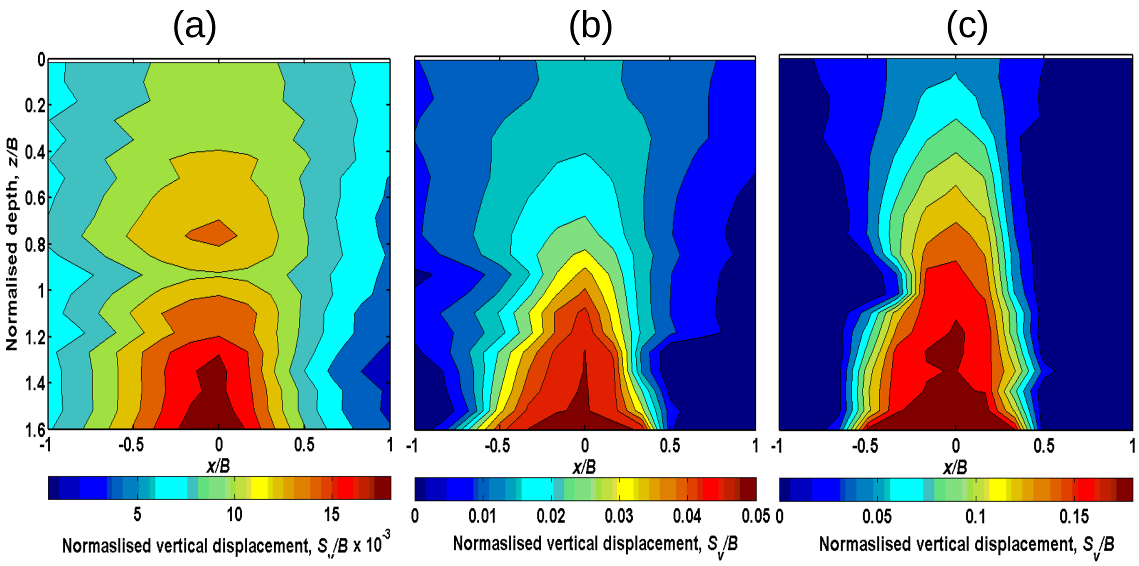

Figure 4.16 Normalised vertical displacement contours, S_v/B, unreinforced soil, B = 30 mm. . (a) δ = 0. 02B, (b) δ = 0.05B, (c) δ = 0.18B

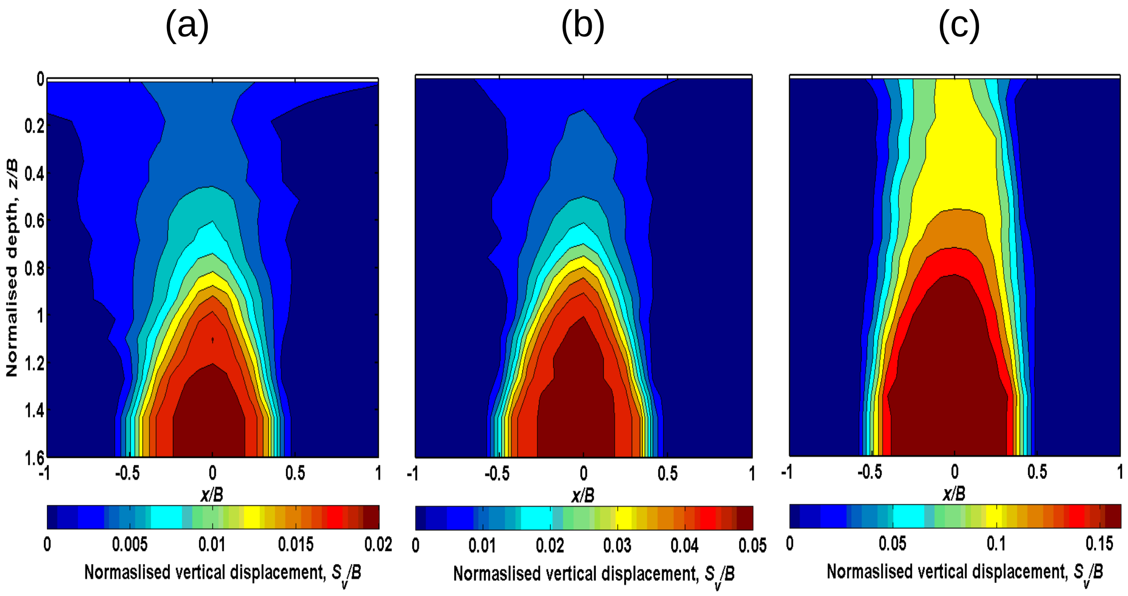

Figure 4.17 Normalised vertical displacement contours, S_v/B, unreinforced soil, B = 60 mm; (a) δ = 0.02B, (b) δ = 0.05B, (c) δ = 0.18B

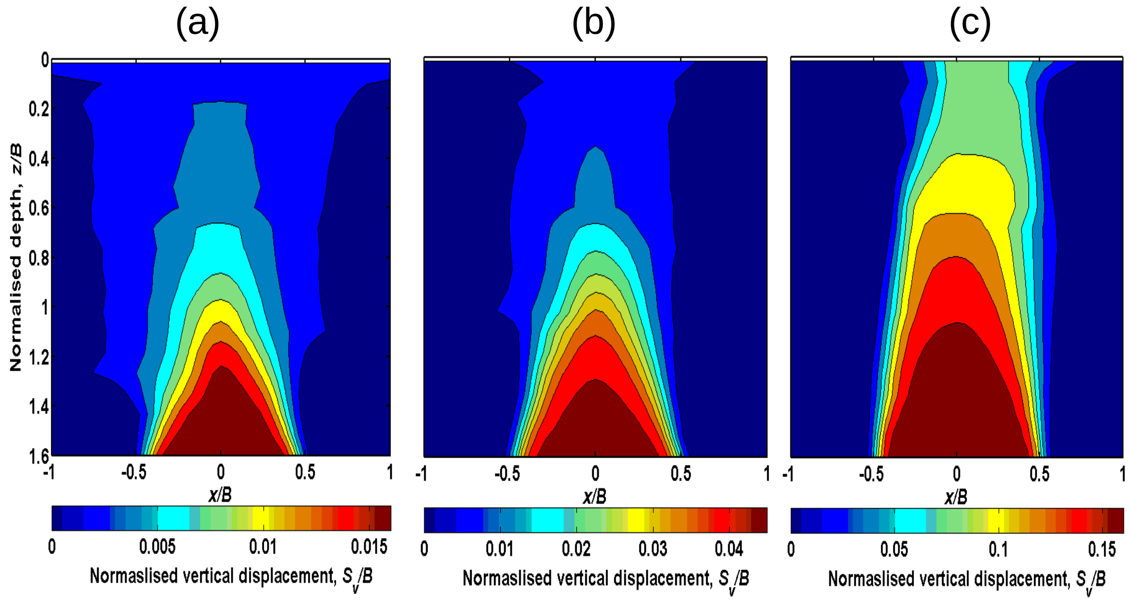

Figure 4.18 Normalised vertical displacement contours, S_v/B, unreinforced soil, B = 105 mm; (a) δ = 0.02*B*, (b) δ = 0.05*B*, (c) δ = 0.18*B*

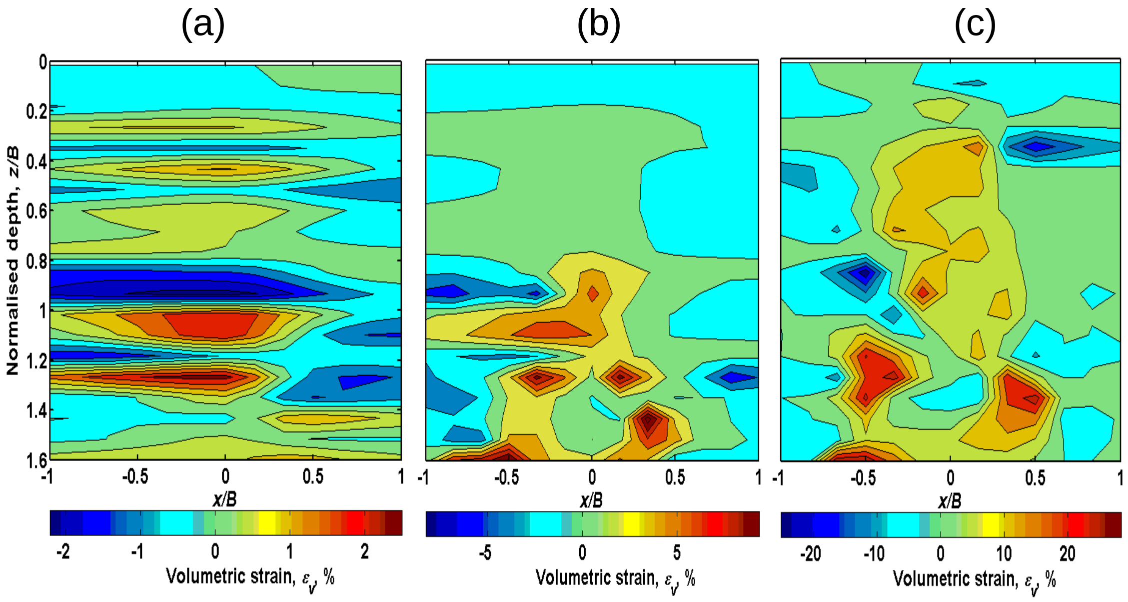

Figure 4.19 Volumetric strain, ε_v, unreinforced soil, B = 30 mm; (a) δ = 0.02*B*, (b) δ = 0.05*B*, (c) δ = 0.18*B*

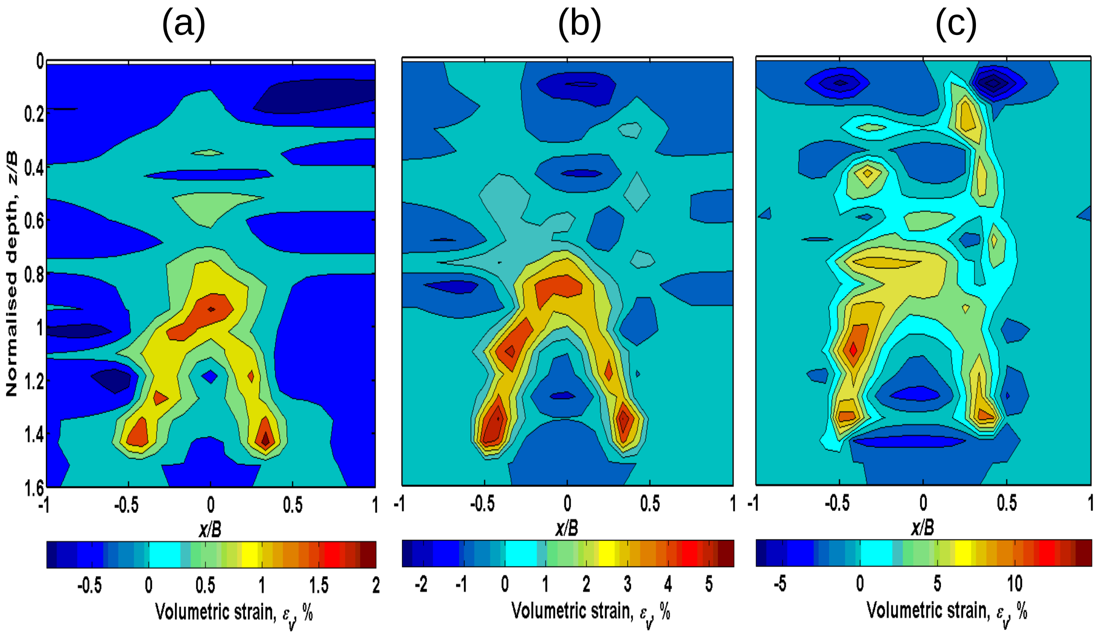

Figure 4.20 Volumetric strain, ε_v, unreinforced soil, *B* = 60 mm; (a) δ = 0.02*B*, (b) δ = 0.05*B*, (c) δ = 0.18*B*

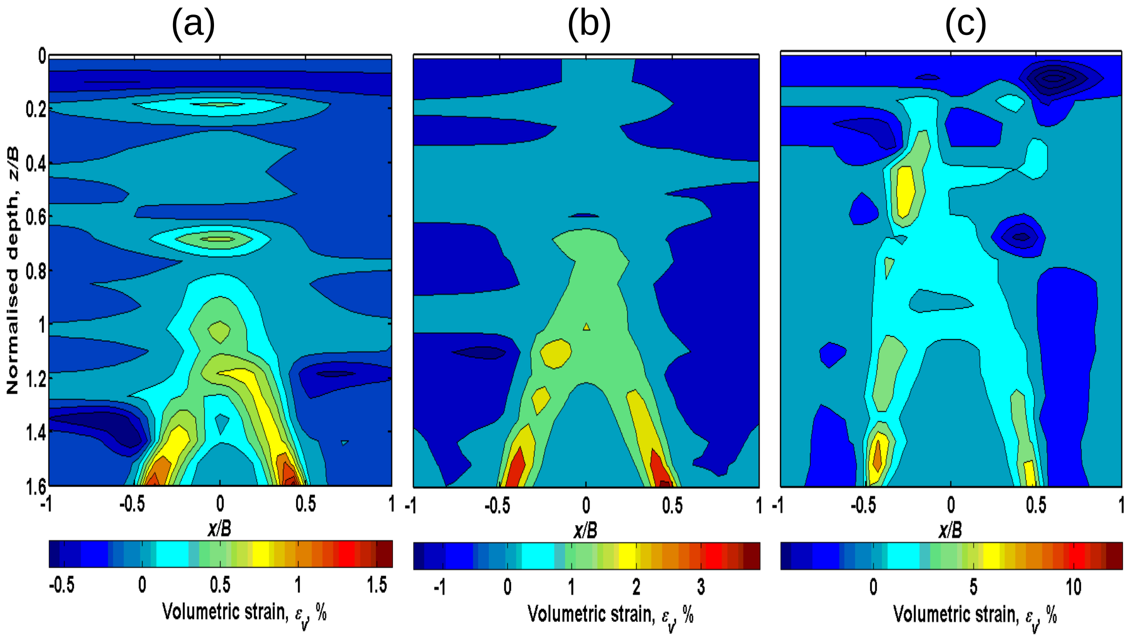

Figure 4.21 Volumetric strain, ε_v, unreinforced soil, *B* = 105 mm; (a) δ = 0.02*B*, (b) δ = 0.05*B*, (c) δ = 0.18*B*

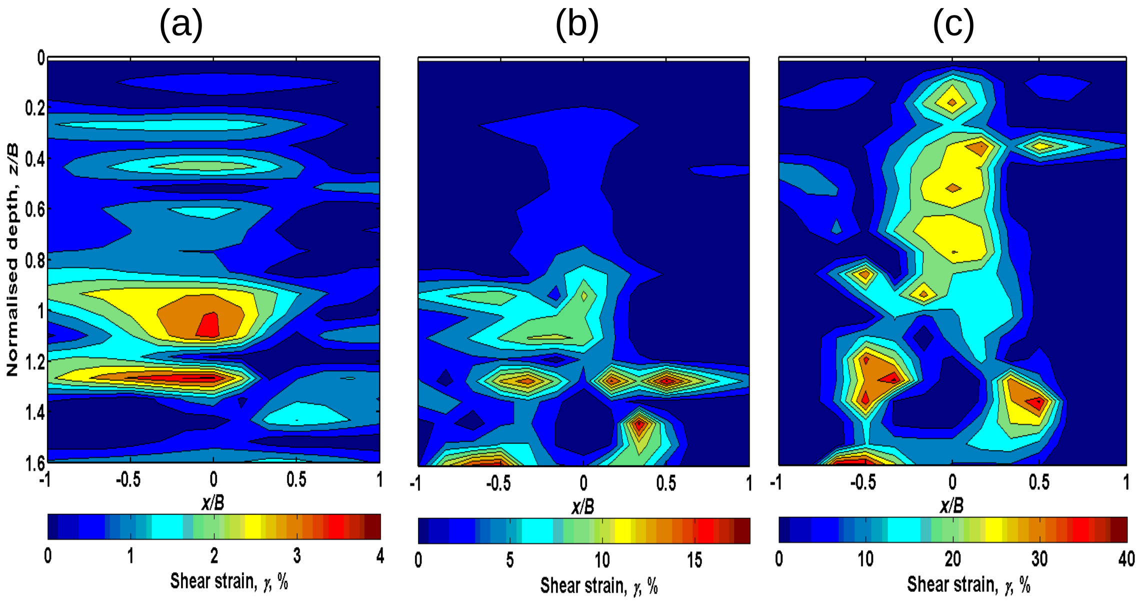

Figure 4.22 Shear strain, γ, unreinforced soil, *B* = 30 mm. ; (a) δ = 0.02*B*, (b) δ = 0.05*B*, (c) δ = 0.18*B*

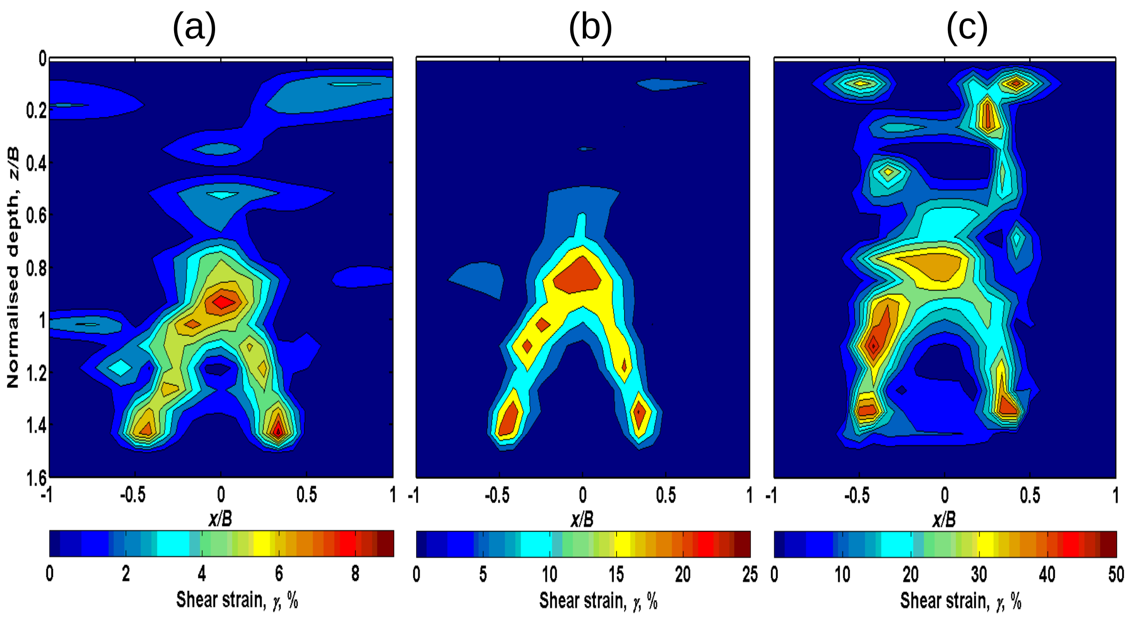

Figure 4.23 Shear strain, γ, unreinforced soil, B = 60 mm; (a) δ = 0.02*B*, (b) δ = 0.05*B*, (c) δ = 0.18*B*

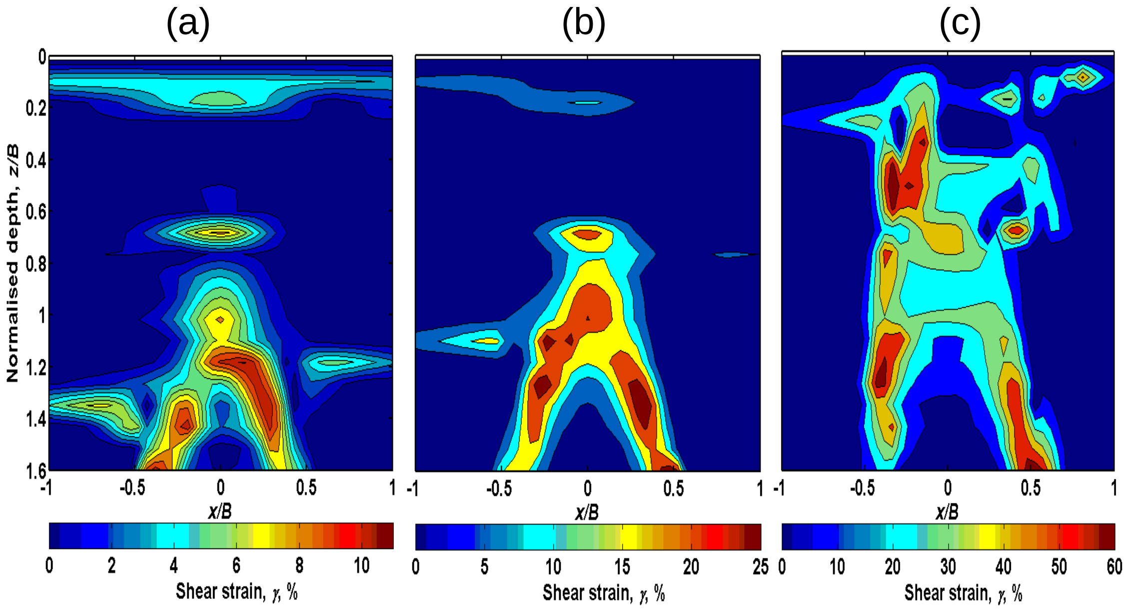

Figure 4.24 Shear strain, γ, unreinforced soil, B = 105 mm; (a) δ = 0.02*B*, (b) δ = 0.05*B*, (c) δ = 0.18*B*

4.3.2 Variation with fibre length

Figures 4.25 to 4.27 show the variation of normalised maximum settlement, S_{max}/B, with normalised trapdoor displacement, δ/B, at depths z of 0*H*, 0.25*H*, 0.5*H* and 0.75*H*. Settlements for the unreinforced test case and for fibre lengths, F_L, of 8 mm, 12 mm, 16 mm and 20 mm are plotted. The fibre content by sand mass, χ_w, was kept constant at ~0.5% for each test. Figure 4.25 shows the responses for the small trapdoor case, *B* = 30 mm, Figure 4.26 shows *B* = 60mm and in Figure 4.27 *B* = 105 mm.

As in the previous section, the general responses for medium and large trapdoor show different results to the small trapdoor due to scaling effects discussed in further detail in Section 5.5. In order to discuss the general mechanism, only the medium and large trapdoor scales are considered in detail.

The solid lines represent the unreinforced soil case. All tests with fibre-soil composite are indicated by markers defined in the figure key. All fibre cases show a significant reduction in the amount of maximum settlement measured at the surface and shallow depths. When the rate of change of maximum displacement with trapdoor displacement is equivalent to the 1:1 lines shown on the figures, the soil is displacing at the same rate as the trapdoor.

The surface plots in Figures 4.26 and 4.27 show that in all tests the magnitude of maximum settlement increases at roughly the same initial gradient with trapdoor displacement, with surface displacements generally being much less than that at the trapdoor. For the unreinforced case, the gradient then increases and tends towards the 1:1 line after a trapdoor displacement of around δ/B = 0.1. This indicates that subsequent surface displacements are thereafter equivalent to trapdoor displacements and the zone of soil above the trapdoor effectively displaces downwards as a rigid body. The plots for the same test case at greater depths show that soil displacements tend towards the 1:1 line at lower values of δ/B compared to the surface, with displacements nearest the trapdoor effectively matching those of the trapdoor throughout the test.

At the surface the gradients for the fibre–soil composites do not tend towards equality until higher displacements have been reached, generally $\delta >$ 0.15*B*. The data indicates that the reduction in settlement (at large displacements) is related to fibre length; surface and shallow depth displacements are generally reduced with increasing fibre length.

The small trapdoor displacements show a broadly equivalent improvement in the amount of settlement at the surface, and throughout the soil layer, at the ultimate stage as in the *B* = 60 mm case. The relation to the 1:1 line shown indicates that, for all *B* = 30 mm tests, the rate of displacement of the soil at the surface does not match that of the trapdoor and the soil is not moving downward in the manner of a rigid body. As already discussed, the zone of soil above the trapdoor behaves differently at this trapdoor scale. The observation that the soil at the surface is not displacing downwards at the same rate as the trapdoor indicates that volumetric expansion is taking place at shallow depths and the shear displacements are not developed at the surface.

Figure 4.28 shows the fitted surface settlement troughs for all fibre lengths at the ultimate stage, where δ = 0.18*B*, normalised by trapdoor width, for the three trapdoor sizes. The unreinforced soil case is plotted for comparison. The amount of relative surface settlement appears to increase with trapdoor width.

The settlement at the surface was reduced by an average of ~36% at the ultimate stage with the small trapdoor. The reduction in settlement ranges from ~30% with 20 mm fibres to ~55% with 16 mm length fibres. The surface settlement reduction is proportional to fibre length up to 16 mm. The exception to this relationship is that 20 mm fibres are less effective than fibres of shorter length at reducing settlement.

For the medium trapdoor case the settlement at the surface was reduced by an average of ~43% with the inclusion of fibre. The reduction in settlement ranges from ~25% with 8 mm fibres to ~50% with 16 mm length fibres. As with the small trapdoor, the reduction in settlement appears to be proportional to fibre length up to F_L= 16 mm. The 20 mm fibres had less of an effect on settlement (~40%) than the 16 mm fibres (~50%).

For the large trapdoor case the surface settlements are reduced by an average of ~57%. The reduction in settlement ranges from ~41% with 8 mm fibres to ~60% with 20 mm length fibres. In this case longer fibres have substantially more effect than with small or medium width trapdoors.

The data points obtained from the PIV analysis are also marked on the figure to give some indication of the accuracy of the curve fitting process. The large trapdoor displacements (Figure 4.28 (c)) are substantially more asymmetric and non-uniform than small and medium width trapdoors. Consequently, the curve fit is also poorer, as the modified Gaussian approximation cannot adequately fit the non-uniform data. The fitted curves do however capture the general trend with increasing displacement. The reduction in settlement trough size and its proportionality with fibre length is clear from the plots, particularly for the large trapdoor case, Figure 4.28 (c).

Figures 4.29 to 4.31 show the volume loss, V_{sl}/B^2, against δ/B in the soil for the unreinforced soil and the same fibre length variations. The 'volume loss' is defined as the effective area of the settlement trough, calculated as the integral of vertical soil displacements at a given depth in model scale. In plane strain situations, it is common to assume the same conditions occur across the breadth of the model, the breadth of the trough is arbitrarily assumed to be 1 m. The calculated volume loss (the trough area) is normalised by B^2. The normalisation allows settlement trough areas from different sized trapdoors to be compared in the same dimensionless units. The plot essentially compares the volume loss of the soil occurring at a specified depth to the volume of the inclusion in the soil created by the trapdoor, $B\delta$, again, normalised by B^2. With normalisation, the horizontal axis is therefore: $B\delta/B^2 = \delta/B$.

The figures show the displacement at four normalised depths. Marshall et al. (2012) used a similar plot of soil volume loss versus tunnel volume loss to explain the cumulative dilative behaviour of the soil. The 1:1 line indicates equality between the induced volume change at the boundary and the volume loss within the soil.

The comparison between the 1:1 line and the soil volume loss, at all depths, describes the general behaviour of the material. As all the volume loss in the material is significantly less than the 1:1 line the implication is that both the soil and fibre-soil composite behaviour is dilative.

As with settlements, the volume loss behaviour is similar for medium and large trapdoors scales but smaller trapdoor results are subjected to scaling effects discussed further in Section 5.5. The following analysis considers the general mechanism occurring for the medium and large trapdoors (Figures 4.30 and 4.31).

In the general case, at relatively small displacements, $\delta < 0.02B$, the soil and the trapdoor volume losses are approximately equal but as the magnitude of shear displacements within the soil increase and dilation increases, the difference between the unreinforced and fibre-composite soil volume losses increases. At the surface, the unreinforced soil and trapdoor volume losses tend towards equality at displacements of $\delta > 0.1B$. The behaviour of the fibre-soil composite is markedly different in this respect; fibre-soil volume losses are significantly less than trapdoor volume losses. As with maximum subsidence, the soil volume loss tends towards equality at higher depth ratios. The soil volume loss is significantly reduced for cases with all fibre lengths compared to the unreinforced test by approximately the same amount.

The plots shows very little variation in volume with fibre length is occurring for the general case (medium and large width trapdoors, *B* = 60 mm and *B* = 105 mm)

For the general case, the unreinforced soil and trapdoor volume losses increase and tend towards equality at relatively large displacements, $\delta > 0.1B$, and with higher depth ratio. The difference between unreinforced and fibre-soil composite volume loss increases at larger displacements.

All responses for the small trapdoor (Figure 4.29) show a large initial increase in volume loss. This effect can be inferred from examining the vertical displacements at the initial phases of tests, where a larger amount of settlement appears to occur across a much greater width of the model, relative to displacement.

For all small trapdoor tests, at the surface, the unreinforced soil and trapdoor volume losses do not tend towards equality, at any displacement, suggesting that a generally different volume loss mechanism is at work at this trapdoor scale.

This observation and other scaling effects are discussed further in Chapter 5. At the surface, the initial increase in magnitude appears to have some relation to fibre length, where medium length fibres, F_L = 12 mm and 16 mm generally have a greater effect. The rate of change of soil volume loss then follows roughly the same reduced gradient with displacement for all fibre lengths, as observed with the general case with larger scale trapdoors. The effect of fibre length is much more apparent at depth in the small trapdoor case, with medium length fibres having the greatest effect. Only at large depth does soil volume loss tend towards equality with trapdoor volume loss.

Medium fibre lengths, 12 mm and 16 mm, appear to have a greater effect than the small and long fibres, 8 mm and 20 mm for the small trapdoor, *B* = 30 mm, case.

The general exception between the large scale trapdoor results and those for other scales being that lower volume losses are observed throughout with fibres of long length, F_L = 20 mm. The rate of change of soil volume loss with displacement, or trapdoor volume loss, appears much lower for the F_L = 16 mm and F_L = 20 mm cases. Generally, long fibres have a significantly larger effect on settlements and volume losses than with smaller trapdoors.

To aid clarity, the detailed displacement and strain results are presented in Figures 4.32 to 4.35 for a single fibre length, F_L = 20 mm and trapdoor width, *B*, of 60 mm (test CMC07) . As can be seen in the maximum settlement and volume loss plots discussed, for all fibre lengths, a broadly similar mechanism is taking place across the range of trapdoor scale; particularly for larger trapdoors where *B* > 30 mm.

Figure 4.32 (a) and (b) show scaled vertical and horizontal displacements, $S_v{}^*$ and $S_x{}^*$, respectively, as defined in Section 4.3.1, plotted against distance from the trapdoor centre, *x/B*, for fibres; F_L = 20 mm with fibre content, χ_w, of 0.5%. As with the unreinforced displacement figures, settlements are plotted at trapdoor displacements of 2, 5 and 18% of the width.

Vertical displacements are significantly smaller than those shown for the medium width unreinforced soil case in Figure 4.14 (a), both at the surface and at shallow depths. The vertical displacements from tests CMC07 are shown in Figure 4.32 (a) for the same trapdoor displacements. The contours at the ultimate stage of the test (Figure 4.33 (c)) show that large displacements do not propagate to the surface as is the case with unreinforced soil.

Calculated volumetric strain, ε_v, and shear strain, γ, are shown in Figures 4.34 and 4.35, respectively, at the same trapdoor displacements. The figures show comparable magnitude of strains with the unreinforced case. When compared to the unreinforced cases (Figures 4.20 and 4.23, respectively), the strains at the ultimate stage do not appear to propagate to the surface with fibre inclusion; a distinct ‘arching area’ of volumetric expansion is defined in the soil and no significant shear bands extend vertically to the surface. The areas of large deformation extending from the trapdoor edges define the failure surface in the soil.

The strain responses agree with the postulation that the soil at the surface is not subjected to shear displacements or displacing as a rigid body. This general assertion is confirmed by the observation that the fibre-soil composite surface settlements of Figures 4.25 to 4.27 and volume losses of Figure 4.29 to 4.31 have a lower rate of change with displacement than the unreinforced case throughout.

In general, a significantly larger area of the fibre-soil composite is subjected to deformation in the region above the trapdoor with fibre inclusion, and there is no evidence of the triangular ‘wedge’ shearing and displacement mechanism observed at the surface in the unreinforced soil case (described in Section 4.3.1); the vertical propagation of strain with displacement is reduced with fibre inclusion.

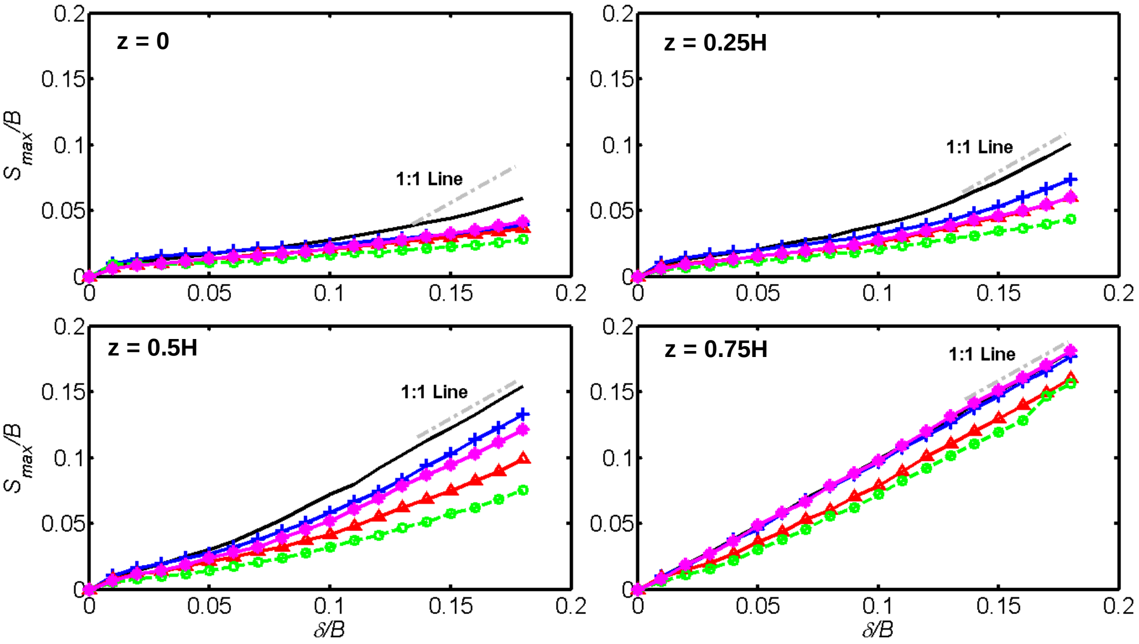

Figure 4.25 Normalised maximum settlement, S_{max}/B, variation with depth and fibre length, F_L. χ_w = 0.5%, B = 30 mm

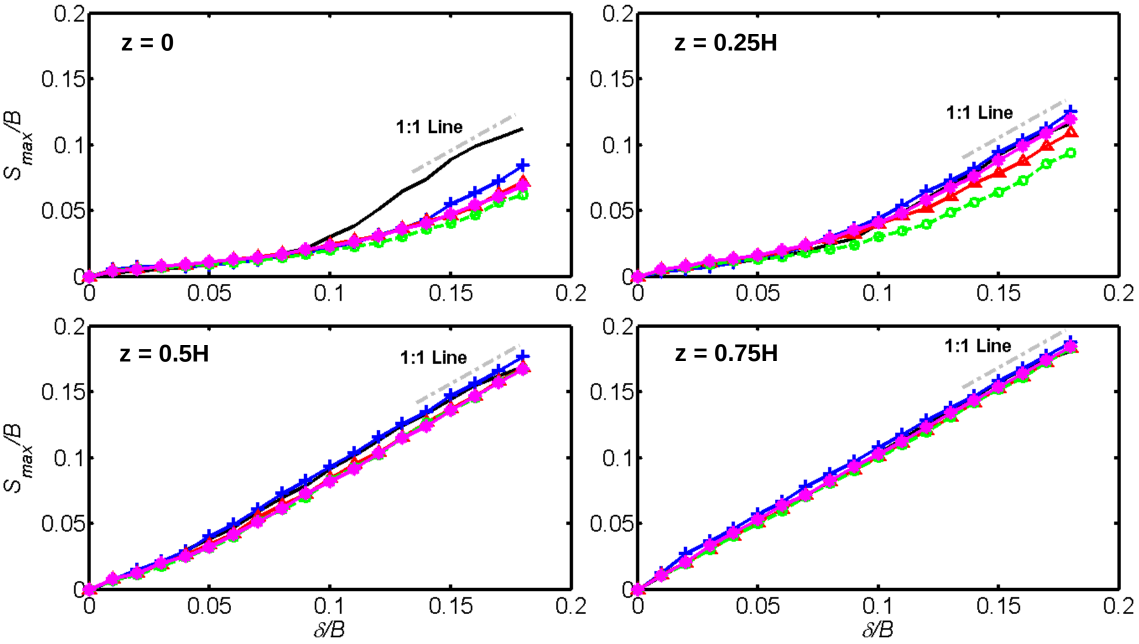

Figure 4.26 Normalised maximum settlement, S_{max}/B, variation with depth and fibre length, F_L. χ_w = 0.5%, B = 60 mm.

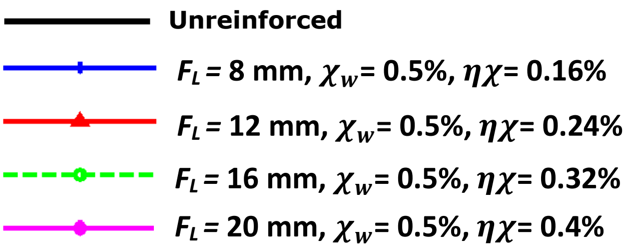

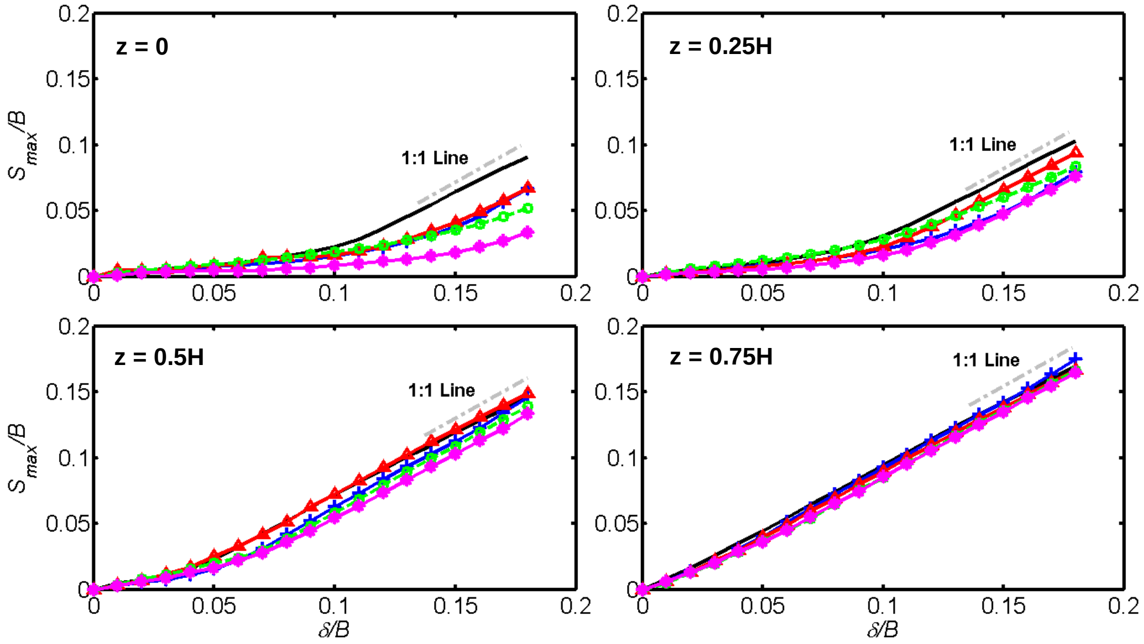

Figure 4.27 Normalised maximum settlement, S_{max}/B, variation with depth and fibre length, F_L. χ_w = 0.5%, B = 105 mm.

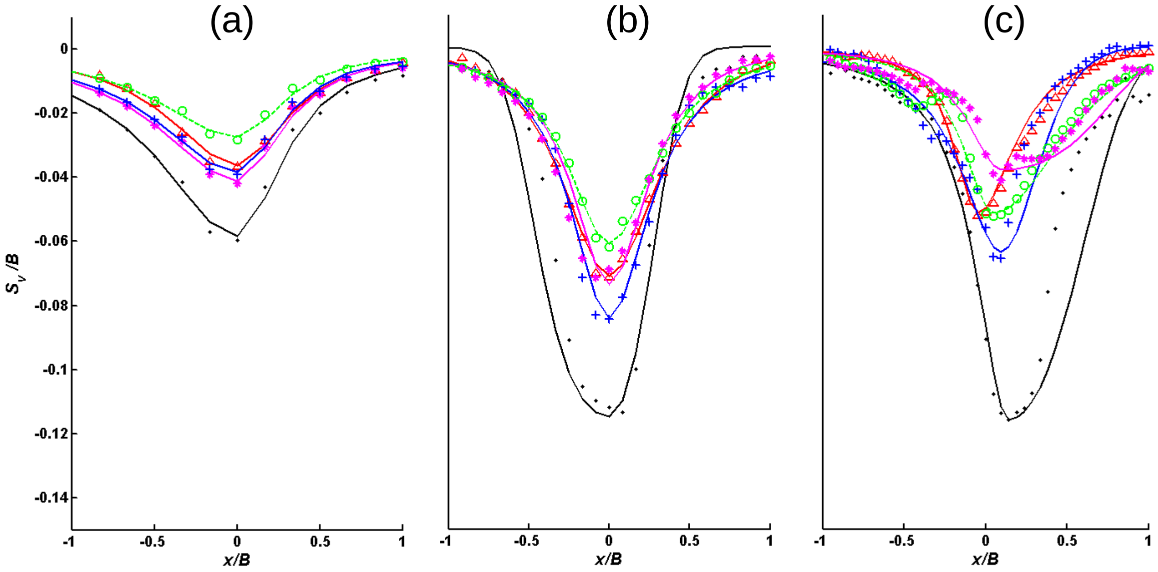

Figure 4.28 Normalised surface settlement, S_v/B, at δ = 0.18B, variation with fibre length, F_L. χ_w = 0.5% (a) B = 30 mm, (b) B = 60 mm, (c) B = 105 mm.

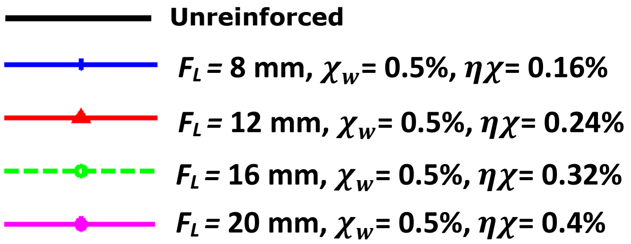

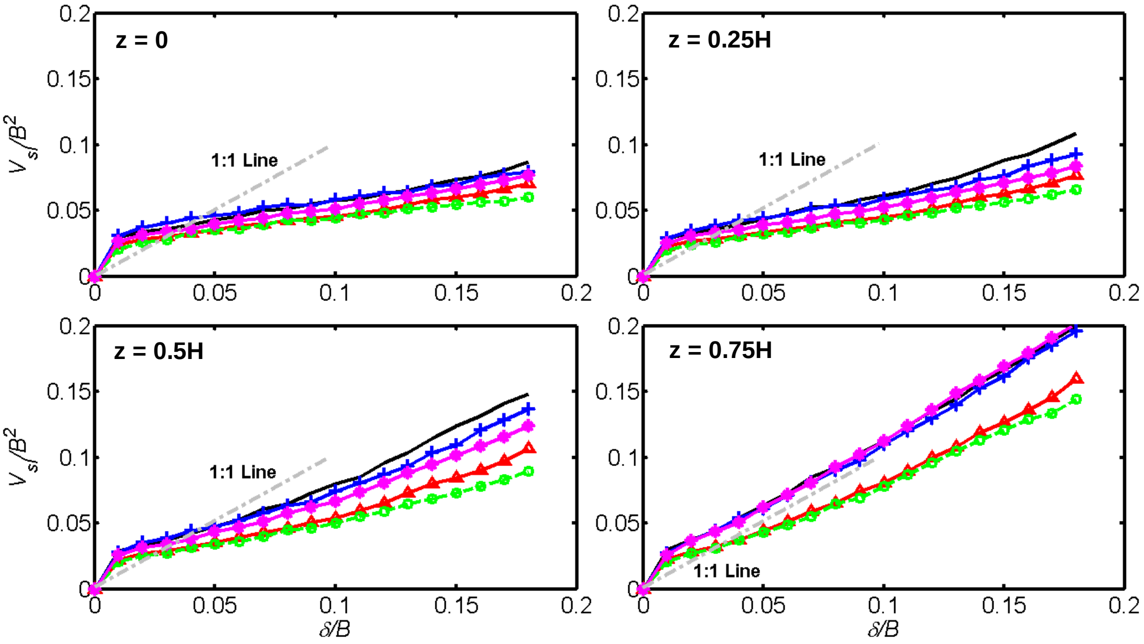

Figure 4.29 Normalised soil volume loss, V_{sl}/B^2, variation with depth and fibre length, F_L. χ_w = 0.5%, B = 30 mm

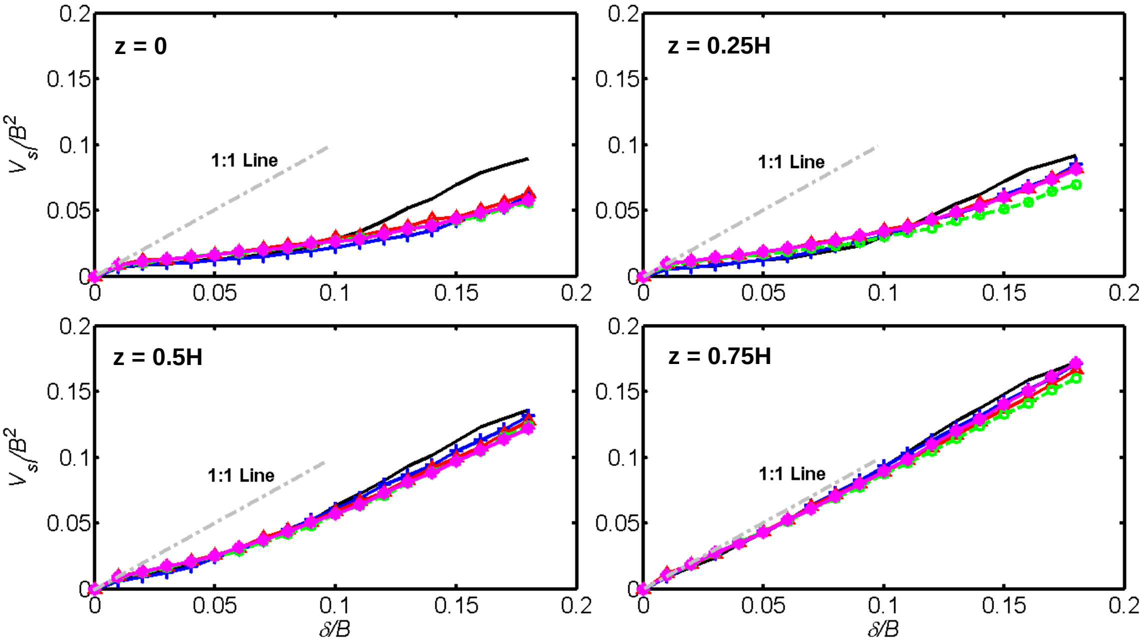

Figure 4.30 Normalised soil volume loss, V_{sl}/B^2, variation with depth and fibre length, F_L. χ_w = 0.5%, B = 60 mm.

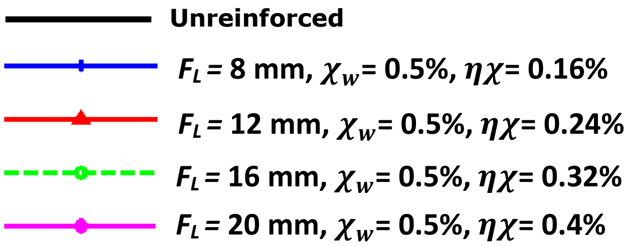

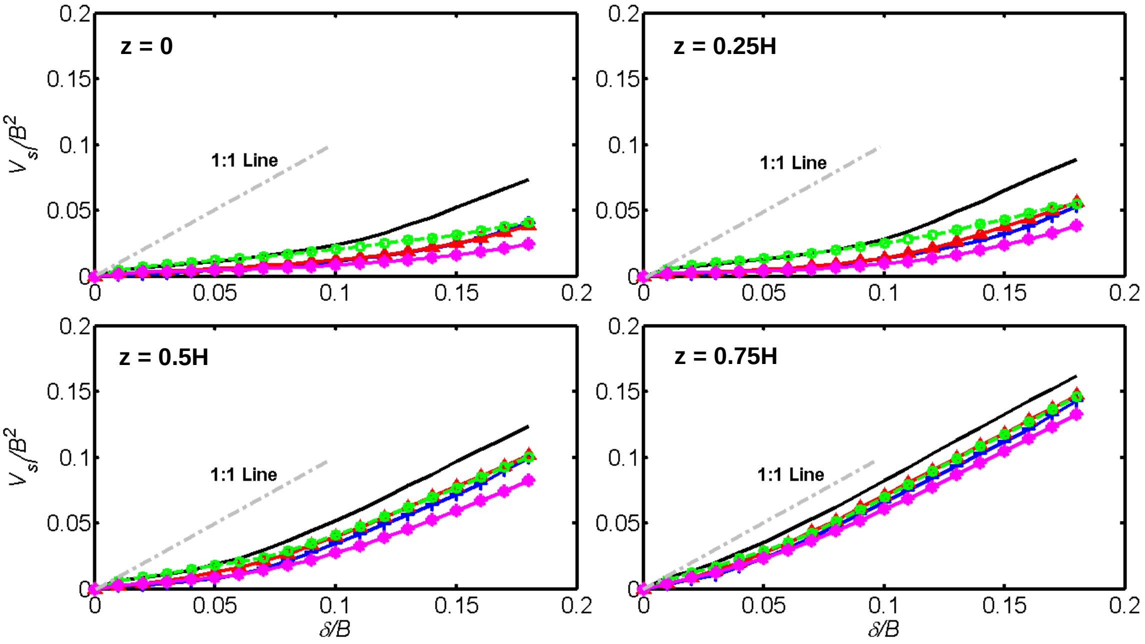

Figure 4.31 Normalised soil volume loss, V_{sl}/B^2, variation with depth and fibre length, F_L. χ_w = 0.5%, B = 105 mm

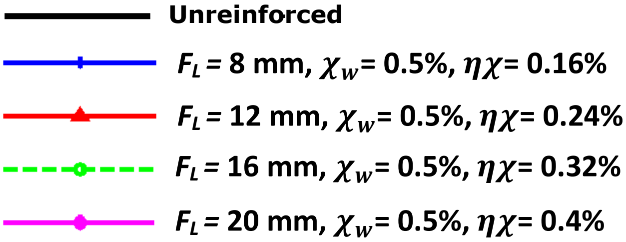

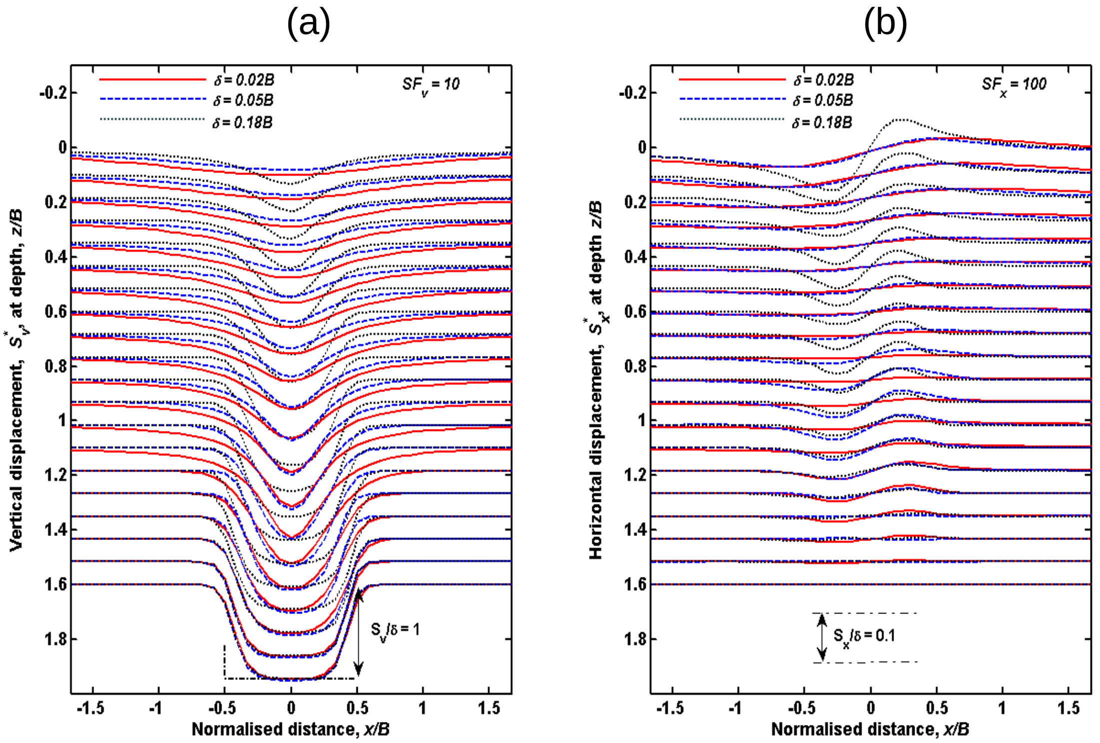

Figure 4.32 Normalised vertical and horizontal displacements, F_L = 20 mm, χ = 0.5%, B = 60 mm; (a) Vertical; (b) Horizontal.

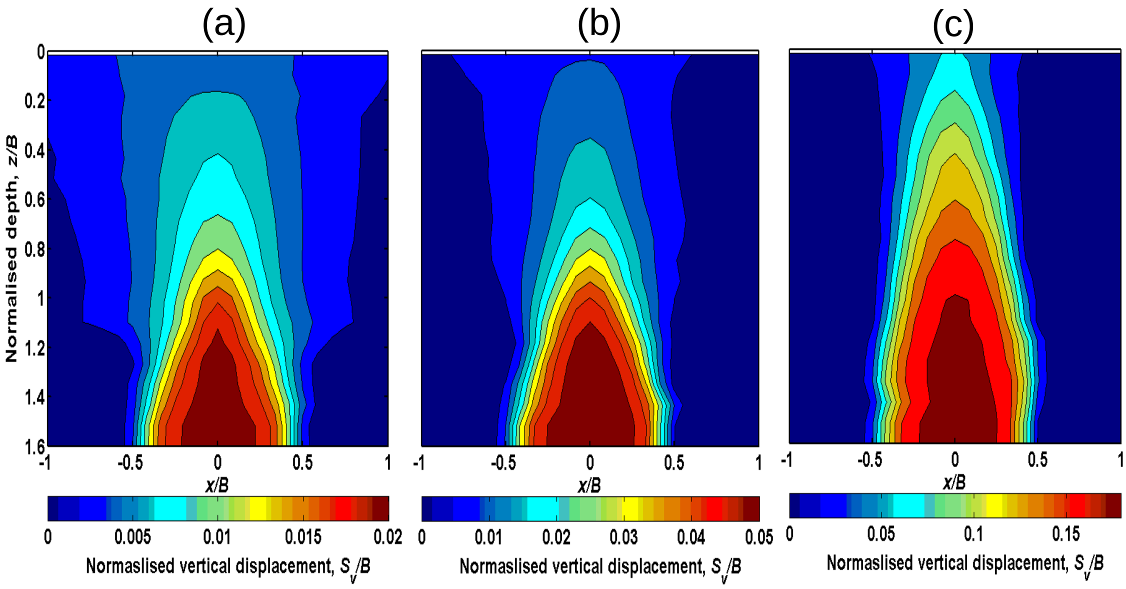

Figure 4.33 Normalised vertical displacement contours, S_v/B, F_L = 20 mm, χ_w = 0.5%, B = 60 mm ; (a) δ = 0.02B, (b) δ = 0.05B, (c) δ = 0.18B

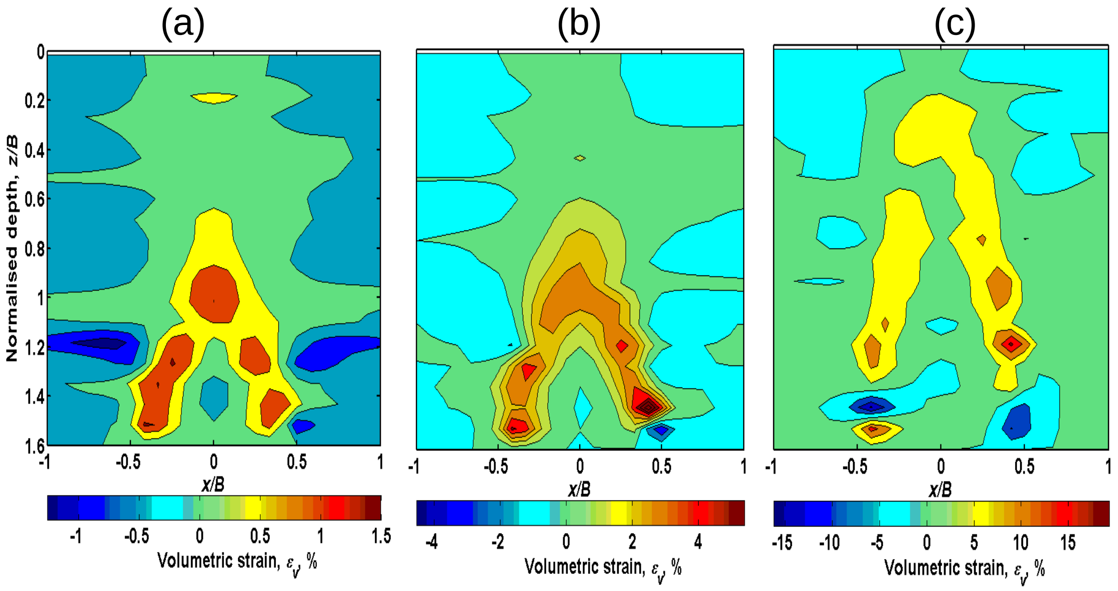

Figure 4.34 Volumetric strain, ε_v, F_L = 20 mm, χ_w = 0.5%, *B* = 60 mm ; (a) δ = 0.02*B*, (b) δ = 0.05*B*, (c) δ = 0.18*B*

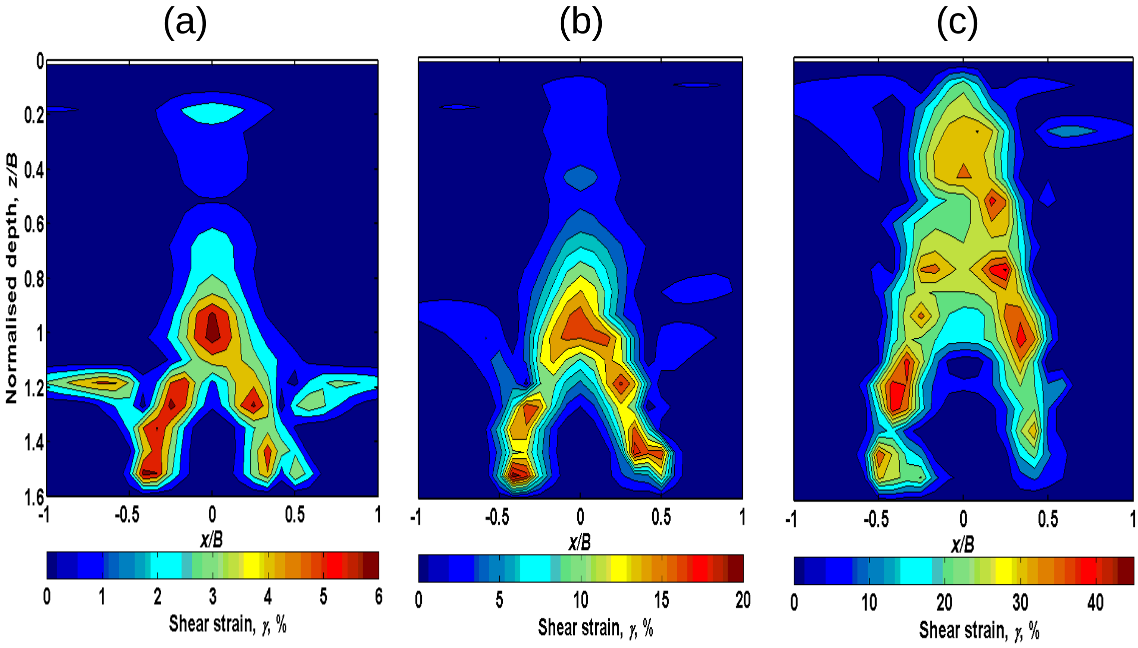

Figure 4.35 Shear strain, γ, F_L = 20 mm, χ_w = 0.5%, B = 60 mm ; (a) δ = 0.02*B*, (b) δ = 0.05*B*, (c) δ = 0.18*B.*

4.3.3 Variation with fibre content

Figures 4.36 to 4.38 show the variation of normalised maximum settlement, S_{max}/B, against normalised trapdoor displacement, δ/B, at depths z of 0*H*, 0.25*H*, 0.5*H* and 0.75*H*. Settlements for the unreinforced case and for fibre concentration by soil mass, χ_w, of 0.25%, 0.5% and 1% are plotted. The fibre length, F_L, for each test was 12 mm. Figure 4.36 shows the responses for the small trapdoor case, *B* = 30 mm, Figure 4.37 shows *B* = 60mm and in Figure 4.38 *B* = 105 mm.

The general observed effects show an equivalent reduction in settlement and volume loss with increasing fibre content as was found with fibre length, F_L, variation tests. Generally higher fibre factor, $\eta\chi$, composites were found to be more effective in reducing settlements and volume loss.

The solid lines represent the unreinforced soil case. All tests with fibre-soil composite are indicated by the same markers used to indicate the different fibre-soil tests throughout. All fibre cases show a significant reduction in the amount of maximum settlement measured at the surface; as already observed in Figures 4.25 to 4.27 and discussed in Section 4.3.2 for fibre length tests, this effect deteriorates with depth, *z*, This is the expected behaviour since the change in displacement at the surface is equal to the integral sum of the volumetric strains throughout the depth.

The results show good agreement with fibre-soil composites of varying fibre length, F_L. The surface settlement is reduced with fibre inclusion for larger displacements, typically $\delta > {\sim}7 - 10\%$ of the trapdoor width *B*. In general, the settlement is reduced with increasing fibre content. The settlements at the surface show the largest decrease when compared with the unreinforced case. The reduction in settlement is proportional to fibre content. The gradients of soil displacement to trapdoor displacement are significantly smaller compared to unreinforced soil at all fibre concentrations. The surface fibre-composite displacements do not reach equality with trapdoor displacements (indicated by the 1:1 line), indicating that the soil at the surface is subject to deformation, and not displacing as a rigid material.

Figure 4.39 shows the fitted surface settlement troughs for all fibre concentrations at the ultimate stage, where δ = 0.18*B*, normalised by trapdoor width, *B*, for the three trapdoor sizes. The unreinforced soil case is plotted for comparison. As observed with the fibre length tests detailed in Section 4.3.2, the amount of relative surface settlement appears to increase with trapdoor width. The data points obtained from the PIV analysis are marked on the figure.

As is the case with increasing fibre length (see Figure 4.28), the surface settlement plots generally show the general trend towards reduction with increasing fibre content. In the large trapdoor case (Figure 4.39 (c)) the trend is proportional with fibre content

For the small trapdoor case, B = 30 mm, the percentages of ultimate surface settlement reduction with fibre content when compared with unreinforced soil, are ~16% with χ_w = 0.25%, 41% with χ_w = 0.5% and ~33% with χ_w = 1%. The average reduction is ~30% across all fibre concentrations.

For the medium trapdoor case, B = 60 mm, the reductions compared with unreinforced soil are ~25% with χ_w = 0.25%, ~41% with χ_w = 0.5% and ~50% with χ_w = 1%, with fibre content, χ; averaging ~39% across all fibre concentrations.

In the large trapdoor case, B = 105 mm, the reductions are ~43% with χ_w = 0.25%, ~50% with χ_w = 0.5% and ~70% with χ_w = 1%.The average reduction is ~54% across all fibre concentrations.

The small trapdoor displacements (Figure 4.36) show some improvement in the amount of settlement at the surface and throughout the soil layer at the ultimate stage when compared with the unreinforced case; however, the effect of high fibre content on the surface settlement is reduced in the small trapdoor tests when compared to larger trapdoors scales. This is the general case with all fibre-composites. Higher values of the composite fibre factor, $\eta\chi$, tend to have a diminished effect on displacement with small trapdoor tests.

The plots exhibit similar trends consistent with the general observed behaviour that the surface soil displacements do not reach equality with the trapdoor for all B = 30 mm trapdoor tests.

Unlike the medium and large trapdoor cases, the settlement reduction does not appear to increase with fibre concentrations greater than 0.5%; the χ_w = 0.5% case appears to have a slightly larger effect than with χ_w = 1% (a difference of ~7%) at the ultimate stage.

At large trapdoor scales, 1% fibre content has substantially more effect and the trend is proportional to fibre content. For medium and large trapdoor tests, higher values of the composite fibre factor tend to substantially reduce displacement.

Figures 4.40 to 4.42 show the comparison of normalised volume loss, V_{sl}/B^2, against normalised displacement, δ/B for unreinforced soil fibre-soil composites with varying fibre content for the small, medium and large trapdoors respectively.

In the general case, where B >30 mm, the fibre-soil volume losses are significantly less than trapdoor volume losses throughout, and the gradients of soil volume loss for composites are substantially less than with unreinforced soil.

In general, the unreinforced soil and trapdoor volume losses tend towards equality at displacements of $\delta > 0.1B$ at the surface. The behaviour of the fibre-soil composite is markedly different in this respect; fibre-soil volume losses are significantly less than trapdoor volume losses and the gradients do not tend towards equality for the displacements tested. This effect appears to be proportional with fibre content; the higher the concentration of fibre, the lower the magnitude and gradient of volume loss throughout the soil.

The plot exhibits the same trend of behaviour as the maximum settlement; the effects of fibre inclusion are generally more discernible at the surface than at soil depth and higher concentrations of fibre have a proportionally larger effect.

As noted in Section 4.3.2, all responses for the small trapdoor (Figure 4.40) show a large initial increase in volume loss followed by a similar general trend to reduction with fibre inclusion than observed with larger trapdoors. However, the effectiveness of the fibre appears to decrease at high fibre concentrations. As with settlement, this characteristic ‘drop-off’ in fibre performance appears to be a function of the fibre factor. General scaling effects are evident for small trapdoor tests this and other scaling effects are discussed further in Chapter 5, Section 5.5.1.

For the large trapdoor, as with the medium trapdoor, increasing fibre content has a proportional effect on both magnitude and rate of volume loss. Higher fibre content composites significantly improve the volume losses throughout. The gradients of the composite volume losses are significantly lower than those observed for unreinforced soil, which, as already discussed in Section 4.3.2, increases at the same rate as the trapdoor at large displacements, $\delta > 0.1B$. The composite responses show no sign of similar post-shear rigid body displacements at the surface, significant volumetric expansion of the soil at shallow depth is taking place within the fibre composite. In general, the fibre composite as a whole is subjected to volumetric expansions over an increased area to accommodate the trapdoor inclusion than the unreinforced soil.

The detailed displacement and strain results are plotted for a single fibre concentration, χ_w = 1% and trapdoor width, *B*, of 60 mm (test CMC07) in Figures 4.42 to 4.46. A broadly similar mechanism was observed to be taking place with fibre-composites of all concentrations.

Figure 4.42 (a) and (b) show scaled vertical and horizontal displacement, $S_v{}^*$ and $S_x{}^*$ respectively, plotted against distance from the trapdoor centre, x/B, for test CMC07.

As is the case throughout, the settlements are plotted at trapdoor displacements of 2, 5 and 18% of the trapdoor width, *B*.

Vertical displacements at the ultimate stage of the test are significantly smaller than those shown for the unreinforced case for the same trapdoor width in Figure 4.17 (c), both at the surface and at shallow depths. The contours of vertical displacement from test CMC04 (long fibres, medium trapdoor) are shown in Figure 4.32 for the same trapdoor displacements.

Again, as is the case with all fibre inclusion tests, the figures show that smaller displacements occur at the surface than is the case with unreinforced soil.

Calculated volumetric strain, ε_v, and shear strain, γ at the same trapdoor displacements are shown in Figures 4.45 and 4.46 respectively. The figures show slightly reduced but comparable magnitudes of strains with the unreinforced case. When compared to the shear strains for the *B* = 60 mm unreinforced case (Figure 4.23). As is the case with the 20 mm fibre length composite test (shown in Figure 4.35), it was found that the shear strains at the ultimate stage do not appear to propagate to the surface: no significant shear bands appear to extend vertically from the arch to indicate failure with fibre inclusion. Clearly, a different mechanism to the general surface failure observed for unreinforced soil occurs within the composite material.

The areas of large volumetric expansion in the soil are broadly enclosed within the diagonal shear bands extending from the trapdoor edges to the centre of the trapdoor.

The shear displacements appear to be contained within the soil without significant failure occurring at the surface; the vertical propagation of strain with displacement is reduced with fibre inclusion.

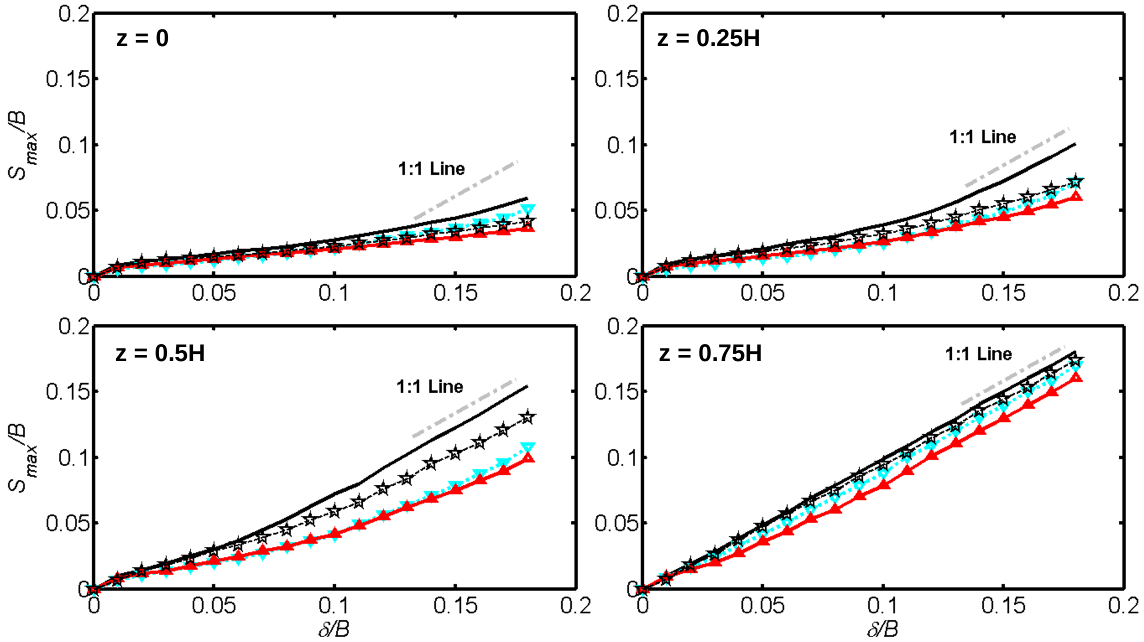

Figure 4.36 Normalised maximum settlement, S_{max}/B, variation with depth and fibre content, χ_w. F_L = 12 mm, B = 30 mm

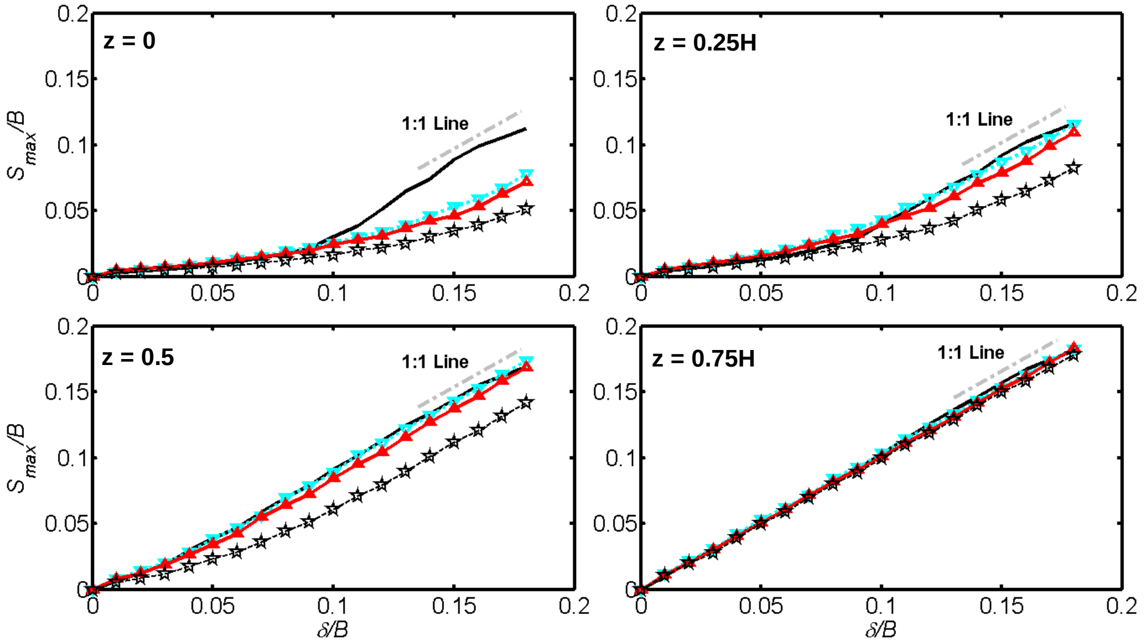

Figure 4.37 Normalised maximum settlement, S_{max}/B, variation with depth and fibre content, χ_w. F_L= 12 mm; B = 60 mm.

Unreinforced

▼ **F_L = 12 mm, χ_w= 0.25%, $\eta\chi$= 0.12%**

▲ **F_L = 12 mm, χ_w= 0.5%, $\eta\chi$= 0.24%**

★ **F_L = 12 mm, χ_w= 1%, $\eta\chi$= 0.48%**

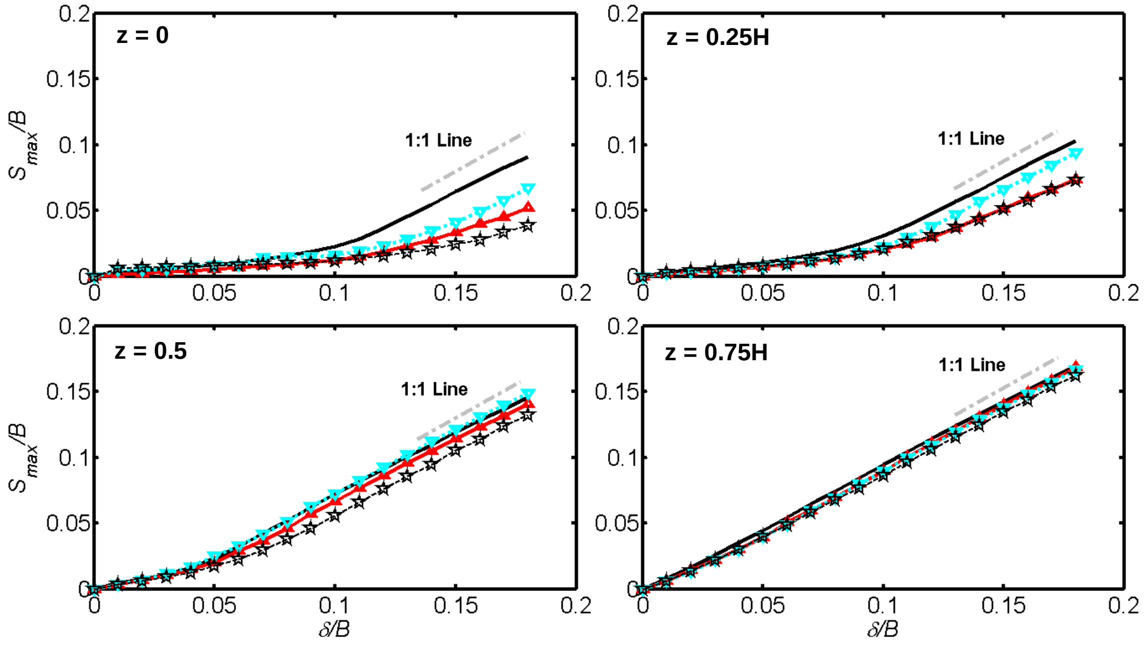

Figure 4.38 Normalised maximum settlement, S_{max}/B, variation with depth and fibre content, χ_w. F_l= 12 mm. *B* = 105 mm.

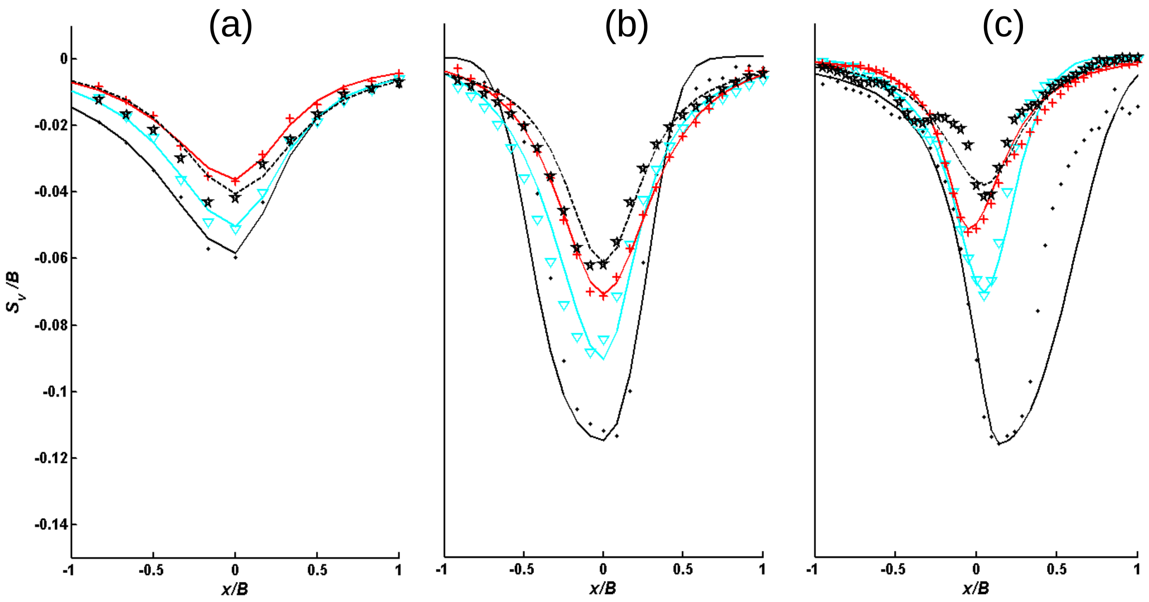

Figure 4.39 Normalised surface settlement, S_v/B, at δ = 0.18*B*, variation with fibre content, χ_w. F_L= 12 mm; (a) *B* = 30 mm, (b) *B* = 60 mm, (c) *B* = 105 mm.

━━━ **Unreinforced**

┈┈▼┈┈ **F_L = 12 mm, χ_w= 0.25%, $\eta\chi$= 0.12%**

━━▲━━ **F_L = 12 mm, χ_w= 0.5%, $\eta\chi$= 0.24%**

- - -★- - - **F_L = 12 mm, χ_w= 1%, $\eta\chi$= 0.48%**

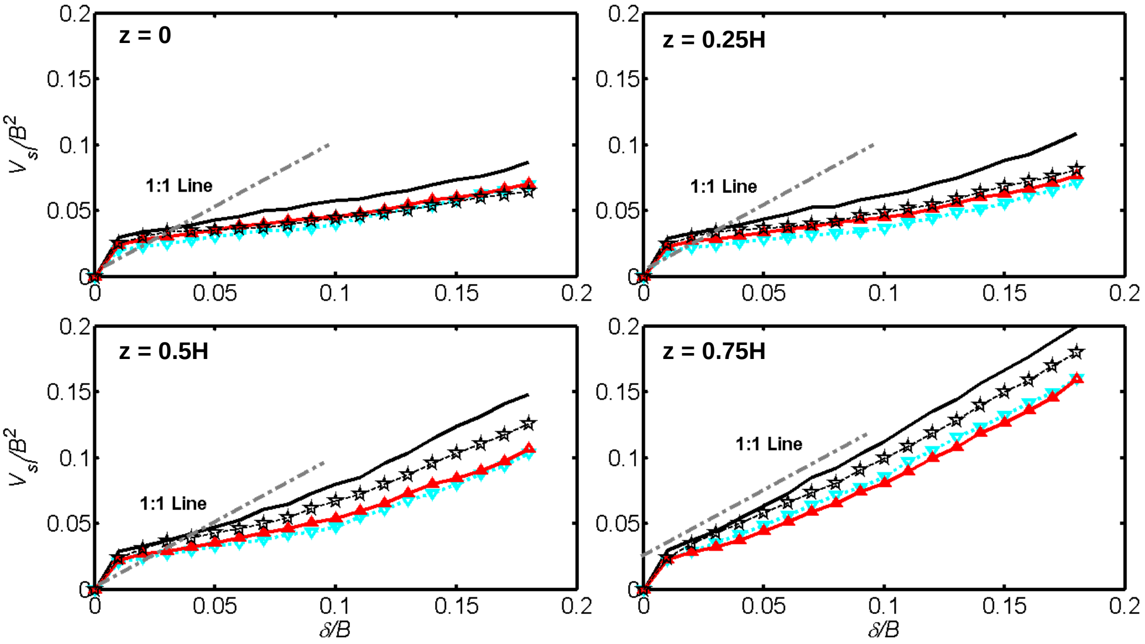

Figure 4.40 Normalised soil volume loss, V_{sl}/B^2, variation with depth and fibre content, χ_w, F_L= 12 mm; *B* = 30 mm

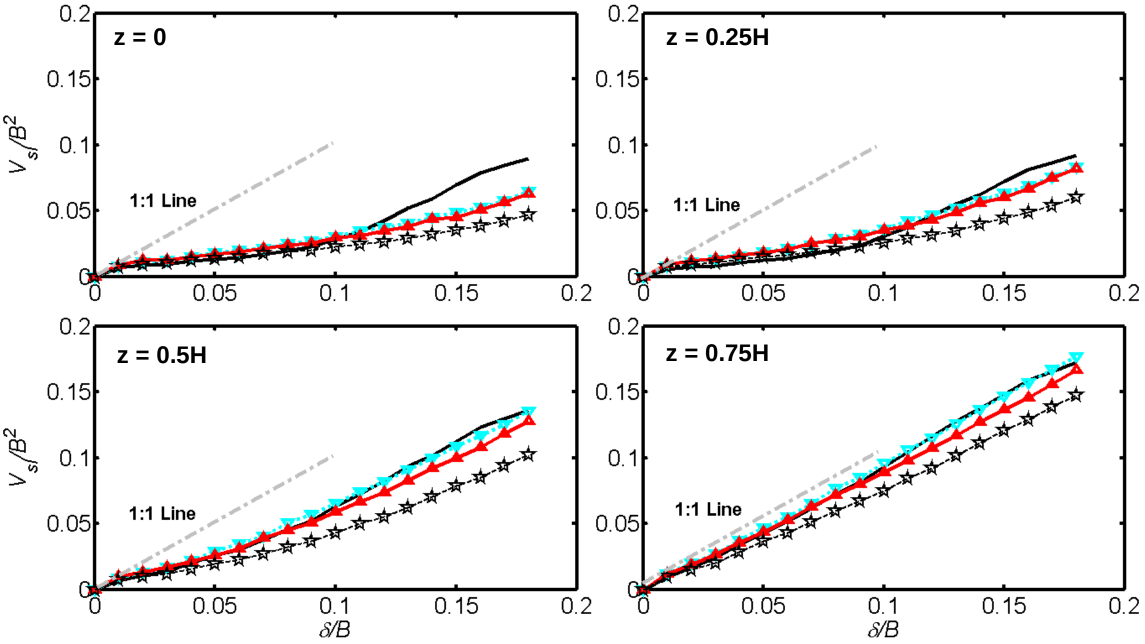

Figure 4.41 Normalised soil volume loss, V_{sl}/B^2, variation with depth and fibre content, χ_w, F_L= 12 mm., *B* = 60 mm.

Unreinforced

F_L = 12 mm, χ_w= 0.25%, $\eta\chi$= 0.12%

F_L = 12 mm, χ_w= 0.5%, $\eta\chi$= 0.24%

F_L = 12 mm, χ_w= 1%, $\eta\chi$= 0.48%

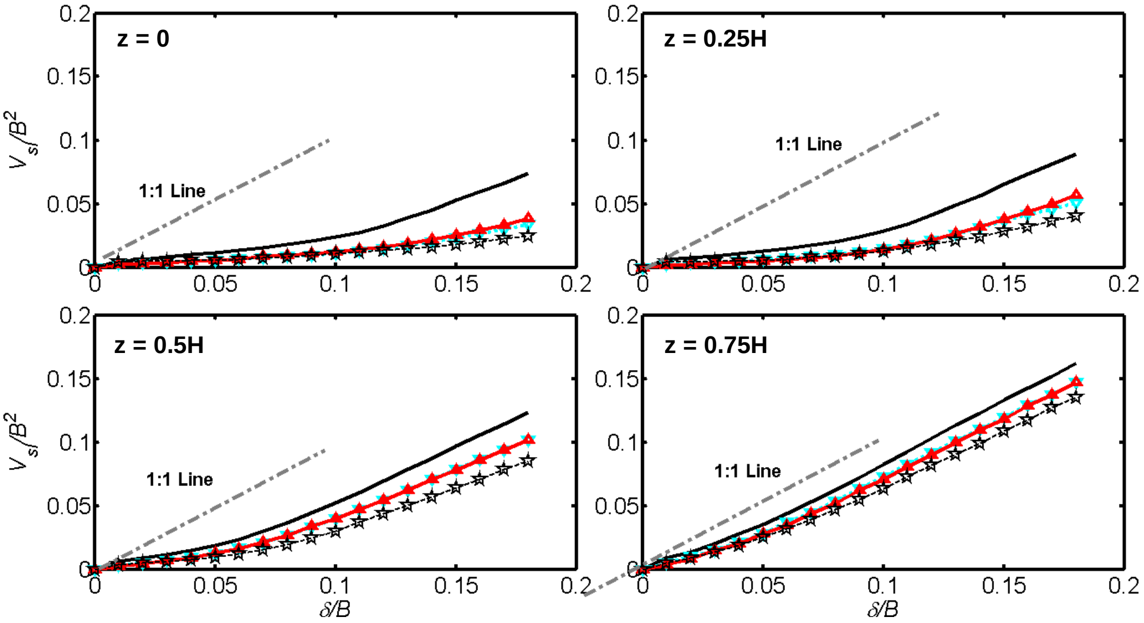

Figure 4.42 Normalised soil volume loss, V_{sl}/B^2, variation with depth and fibre content, χ_w. F_L = 12 mm; *B* = 105 mm.

Unreinforced

F_L = 12 mm, χ_w = 0.25%, $\eta\chi$ = 0.12%

F_L = 12 mm, χ_w = 0.5%, $\eta\chi$ = 0.24%

F_L = 12 mm, χ_w = 1%, $\eta\chi$ = 0.48%

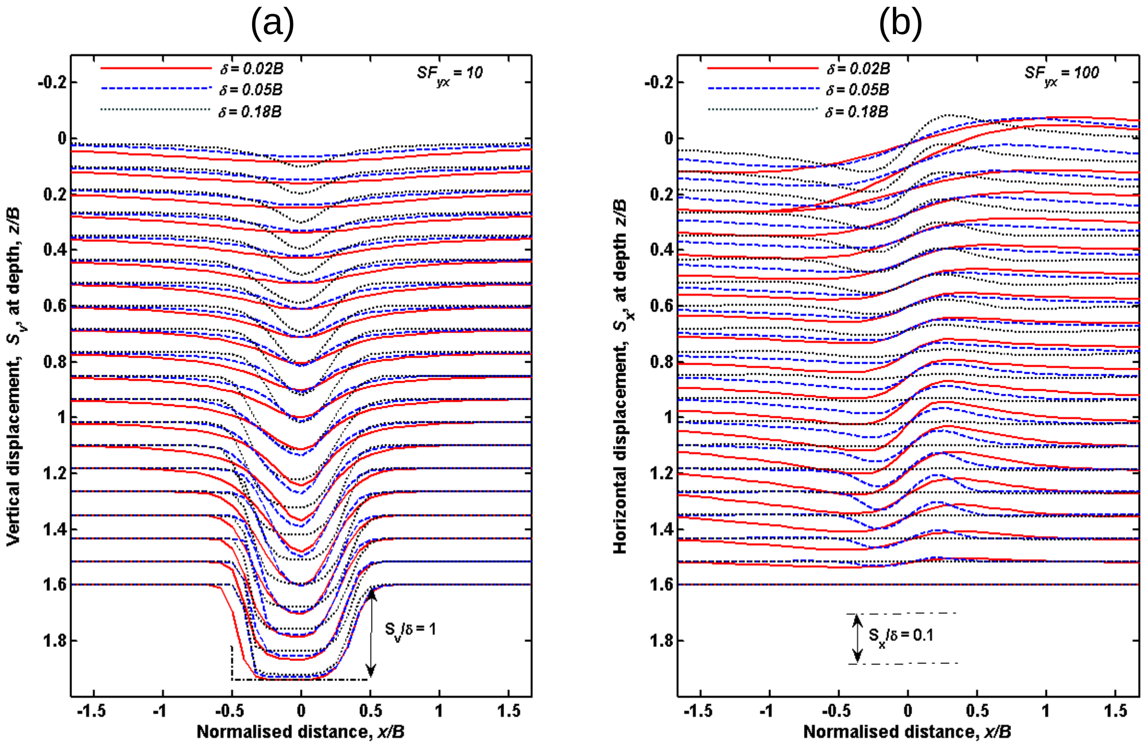

Figure 4.43 Scaled vertical and horizontal displacements, $S_v{}^*$ and $S_x{}^*$; F_L = 12 mm, χ_w = 1%, *B* = 60 mm. . (a) vertical; (b) horizontal

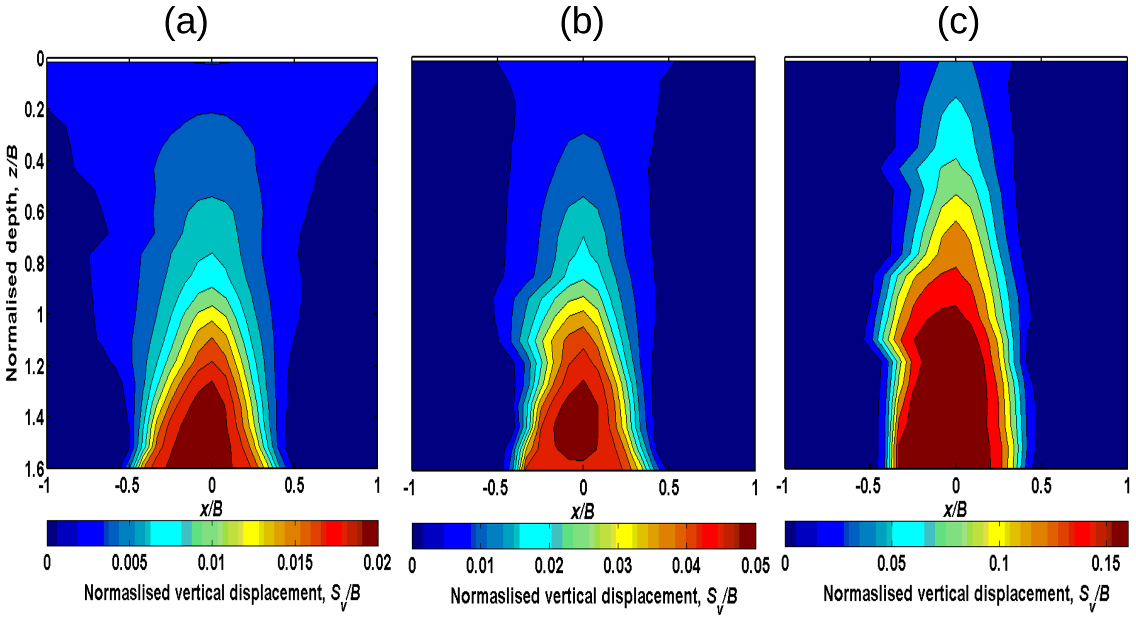

Figure 4.44 Normalised vertical displacement contours, S_v/B. F_L = 12 mm, χ_w = 1%, *B* = 60 mm; (a) δ = 0.02*B*, (b) δ = 0.05*B*, (c) δ = 0.18*B*

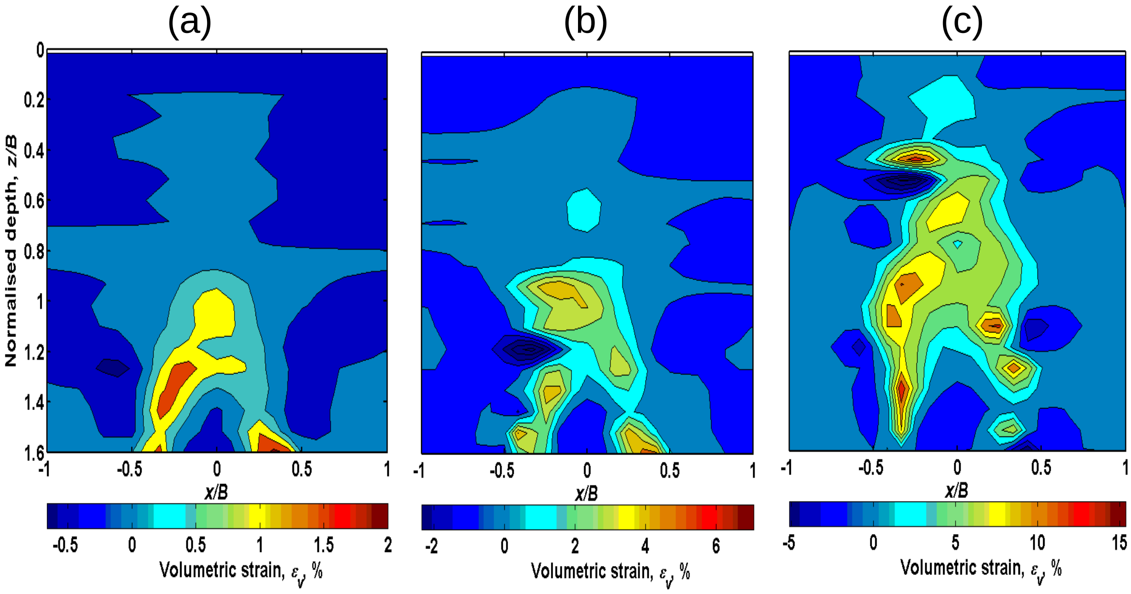

Figure 4.45 Volumetric strain, ε_v, F_L = 12 mm, χ_w = 1%, B = 60 mm; (a) δ = 0.02B, (b) δ = 0.05B, (c) δ = 0.18B

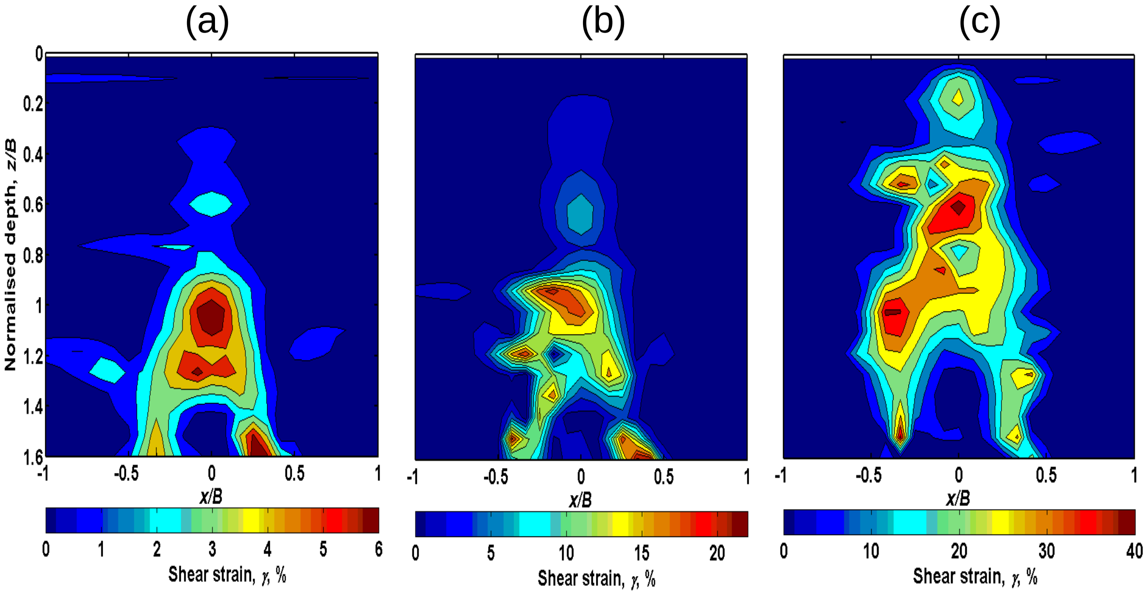

Figure 4.46 Shear strain, γ, F_L = 12 mm, χ_w = 1%, B = 60 mm; (a) δ = 0.02B, (b) δ = 0.05B, (c) δ = 0.18B

4.3.4 Displacement results summary

4.3.4.1 Unreinforced soil

The displacement and strain mechanism observed for the unreinforced soil, in all trapdoor scaling cases, show trends consistent with an arching mechanism taking place within the soil layer.

As the trapdoor is lowered, areas of deformation are seen to extend from the trapdoor edge to a point in the soil, in the region of the crown of the arch above the trapdoor centre, at an inclination to the vertical, θ_i. Observations of this angle for the unreinforced medium trapdoor are presented in Table 5.1 in Section 5.4 The deforming region propagates vertically until failure of the arch follows, and shear displacements propagate to the surface; indicated by vertical shear planes extending from the failure region to the soil surface above the trapdoor edges.

Thereafter, the soil mass is translated, proportionally along the shear planes, at the same rate as the trapdoor displacement. At the surface, the maximum settlement and volume loss tends to increase in proportion with trapdoor displacements of $\delta > 0.1B$, indicating that thereafter, the soil is displacing as a rigid body where volume losses increase in the soil equally with further trapdoor induced volume losses.

4.3.4.2 General scaling effects

Significantly smaller magnitudes of displacement were observed, particularly at the surface, with the small trapdoor test, indicating the presence of particle size to trapdoor width, d_{50}/B, scaling effects between the trapdoor prototype scales. The small trapdoor tests with unreinforced soil show reduced settlements and volume losses, particularly at the surface, where the rate of settlement is significantly less than that of the trapdoor throughout. The results show that the surface soil is generally dilating and the vertical shear bands observed in larger trapdoor tests, which are consistent with surface failure, are absent throughout. Clearly, the small scale of the trapdoor affects the development of the surface failure.

Shear band thickness has been shown to be related to particle size. The ratio of the approximate thickness of the shear band to trapdoor width, *t/B,* indicates that *t* increases with reducing trapdoor width, when at prototype scale. There is some evidence from the observed shear strains that the shear band is considerably thicker for the small trapdoor, and in general that the shear band thickness, *t*, is inversely proportional to *B*. At high d_{50}/B ratios, the results show that the surface and shallow depth displacements are reduced, indicating that the displacements and strains are related to both trapdoor width, *B*, and displacement, δ. As the trapdoor width is increased, relative to particle size, the horizontal effects of shear stresses developed on the opposing trapdoor edge are reduced; the trapdoor is sufficiently wide to avoid particle scale shearing effects caused by the relative proximity of the shear bands.

4.3.4.3 FRS composite

In all test cases, the settlement at the surface was reduced significantly with the inclusion of fibre compared with unreinforced soil. The general trends for all trapdoor scales tend toward the reduction of settlement, S_{max}, and volume loss, V_{sl}, with increase in both the length and the concentration of fibres. The effectiveness of the fibre, in terms of reduction of displacement, appears to be, in general, related to the 'fibre factor', $\eta\chi$.

The results show a different failure mechanism for FRS than observed with unreinforced soil. In the case of medium and large width trapdoors, *B* = 60 mm and *B* = 105 mm, respectively, the unreinforced soil tests show distinct signs of a general failure occurring at the soil surface. These general signs of failure include; significant shear bands extending from the crown of the arch to the surface and rates of settlement and volume loss equivalent with the trapdoor. In the composites tested these indicators of failure were found to be largely absent. The results show that fibre inclusion appears to affect the volumetric expansion over a larger area of the soil than observed in the unreinforced case. At the end of the test, the composite soils show signs of deformation at the surface, rather than evidence of the surface soil displacing as a rigid body (as seen with unreinforced soil).

A ratio of the maximum settlement of fibre composite, S_{maxf} to that of unreinforced soil, S_{maxu} is a measure of the extent of improvement in settlement obtained for fibre-soil composites compared to unreinforced soil. This ratio, when multiplied by the normalised trapdoor displacement, δ/B, yields an improvement, as a magnitude of normalised displacement: $(S_{maxf}/S_{maxu})\delta/B$. The improvements in settlement, S_{maxi}, and volume loss, V_{sli}, are given in Equations 4.14 and 4.15 below.

$$S_{maxi} = \left(\frac{S_{maxf}}{S_{maxu}} - 1\right)\frac{\delta}{B} \quad (4.14)$$

$$V_{sli} = \left(\frac{V_{slf}}{V_{slu}} - 1\right)\frac{\delta}{B} \quad (4.15)$$

Positive values of S_{maxi} and V_{sli} infer larger displacements and volume losses in the fibre composite than unreinforced soil. Negative values infer composite settlements are less than unreinforced soil, expressed as a percentage of the trapdoor width, *B*.

Figures 4.47 to 4.49 show the magnitude of the improvement, S_{maxi}, against δ/B with small medium and large trapdoor width. The plots give an indication of the extent of improvement in terms of displacement throughout the soil depth.

As trapdoor displacement increases beyond 0.08*B* the traces, indicating different fibre composites, begin to reduce from zero at a gradient broadly proportional to the fibre factor, $\eta\chi$, of the composite.

The rate of change of settlement at the surface is significantly reduced for all fibre-soil composites when compared with unreinforced soil.

In small and medium trapdoor tests (Figures 4.47 and 4.48) fibres of long length, F_L = 20 mm, $\eta\chi$ = 0.4%, appear to have a reduced effect on settlement compared to medium length fibres, F_L = 12 mm and 16 mm, ($\eta\chi$ = 0.24% and 0.32%, respectively). The medium and large scale trapdoor tests with high fibre content, χ_w = 1%, $\eta\chi$ = 0.48%, show the greatest improvement; these results show a reduction in surface settlement of ~0.1*B* at the ultimate stage (when compared to unreinforced soil) which corresponds to ~300 mm at prototype scale.

Figure 4.49 to 4.51 show the improvements in soil volume loss, V_{sli} , as calculated in Equation 5.2, for fibre soil composites compared to unreinforced soil against normalised displacement, δ/B, for the small medium and large trapdoor widths, respectively.

All fibre inclusion tests show a reduction in volume loss compared with unreinforced soil. In general the figures show a similar trend to the maximum settlement, where the volume loss throughout the soil reduces broadly in proportion with the fibre factor. All responses show equivalent volume losses with the unreinforced case at displacements, δ, of less than 5% of trapdoor width, *B.*

The settlement and volume results show a clear tendency towards improvement for displacements beyond 5% of the trapdoor width, *B*.

Small trapdoor, *B* = 30 mm, results show the maximum displacements are reduced throughout the soil compared with the unreinforced soil case. The effectiveness of the fibre inclusion does not appear to deteriorate with depth in the same manner as observed with larger trapdoors. Composites with higher $\eta\chi$ values (>0.32%) also appear to be less effective at reducing settlement. This same general observation, where long fibres have a slightly lessened effect, was made with the medium trapdoor. High fibre content composites, χ_w = 1%, F_L = 12 mm, $\eta\chi$ = 0.48%, have a reduced effect on both settlement and volume loss compared with χ_w = 0.5%, which is contrary to the results obtained with larger trapdoors where the effect is, in general, proportional to fibre content, length and factor.

The medium and large trapdoor settlement and volume loss improvement results show composites with higher fibre factor values are generally more effective. The effect is related to both fibre content and length, composites with a high fibre factor show a proportional reduction in settlement and volume loss. Generally the effectiveness of the composite is increased with increasing fibre length and content. The effects of fibre inclusion generally deteriorate with depth.

All results, at all trapdoor scales, show that significant improvement is achieved with fibre-soil composite at trapdoor displacements > 5% of the trapdoor width, *B* improvements below this displacement are comparatively small.

The volumetric and shear strains with fibre inclusion (shown in Figures 4.34 and 4.35. for test CMC07 and Figures 4.45 and 4.46 for test CMC04) show slightly reduced but comparable magnitude of strain with the unreinforced case.

The large-displacement strains (at the ultimate stage where δ = 0.18*B*) do not appear to propagate to the surface with fibre inclusion. The areas of large volumetric expansion and high shear deformation extending from the trapdoor edges define the failure surface in the soil. The failure surface region appears to be contained within the soil, without significant failure occurring at the soil surface; indicated by the absence of shear bands extending to the surface as seen in unreinforced soil tests.

Figure 4.53 shows the variation of normalised maximum settlement, S_v/B, and volume loss, V_{ls}/B^2 with fibre factor, $\eta\chi$, at the ultimate stage of the tests where δ = 0.18*B* at the soil surface, *z* = 0, and at shallow depth, *z* = 0.25*H*. The plots clearly show the relationship between the reduction in both settlement and volume loss with fibre factor.

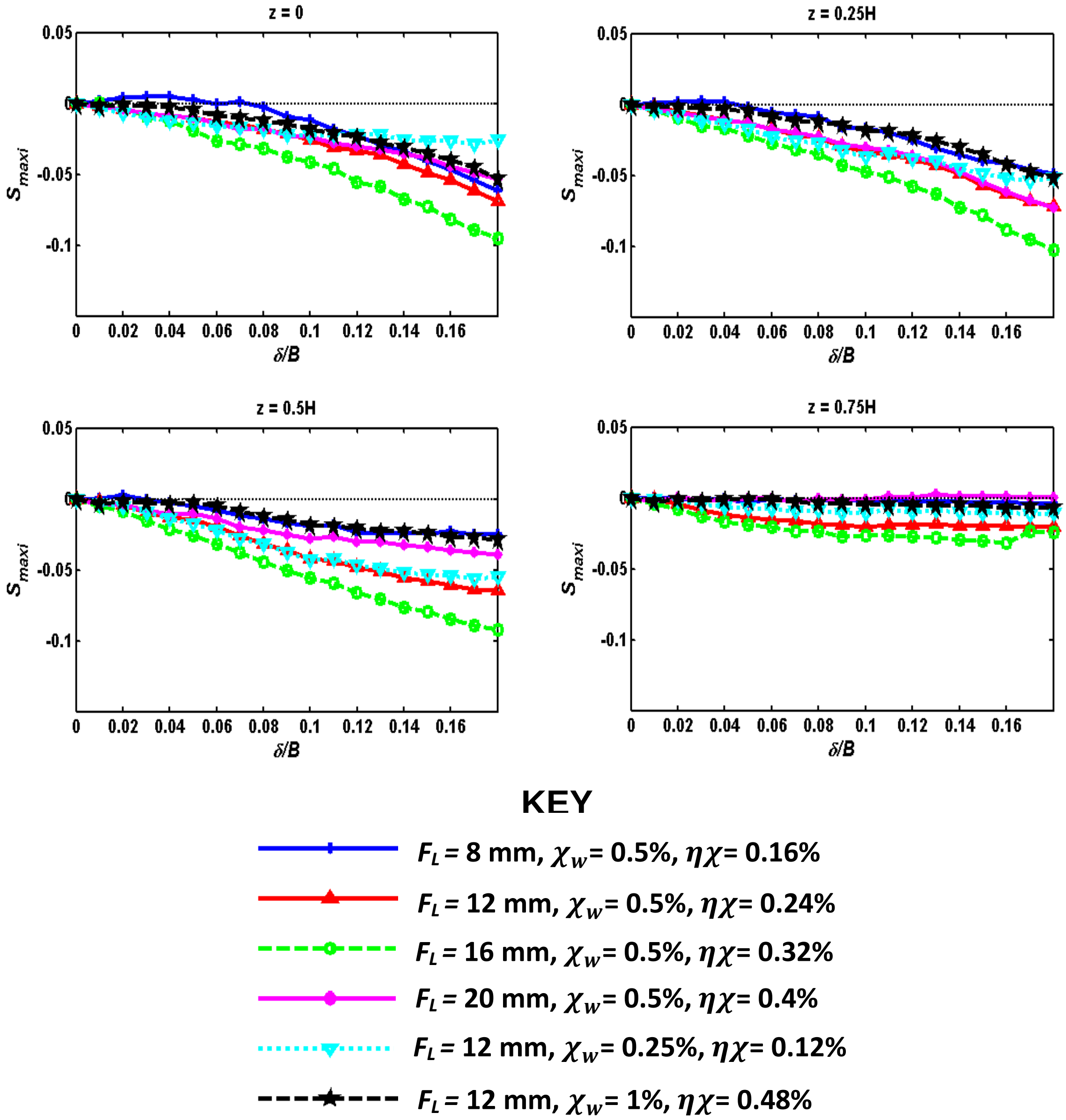

Figure 4.47 Total improvement in displacement, S_{maxi}, variation with depth, *z*, and normalised displacement, δ/B, *B* = 30 mm

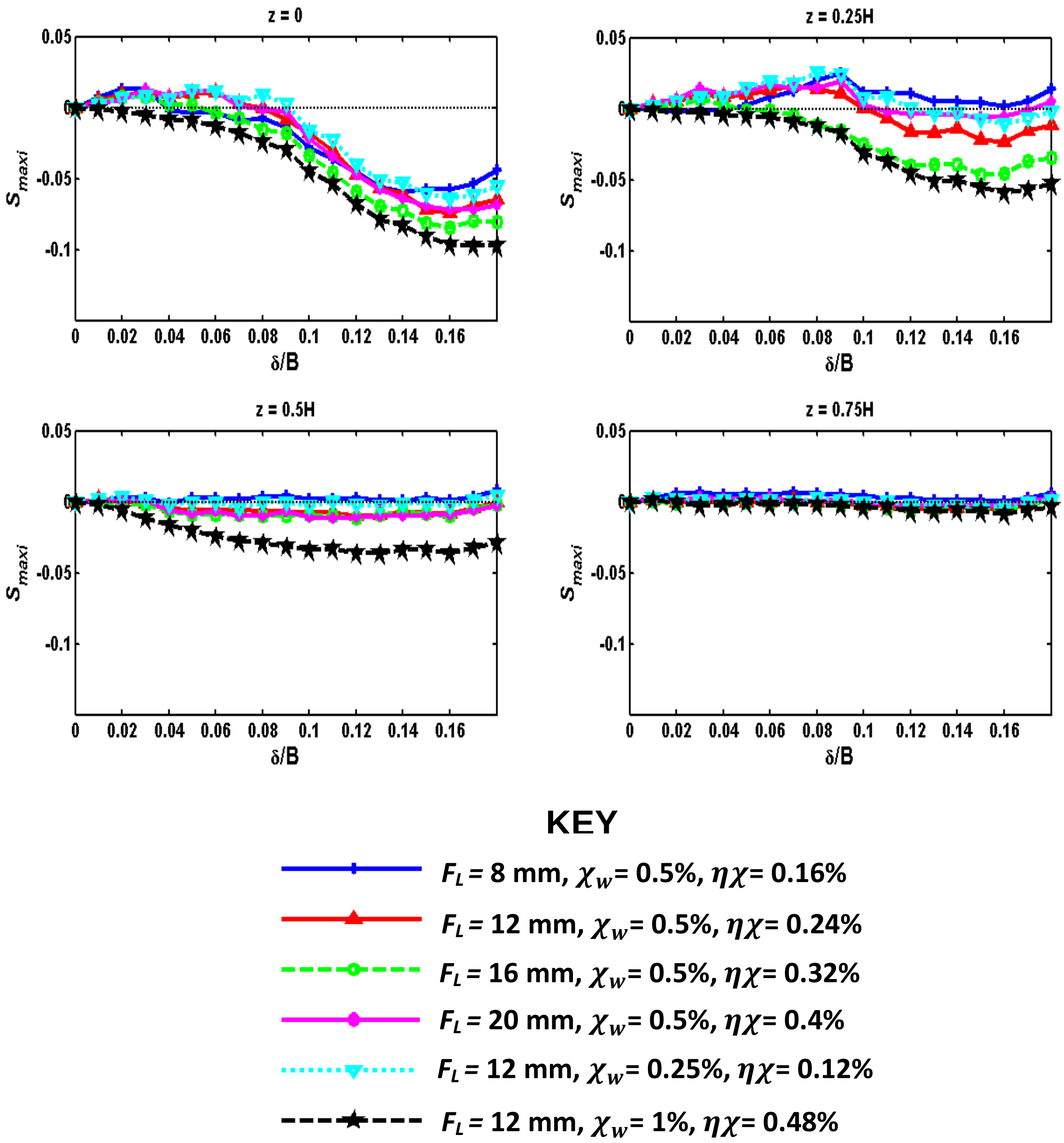

Figure 4.48 Total improvement in displacement, S_{maxi}, variation with depth, *z*, and normalised displacement, δ/B, *B* = 60 mm

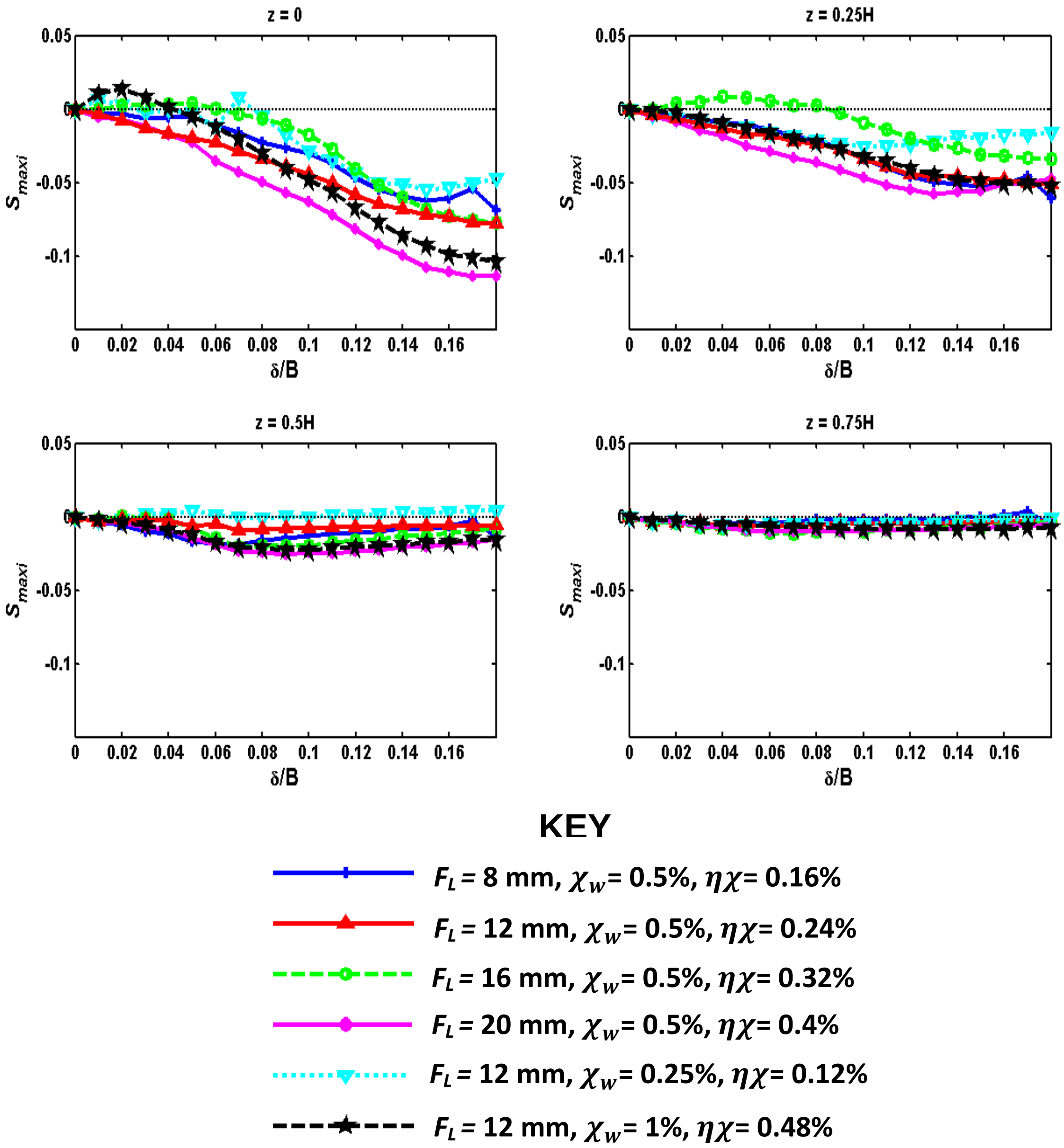

Figure 4.49 Total improvement in displacement, S_{maxi}, variation with depth, *z*, and normalised displacement, *δ*/*B*, *B* = 105 mm

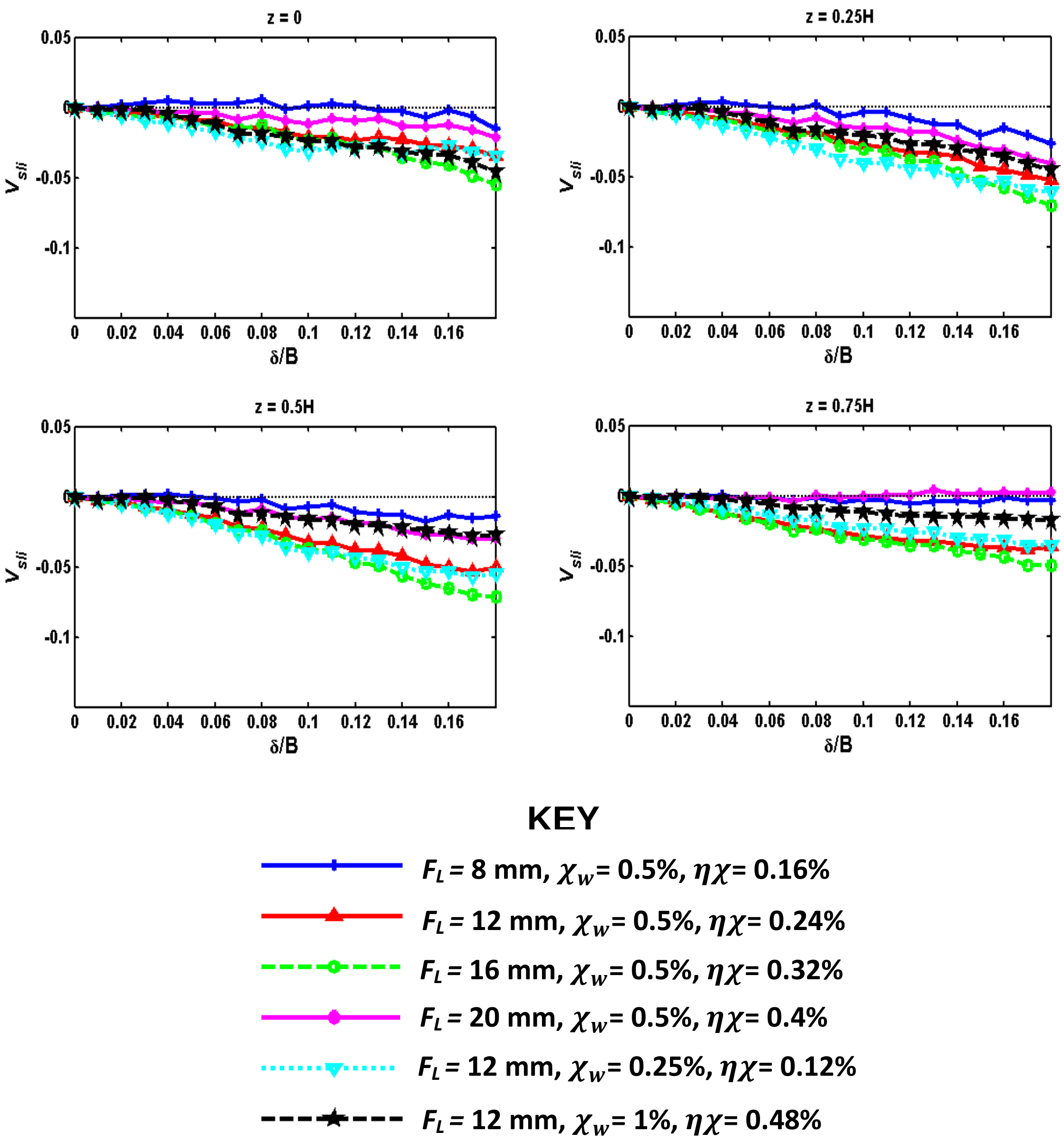

Figure 4.50 Total improvement in volume loss, V_{sli} variation with depth, z, and normalised displacement, δ/B, B = 30 mm

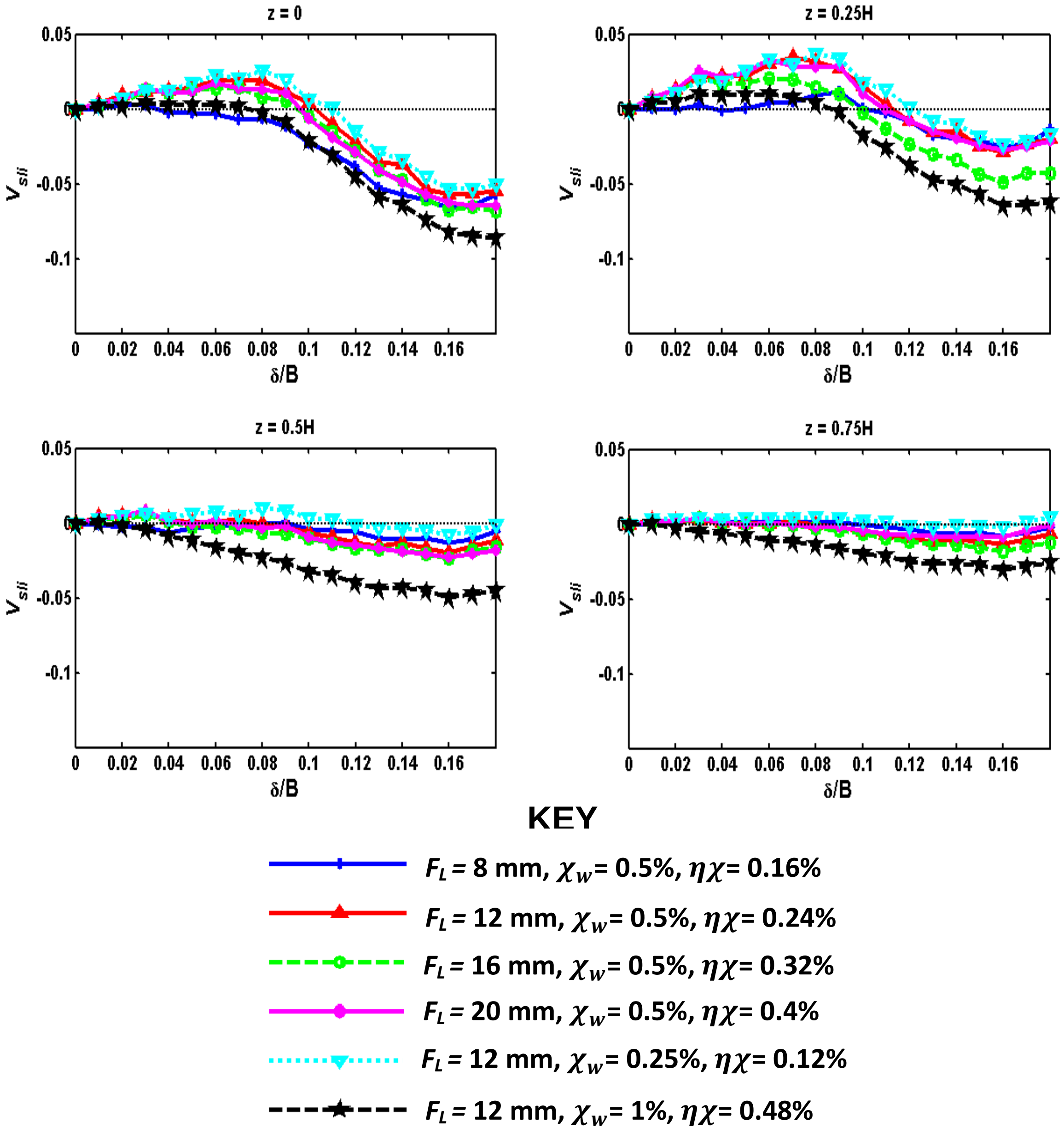

Figure 4.51 Total improvement in volume loss, V_{sli} variation with depth, z, and normalised displacement, δ/B, B = 60 mm

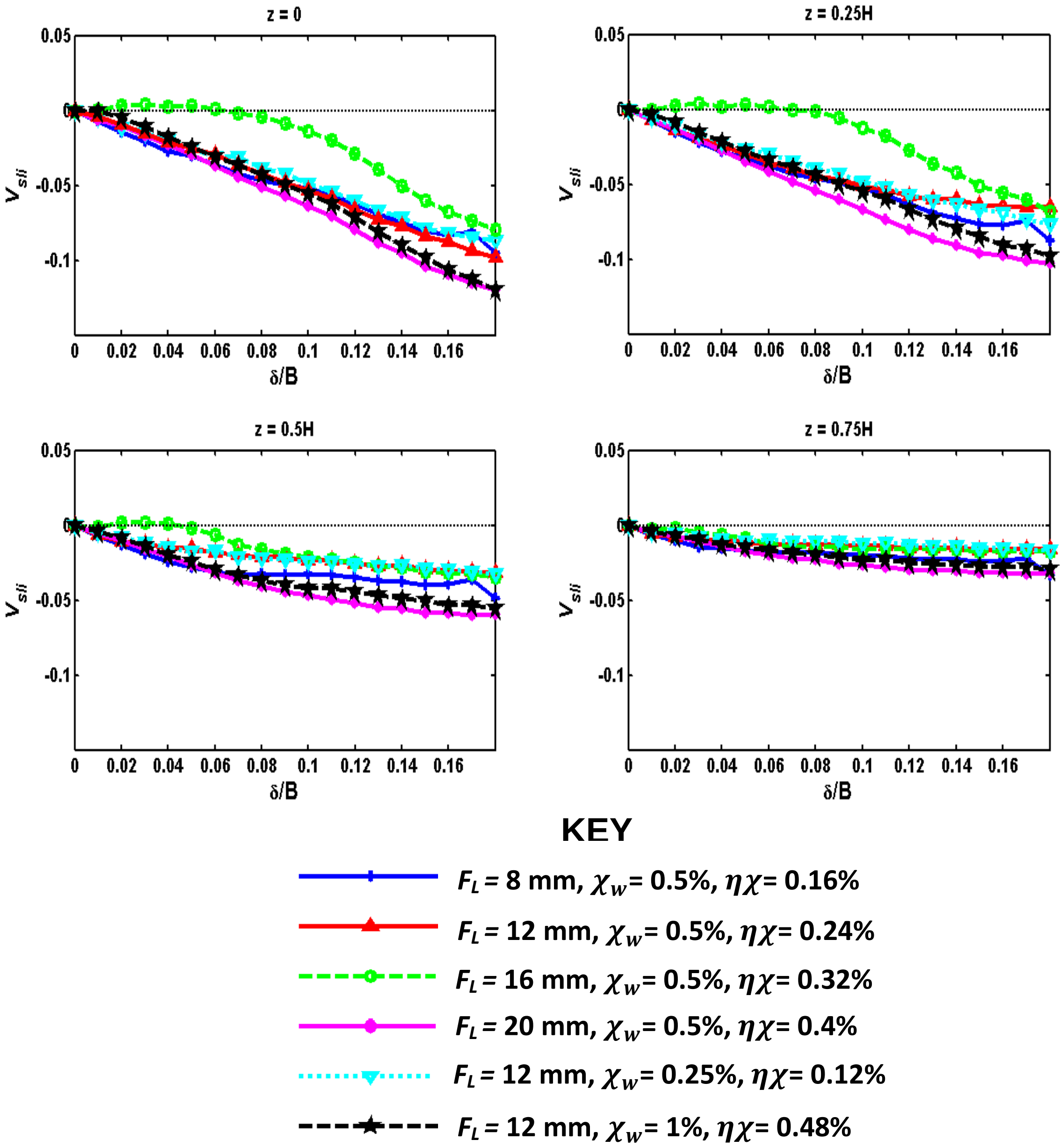

Figure 4.52 Total improvement in volume loss,V_{sli} variation with depth, z, and normalised displacement, δ/B, B = 105 mm

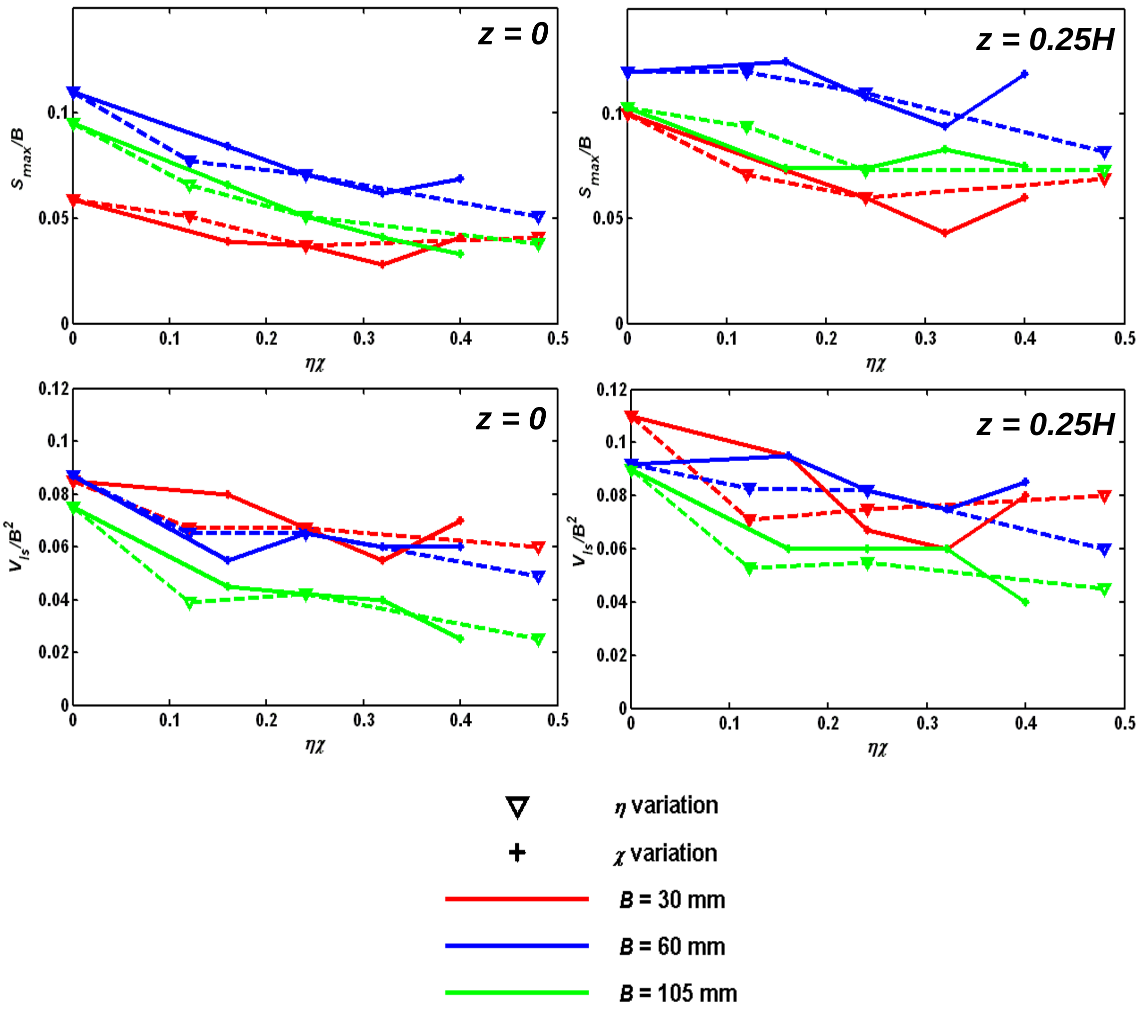

Figure 4.53 Surface and shallow depth settlement and volume loss variation with fibre factor, $\eta\chi$.

CHAPTER 5 DISCUSSION OF RESULTS

5.1 Introduction

The results from all tests are discussed in this section. Firstly comparisons are made between theoretical estimates and measured loads for the general unreinforced soil case.

Comparisons are then made between the observed displacement and strain mechanisms and those reported in the literature for trapdoor type tests with unreinforced soils.

The general aim, and novel content, of the research reported herein, is the investigation of the effects of fibre inclusion on the loading and displacement behaviour of the composite material when compared to unreinforced soil

The effectiveness of fibre reinforcement, in terms of loading, displacement and strain behaviour is discussed, for composites of varying fibre size and concentration. Relationships are drawn between the general effects reported in the literature for variation of fibre conditions. The strength envelope of the unreinforced soil, derived from direct shear tests, was compared with theoretical estimates of improved strength with fibre-reinforcement. The results from tests with fibre inclusion were then compared with the theoretical estimates.

Fibre length scale effects were investigated, by means of variation of fibre length and trapdoor scale, effectively varying the fibre to structure ratio, F_L/B. A modelling of models exercise was conducted, whereby the model trapdoor scale, stress level and soil layer height were varied in order to model the same prototype conditions. The intention of this exercise is to determine if particle size effects, and consequently particle-fibre interactions are consistent across all trapdoor scales and to determine the suitability and limits of the application of fibre reinforcement in small scale physical models.

5.2 Loading response

All tests conducted showed similar results in terms of the loading characteristic shape of the GRC. Fibre inclusion was found to have negligible effects on the response. Figures 4.4 and 4.6 show averaged loading response with fibre length and content variation respectively. All responses in these figures lie within ±7% of the overall mean. No distinct trend in loading between fibre composites is apparent.

Figure 5.1 shows the overall mean GRC, averaged across all tests, for comparison with theoretical estimates of trapdoor stress detailed in Chapter 2.

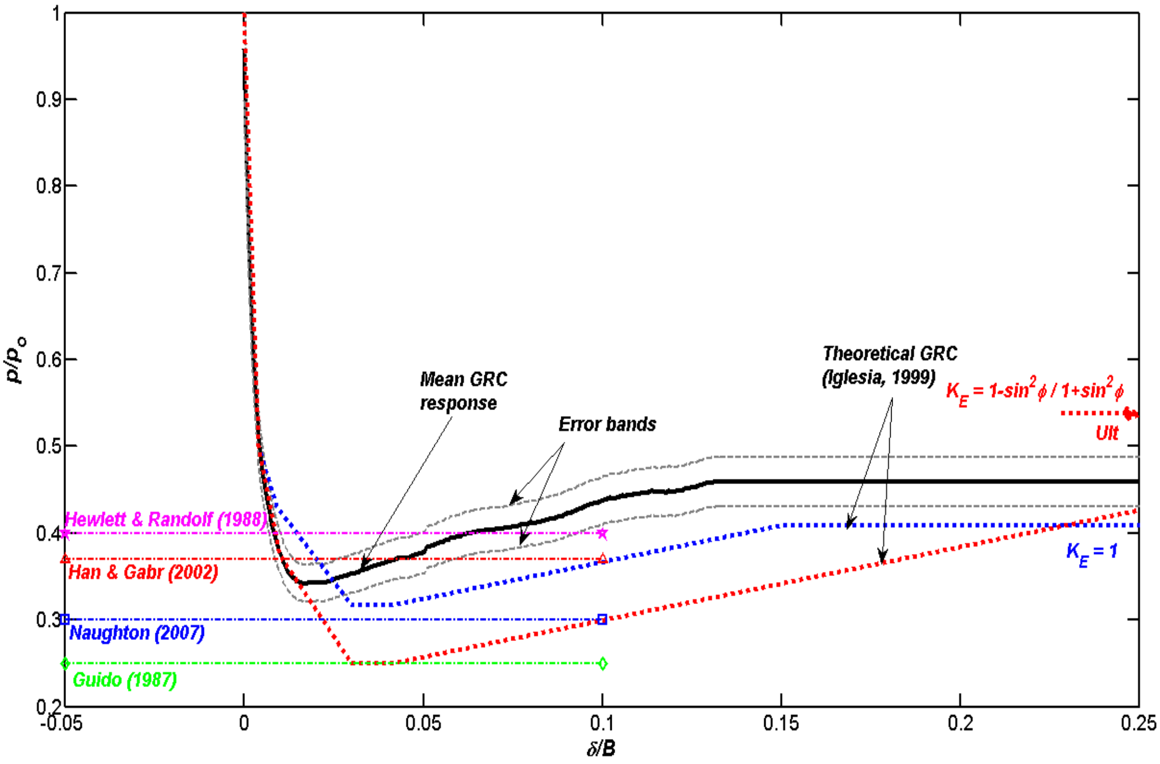

Figure 5.1 GRC comparison with theoretical estimates

The black trace of Figure 5.1 shows the averaged trapdoor loading response of all tests normalised by the geostatic load, p/p_0, against trapdoor displacement, normalised by trapdoor width, δ/B. The dashed grey bands represent the total variation in measurement over all tests conducted. This variation is due, partially, to fibre composite effects and partially to experimental differences between the test setup such as variation of frictional forces acting on the trapdoor as it displaces (see Section 3.2.2.3). Some consideration was made of frictional forces and attempts to compensate the GRC response for these effects were made. As discussed in Section 3.2.2.3, the overall confidence in the measurement accuracy is ~±5%, which is of a similar order to the observed variation due to fibre composite characteristics. The general conclusion, that the general mechanism and magnitude of the trapdoor loading response is unaffected with fibre, is discussed further in Section 5.2.

The observed loading on the trapdoor shows good overall agreement with that predicted by theory. GRCs predicted using the method of Iglesia (1999) are shown in dashed red and blue lines. The appropriate value of active earth pressure, K_E, is used to calculate the loading response. The value of K_E is subject to some disagreement (see Section 2.2). Two theoretical GRCs are plotted; the blue dashed line shows the GRC with K_E = 1, the red dashed line shows the GRC with K_E = 0.54, as calculated using Equation 2.8. The theoretical GRCs show generally good agreement, in terms of the initial gradient, minimum and ultimate loading and load recovery of the response. The approximated curve with a value of K_E = 1, shows particularly good agreement with the averaged result.

As noted in Section 4.2, the initial gradient, M_A, is significantly less for the small trapdoor.

The rate of change of trapdoor loading was observed to be roughly constant for all tests and therefore invariant with trapdoor width.

The implication of this is that the initial response of the GRC is a function of δ rather than δ/B. Practically, this means that the arch begins to form at the same initial rate regardless of relative trapdoor scale. This behaviour is to be expected since displacements and strains need to be sufficiently developed for the arch to start to form. The equivalence of the gradient indicated that the initial rate of arch formation was approximately equal for all tests, regardless of trapdoor scale.

Figure 5.2 (a) shows p/p_0 plotted directly with δ (rather than against δ/B, as in the GRCs considered elsewhere herein) for all trapdoor widths for the unreinforced soil case. The figure shows that the initial gradient at model scale, M_{Am}, is roughly equal ~3.5 mm^{-1}. The modulus of arching, M_{Am}, was roughly constant with trapdoor width at the scales tested. The equivalent arching modulus, M_A', can be calculated by multiplying by trapdoor width, $M_A' = BM_{Am}$, resulting in the conversion of M_{Am} to a gradient where displacement is normalised by width, δ/B. The calculated values of M_A' for each trapdoor scale are shown in Figure 5.2 (b), the approximated loading, calculated using derived values of M_A' for each trapdoor scale is shown against normalised displacement, δ/B. When compared with the unreinforced soil loading data, the approximated gradients show a reasonable relationship to the results. The vertical stresses in the soil will vary considerably when compared with initial values of δ/B. As, effectively, different stages of the arch forming process are being compared (as p/p_0 is not equal at the same relative displacement for different trapdoor widths). The vertical stress, acting on the trapdoor can be calculated from the arching modulus; $p/p_0\gamma_s H$, therefore as the ratio used in calculation of the GRC p/p_0 is dependent on trapdoor scale, considerable differences in stress between trapdoor scales are present when compared against δ/B.

When loading response is averaged across the three trapdoor sizes the gradient is much closer to that predicted by Iglesia et al (1999), plotted in black on Figure 5.2 (b) for comparison.

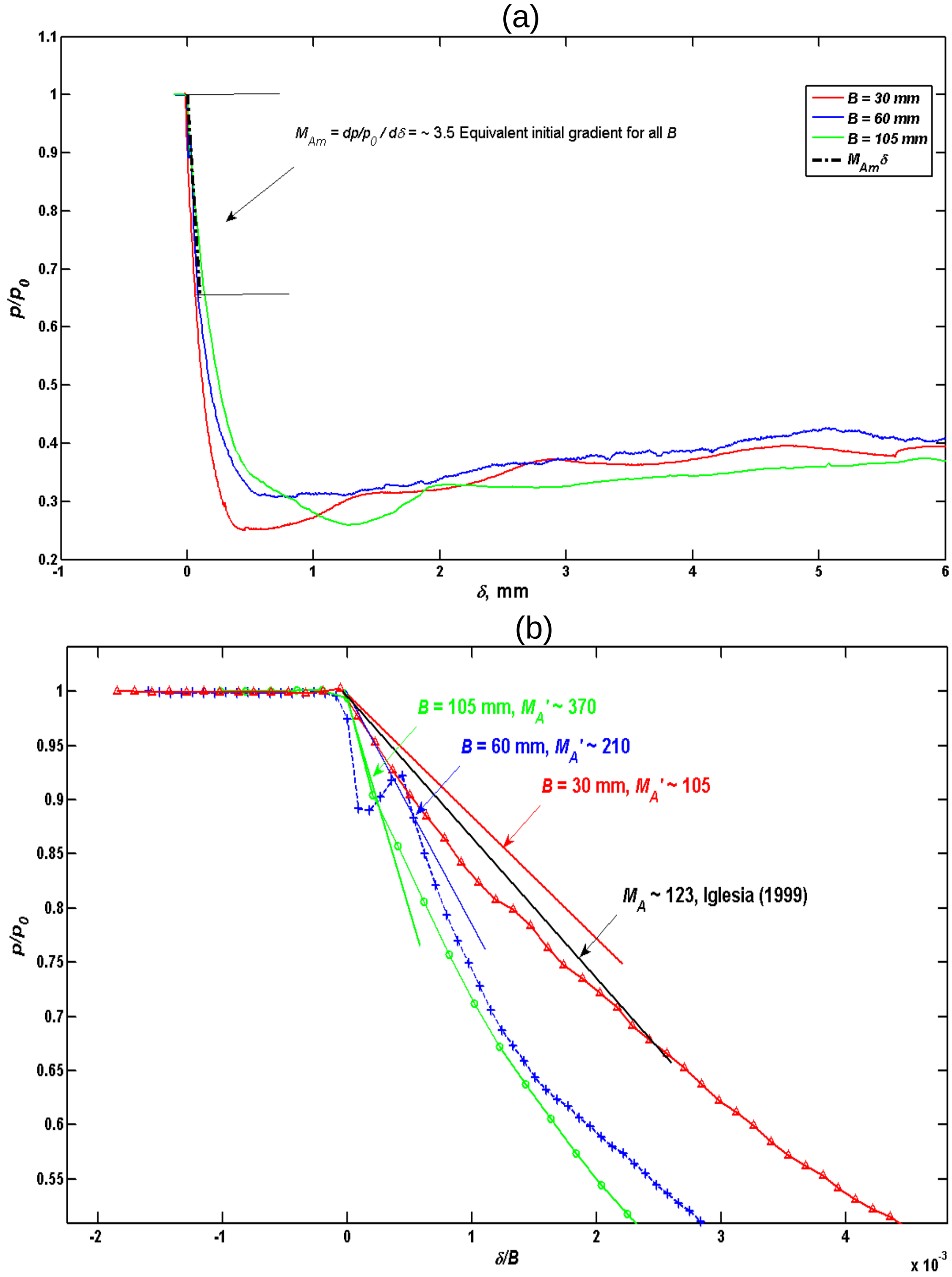

Figure 5.2 Normalised loading initial gradient, M_A, variation with; (a) displacement, δ; (b) displacement normalised by trapdoor width, δ/B.

Iglesia et al (1999) and others (Terzaghi, 1943) found that the arching action cannot be fully sustained in cases where the overburden depths are relatively shallow. Terzaghi (1943) estimated this lower limit of ratio of soil height to trapdoor width, *H/B,* to be in the range 1.5 – 2; below this value, substantial redistribution of soil stresses cannot occur above the trapdoor and an arch is prevented from forming (Iglesia et al, 2014). The *H/B* ratio for all tests conducted was 1.66, lying in the transition region of arch formation where diminishing arching effects are reported. Reduced arching action would be manifested in the GRC as a higher normalised trapdoor loading with displacement. The results show that the loading of the averaged GRC for all tests is roughly 5-15% higher the than theoretical GRCs, indicating a reduced arching effect compared to that predicted. The general increase in stress is consistent with the reported behaviour at shallow depth (low *H/B* ratios) where arching effects are diminished as the *H/B* ratio is reduced towards 1.5.

Estimates of load reduction based on geometrical shape of the displacing soil region are shown in Figure 5.1. Three different arching estimates are plotted, triangular, trapezoidal and semi-circular. The green line shows the reduction estimate obtained using the Guido method, see Section 2.4.3, which was arrived at through experiments using layered geo-textile reinforcement. The method predicts the formation of a triangular arch, it follows from Equation 2.17 that the stress is reduced on the trapdoor by 75%, which is somewhat affected by the role of the reinforcement and is consequently higher and to some extent irrelevant. However, the Guido results are plotted for general comparison. Han and Gabr (2002) and Carlsson (1987) suggested that a trapezoidal area forms above the soil where the apex is 30º. The consequent reduction in stress on the trapdoor is ~63%. The Naughton (2007) method approximates a shape based on a log spiral of the friction angle, given by Equations 2.18 to 2.20, and illustrated in Figure 2.11. The method calculates a reduction in trapdoor stress, based on an approximate peak friction angle, ϕ_{pk}, of 35º, of 70%.

Hewlett and Randolph suggest a method for estimating the stress based in a semi-circular arch. A similar estimate can be made if a physical circular arch, of diameter *B,* is assumed to form as the trapdoor displaces .An area can be calculated based on the circular arch shape, as described in Section 2.3. The vertical stress can be estimated by firstly considering a semi-circular area of soil, the same diameter as the trapdoor, as illustrated in Figure 2.8. If this area is presumed to be displacing with the trapdoor as a rigid body, then the stress acting on the trapdoor, resulting from the weight of this ‘infilling’ material underneath the arch, σ_0, can be approximated using Equation 5.3. As described in Section 2.3, an expression can be derived for estimating the radial stresses immediately beneath the arch, σ_r. Equation 5.2 is adapted from Low et al (1994), where, in this case, the radius of the arch half the trapdoor width, $r_i = B/2$. An estimate of the radial stress acting on the trapdoor/subsoil is then given in Equation 5.2.

The total vertical stress acting on the trapdoor, σ_v is obtained by adding the radial stress to the stress due to the infilling material beneath the arch, σ_0 :

$$\sigma_v = \sigma_0 + \sigma_r \quad (5.1)$$

Where;

$$\sigma_r = \left({B^2}/{2} \right)^{K_p - 1} + \frac{\gamma_s B}{2K_p - 4} \quad (5.2)$$

$$\sigma_0 = \frac{\gamma_s B^2 \pi}{8B} \quad (5.3)$$

The calculated radial stress, σ_r, using a peak friction angle, ϕ_{pk}, of 35º is 14 kPa. The stress resulting from the arch in-fill material, σ_0, is calculated to be 20 kPa from Equation 5.3. The total vertical stress acting on the trapdoor, σ_v , is then calculated to be 34 kPa. Giving an estimated stress reduction, σ_v/σ_{td}, of 0.4 where σ_{td} is the vertical stress at the trapdoor $\gamma_s H$. The semi-circular estimates of Low et al. (1994), and Naughton’s (2007) log spiral approach, are estimates based on peak friction angles which provide an estimate based on failure and are therefore equivalent to minimum loading estimates in the low strain region of the GRC, precluding failure.

All theoretical approaches show good relative agreement with the general GRC. The estimated total increase on the support loading, $2\Sigma\, p_s/p_{s0}$, with trapdoor displacement is shown in Figure 4.3. Significant differences between the trapdoor and support loading are present at displacements of δ < 0.1B. The drop in vertical load on the trapdoor is not equivalent to the increase acting on the support at small displacements, where the GRC is in its transient stage, where changes in normalised loading with displacement are high.

This effect can be explained by consideration of Figure 2.7 (a) and (b). In trapdoor induced arching, the soil in the general triangular region due to the displacing trapdoor. The major principal stress in this region is in the horizontal direction; $\sigma_1 = \sigma_h$, and vertical stress is reduced.

Above the supporting region the soil is in an active state where the major principal stress is vertical, $\sigma_1 = \sigma_v$, hence, the vertical stress (and consequently measured load) acting on this area is increased. Figure 2.7 (b) shows a triangular region between the trapdoor and supporting areas where the major principal stress direction is in transition between the two states. In this transitional area, horizontal stresses are increased and some of the stress is transferred onto the soil above the supports. This stress transference has the effect of reducing the vertical stress acting on the support area immediately adjacent to the trapdoor. Consequently, the measured reduction in trapdoor loading is not equal to the measured loading increase on the support during the stage where the arch is developing.

The transitional area of soil between trapdoor and support has a significant horizontal stress component, which is largest closer to the edge of the trapdoor and diminishes with distance until the soil is in its neutral ‘at rest’ state where the ratio of horizontal to vertical stress is equal to K_0.

At higher displacements, when general failure has occurred, the soil reaches a post-failure stage where the vertical pressure above the support is increased; the trapdoor and support vertical pressures tend towards equality. The horizontal stresses during this phase are low, as the soil has reached a critical state.

As shown in Figure 4.3, the same characteristic difference between trapdoor and support loading at small displacement is relatively unaffected by trapdoor scale. This is discussed in more detail in Section 5.5. Some differences are indicated which can be attributed to experimental error between the test setups for different trapdoor widths.

5.3 Unreinforced soil displacements and strains

The variation in stresses detailed in the previous section and the changes in shape of the region of soil displacing with the trapdoor are consistent with the postulation by Iglesia et al (1999) that ‘a curved arch emerges with small downward displacements of the trapdoor; medium relative displacements lead to a triangular arch shape; and large relative displacements tend to mobilize a volume of soil mass with vertical sides’ (rectangular arch) settling with the inclusion. Vardoulakis et al. 1981; Evans 1983; Dewoolkar et al. 2007 and others have all conducted large displacement tests, considerably in excess of the 20% of trapdoor width displacements reported herein, where the soil is in this final ‘rectangular arching’ stage.

Contours of vertical displacement for unreinforced soil are shown in Figures 4.13 to 4.15, for small medium and large trapdoor widths. The contours show trends consistent with an arching mechanism taking place, at displacements of $\delta/B < 0.1$, where the displacement at the surface is considerably less than that of the trapdoor. In this stage, the soil is dilating and deforming considerably, as indicated by the volumetric and shear strains shown in Figures 4.15 and 4.16 (a) and (b). The responses indicate that the region of soil subjected to high strains, appears to change shape from an initially curved to a slightly more triangular arch with displacements $\delta<0.08B$. A graphical representation of the different stages of the failure mechanism for unreinforced soil is shown in Figure 5.3. The white arrows on the left hand side plots are representative of the direction and magnitude of displacements. Regions of high strain and shear bands are indicated on the right hand plots by solid white lines.

The crown of the arch is observed to form above the trapdoor centreline, at a height above the trapdoor approximately equal to the equivalent trapdoor radius, $B/2$. In the general case this occurs at relative displacement in the region of ~0.01 to $0.02B$

The vertical inclination of the shear bands originating from the trapdoor edges appears to increase as the trapdoor is displaced. Costa et al (2009) observed a similar mechanism taking place, described in more detail in Section 2.4.2, where the inclination of the failure surface increases and the angle, θ_i, which is equivalent to the dilation angle of the soil, ψ, reduces towards zero with further displacement.

The strain mechanism for the unreinforced soil is presented in Section 4.3.1. For small trapdoor displacements, $\delta < 0.03B$ soil surface displacements are small and occur over a relatively wide area. The displacements throughout the soil are generally of a more uniform magnitude. In this small strain region of the stress-strain response of the soil, the displacements and strains can be considered to be dominated by elastic deformation behaviour.

The strain results from unreinforced tests indicate that a single failure surface at each corner of the trapdoor developed with trapdoor displacement. As highlighted in Figure 5.3, the vertical inclination of the failure surface reduces with displacement the angle, θ_i is approximately equal to the soil dilation angle, ψ, and reduces with increasing trapdoor displacement (see Figure 5.3) Initially, θ_i has an initial value close to the friction angle, ϕ, towards zero as the failure propagates toward the surface.

Evans (1983) and Iglesia et al. (1999) proposed a curved arch shape with an angle ϕ to the vertical in order to determine the minimum trapdoor load. This assumption is based on analysis of the plastic flow rule presented in Evans (1983). Accordingly a material dilates when ψ > 0°, while for ψ = 0 no volume change in the material occurs. Atkinson and Potts (1975) showed that ψ must be less than or equal to ϕ for the rate of plastic work to always be non-negative and that the plastic strain deformation behaviour is defined by the failure criterion (Evans, 1983). This assumption is an ‘associated flow rule’ allows the simplification that $\psi = \varphi$ initially, decreasing thereafter until $\psi = 0$ at large displacements, where the material has reached its critical state.

The approximated angle of dilation, θ_i, determined from approximating the angle from the trapdoor’s edge to the crown of the arch (see Figure 5.3) defines the failure surface shape.

In the initial stages (δ<0.05B) of unreinforced tests was θ_i=~34°, closely reflecting the determined peak friction angle ϕ = 35° of the soil.

In the maximum arching phase of the test, generally occurring in the range 0.03$B > \delta >$ 0.06B an increased amount of soil within the region above the trapdoor is subjected to plastic deformation, the displacements at shallow depths are small relative to those close to the trapdoor. The inclination of the failure surface, θ_i (which is equivalent to the angle of dilation, $\theta_i \sim \psi$) averaged over the soil layer depth is ~26º, which is less than the peak friction angle ϕ_{pk} of the soil. This high deformation stage is indicated in Figure 5.3 by displacement vectors of different length throughout the soil depth.

At the latter stages of the tests, the increased deformation of the soil with trapdoor displacement cannot be sustained and shear failure occurs. The shear planes extend vertically toward the surface, as θ_i reduces and reaches a minimum of 7.2º; the arch progressively fails in the region of the crown. The failure surface inclination, θ_i, at shallow depths approaches zero, indicating no significant volume change is occurring (see Evans (1983) in Section 2.4.2). The signs of this failure are clear from plots of S_{max}/B (see Figures 4.25 to 4.27 in Chapter 4) and V_{sl}/B (see Figures 4.36 and 4.38 in Chapter 4) at the soil surface, where the rate of change of settlement and volume loss with trapdoor displacement abruptly increases at displacements greater than 10% of the trapdoor width, *B*.

Thereafter the soil is translating vertically downward, as a rigid body, at the same rate as the trapdoor is lowered without further change in volume, relative to trapdoor induced volume since the volume losses in the soil change at the same rate as the trapdoor volume loss. The assumed shape of the failure surface is indicated on the ultimate stage strain graphic of Figure 5.3, the planes extend vertically from the crown of the arch to a region at the surface above the edges of the trapdoor. Initial failure begins at the crown of the arch as it collapses. Subsequent displacement and strain results, at larger displacement, indicate the development of a general vertical failure surface along vertical lines extending from the trapdoor edges, in this stage the soil can be considered to have achieved critical state conditions.

Evans (1983) constructed a free body diagram to describe this stage where the dilation angle, ψ, tends towards zero (see Figure 2.7 (d) in Section 2.4.2) indicating vertical shearing.

Costa et al (2009) conducted trapdoor experiments where the failure surface was determined for higher relative trapdoor displacements, $\delta = 0.6B$. They reported that further displacements, beyond those which caused the soil to fail along vertical shear planes (as is the case in the tests reported herein), instigated the emergence of multiple external failure surfaces initiating from the trapdoor edges and extending outside the limits of the trapdoor. In this study, the ultimate stage is considered to be reached when failure has occurred at the soil surface and the loading response is constant with displacement, thus showing signs of steady, critical-state behaviour.

The mechanism described by Costa et al. (2009) is based on trapdoor induced displacements in deep conditions where *H/B* > 3. Muir-Wood and Stone (1992) conducted trapdoor experiments in shallow conditions, *H/B* < 1, and found significant differences in the failure mechanism. In shallow conditions, successive failure surfaces with approximately constant vertical inclinations θ_i are reported to emerge with larger displacements. The failure propagation in this case is reported to switch between subsequent failure surfaces in a sudden manner. The soil between the two failure surfaces can be considered as a rigid body playing no role in the deformation process (Stone and Muir Wood, 1992). Particle size effects were found to be significant in the development of failure surfaces in shallow conditions, since the shear band thickness and relationship between dilatancy and relative displacement across the deforming soil is a function of particle size.

In all tests reported herein a single failure surface developed; initiating from the trapdoor edges towards the trapdoor centre at a vertical inclination, θ_i, which reduces with increasing trapdoor displacement. No further failure surfaces are observed to have developed in the range of displacement tested. This is in agreement with the behaviour for deep conditions (*H/B* > 3) reported by Costa et al (2009), signifying that the overburden to trapdoor width ratio tested herein, *H/B* = 1.66, is of sufficient depth for the redistribution of stresses associated with failure in deep conditions to occur.

Costa et al report that the thickness of the failure surfaces also increases with increasing trapdoor displacement relative to width. The shear band thickness has also been reported to increase with shallow soil layer depths relative to trapdoor width, (where $H/B \leq .1.5$) As discussed in Section 4.3.1 the shear band thickness, *t*, was observed to appear wider at small trapdoor scales where shear strains are plotted against normalised distance *x/B* (see Figures 4.22 to 4.24). When strains are plotted with the model distance, *x* (in absolute scale), the shear bands appear broadly the same thickness in agreement that the thickness appears to be a function of particle size. The relative thickness of the shear band, as a function of trapdoor scale, *B,* is considered in Section 5.5. For the medium trapdoor case, *t* is estimated to be in the region 0.166-0.2*B,* which is ~10-12 mm in model dimension giving a thickness to particle size ratio, t/d_{50}, of 20 – 24. A generally accepted ratio is of the order of 10, although a wide variation of *t* is reported in the research, Costa et al (2009) reported a t/d_{50} ratio of ~30 in deep conditions, Muir Wood (2002) reported values in the range 7.3-18.5 and Vardoulakis (1981) reported t/d_{50} values ranging from 10 to 21 in experiments involving *H*/*B* ratios from 0.5 to 2.

The general displacement and failure mechanisms reported by a number of researchers, described in the Chapter 2, are in good general agreement with those observed in the unreinforced soil tests reported in this research.

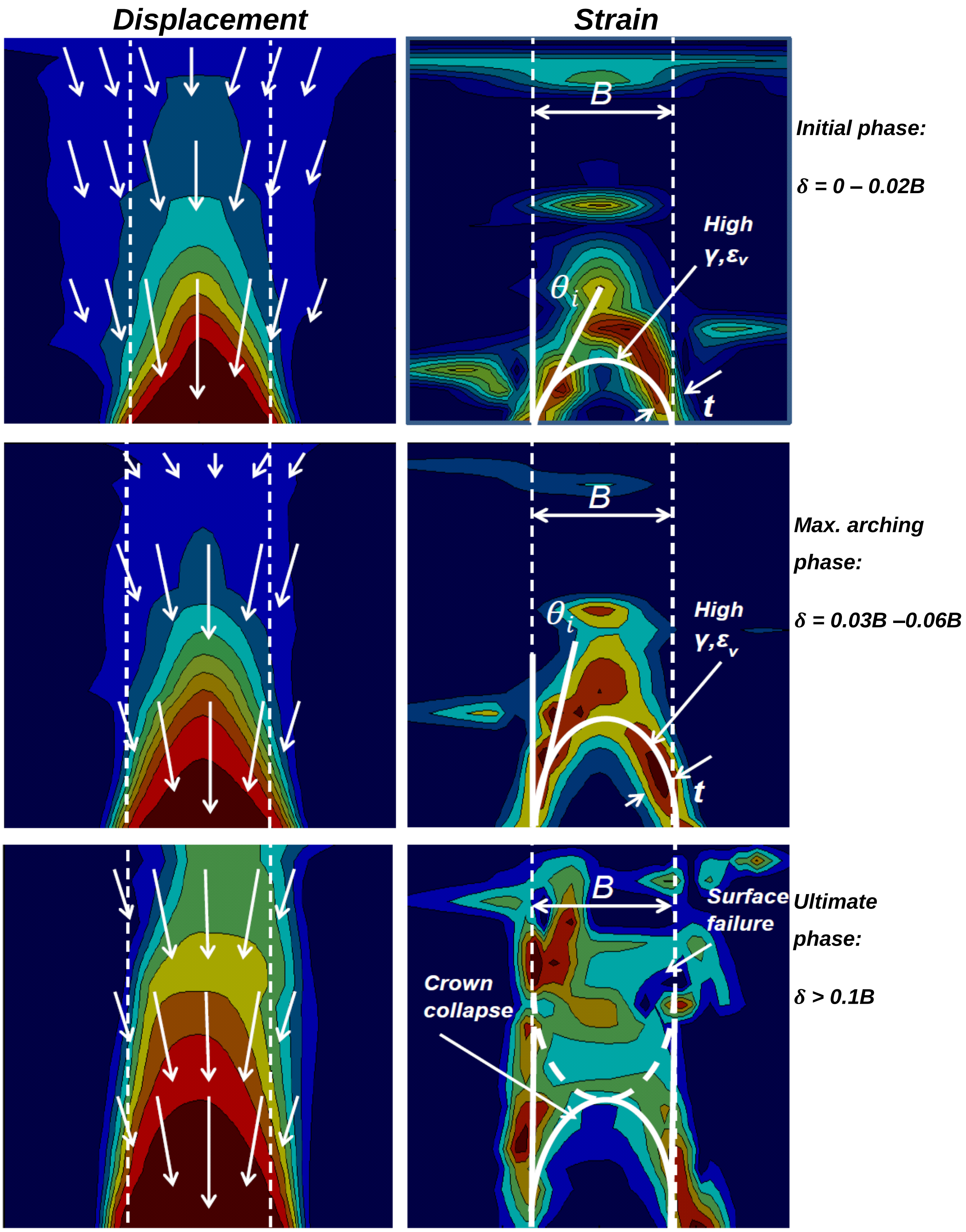

Figure 5.3 Generalised displacement and strain mechanism for unreinforced soil

5.4 Fibre reinforced soil displacements and strains

As shown in Sections 4.3.2 and 4.3.3 the maximum settlements and volume losses in the soil, compared to trapdoor volume losses, were significantly reduced at large displacements (greater than 10% of the trapdoor width) compared with the unreinforced soil.

The amount of settlement at the surface has been shown to be broadly related to the fibre factor, $\eta\chi$, of the composite - with the exception of the small trapdoor tests discussed in Section 5.5.

The general surface failure mechanism characteristics for unreinforced soil, discussed in Section 5.3, are largely absent in the calculated shear strain, γ, results for fibre-soil composites (see Figures 4.35 and 4.46). The areas of deformation are contained within the soil mass. The volumetric strains, ε_v, (see Figures 4.34 and 4.45) show substantial dilation (positive volumetric strain) is taking place over a larger area of soil at large displacements than is the case with unreinforced soil. The general pattern of soil volumetric strain is reflected in the settlement and volume loss results, where the rates of change of settlements and soil volume losses do not reach equality, indicating volume change is occurring within the material and that, at no stage, is the material displacing as an essentially rigid body, as is the observed behaviour with unreinforced soil.

A graphical representation of the different stages of the failure mechanism for fibre reinforced soil is shown in Figure 5.4. The white arrows representing soil displacements on the left hand side plots show the general trend where surface settlements are reduced relative to displacements at depth at all stages of the test since, as mentioned, no rigid body displacements occur at the surface. The failure surface of the soil can be determined from the general shape of the deformation region. The main difference between the unreinforced and fibre-reinforced failure surfaces is apparent at large displacements where an arch is clearly maintained in the soil in the FRS case, the inclination to the vertical of the failure surface, θ_i, reaches a minimum but does not approach zero. Since θ_i is approximately equal to the dilation angle, ψ, the condition $\psi = 0$ defines failure along vertical surfaces where there is no volume change in the material.

Table 5.1 lists values of θ_i for the test cases referred to in the main text to explain general strain behaviour with tests using long fibres (F_L = 20 mm, χ_w = 0.5%), and with a high concentration, (χ_w = 1%, F_L = 12 mm) of fibres. It should be stated that the dilation angle varies with overburden depth of the failure surface, and θ_i is effectively an approximation of the dilation angle close to the trapdoor edges. The values of θ_i were determined manually from inspection of the angles of high shear concentration initiating from the trapdoor edges in Figures 4.16, for the unreinforced case, and Figures 4.23 and 4.30 for fibre reinforcement tests.

Table 5.1 Comparison of observed values of failure surface inclination, θ_i, with trapdoor displacement, δ. *B* = 60 mm.

Displacement, δ	Unreinforced soil Test CMC01	FRS: $\mathrm{F_L}$= 20 mm, χ_w = 0.5%, ηχ = 0.4% Test CMC07	FRS: $\mathrm{F_L}$= 12 mm, χ_w = 1%, ηχ = 0.48% Test CMC04
0.02B	33.7°	36.7°	40.3°
0.05B	26.6°	33.6°	33.7°
0.18B	7.2°	21.5°	24.6°

As discussed in Section 5.3 the angles of dilation and friction can be assumed to be essentially equal for small displacements, thus; $\phi \cong \psi \cong \theta_i$. An increase in the angle θ_i, relative to the unreinforced angle, at 'small' displacement ($\delta \leq 0.02B$), therefore represents an increase in the strength of the composite. For the fibre reinforced soil the angle θ_i for small displacements presented in the Table 5.1, is 36.7° for test CMC07, reported in detail in Section 4.3.2 and θ_i = 40.3° for test CMC04, reported in Section 4.3.3.

The macroscopic friction angle, $\bar{\phi}$, was introduced by Michalowski and Cermák (2002) to characterise the anisotropic strength of the fibre reinforced soil. Using the fibre factor, $\eta\chi$, values for tests CMC07 and CMC04 of 0.4% and 0.48%, and assuming a similar peak interface angle of friction between fibre and soil, ϕ_W, to those reported in Michalowski and Cermák (2002) of ϕ_W~17° values of $\bar{\phi}$ = 38° and $\bar{\phi}$ = 37° are calculated for tests CMC07 and CMC04 respectively using Equation 2.31 in Section 2.6.1. These estimated values are in reasonable agreement with those observed in Table 5.1 considering that θ_i is by nature an approximate estimation of dilation angle and hence strength (for initial pre-failure states) which was deduced by fitting a line of best fit to strain data over depth which is subjected to a degree of measurement scatter. The value of ϕ_W assumed may also be a potential source of error as no tests have been carried out to determine the interface angle of friction between fibre and soil for the materials tested. It is expected that the shear resistance of the of the fibre-soil interface, ϕ_W, is usually lower than that of the unreinforced soil, which, consequently can lead to potential planes of weakness within the material.

Zornberg (2002) suggests Equation 2.26 of Section 2.6.1 to estimate the strength of the fibre soil composite, ϕ_{fs}. As with the macroscopic friction angle, $\bar{\phi}$, of Michalowski and Cermák (2002), empirical coefficients accounting for the orientation, and interaction of the fibre with the soil, c_α and $c_{i\phi}$, respectively are estimated to be: $c_\alpha = 1$ and $c_{i\phi}$ = 0.8 as assumed in Zornberg (2002). This is reasonable since $c_\alpha = 1$ describes a condition where the fibres are randomly orientated within the soil, a value $c_\alpha < 1$ would indicate that the fibres are oriented in some preferential orientation coincident with the shear planes and consequently the reinforcement is less effective. It is expected that the fibres have some degree of preferential orientation to the horizontal, due to the sample preparation process. The coefficient $c_{i\phi}$ of 0.8 was arrived at by measurements of fibre interaction obtained during pull-out tests Zornberg (2002). It should be stated that the assumption made in order to calculate the equivalent shear strength of a fibre composite (Equation 2.30) is that the normal stress acting on the failure plane, is less than the critical value, σ_{nc}, defined by the tensile breakage of the fibres. Zornberg (2002) suggests Equation 2.29 to obtain the critical stress below which failure is induced though fibre pull-out rather than tensile breakage. Using a value of ultimate tensile strength, σ_{fu}, obtained through tensile testing of the fibres, of roughly ~40 MPa (see Figure 3.16), the critical normal stress, σ_{nc}, (which is a function of fibre aspect ratio, η) is calculated to be ~300 kPa for long fibres (F_L= 20 mm) increasing to ~1.2 MPa with short fibres of length F_L= 8 mm.

The normal geostatic stress at the trapdoor, σ_{td}, is ~85 kPa; therefore normal stresses throughout the soil, and therefore average normal stresses, σ_{na} are sufficiently less than the critical stress σ_{nc}, hence, estimates of fibre composite strength using Equation 2.30 are valid and the mechanism of failure is governed by fibre pull-out in the stress ranges encountered in the tests.

For the condition $\sigma_{na} > \sigma_{nc}$ the unreinforced soil residual friction angle, ϕ_r, should be used as the fibres no longer play an active role in the composite strength since they are in a yielding condition.

The estimated strengths using Equation 2.30 are ϕ_{fs} = 42°, for test CMC07 and ϕ_{fs} = 44° for test CMC04, which is in good agreement with the estimated increase in strength determined from θ_i in Table 5.1. This value reduces to ϕ_{fs}= 37° for fibre composites with lower fibre factor values (calculated based on fibre factor of $\eta\chi$.= 0.12% from tests with F_L = 12 mm and χ = 0.25%)

It should be stated that variances are to be expected in the achieved strength of the fibre soil composite due to the inherent differences between sample compositions.

Although considerable effort was paid to achieving a uniform fibre density in the sample preparation process, the structural arrangement of the composite will inevitably vary between tests. Samples with different distributions of fibre orientation and density will emerge. The general assumption is that the composite sample size is large enough to be treated as a homogenous material. If the number of fibres in the sample is small then it is reasonable to expect this assumption is invalidated somewhat, and that variability in orientation and density distribution between samples may be expected to have an increased effect on composite strengths. This and other scaling considerations are discussed further in Section 5.5.

Figure 2.22 (a) shows the generalised fibre-soil composite behaviour in terms of equivalent shear strength as presented in the discrete framework method of Zornberg (2002). The figure depicts a bilinear characteristic of equivalent shear strength of fibre-soil composite compared to unreinforced soil. The estimated fibre induced tension is constant for stresses above the critical stress, σ_{nc}, thereafter, the fibres are subject to tensile breakage which defines the composite rather than fibre pull-out failure. The estimates of equivalent shear strength, ϕ_{fs}, of Zornberg (2002) and macroscopic friction angle, $\bar{\phi}$, approach of Michalowski and Cermák (2002) are defined as a function of the unreinforced properties of the soil and the fibre properties, the implication being that the shear strength behaviour of the composite can be defined without undertaking direct tests on the composite specimens.

Figure 2.22 (b) depicts a representation of strength envelope of for unreinforced soil compared to fibre reinforced soil (Zornberg, 2002). The figure clearly shows the difference in post peak strength behaviour between unreinforced soil and composite. In Zornberg (2013), it was found that the shear strength of the fibre-composite specimens was mobilised at higher strain levels. For example, Zornberg (2013) observed that for a fibre soil composite with χ = 0.4%, the shear strain at the peak strength was ~10% compared to ~5% for unreinforced soil. The mobilisation of composite shear strength at relatively high strains is consistent with observations from the composite tests. The improvements in maximum settlement, S_{maxi}, are shown in Figures 4.47 to 4.49 and volume loss improvements, V_{sli}, are shown in Figures 4.50 to 4.52. The figures show that significant improvements, defined as reductions in composite displacement compared to unreinforced soil, are only apparent at relatively large trapdoor displacements, where δ is greater than ~8-10% of the trapdoor width, *B*. A general conclusion from fibre composite tests is that significant strains are required to mobilise the strength of the fibres in the composite, and fully utilise the fibre soil interactions.

The results show that, in general, the increase in composite strength is in proportion with the fibre factor of the composite. This is in agreement with the soil testing results reported by many researchers such as Zorberg (2002 & 2013), Michalowski and Cermák (2002), Sadek et al (2010), Gray and Ohashi (1983), Gray and Maher (1989) and Diambra et al. (2009).

From a practical standpoint, it may be preferable to construct composites using relatively small concentrations of fibre with higher aspect ratio (longer fibres) to achieve a similar improvement to that gained by increasing the volumetric content of shorter fibres; since the volume of material required is much lower. However, consideration must be paid to the value of estimated normal critical stress, σ_{nc}, given in Equation 2.29, which is a function of the fibre aspect ratio, η. For fibre aspect ratios which significantly reduce σ_{nc}, giving rise to the condition $\sigma_n > \sigma_{nc}$, the strength of the composite will be governed by the soil strength, since the yield stress of the fibre is exceeded and it plays no role in reinforcing the composite.

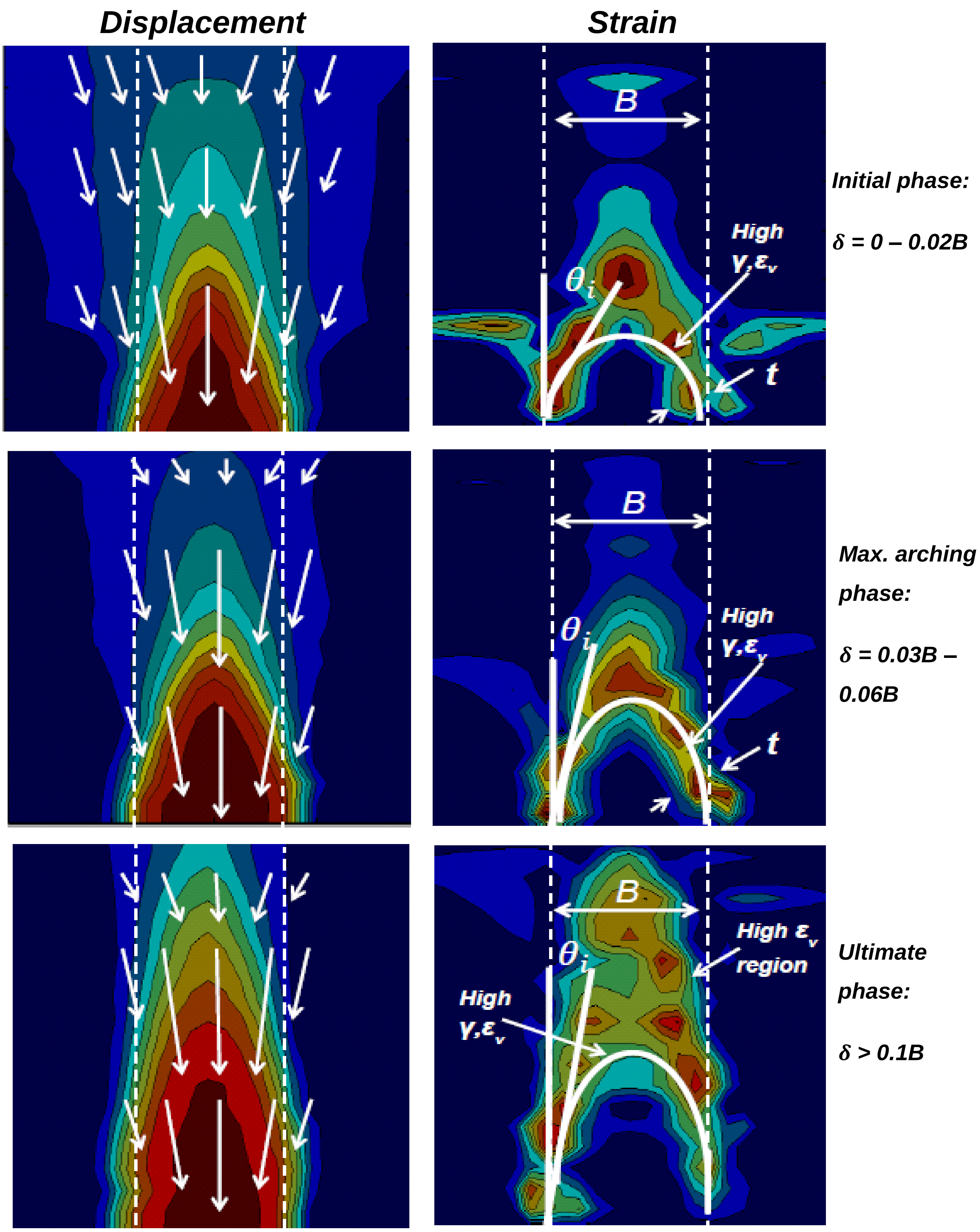

Initial phase:

$\delta = 0 - 0.02B$

Max. arching phase:

$\delta = 0.03B - 0.06B$

Ultimate phase:

$\delta > 0.1B$

Figure 5.4 Generalised displacement and strain mechanism for fibre reinforced soil

5.5 Trapdoor width and fibre scaling effects

5.5.1 Trapdoor scaling effects

The displacement and strain results for unreinforced soil at trapdoor widths, $B = 60$ mm and $B = 105$ mm show relatively good agreement in terms of magnitude, shape and development of the failure surface and surface displacements.

Specifically, an equivalent failure mechanism was observed to take place at these scales for the unreinforced soil tests at trapdoor displacements of the order of $\delta > 0.1B$. The signifiers that general failure of the arch has occurred, discussed in more detail in Section 5.3, are largely absent for the small scale trapdoor tests where $B = 30$ mm.

In the small trapdoor tests, the rate of change of settlement at the surface (see Figures 4.25 and 4.36) is significantly lower than the 1:1 gradient line throughout, indicating surface and trapdoor displacements are dissimilar and the zone of soil above the trapdoor is dilating more than is the case with larger trapdoors. The hypothesis that the soil in the small trapdoor tests has not reached the same conditions of failure as with larger scale trapdoors is confirmed by examination of the volume losses. Figures 4.29 and 4.40 show that trapdoor and soil volume losses at the surface do not reach equality, hence, dilative volume change is occurring to a greater degree than observed with larger trapdoors.

This effect may be partially attributable to an increased variation of normal stress across fibres with considerable vertical alignment, for small trapdoor scales. As this relative stress variation increases it will mobilise tensile strains across the fibre, as it spans a greater proportion of the soil depth.

Figure 4.22 shows the development of a failure surface for unreinforced soil, for the small trapdoor test, which is similar to that described for fibre-soil composites (see Figures 4.35 and 4.46). The implication being that active arching continues at larger relative displacements for the small trapdoor in all unreinforced and fibre-reinforced soil tests. No signs of surface shear displacements are present at any trapdoor displacement.

Figure 5.5 shows measurements of shear strength, τ, against estimated shear strain, γ_e, obtained from direct shear testing at an effective normal stress, $\sigma_n = \sigma_{td}$, of ~85 kPa.

Shear strain can be estimated from the horizontal displacement, x_s, using the approximation of (Knappett & Craig, 2012) given in Equation 5.4.

$$\gamma_e = \frac{x_s}{h_0} \quad (5.4)$$

Where; h_0 =h_{sb}= 25 mm; and h_{sb} is the height of the shear box sample.

There is some uncertainty as to the appropriate value of h_0 to use to determine shear strain. This relates to the thickness of the shear zone, *t*, developed within the shear box for which h_{sb} is an approximation. In the tests reported in this study it was possible to approximate the shear zone thickness, *t*, directly from the shear strain data (see Section 5.2). Therefore the assumption, $h_0 = t$ was used for calculation of the shear strain estimate, γ_e, where *t* = ~10 mm.

Estimates of average shear strain, γ_a, for each trapdoor scale, were obtained from examination of the shear strain contours in Figures 4.21 to 4.23 and are indicated in the figure. Average shear strain for the small trapdoor, *B* = 30 mm, was found to be γ_a ~ 12% at the ultimate stage of the test compared to γ_a ~ 23% for *B* = 60 mm and γ_a ~ 30% for *B* = 105 mm. The shear strains developed in the small trapdoor tests show the soil is in an earlier stage of the stress-strain response, where the strength of the soil at the ultimate stage of the *B* = 30 mm test, τ_{bs} , is close to the peak strength, τ_{pk}. By comparison the strength of the soil at the same relative displacement with *B* = 105 mm is closer to the residual post-failure strength, τ_r. The consequent difference in friction angle between the trapdoors is of the order of 20%. Therefore, as significantly larger shear strains are developed with larger scale trapdoors, consequentially, the strength of the soil is reduced towards the soils residual strength, ϕ_r according to the stress strain relationship presented in the figure.

The comparatively lower shear strains developed in the small trapdoor tests to a large degree explain the differences in the observed strain mechanism. Since lower shear strains are observed throughout, the strength of the material is higher, and post peak conditions associated with failure in larger width trapdoor tests are largely absent. This is manifested in the shear strain response for the small trapdoor in that the formed arch is sustained at larger relative displacements (see Figure 4.22). As discussed in Section 5.2, the stresses during the initial phase are significantly higher, when compared with normalised displacement, δ/B, which is consistent with an earlier stage in the formation of the arch when compared with larger trapdoor scales at equivalent δ/B ratios.

As discussed in Section 5.2, it was found that the initial rate of change of trapdoor loading with displacement, M_{Am}, is roughly constant across all scales.

The implication of M_{Am} being constant is that the initial rate of formation is a function of absolute displacement, since a small amount of displacement is required to mobilise the horizontal stresses and enable an arch to form. As previously discussed, the shear strains are not as developed in the small trapdoor as in larger trapdoor scales effectively resulting in behaviour consistent with a higher strength material, where the arch is maintained at significantly larger displacements.

By analysing the soil displacements at trapdoor displacements relative to trapdoor scale, for example at δ = 0.01*B*, displacements are obtained at a higher relative loading, closer to the geostatic loading condition, p_0, when the arch is in an earlier stage of formation compared to larger trapdoor scales. This is reflected in the displacements and strains observed at the initial stages of the test for the small trapdoor (see Figures 4.16, 4.19 and 4.22). Larger relative displacements are measured throughout the soil (see Figures 4.13 (a) and 4.16 (a)) as the arch is in an earlier stage of formation, where absolute displacements, δ, are not large enough to enable the redistribution of stresses required to form an arch. The strains from the initial stages of the test show the deformation is occurring across a larger area of the soil compared with larger trapdoors, which, at the same relative displacement, show localised regions of high strain forming a distinctive failure surface above the trapdoor.

If the initial rate of loading, and arch formation, is a function of absolute displacement, it is reasonable to expect that soil strains, and displacements, will be comparatively lower for the small trapdoor when compared with displacements normalised by trapdoor width, δ/B. As discussed earlier, a finite amount of displacement is required for the redistribution of stresses necessary to form an arch. For the small trapdoor displacements of δ = 0.01B are equivalent to δ = 0.3 mm. At this very small level of absolute displacement, less than the average particle size, d_{50}, it is to be expected that small strain ‘elastic’ behaviours are dominant as the absolute induced displacement in the soil is insufficient to allow for the physical reconfiguration of the soil matrix associated with plastic deformations necessary for the arch to form.

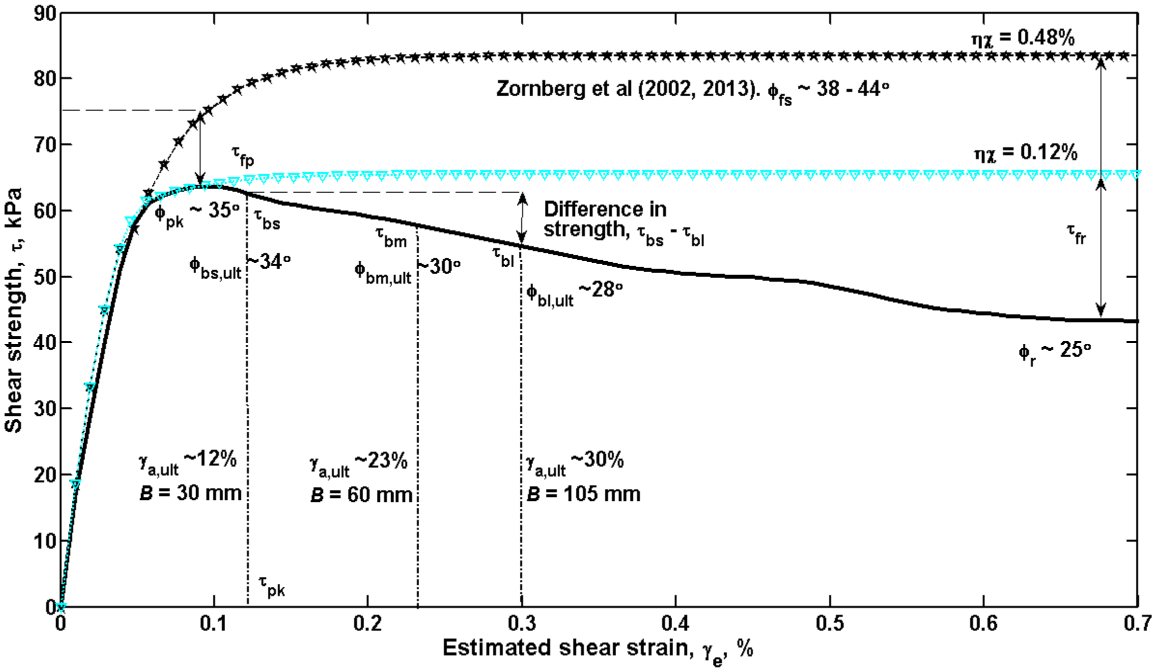

Figure 5.5 Shear strength, τ, against estimated shear strain from direct shear tests

As discussed in Section 5.2, the shear band thickness, *t*, is reported to be a function of the particle size. The t/d_{50} ratio estimated from the tests in the approximate range 20-24. This corresponds to a physical dimension of ~10-11 mm, which is not scalable with g-level (see Section 3.1.2 for centrifuge model scaling considerations). The thickness is invariant with trapdoor width. The thickness relative to trapdoor width ratio, *t/B,* is larger (~0.33) for the small trapdoor. The smaller the trapdoor, the larger the degree of interaction of shear bands across the trapdoor width. Shear band thickness is related to the shear strain development, as the soil in the failure surface shears, the general dilatancy decreases, and the soil within the shear band becomes involved in the deformation process. If the relative thickness *t/B* is large, then a higher proportion of the soil area above the trapdoor is affected by the deformations taking place within the shear band; shear strains are less localised as a larger relative area of the soil is involved in the deformation process. As shear strains are lower for the small trapdoor, the angles of friction and dilation mobilised in the soil are higher. This is consistent with observations that the general surface failure mechanism, characterised by low dilatancy angles, ψ, and post-peak residual strength behaviour, where; $\phi \cong \phi_r$, is not observed in small trapdoor tests.

The increased relative thickness of the shear bands, and their relative proximity at small trapdoor scales, effectively increases the horizontal stress at the crown of the arch which is consistent with a higher strength arch, where the strength developed is closer to the peak strength of the material. This increased strength is manifested in the lower levels of measured shear strain for the small trapdoor.

The volume loss responses for the small trapdoor show a large initial increase at $\delta = 0.01B$. As shown in Figures 4.29, where the 1:1 line indicates equality between the two volume losses. At relatively small displacements of $\delta < 0.01B$, the soil volume loss exceeds the trapdoor volume loss implying that the initial behaviour is contractive, in line with the generally observed small strain behaviour for dense soils, but as the magnitude of shear displacements within the soil increases and volumetric dilation increases, the difference between the two volume losses increases at a lower rate than tests with larger trapdoor widths. This is a further indication that the strength relative to trapdoor width is higher as the soil behaves in a manner consistent with the peak envelope of the soil; the soil dilation is larger, average shear strains are lower, and significant shear failure has not emerged at large relative displacements, consistent with higher angles of dilation, ψ . Higher values of ψ are postulated throughout for the small trapdoor case (as determined from estimates of the failure surface inclination, θ_i) showing an increase in the initial dilatancy angle and therefore, assuming the relationship $\psi \cong \phi$ an increase in friction angle of the order of ~3^o compared to those observed in Table 5.1 for medium scale trapdoors. The relative increase in strength is illustrated in Figure 5.5 where average shear strain $\gamma_{a,ult}$, was determined for the small trapdoor to be ~12%, as discussed, according to the stress strain characteristic, the resultant strength for the small trapdoor, at the ultimate stage of the test, $\phi_{bs,ult}$, is determined to be ~33^{o} comparatively, much closer to the peak angle of friction of ~35^{o}, than values of inferred medium and large trapdoor ultimate friction angle; $\phi_{bm,ult} \cong$ 30^{o} and $\phi_{bl,ult} \cong$ 27^{o}, respectively. The associated average shear strains of $\gamma_{a,ult}$ ~ 23% and $\gamma_{a,ult}$ ~ 30% for the medium and large trapdoors, respectively, were used to determine the friction angles $\phi_{bm,ult}$ and $\phi_{bl,ult}$.

It is worth reiterating that the relative displacement of 0.01*B* corresponds to a trapdoor displacement of the order of 0.3 mm, with surface displacements being significantly less than this value. These displacements are less than the average particle size of the soil, where small strain behaviour is dominant. Displacements of this magnitude are less than can be reliably determined from the photogrammetry method and may therefore be subjected to inaccuracies.

5.5.2 Fibre scaling effects

In general the effects of fibre inclusion in terms of displacement, volume losses and strains are proportional to the fibre factor, $\eta\chi$. The higher the fibre factor, the more effective the reinforcement. This is particularly the case for large trapdoor tests where all fibre inclusion tests show an equivalent improvement which is directly related to the fibre factor. For small and medium trapdoors some exceptions to this general trend were observed:

1. Generally smaller overall fibre reinforcement effects, in terms of maximum displacement were observed in the small trapdoor tests when compared to larger scales.
2. Fibres of long length, F_L = 20 mm, appear to be less effective at reducing settlements and volume losses at the surface for trapdoor widths of *B* = 30 mm and *B* = 60 mm.
3. Higher fibre concentrations (χ_w = 1%) appear to be less effective at reducing settlements and volume losses with the small trapdoor.

Figure 5.5 shows the approximated theoretical stress strain relationships for fibre composites with fibre factor, $\eta\chi$, in the range 6 to 24%. The estimated peak strength of the fibre-soil composite, ϕ_{fs}. was calculated using the method of Zornberg (2002) detailed in Section 2.6.1 The characteristic shows no significant post peak loss of strength with all fibre composites and significantly higher theoretical peak strength $\tau_{fp} = \tau_{eq}$, as calculated using Equation 2.27 in Section 2.6.1. As a consequence of the equality between post peak and residual strength of the composite, the increase in strength with fibre is at a maximum when the shear strains in the composite are high, and the corresponding strength of the unreinforced soil is reduced to residual strengths; $\phi = \phi_r$. As discussed in the previous section, the shear strains are generally lower for the small trapdoor, *B* = 30 mm case when compared with larger trapdoor scales at equivalent normalised displacements, δ/*B*. Thus the soil behaviour is closer to that at the material's peak strength. As can be seen in Figure 5.5, the increase in strength due to fibre inclusion is lower closer to the peak strength than at residual strengths, since, $\tau_{fp} < \tau_{fr}$. This is consistent with the generally lower magnitudes of improvement ratio, S_{maxi}, observed in Figure 4.47 compared with those at larger scales plotted in Figure 4.48 and Figure 4.49.

Figures 4.28 and 4.39 compare normalised surface settlement variations, S_v/B, across trapdoor scales at the ultimate stage of the test. The surface displacements show clearly that fibre inclusions are more effective at larger trapdoor scales, where the strength of the unreinforced soil is closer to the residual strength, $\phi = \phi_r$. As shown in Figure 5.5, the residual contribution to strength from the fibre reinforcement, τ_{fr}, is highest when the residual strength of the unreinforced soil, τ_r is reduced at higher shear strains.

The calculated mean friction angle for fibre reinforced soil, averaged across the fibre factor range across all composites, $\overline{\phi_{fs}}$ is ~40.5°.

The determined unreinforced soil strengths at the final stage of the test are $\phi_{bs,ult}$ ~34°, $\phi_{bm,ult}$ ~30°,$\phi_{bl,ult}$ ~28° respectively for small, medium and large trapdoors of *B* = 30 mm, *B* = 60 mm and *B* = 105 mm, respectively.

An improvement ratio, r_{fi}, can determined using Equation 5.5, based on the theoretical friction angle of the reinforced soil and an estimate of the friction at the ultimate stage of the test for the particular trapdoor setup, ϕ_b. It gives estimates based on the difference between the ultimate stage strength of the test under consideration and the true residual strength of the unreinforced soil.

$$r_{fi} = \frac{\tan\phi_{fs} - \tan\phi_b}{\tan\phi_{fs} - \tan\phi_r} \qquad (5.5)$$

Where:

ϕ_b is the calculated ultimate state angle of friction for trapdoor width, *B*.

Assuming that: $\phi_b = \phi_{bs,ult}$, and the mean fibre composite strength is that with the high fibre factor composite, $\eta\chi$ = 0.48%; ϕ_{fs} = 44.1^o, the improvement ratio r_{fi} is calculated to be ~52%, whereas at the large trapdoor width $\phi_b = \phi_{bl,ult}$ the ratio is increased to ~84%. A calculated difference of ~32% between fibre effectiveness at small and large trapdoor scales exists. This is due to the mobilisation of fibre induced tension in the soil, at the different levels of ultimate strength, ϕ_b, encountered in the small and large trapdoor tests. As the fibres are more effective when the unreinforced soil strength is close to the residual strength, ϕ_r.

The assumption is based on the obtained residual friction angle for unreinforced soil ϕ_r of ~25^o.

Evidence of the increased effectiveness of the fibre at large trapdoor scales, and consequent evidence that the strength envelope of the soil is significantly varied between tests, can be seen in the surface settlement variation plots for different trapdoor scales at the ultimate stage of the test shown for FRS in Figures 4.19 and 4.26.

The definition of the ultimate stage herein is in terms of large relative trapdoor displacement, i.e., δ = 0.18*B,* rather than large imposed shear strains implying that the soil having reached the true critical state conditions, consistent with a residual strength of ϕ_r.

The general improvement in terms of maximum settlement is given by the expression: $1 - S_{maxf}/S_{maxu}$, where S_{maxf} and S_{maxu} are the maximum settlements of fibre-reinforced and unreinforced soil respectively. For the small, *B* = 30 mm, trapdoor this value is roughly ~30% whereas the improvement increases to ~38% and ~55 to 60% for the medium and large trapdoor widths; *B* = 60 mm and B = 105 mm, respectively.

A difference in maximum settlement of ~29% exists between small and large trapdoor scales at the surface. Fibre effectiveness appears inversely proportional to the trapdoor width, *B*.

Whilst the relative strength of the composites may not be directly proportional to the observed displacements, the findings are in general agreement with the prediction that the improvement in composite strength, compared to unreinforced strength, is ~32% between the small and large trapdoor scale tests (based on improvement ratios, r_{fi}, calculated in Equation 5.5).

Generally fibres of long length were found to be less effective for tests with small trapdoor width. The relative trapdoor and fibre dimension can be visualised in Figure 5.6. The relative scales of long (F_L = 20 mm) and short fibres (F_L = 8 mm) are shown against the scale of trapdoor width, *B*. The dashed red lines represent a typical failure surface defining a high shear deformation region near the crown of the arch.

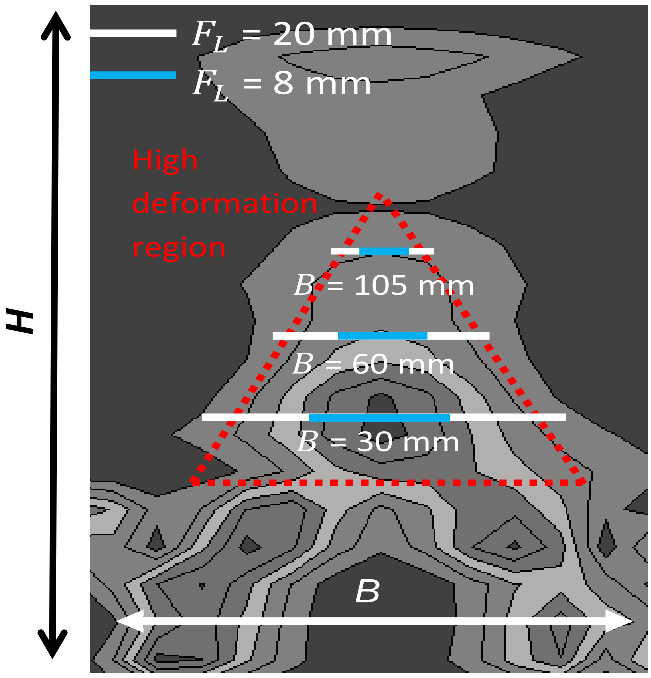

Figure 5.6 Comparison of fibre length, F_L to relative trapdoor scale, *B*.

The tension developed over an individual fibre is related to the relative orientation of the fibre with the preferential plane of shear. Longer fibres cover a larger proportion of the failure surface in the soil, and therefore are subjected to a larger range of shear strain. As fibre length, F_L, is increased towards equivalent model trapdoor scales, significantly less of the total fibre length is orientated in preferential directions coincident with the shear plane, making the fibre reinforcement less effective as the tension developed within it is reduced.

If an individual fibre is over a critical length, relative to the trapdoor width, and long enough to cross through the failure zone, depicted in Figure 5.6, then to some degree the fibre will be effectively embedded in the stationary soil to either side of the failure surface. In this circumstance, the confining stress conditions at either end of the fibre will be comparable, and tensile strains resulting from the soil displacing with the trapdoor will be developed towards the centre of the fibre. In this case the forces acting at either end of the fibre will be reduced and consequentially the bonding between areas of soil at either side of the shear surface will reduce.

In order to maintain the constant height to structure width ratio, H/B =1.66 the height of the soil layer, H, must be 50 mm at the B = 30 mm model scale. In small model scale tests the number of fibres, n, located in the areas actively involved in the high deformation region is significantly less.

If, for explanation purposes, this active area is roughly defined as the triangular region above the trapdoor, defined by approximating the initial dilation angle, ψ, in order to calculate the geometry, then n varies from ~150 for F_L = 20 mm to ~400 for F_L = 8 mm lengths of fibre. In the fibre content tests, n is ~160 at χ_w = 0.25% and n is ~500 for χ_w = 1% (F_L = 12 mm). For the large, B = 105 mm, trapdoor, n is increased roughly by a factor of 3.5, giving a much larger number of fibre-soil interactions across the critical high deformation areas of soil.

Although the fibre concentrations are the same at different trapdoor scales, with a small trapdoor a relatively low number of fibres are actively involved in high deformation areas, it may be expected that discrete effects, due to the relatively non-homogenous nature of the composite, may present themselves as significant variations between test results.

It appears that composites with high fibre factor ($\eta\chi$ >0.32%) are less effective (in terms of reducing composite displacements, S_{maxf}) in tests using the small trapdoor setup.

The results suggest that, at the small trapdoor scale, high fibre factor tests which are achieved either by increase in length (n is small) or by increasing content (n is large) show the same trend towards reduced effectiveness.

Therefore the number of fibres, n, is sufficient to produce results which reflect the expected behaviour, in tests where F_L < 20 mm, where strength of the composite is increased as a function of fibre factor, $\eta\chi$.

It is reasonable to expect that in tests with high F_L/B ratios tensile forces developed across the fibre will be somewhat reduced.

As the spread of the fibre across the inclusion is increased above a limit, the tensile mobilisation of the fibre is reduced. The general expectation is that fibres are less effective if they cross shear zones, in the B = 30 mm trapdoor case for

F_L = 20 mm a significant number of fibres will intersect both shear zones and span a larger width of the failure surface than at larger trapdoor scales.

A general observation made when preparing the tests was that for longer fibres, which were visible through the Perspex front window, there appeared to be more voids around the perimeter of the fibre. Therefore, the efficiency of the compaction method may be lessened with larger fibres causing localised discrete variations in density in the achieved composite. The voids around the fibre may lead to detrimental effects in terms of fibre effectiveness. As longer fibres deform, voids around the fibre become more significant, reducing the interaction between particle and fibre. It is reasonable to suggest that this effect will bear some relation to F_L/B ratio as a larger proportion of the failure surface is spanned by the influenced fibre.

Visvanadham et al (2009) reported a similar result where longer fibres were less effective in reducing heave in centrifuge tests of expansive soils. Compaction efficiency was also found to be lessened for longer fibres in the tests reported by Visvanadham et al (2009).

The expected variation in estimates of reinforced composite strength using the macroscopic friction angle method of Michalowski and Cermak (2003) and the discrete framework method proposed by Zornberg (2002) is of the order of ~5-7° for the range of composites tested. It is to be expected then that due to the inherent structural differences within the composite, significant variations in composite strength will arise and behavioural trends within this small range will be difficult to discern; particularly, for small trapdoor case where the number of fibres in the affected zone is reduced.

5.6 Discussion of FRS applicability

5.6.1 Reduced model scale test considerations

As described in Section 5.3, the shear band thickness of the soil is related to particle size. In small trapdoor tests, where the ratio; d_{50}/B is relatively large, full shearing behaviour does not emerge, and shear strains are lower throughout compared to the larger trapdoor tests. This significantly affects the strength behaviour of the soil as shear strains consistent with reduced residual soil strength, ϕ_r, do not fully develop. Therefore trapdoor width, *B,* plays a significant role in defining the minimum scale which the full arching strength envelope can be tested. Since the effects of fibre reinforcement are reduced at peak strengths, it follows that this should be taken into consideration when modelling representative prototype scales.

From a practical viewpoint, the ratio, *t/B*, should be sufficiently small enough to effectively induce conditions representative of prototype scales considered herein, where the relative thickness t/B_P, (at prototype trapdoor width, B_P = 3 m) is around two orders of magnitude smaller. This direct scaling is misleading however, as the general premise of the scaling laws considered in Section 3.2.1 is that representative soil behaviour emerges at large grain to structure ratios, d_{50}/B, as are generally considered in reduced scale centrifuge model tests.

In general, the relative thickness of the shear band, *t/B* appears to be related to the strength of the formed arch, as the observed deformations above small trapdoor tests are consistent with higher strength behaviour.

The model trapdoor width should be large enough such that particle scale and consequent shear band size effects are not encountered. This is an important point since the strength envelope of the soil in the small trapdoor tests increased at trapdoor relative displacements compared to larger scale trapdoor tests, and subsequent approximated behaviour will likely overestimate the strength of the soil in a practical prototype situation.

The ratio of fibre length to trapdoor width, F_L/B, can be used to determine if the relative length is small enough to avoid length scaling effects, mentioned in Section 5.5. The results suggest that, in general, the smaller this ratio, the greater the tendency for the results to show predictable improvements based on the composite properties of fibre length and content, F_L and χ_w. For example, for large trapdoor tests (*B* = 105 mm) the increase in improvement is directly proportional to fibre length; where long length fibres; F_L = 20 mm, are most effective at reducing settlements and volume losses. For trapdoors of smaller scale, the long fibres were found to be less effective than medium fibres (where, in this context, ‘medium’ fibres are defined as fibres in the range: F_L = 12 -16 mm).

The tension developed over an individual fibre is related to the relative orientation of the fibre with the preferential plane of shear. Longer fibres cover a larger proportion of the failure surface in the soil, and therefore are subjected to a larger range of shear strain. As fibre length, F_L, is increased towards equivalent model trapdoor scales, significantly less of the total fibre length is orientated in preferential directions, coincident with the shear plane. The fibres spanning a critical length of the high deformation region are less active; making the fibre reinforcement less effective as the tension developed within it is reduced.

5.6.2 Field applications

Fibre reinforcement has been shown to be most effective where relatively large scale displacements and strains are induced, at strains where the residual strength of the unreinforced soil is significantly less than the peak.

This should be taken into account in the design of reinforcement schemes above yielding buried structures. If relatively large strains cannot be tolerated, then the fibre tension cannot be fully mobilised and equivalent performance is achieved, in terms of displacements as with unreinforced soil.

This behaviour makes application of FRS more suited to foundations where significant inclusions are expected to occur in the soil; such as above landfill and potentially above mine-works and sinkhole type structures. FRSs have found general application across a broad range of scenarios where the peak strength of the unreinforced soil was found to be significantly increased with fibre inclusion. Soils which exhibit a significant loss of post peak strength will benefit considerably from fibre inclusion as generally fibre increases the ductile behaviour of the soil, and no significant post peak loss of strength is encountered.

The results reported herein show that generally the effectiveness of the fibre is a relative function of the fibre factor, $\eta\chi$, of the composite. In the general case, significantly smaller material amounts of long fibre are required to produce the equivalent effect of high concentrations of short fibre. This could significantly impact the cost in large scale applications.

Intentionally blank page

CHAPTER 6 CONCLUSIONS AND FURTHER WORK

6.1 General conclusions

A trapdoor apparatus has been developed to model the arching in sands and sand-fibre composites, resulting from loss of support, in a geotechnical centrifuge.

The width of the trapdoor was varied in order to investigate a range of fibre length to trapdoor width and determine the suitability of the use of fibre reinforced composites in reduced scale centrifuge model testing. The sand height and scale factor (test g-level) were adjusted accordingly to maintain a constant sand height to trapdoor width, *H/B*, ratio of ~1.66 and normal stress of ~85 kPa at trapdoor depth.

Leighton Buzzard fraction C soil with an average particle size, ~0.5 mm was used in the tests. The relative density of the material for each test was above 90%.

To test the effects of fibre concentration on fibre-soil composite performance composites were tested with a fixed fibre aspect ratio and fibre content by dry soil mass, χ_w, of 0.25%, 0.5% and 1% and compared to an unreinforced 0% fibre case.

The fibre aspect ratio, η of 0.5 mm diameter polypropylene fibres was varied from 4-24, corresponding to a range of fibre length, F_L, from 8 to 20 mm, whilst fibre content by mass, χ_w was fixed at 0.5%.

Trapdoor loads in unreinforced soil tests show good overall agreement with theoretically estimated loading based on: *H/B* ratio, soil friction angle, ϕ, and d_{50}.

The average increase in loading across the support structure is consistent with the expected vertical stress behaviour during arching. The increase in loading on the support structure decays in a broadly exponential relation with distance from the trapdoor.

The volumetric and shear strains are consistent with failure mechanisms reported in the literature in trapdoor tests of unreinforced soil. Marked signs of surface failure are observed in unreinforced soil tests at large trapdoor displacements, such as; vertically extending shear bands, low angle of dilation, rigid-body displacements and low volume change in the soil above the trapdoor.

For trapdoor displacements less than 20% of the trapdoor width and fibre composites in the range of aspect ratio and concentrations considered herein the following general conclusions can be drawn from the obtained results:

- No discernible differences were observed between unreinforced and composite loading responses on the trapdoor or across the support structure.
- For all tests conducted, fibre inclusion significantly reduced the magnitude of displacements at the surface and shallow depths for trapdoor displacements greater than 10% of the width.
- Fibre inclusion significantly reduces the volume loss induced in the soil compared to the inclusion volume created by trapdoor displacement at displacements greater than ~1% of the trapdoor width. Changes in soil volume are evident at large displacements.
- Generally lower levels of shear strain are observed at comparable displacements, indicating increased composite strength compared to unreinforced soil.
- Large deformations are observed throughout the soil at large displacements with no evidence of vertical shear displacements apparent at the surface.
- The failure surface maintains an arched shape over the trapdoor that is contained within the soil mass and does not extend to the soil surface at any displacement.
- Comparatively high dilation angles, consistent with pre-failure deformations and volume changes in the soil, are apparent at large displacements.

For the range of soil composites tested the effects of fibre inclusion are, in general terms, proportional to the ‘fibre factor’ defined as the product of the composite aspect ratio and volumetric fibre content, $\eta\chi$. This is in good agreement with the reported behaviour effects of increasing composite fibre factor in the literature.

Some differences in fibre performance were found to be evident between different trapdoor widths. The fibre composite effectiveness was highest in the large scale trapdoor tests (*B* = 105 mm) where displacements at the ultimate stage of the test were reduced by up to 70% compared to the unreinforced case. The FRS effectiveness appears to reduce proportionally with trapdoor width. In small trapdoor tests (*B* = 30 mm), fibre composites were found to be roughly ~25% less effective (in terms of surface displacements) than in tests conducted with the large trapdoor.

The general strain response for the small trapdoor shows significant differences to that for the larger trapdoors.

Higher levels of shear strain are observed in unreinforced tests with the medium and large scale trapdoors. At large relative trapdoor displacements, the strains and general mechanism is consistent with residual soil strength behaviour.

The corresponding strength envelope for small trapdoor tests, inferred from the lower levels of shear strain and general absence of surface failure, is closer to the peak strength behaviour of the soil.

It is well-documented that fibre composites are found to be most effective at post-peak strain levels, where the tension in the fibre can be fully mobilised.

Therefore, the effectiveness of fibre composites in small trapdoor tests is reduced in proportion to the difference between the residual and peak strength behaviours observed between large and small trapdoor tests, respectively.

Some exceptions to the general trend in increasing effectiveness with increasing fibre factor are noted from the tests:

- Fibres appear to be less effective in small and medium trapdoor tests when the fibre length is increased beyond a critical level.
- Fibres appear to be less effective in small trapdoor tests when the fibre content, by mass, is relatively high (~1%).

For the small trapdoor, the loss of fibre effectiveness can be characterised by the fibre factor, as this value increases beyond ~0.32% the effectiveness of the fibre was found to be reduced.

This general effect can be attributed to the loss of fibre contact and interaction with the soil as the fibre is deformed along the fibre length. The degree to which an individual fibre is deformed increases with the ratio of fibre length to trapdoor width. This ratio is essentially a measure of the coverage of the high deformation area above the trapdoor by an individual fibre.

As the fibre length exceeds a critical length, relative to B, it is postulated that it will become less effective as the net tensile forces developed along its length will be lower due to the loss of interaction caused by the increased bending and twisting deformations the fibre is subjected to across the area of high deformation.

6.2 Further work

In order to fully investigate the soil-fibre interaction in a ground loss scenario, trapdoor tests varying the ratio of d_{50}/B should be conducted. If the average grain size of the material used is reduced to ~0.1 mm this ratio is significantly reduced for all the trapdoor widths considered in this study. The shear band thickness will be accordingly reduced to values of the order of ~1 mm, giving a thickness to trapdoor width ratio, t/B, of 1/30 for the small trapdoor, an order of magnitude smaller than that reported in this study.

At small relative shear band thicknesses, it is to be expected that higher shear-strains will develop with relative displacement (as reported for the larger trapdoor widths) and lower strength behaviour of the unreinforced soil will emerge at large displacements. If a similar unreinforced soil strength envelope is tested for each trapdoor scale, it is to be expected that the general effectiveness of the fibre will be similar across the trapdoor scales.

The scaling effects reported in this study could be investigated further by conducting tests with longer fibres to investigate further the critical length where the fibre effectiveness is reduced and to determine the corresponding minimum structure width that can be used, such that scaling related limitations are avoided in small scale model tests.

The use of X-ray scanning techniques could be employed to investigate the variability of samples produced using typical soil compaction methods, and further determine the effect of fibre orientation and dispersal on composite strength through soil testing.

The ratio of soil cover height to structure width, *H/B*, was maintained at ~1.66 throughout in the tests reported herein. This ratio is thought to be in the transitional region between shallow and deep behaviour. As the ratio is reduced further it is expected that arching effects in the soil will lessen (trapdoor loading will reduce to a lesser extent), and displacements and shear strains at the surface will be increased. Whereas increasing the *H/B* ratio is reported to have little effect on the formed arch shape over the trapdoor, or the loading response, but significantly reduces the surface settlement.

The effectiveness of the fibre composite in the extreme conditions could be assessed by conducting centrifuge tests over a variety of *H/B* ratios.

In this study only a single polypropylene fibre type has been used. Similar trapdoor tests could be conducted in which other fibre types of differing strength, stiffness and dimension could be used in order to determine the effect on settlement response and gain a better insight into the fibre-soil interactions taking place. The range of fibre factor, $\eta\chi$, considered in this study is relatively low (~0 to 0.48%) further work could be done to investigate higher ratios by changing the aspect ratio and increasing the concentration of the fibre. Smaller diameter fibres of similar lengths could achieve this if a reliable method of mixing and evenly distributing finer polypropylene fibres (typically of diameter ~10-100 μm) can be found.

A potential application for fibre-soil reinforcement is reducing heave displacement in expansive soils where passive arching is taking place. The methods employed herein to study active arching displacements could easily be adapted to model this scenario. The trapdoor setup can be used to study passive arching situations whereby a trapdoor mechanism is simply raised rather than lowered.

REFERENCES

Aslam, R. (2008). *Centrifuge modelling of piled embankments*. PhD thesis, University of Nottingham.

Atkinson, J. H. & Potts, D. M. (1977). *Stability of a shallow circular tunnel in cohesionless soil*. Geotechnique, 27(2), 203–215.

Attewell, P. B., Yeates, J. & Selby, A. R. (1986). *Soil movements induced by* tunnelling and their effects on pipelines and structures. Blackie and Son Ltd, London.

BS8006, (1995). *Code of practice for strengthened/reinforced soils and other fills*. British Standards Institution.

Carlsson B. (1987), *Reinforced soil, principles for calculation*, Terratema AB, Linköping (in Swedish).

Celestino, T. B., Gomes, R. A. M. P. & Bortolucci, A. A. (2000). *Errors in ground distortions due to settlement trough adjustment*. Tunnel. Undergr. Space Technol. 15(1), 97–100.

Costa, Y. D., Zornberg, J. G., Bueno, B. S. & Costa, C. L. (2009). *Failure mechanisms in sand over a deep active trapdoor.* J. Geotech. Geoenviron. Eng., 10.1061/(ASCE)GT.1943-5606.0000134, 1741–1753.

Diambra, A., Bennanni, Y., Ibraim, E., Russell, A.R. & Muir Wood, D., 2008. *Effect of sample preparation on the behaviour of fibre reinforced sands*. In: Proc. 4th International Symposium on Deformation Characteristic of Geomaterials, IS-Atlanta 2008. IOS Press, 629–636.

Diambra, A., Ibraim, E., Russell, A. R. & Muir Wood, D. (2013), *Fibre reinforced sands: from experiments to modelling and beyond*. Int. J. Numer. Anal. Meth. Geomech., 37: 2427–2455.

Ellis, E.A. & Aslam, R. (2009a). *Arching in piled embankments: comparison of centrifuge tests and predictive methods – Part 1 of 2.* Ground engineering, June 2009, 34-38.

Ellis, E.A. & Aslam, R. (2009b). *Arching in piled embankments: comparison of centrifuge tests and predictive methods – Part 2 of 2.* Ground engineering, July 2009, 28-31.

Ellis, E.A., Cox, C.M. & Yu, H.S. (2006). *A new geotechnical centrifuge at the University of Nottingham, UK.* In: C.W.W. Ng, L.M. Zhang, Y.H.Wang, (eds.), Physical Modelling in Geotechnics - 6th ICPMG ’06: 129–133. Hong Kong: Taylor and Francis.

Engesser, Fr. (1882). *Ueber den Ердduck gegen innere Stützwande (Tunnelwande)*. Deutsche Bauzeitung, 16, 91–93 (in German).

Evans, C. H. (1983). *An examination of arching in granular soils*, S.M. thesis, Dept. of Civil Engineering, MIT, Cambridge, MA.

Gao, Z. & Zhao, J (2013). *Evaluation on Failure of Fiber-Reinforced Sand* . J. Geotech. Geoenviron. Eng.(139), 95-106

Gray, D. H. & Al-Refeai, T. (1986). *Behaviour of fabric versus fiber-reinforced sand*. ASCE J. Geotech. Engng 112, No. 8, 804–820.

Gray, D.H. & Ohashi, H. (1983). *Mechanics of Fiber-reinforcement in Sand*, ASCE J. Geotech. Engrg. 109(3): 335-353.

Gregory, G. H. & Chill, D. S. (1998). *Stabilization of earth slopes with fiber-reinforcement*. Proc. 6th Int. Conf. Geosynthetics, Atlanta, 1073–1078.

Guido, V.A., Knueppel, J.D. & Sweeny, M.A. (1987). *Plate loading tests on geogrid – reinforced earth slabs.* Proceedings Geosynthetics 87 Conference, New Orleans, 216-225.

Handy, R.L. (1985). *The arch in soil arching.* ASCE Journal of Geotechnical Engineering, Vol. 111, No. 3, 302-318.

Han, J. & Gabr, M.A. (2002). *Numerical analysis of Geosyntheticreinforced and pile-supported earth platforms over soft soil*. Journal of Geotechnical and Geoenvironmental Engineering, January 2002, 44-53.

Hewlett, W.J. & Randolph, M.F. (1988). *Analysis of piled embankments.* Ground Engineering, April 1988, 12-18.

Hoare, D. J. (1979), *Laboratory study of granular soils reinforced with randomly oriented discrete fibers.* Proc., Int. Conf. on Soil Reinforcement: Reinforced Soil and Other Techniques, Ecole Nationale des ponts et chaussées, Paris, 47–52.

Iglesia, G.R., Einstein, H.H. & Whitman, R.V. (1999). *Determination of vertical loading on underground structures based on an arching evolution concept*. Proceedings 3rd National Conference on Geo-Engineering for Underground Facilities, 495-506.

Iglesia, G.R., Einstein, H.H. & Whitman, R.V. (2014). *Investigation of Soil Arching with Centrifuge Tests.* J. Geotech. Geoenviron. Eng., 140(2).

Jaky, J. (1944).*The coefficient of earth pressure at rest*. Journal for Society of Hungarian Architects and Engineers, Budapest, October 1944; Vol. 7, 355-358. (in Hungarian).

Kaniraj, S.R. & Havanagi, V.G (2001). *Behavior of cement-stabilization fiber-reinforced fly ash-soil mixtures*. Journal of Geotechnical and Geoenvironmental Engineering 127(7)

Knappett, J. & Craig R.F (2012), *Craig's Soil Mechanics, Eighth Edition* CRC Press.

Koutsabeloulis, N. C. & Griffiths, D. V. (1989). *Numerical modelling of the trapdoor problem*. Geotechnique, 39(1), 77–89.

Liu, W. (2010). *Axisymmetric centrifuge modelling of deep penetration in sand.* PhD thesis. University of Nottingham.

Low, B.K., Tang, S.K. & Choa, V. (1994). *Arching in piled embankments.* ASCE Journal of Geotechnical Engineering, Vol. 120, No. 11, November, 1994, 1917-1938.

Maher, M. H. & Gray, D. H. (1990). *Static response of sand reinforced with randomly distributed fibers. ASCE Journal of Geotechnical Engineering 116, No. 11, 1661–1677.*

Maier, C. & Calafut, T (1998), *Polypropylene: the definitive user's guide and databook*. William Andrew. p. 14. ISBN 978-1-884207-58-7.

Marshall, A. M., Farrell, R.P., Klar, A. & Mair, R. (2012). *Tunnels in sands: the effect of size, depth and volume loss on greenfield displacements*. Geotechnique, 62(5), 385–399.

McKelvey, J.A. (1994). *The anatomy of soil arching*. Geotextiles and Geomembranes 13, 317-329.

Michalowski, R. L. & Cermak, J. 2003. *Triaxial compression of sand reinforced with fibers*. J. Geotech. Geoenviron. Eng., 129(2), 125–136.

Naughton, P.J. (2007). *The significance of critical height in the design of piled embankments*. Proceedings of Geo-Denver 2007, Denver, Colorado

National Coal Board Mining Dept. (1975), *Subsidence Engineers' Handbook*, 2nd Edition, 1975.

Peck, R. B. (1969). *State-of-the-art report: Deep excavations and tunnelling in soft ground*. Proc., 7th Int. Conf. in Soil Mechanics and Foundation Engineering, Mexico City, 225–290.

Russell, D. & Pierpoint, N. (1997). An assessment of design methods for piled embankments. *Ground Engineering*, November 1997, 39-44.

Santichaianaint, K. (2002). *Centrifuge modelling and analysis of active trapdoor in sand*. Ph.D. thesis. Dept. of Civil, Environmental and Architectural Engineering, Univ. of Colorado at Boulder.

Sadek. Najjar, S.S. & Freiha, F. (2010). *Shear Strength of Fiber-Reinforced Sands.* J. Geotech. Geoenviron. Eng., 136(3), 490-499.

Santoni, R.L., Tingle, J.S. & Webster, S.L. (2001). *Engineering properties of sand fiber mixtures for road construction.* J. Geotech and Geoenv. Eng. ASCE, 127 (3), 258-268.

Stone, K. J. L. & Muir Wood, D. (1992). *Effects of dilatancy and particle size observed in model tests on sand*." Soils Found., 32(4), 43–57.

Taylor, R. N. (1995). *Geotechnical centrifuge technology*. London: Blackie Academic and Professional.

Terzahgi, K. (1943). *Theoretical Soil Mechanics*. John Wiley and Sons, New York.

Vardoulakis, I., Graf, B. & Gudehus, G. (1981). *Trap-door problem with dry sand: A statistical approach based upon model test kinematics*.

Visvanadam B.V.S. (2009). *Centrifuge Testing of Fiber-Reinforced Soil Liners for Waste Containment Systems*. Practice Periodical of Hazardous, Toxic, and Radioactive Waste Management, 13(1) ,45-58.

Vorster, T. E. B. (2005). *The effects of tunnelling on buried pipes*. PhD thesis, Engineering Department, Cambridge University.

White, D. J., Take, W. A. & Bolton, M. D. (2003). *Soil deformation measurement using particle image velocimetry (PIV) and photogrammetry*. Geotechnique, 53(7), 619–631

Whittaker, B. N. & Reddish, D. J (1989), *Subsidence: Occurrence, Prediction and Control,* Elsevier Science Publishing Company Inc., New York.

Zeng, X. & Lim, S.L. (2002), *The influence of centrifugal acceleration and model container size on accuracy of centrifuge test*, Geotechnical Testing Journal, ASTM, March.

Zhuang, Y. (2009). *Numerical modelling of arching in piled embankments including the effects of reinforcement and subsoil.* PhD thesis, University of Nottingham

Zornberg, J. G. (2002). *Discrete framework for limit equilibrium analysis of fiber-reinforced soil*. Geotechnique, 52(8), 593–604.